# The role of water properties and specific ion effects on the evolution of silica nanoconfinement

Markus Baum

# THÈSE POUR OBTENIR LE GRADE DE DOCTEUR DE L'UNIVERSITÉ DE MONTPELLIER

**En Chimie des Matériaux**

**École doctorale Sciences Chimiques Balard**

**Unité de recherche Institut de Chimie Séparative de Marcoule**

# The role of water properties and specific ion effects on the evolution of silica nanoconfinement

**Présentée par Markus BAUM**
**Le 09 Novembre 2018**

**Sous la direction de Diane REBISCOUL**

**Devant le jury composé de**

| | |
|---|---|
| Diane REBISCOUL, Expert senior, ICSM | Directrice |
| Pierre LEVITZ, Directeur de Recherche, PHENIX | Rapporteur |
| Alejandro FERNANDEZ-MARTINEZ, Chercheur CNRS, ISTERRE | Rapporteur |
| Thomas ZEMB, Professeur INSTN, ICSM | Président du jury |
| Jean-Marc, ZANOTTI, Directeur de Recherche, LLB/ILL | Examinateur |
| Samuel TARDIF, Chercheur, INAC/ESRF | Examinateur |
| Francois RIEUTORD, Directeur de Recherche, INAC | Examinateur |

UNIVERSITÉ DE MONTPELLIER

*Success consists of going from failure to failure without loss of enthusiasm*

*Winston Churchill*

**Acknowledgements**

The work for this thesis was carried out in the Laboratory for Nanomaterials in Energy and Recycling (LNER), part of the Institute de Chimie Séparative de Marcoule (ICSM). Besides, several research stays at the European Spallation and Radiation Facility (ESRF) in Grenoble and at the Paul-Scherrer-Institute in Villingen, Switzerland were performed. The thesis was supervised by Dr. Diane REBSICOUL and Dr. Francois RIEUTORD, CEA Grenoble.

First, I would like to thank the CEA and the ICSM for giving me the possibility to do my PhD thesis under these excellent conditions.

I wish to express my warm and sincere thanks to my PhD director Dr. Diane Rébiscoul without whom this PhD would also not have been possible. Her great advice, supervision, help and especially patience made it a great pleasure for me to work with her. With her support in endless nights of beam time at the ESRF / PSI she contributed in a large extent to the success of this work. I will miss her optimism and her positive way of thinking.

Furthermore, many thanks to my co-director Dr. Francois Rieutord for his fruitful discussion and the help during many research stays at the ESRF, Grenoble. In this context, Samuel Tardif is acknowledged, who was always available in his position as local contact at the ESRF.

I am also thankful to Vainina Russello and Helene Martin who cared about all administrative issues (which I would not have been able to deal with myself).

I would like to express my deeply thanks to all collaborators and coworkers at the ICSM who contributed direct or indirect to this work. The family like atmosphere at work helped a lot, especially at the beginning of my PhD: Michael, Max, Mario, Aurelio, Remi, Baptiste, Susan, Carlos, Manuel, Robert, and many more. Thank you for sharing these three years together.

Many thanks go to my friends that I have met during my stay in France. Furthermore, I would like to express my sincere thanks to Pauline and her family for their support and for giving me a warm welcome during one year of this PhD.

Großer Dank geht auch an meine zahlreichen Freunde in Deutschland, die trotz der großen Entfernung, immer für mich da sind. Hier besonders erwähnen möchte ich vor allem meine

wöchentliche Skype-Runde und gleichzeitig engsten Freundeskreis (Tobias, Markus, Dominik, Hansal und Kilian).

Außerdem möchte ich meinen Eltern, meiner Schwester und meinen Brüdern danken. Ohne ihre Unterstützung jeglicher Art wäre mein Studium und meine Promotion nie möglich gewesen. Euch gilt der größte Dank.

# Table of contents

# Introduction and scientific approach of this work

Solid-liquid interfaces are ubiquitous in nature and technology. Physical and chemical processes are strongly influenced by the characteristics of this interface. The understanding and the prediction of materials behavior in the fields of construction, membranes, catalysis, and nuclear wastes require the investigation of processes occurring within this interfacial layer. Several materials taking part in the nuclear fuel cycle (cementitious materials, corrosion products, clay materials, secondary minerals, membranes, spent nuclear fuel etc.) are completely or partially nanoporous (Figure 1). They consist of a set of confined media having a complex form and filled with water and ions depending on the processes, their use or their formation. The processes such as ions sorption[1], electrolyte diffusion[2], phase precipitation[3], pore wall dissolution or the recondensation of dissolved species[4,5] occurring in nanometer-sized porosities in contact with aqueous solution differ from those of bulk materials. Since this nanoporosity accounts for a non-negligible fraction of the total porosity in these systems, there is a significant impact on their macroscopic behavior.

Typically, water is confined in small pores of either minerals (soils, cements and cracks in rocks), biological matrices (cells, hydration shells of proteins), or many porous materials used for practical purposes, having a pore size in the nanometer range. As shown in Figure 2, water molecules will adapt their dissociative hydrogen bond network with respect to the media. For instance, water molecules in the bulk phase will assemble hydrogen bonds with their adjacent neighbors arranging themselves in tetrahedral coordination. The presence of electrolytes and charged surfaces can dramatically change the water organization and therefore its properties. Indeed, the water properties are strongly affected by electrostatic interactions and hydrogen bonding between water molecules and pore surfaces, structuring water and slowing its dynamics from nanoscale to macroscale.[6,7]

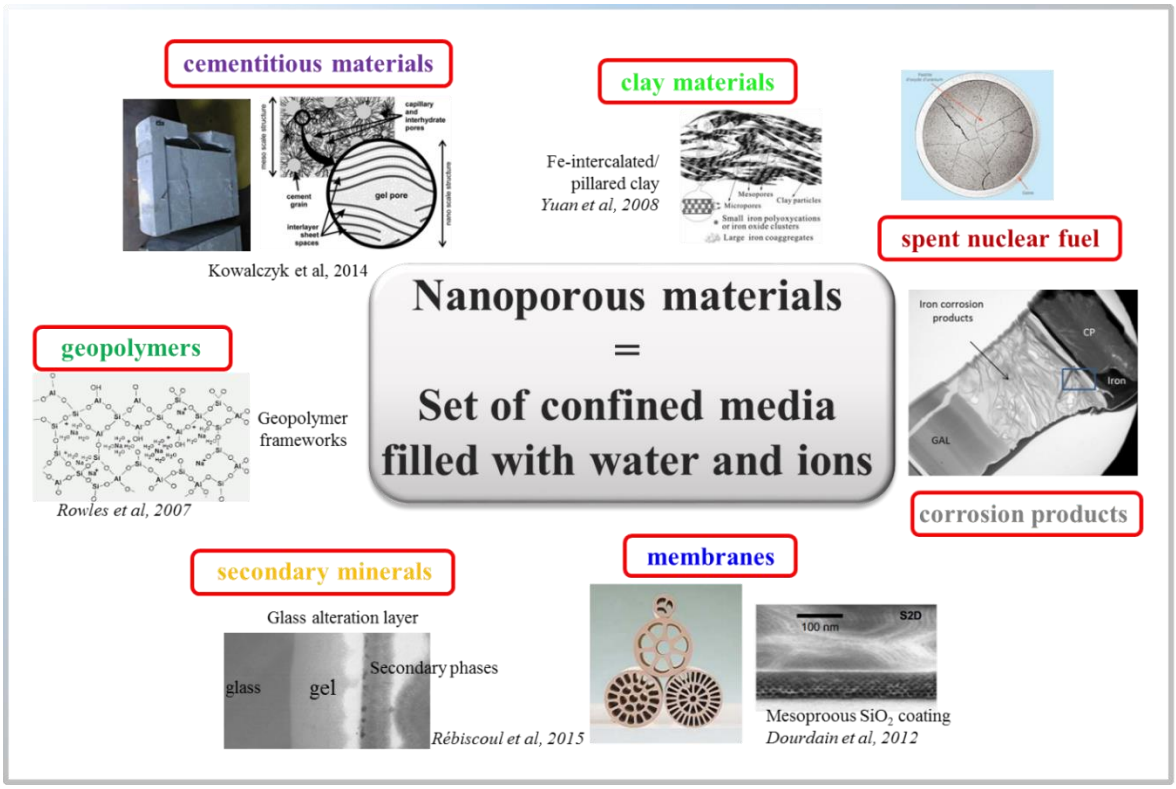


*Figure 1: Nanoporous materials occurring in various fields of application, such as geopolymers, cementitious, clay materials biomaterials and in the nuclear waste treatment.*[8–17]

Also, the presence of solvated ions and ions adsorbed on the nanopores surface, modifies the electrostatic interactions in the system and thus the interfacial layer at the solid-liquid interface.[18,19] These structural and dynamical changes in confinement and the presence of ions are expected to alter the water reactivity. Even though, there are many publications dealing with the solid-liquid interface, using an experimental and modelling approach.[20–22] In addition, few studies of atomistic modelling of water in confinement can be found. However, experimental data are still lacking in nanoconfinement. Since chemical reactions in such materials are controlled by an interfacial layer, all the processes occurring in nanoconfinement and their prediction remain scientific challenges.

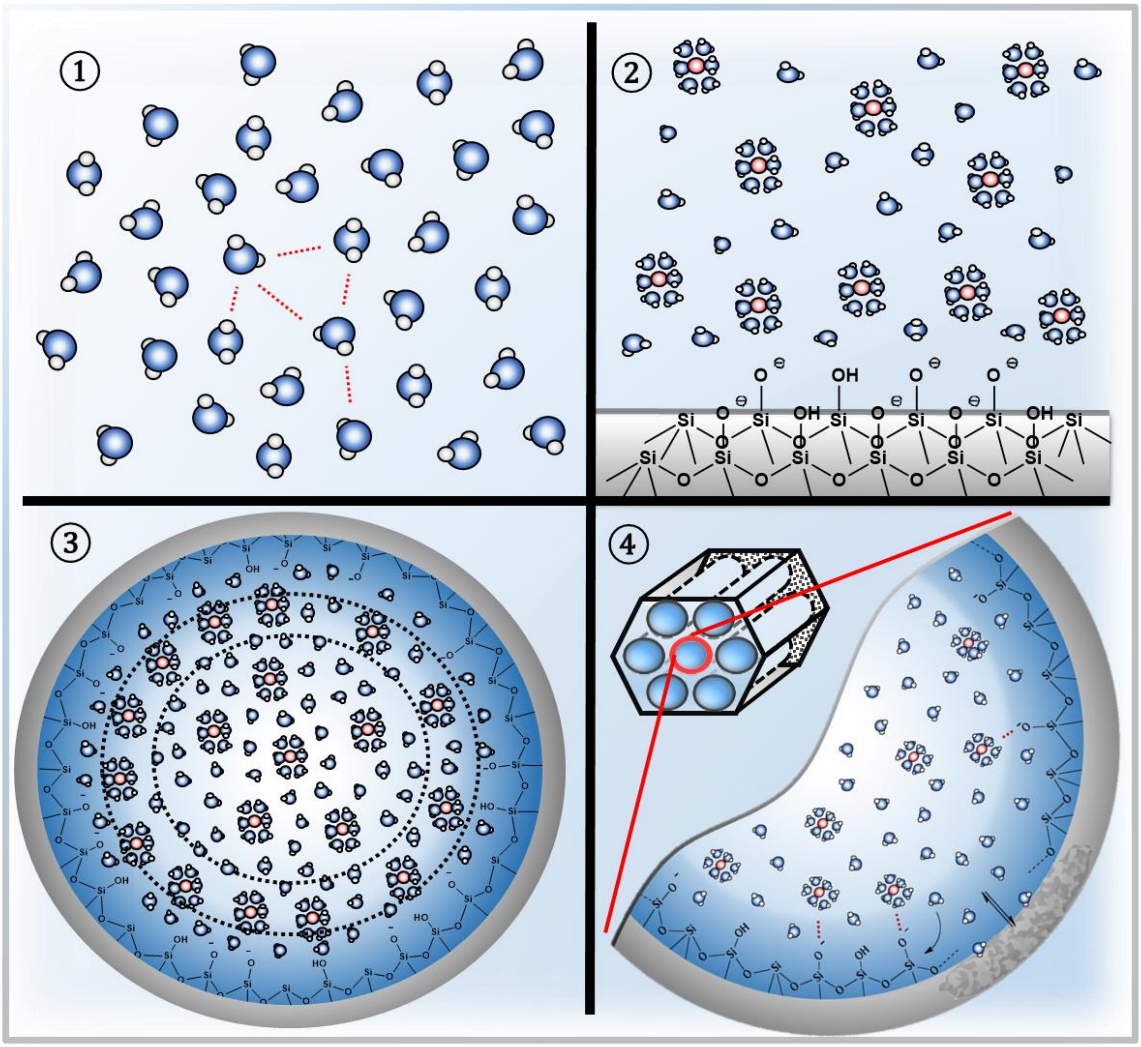


*Figure 2: ① Water molecules in the bulk phase build up a hydrogen bond network assembling a tetrahedral coordination for each molecule. ② Ions present in water are solvated and arrange with respect to a plane charged surface or ③ to a curved cylindrical pore ④ Chemical reaction in nanoconfinement changes with ion-water-surface silanol interaction (dissolution, precipitation, recondensation…). For the sake of readability, solvated anions are not shown.*

Predictions of the material evolution in terms of dissolution, precipitation and, recondensation often require the use of modelling, which is generally not adapted to nanoconfined media.[1] Many computer programs (PHREEQC, JChess, HYDROGEOCHE, etc.) as well as surface

complexation models (1-pK, 2-pK, MUSIC, etc.) use thermodynamic models and rate laws obtained from data measurements in bulk solution (concentration of dissolved ions, pH, kinetics and thermodynamic constants etc.). However, models arising from bulk solution measurements can be defective in confinement and raises the question, if the validity of these models and rate laws are still correct in nanoconfined media.

In the following chapter, we present a summary of the recent research in confinement and we discuss open questions and challenges occurring in experimental and theoretical investigation of confined aqueous interfaces and the corresponding structure and dynamics. We outline how water molecules behave adjacent to dissolved ions and what impact these solvation processes have on the water properties. Moreover, we pinpoint how the solid-aqueous interface and the confinement impact on the chemistry of water. What role does the interfacial layer between the solid and liquid bulk region have on the reactivity? The last part deals with the ion effects on the bulk dissolution behavior of silica.

The main scientific objective of this thesis is to relate the properties of confined water in presence of electrolytes to the evolution of mesoporous silica materials. To reach this goal, our original approach, consisting in the following chapter, was to use various electrolyte solutions having more or less kosmotropic properties $XCl_2$ (X = Ba, Ca, Mg) confined in model systems such as two parallel and plane silica surfaces spaced of 3 and 5 nm (nanochannels) and highly ordered mesoporous silica materials represented by SBA-15 (around 6 nm pore size and microporous walls) and MCM-41 (3 nm pore size and dense walls) to determine the impact of the curvature.

After a brief state of the art (Chapter I), the first step of our approach (Chapter II) was intended to determine the impact of the size of the confinement on the transport at a large scale, i.e. few mm, and on the interfacial layer between two parallel and plane silica surface spaced of 3 and 5 nm. These nanochannels were filled with electrolyte solutions and characterized during their filling using hard X-Ray reflectivity. From these results, the solution density inside the nanochannels was determined and the surface ion excess at the $SiO_2$ surface were calculated. The experimental results were compared with the results obtained from molecular dynamics simulations.

In a second step (chapter III), we studied the water properties in nanoconfinement made of silica concave surfaces such as cylinders. We intended to relate the confined water structure and its diffusion at a picosecond scale, to the pore size and the electrolyte nature. To reach this goal, several highly organized mesoporous silica presenting different pore sizes and walls (dense or microporous) were used as model materials: SBA-15 (pore size around 6.6 nm and microporous silica wall), MCM-41 and grafted MCM-41 (pore size varying from 2.9 to 2.4 nm and dense silica wall). These properties were extrapolated to the properties of water molecules located in the interfacial layer.

In the last step (Chapter IV), we have determined the evolution of the morphology and the structure of the same mesoporous silica, during short-term alteration by water and the electrolyte solutions. Both silica materials were characterized by in-situ Small Angle X-ray Scattering during their alteration at 50 °C. From the obtained results, we intended to relate the evolution of the confinement with the nature of the silica, the pore size and the electrolyte to find a relation between the water properties and the silica evolution.

# Chapter I - State of the art

The state of the art presents an overview about the research on water properties either in bulk solution or in the vicinity of solid-aqueous interfaces and in the presence of ions. We outline the fundamental thermodynamic equations that are necessary to understand changes in thermodynamic properties, structure and dynamics of water.

Furthermore, an ion classification is given in order to divide the nature of ions with respect to their ability to order or perturb the water structure. The last part deals with the catalytic ion effect on the dissolution process in silica.

## A. Bulk water properties and specific ion effects

Aqueous solutions play a prominent role in various geochemical and industrial processes. The physico-chemical properties of aqueous solutions are directly related to their structural and dynamical properties and more particularly to their ability to form hydrogen bonds.[23] In this part, we present how ions affect the thermodynamical properties of bulk water and therefore their impact on the structure and dynamics of water molecules.

### 1. Thermodynamical properties of water

For a better understanding of the ion effect on the thermodynamic properties of water, we need some basic thermodynamic energy functions and variables. Considering electrolyte solutions as a one-phase system (here: water) with *k* components, we obtain the internal energy of the system as a function of the volume *V*, entropy *S* and the amount of components $n_i$ yielding to the fundamental equation of thermodynamics[24]:

$$dU = -pdV + TdS + \sum_i \mu_i dn_i \qquad (1)$$

and its Legendre transform

$$dG = Vdp - SdT + \sum_i \mu_i dn_i \qquad (2)$$

where *G* denotes the Gibbs energy and $\mu_i$ the chemical potential of a component *i*. The Gibbs energy is very common in chemistry since it is usually used to describe changes occurring at constant temperature and pressure.

Using the Gibbs-Duhem equation $0 = -\mathrm{Vdp} + \mathrm{SdT} + \sum_i \mu_i n_i$ at a constant pressure and temperature, the total Gibbs energy follows the chemical potential of solute and solvent. The chemical potential can be defined as partial molar Gibbs energy for every solute

$$\mu_i = \left(\frac{\partial G}{\partial n_i}\right)_{p,T} \quad (3)$$

For its use in thermodynamical calculations, the chemical potential is split into two parts relating to a reference potential, $\mu_i(p,T)$ and a corresponding activity $\overset{*}{a_i}$

$$\mu_i(p,T) = \overset{*}{\mu_i}(p,T) + RTln\overset{*}{a_i} \quad (4)$$

Since we are dealing with real solutions, taking into account intermolecular interactions and the fact that solutes are influenced by their neighbors, we define the corresponding activities of solvent and solute, using the mole fractions $x_i$ and the activity coefficients $f_i$

$$a_i = x_i f_i \quad (5)$$

In general, the activity depends on any factor that alters the chemical potential. Such factors may include: concentration, temperature, pressure, interactions between chemical species, electric fields, etc. It is important to note that the activity depends on the choice of standard state such that changing the standard state will also change the activity. This means that activity is a relative term that describes how "active" a compound is compared to when it is under the standard state conditions.

How can solutes, for instance dissolved ions, change the chemical potential and the thermodynamics properties of a pure liquid such as water? In the following part, we consider colligative properties, so properties in dilute solutions, which depend only on the number of solutes present in the solvent. All the colligative properties stem from the reduction of the chemical potential of the liquid solvent as a result of the presence of solute.

For an ideal-dilute solution, the reduction is from $\mathring{\mu}_i$ for the pure solvent to $\mathring{\mu}_i + RTlna_i$ when a solute is present. Because the entropy of the aqueous solution is already higher than that of the pure liquid, the enhanced molecular randomness of the solution opposes the tendency to freeze. The evolution of the chemical potential as a function of the temperature is highlighted in Figure 3.

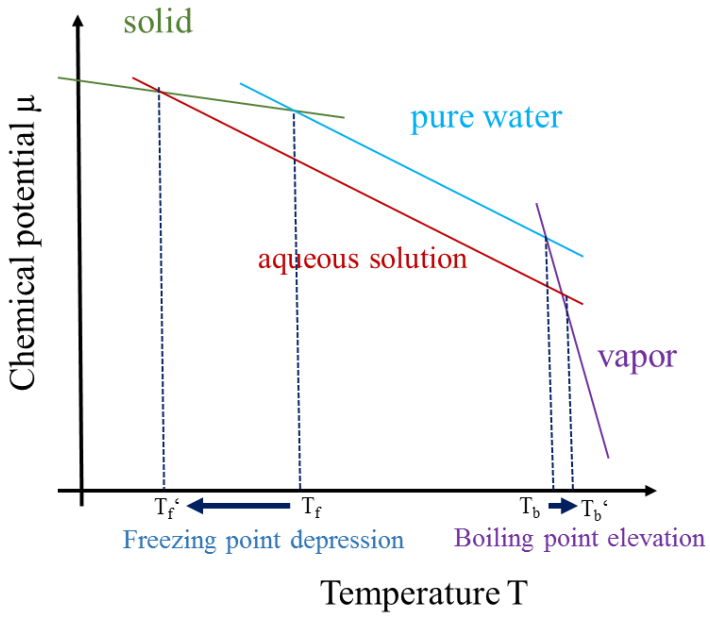


*Figure 3: The chemical potential of a solvent in the presence of a solute. The lowering of the liquid's chemical potential has a greater effect on the freezing point than on the boiling point. The temperature shifts are related to a higher entropy of the electrolyte solution. Figure adapted from ref* 25.

These colligative properties are the cause for several effects like lowering of the vapor pressure, the depression of the freezing temperature, the elevation of the boiling temperature and the osmotic pressure of a pure solvent into an aqueous solution. These colligative properties do not refer to the nature of the solute, only to the mole fraction. However, the addition of various salts alters the water properties in a different way. The dissolution of electrolytes in water leads to a disruption of the hydrogen-bonding network and to the formation of hydration shells depending on

the ion nature. The next subchapter deals with specific ion effects on the structure of their surrounding water molecules.

## 2. Water structure

It is well-established that water is a highly structured liquid assembling an extensive hydrogen bond network. The hydrogen bond is a relatively strong intermolecular interaction between a hydrogen atom of one molecule and a nitrogen, oxygen or halogenic atom (higher electronegativity) of another molecule. Normally in water, every molecule can form up to four hydrogen bonds with other water molecules donating two hydrogen bonds and accepting two from their neighbors.[26] These hydrogen bonds are highly directional in nature, and have a near-tetrahedral arrangement around the oxygen atom of the water molecule. As a result, liquid water contains extended hydrogen-bonded networks and shows a high dielectric constant. Regarding the dissolution of electrolytes, the role of water as a solvent is to provide a medium of high relative permittivity ($\varepsilon_r$ = 78 at 25 °C) and therefore, the salt can dissociate into its constituent ions. The water molecules provide electron pairs to hydrate cations and hydrogen bonds to hydrate anions in hydration shells. In particular, ions are expected to have a strong effect on the hydrogen-bond structure of liquid water, because of the strong electric fields associated to their charges. In this context, it is important to know these specific ion effects and to categorize the ions with respect to their impacts on the structure.

Almost 120 years ago the first approach was done by *F. Hofmeister* who tried to classify the influence of various salts on the solution behavior of macromolecules and living tissue. This classification (Hofmeister series) should give idea about the ability of salts to precipitate proteins from aqueous solutions.[27] As shown in Figure 4, ions were divided according to their water

ordering ability, where kosmotropic ions strengthen the water structure (structure-maker) and chaotropic ions perturb the water structure (structure-breaker).

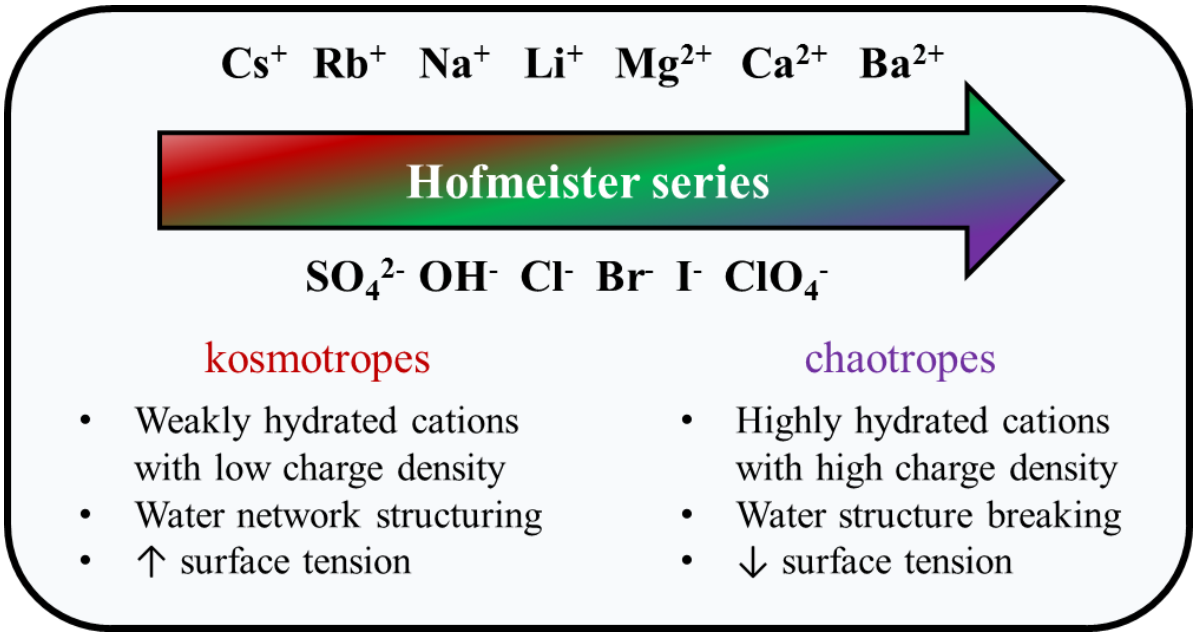


*Figure 4: Classification of ions in the Hofmeister series and their specific impact on aqueous solutions in biological media. Figure adapted from ref* 28.

Later this formalism was extended by Collins.[29] Basically, kosmotropes are considered to be highly hydrated ions with a strongly attached hydration shell. Due to their high charge density (small ions with high electric charge), kosmotropic ions exhibit low polarizability and may precipitate proteins from aqueous solutions (salting-out effect). In contrast, chaotropes are more polarizable ions, which are surrounded by a weakly attached hydration shell. Since this hydration shell is only weakly attached, surrounding water molecules can be shed off easily.[30] The exact classification of kosmotropes and chaotropes remains a highly discussed debate.

In contrast to the work of *Omta et al.*[31], which revealed that ions do not strengthen or break the water structure, several studies have shown that indeed ions have effects on the water structure. First studies of *Walrafen and coworkers* have shown the structure-breaking effect of $ClO_4^-$ ion on

the water structure using Raman spectroscopy.[32] In a more recent study, *Sun et al.* have confirmed that the addition of NaCl to water breaks the tetrahedral hydrogen bonding.[33] Generally, halides were found to a have a structure-breaking effect on the tetrahedral structure of water due to strength of halogenic ion-water compared to water-water interaction.[34] *Mancinelli et al.* have concluded from neutron scattering experiments and molecular dynamics simulation that there is an ion-induced perturbation even for rather dilute (~ 1 M) solutions in the first hydration shell and even beyond.[35,36] The near-IR spectral study of pure water and aqueous solutions concluded that water within the hydration shell of cations assembling hydrogen bonds whereas the number and strength are increasing with the cation charge density.[37] *Kropman et al.* have studied the relaxation of the O-H stretch vibration of water using pump-probe spectroscopy.[38–40] Mechanism and lifetimes of vibrational relaxation of water molecules in the solvation shells of various anions ($Cl^-$, $Br^-$ and $I^-$) and cations ($Li^+$, $Na^+$ and $Mg^{2+}$) were analyzed. The results suggest that the lifetime in the vicinity of anions show slower kinetics than for pure water. The frequency of the O-H vibration increased in the order $Cl^-$, $Br^-$ and $I^-$, which can be related in weaker hydrogen bonds. The effects are less pronounced for cations and do not affect the orientational dynamics outside the first hydration shell, but the strength of the hydrogen bond is found to decrease with the polarizability. Dielectric relaxation spectroscopy (DRS) of aqueous solutions of NaCl, KCl and CsCl have shown that the solute impact on the water structure decreases in the sequence NaCl > KCl > CsCl being proportional to the surface-charge density of the cation.[41]

MD simulations for ion solvation confirmed that the charge densities govern the interactions of ions with water, and that a balance of forces determines the water structure. Smaller ions were found to bond more closely to water molecules than are larger ions.[42]

## 3. Dynamical properties of water

Water molecules can undergo various types of motions: vibrational motion, rotational motion (hydrogen atoms around an OH bond) and translational motion at short and long distances. Since the time scales of these motions are different, the diffusion coefficients are not the same for investigations at different time scales. In Figure 5, several temporal resolutions for characterizations techniques are highlighted as well as the corresponding time scales of motions at the atomic and/or molecular scale.

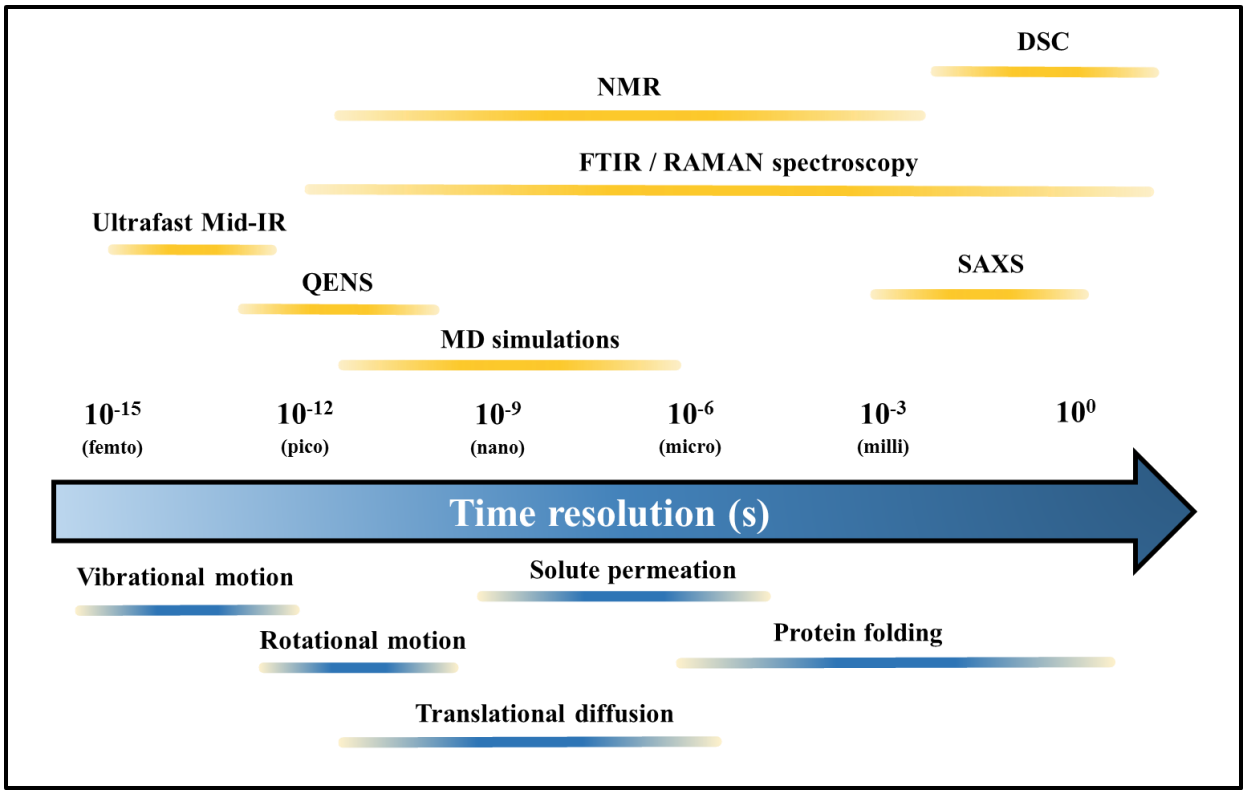


*Figure 5: Temporal resolution of various characterization techniques. The time scales of some fundamental atomic and/or molecule-scale motions are shown below.*

The dynamics of aqueous salt solutions have been studied with various experimental techniques like quasi-elastic neutron scattering, NMR, and DRS.[43] However, an often occurring

problem is that the intrinsic measuring times are too long (nano- to micro-second) compared to the water processes and their corresponding dynamics (for hydration shell exchange rates typically in the pico-second time scale). Moreover, sometimes it is very difficult to distinguish the different contributions to the dynamical behavior (dynamics of solvation shells and from the bulk). Self-diffusion coefficients of water as a function for ionic concentrations using the NMR spin-echo method were investigated in various studies.[44–46] Divalent ions like $Mg^{2+}$, $Ca^{2+}$ and $Ba^{2+}$ were found to reduce the water mobility with increasing concentration. $Mg^{2+}$ decelerates the water dynamics more pronounced than $Ca^{2+}$ and $Ba^{2+}$. *Hewish and coworkers* have revealed in a neutron scattering study the same influence of present ions on the water dynamics.[47] *Ben-Ishai et al.* classified the change in the translational diffusion coefficient with respect to ions having kosmotrope (NaCl) and chaotrope (KCl) properties.[18] Structure-making ions were found to decrease the water diffusion, whereas structure-breaking ions lead to an increase of the dynamical properties.

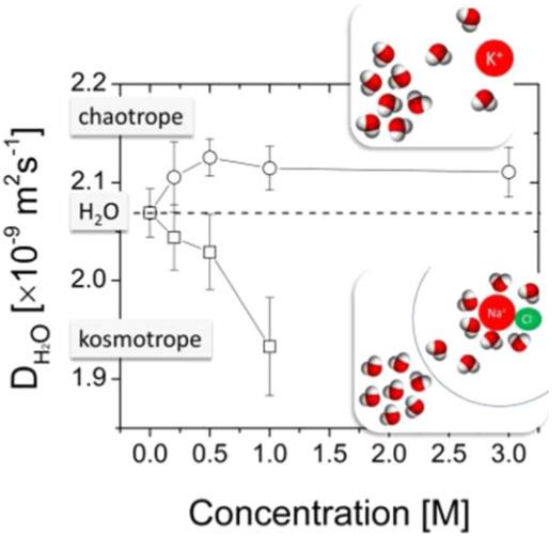


*Figure 6: The Q-averaged diffusion coefficients for NaCl and for KCl as a function of concentration. There is a marked difference between the diffusion of water molecules in the presence of potassium or sodium. Figure adapted from ref* 18.

Furthermore, *Buchner et al.* have concluded a significantly perturbation of the water dynamics in the presence of dissolved ions.[48] The DRS results exhibit that the rotational dynamics in aqueous solutions generally decrease with electrolytes, whereas the viscosity increases. For other types of electrolytes, the behavior can be more complicated. The ion-water interactions do not go beyond the first hydration shell. Thus, these results contrast with the results of *van der Post et al.* showing an impact for dissolved cations above a concentration of 3 M.[49]

Many attempts were made to relate inherent ion properties like size, hydration energy and charge with their role on the water structure and dynamics. The main physical properties of the cations used in the framework of this thesis are summarized in Table 1.

*Table 1: Main physical properties of the cations such as electronegativity, R = ion radius, $R_{hyd}$ = hydrated ion radius, $N_{H2O}$ hydration number, $D_{cation}$ = diffusion coefficient of the cation in water and $D_{H2O}$ = diffusion coefficient of water electrolyte solution at 1 M [26,50–55](NMR spin-echo).*

| Cation | $z/r_{ionic}$ | R (Å) | $R_{hyd}$ (Å) | $N_{H20}$ | $D_{cation}.10^{-10}$ ($m^2.s^{-1}$) | $D_{H2O}.10^{-9}$ ($m^2.s^{-1}$) at 1 M | |
|---|---|---|---|---|---|---|---|
| Mg | 2.9 | 0.7 | 4.3 | 6 | 7.1 | 1.8 | Chaotropic properties ↓ |
| Ca | 2.0 | 1.0 | 4.1 | 8 | 7.9 | 2.0 | |
| Ba | 1.4 | 1.4 | 4.0 | 9.5 | 8.5 | 2.1 | |

Not only the presence of ions are expected to affect the structural and dynamical water properties but also the interactions with the solid interface. Charged surfaces interact with water molecules and ions. These interactions lead to an interfacial layer with depends on the surface potential.

## B. Aqueous solutions at a solid dense planar surface

Generally, solid-liquid interfaces can be described with four distinct regions: (1) the bulk liquid, (2) the interfacial layer, (3) the solid interface in contact with the liquid, and (4) the subsurface where the properties of the bulk phase are recovered. Since the properties of the interfacial layer and the surface-near region are governed by mass and charge transport processes, a real impact on dissolution, catalytic and corrosion reactions is expected.

### 1. Conceptual models

Chemical reactions occurring at the mineral–water interface are controlled by an interfacial layer, few nanometers thick, whose properties deviate from those of the respective bulk mineral and water phases.[56] This interfacial layer can be successfully described by different models. In the following section, we present the electric double layer model and the Poisson-Boltzmann model.

#### 1.1 Electric double layer model

Whenever surfaces with ionizable groups are exposed in a polar solvent, for instance water, electric double layers are formed spontaneously. The high dielectric constant ε of water favors the dissociation of surface groups, resulting in a net surface charge. This surface charge tends to be screened by building up a charge density (coions and counterions in electrolyte solutions) of opposite sign with respect to the surface charge. This so-called electric double layer is determined by the competition between the electrostatic interactions and the thermal motion of ions.

The molecular-scale structure of this interfacial layer, however, is poorly constrained, and correlations between macroscopic phenomena and molecular-scale processes remain speculative. In order to characterize the ion distribution in these double layers between two bulk phases, several models were proposed and have been adjusted throughout the years. The first attempt was given

by Hermann von Helmholtz in 1879. However, this net static model had only taken into account the capacity and the double layer thickness, but neither the ion diffusion in the solvent nor the possible sorption of ions. Thus, the initial model was improved in 1924 by L. G. Gouy and D. L. Chapman considering the thermal motion of the solutes and water molecules leading to a diffused layer extending over several molecular layers, the so-called Gouy-Chapman double layer.[57] In this model, the charge distribution of ions in the electrolyte is understood as a function of the distance from the metal surface and can be described by the Maxwell-Boltzmann distribution. This means that the electric potential decreases exponentially from the surface into the liquid. Failing for highly charged double layers, O. Stern combined the theory of Helmholtz with the one of Gouy-Chapman.[58]

The EDL is composed of a rigid and a diffuse layer, called Stern layer, and ions having a finite size. In 1947, D. C Grahame modified the "Stern-model" by taking into account the adsorption, solvent and solvation processes. Consequently, the "Graham-model", presented in Figure 7, is built up from three different layers: a solvent layer (inner Helmholtz layer), a layer with solvated counterions (outer Helmholtz layer) and a diffuse layer. The thickness of this interfacial layer is expected to be around three molecular layers away from the surface. In the following, the term "interfacial layer" denotes the region from where the surface potential decreases to the electroneutrality of the bulk solution.

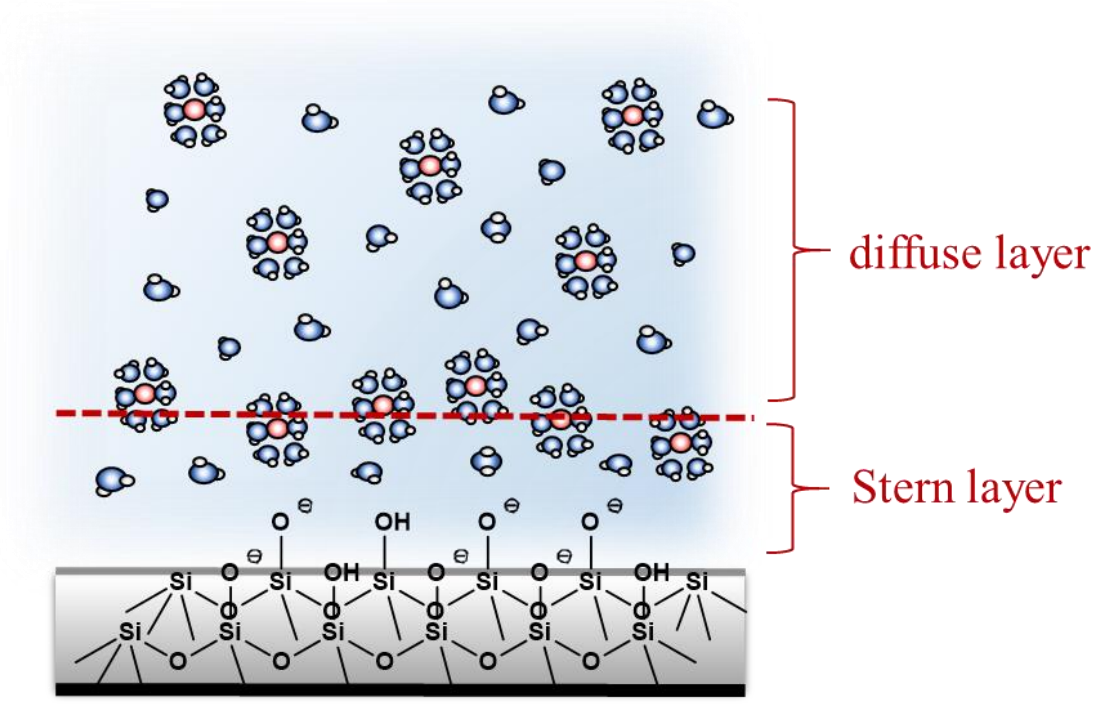


*Figure 7: Schematic representation of the double layer concept near a planar solid - aqueous solution interface: Inner and outer Helmholtz layer and a diffuse layer at higher distance to the surface. Solvated anions are not shown here.*

### 1.2 Poisson-Boltzmann theory

In addition to the EDL model, the structure of the EDL has long been modelled using Poisson-Boltzmann (PB) theory. The PB theory incorporates Coulombic interactions among charged particles but treating them as point charges and neglecting their finite size. For most charged surfaces, the actual charge is determined by an equilibrium process involving exchange of charge species between the bulk solution and the interface. The final equilibrium state is determined by an interplay between three free energy contributions: the short range chemical interactions at the surface that promote adsorption; the long-range electrostatic interactions that act to prevent the formation of highly charged surfaces; and the entropy of the adsorbing ion, which typically favors desorption and the formation of the charged surface.

Charged surfaces are characterized by a surface charge density $\sigma$ and *a* potential $\Phi_0$. The adjacent solution contains electrolytes and is characterized by the bulk concentration $c_i$, ion valency $z_i$, and the solvent dielectric constant $\varepsilon_r$ .

If we want to determine the relationship between $\sigma$ and $\Phi_0$ and how the potential and distribution of ions in the solutions varies with distance from the charged interface we can solve the Poisson equations. In the region of the solution, this equation takes the form[59]

$$\varepsilon_0 \varepsilon_r \vec{\nabla}^2 \Phi = -\rho_{free} \qquad (6)$$

where the solution's charge distribution is expressed as

$$\rho_{free} = e \sum_i z_i c_i(r) \qquad (7)$$

where $c_i$ represents the local concentration of ions. Because the ions in the solution are free to respond to the electrical fields, the solution's charge distribution $\rho$, is not independently known. In addition to the electrostatic interaction energy, we must also consider the entropy associated with the solution's ion distribution. The electrostatic interaction favors an ordered and much localized ion arrangement, but entropic factors strive to generate a random uniform distribution of ions.

In an external potential, this compromise between energy and entropy results in a Boltzmann distribution:

$$c_i(r) = c_i(r) exp(\frac{-z_i e \phi}{kT}) \qquad (8)$$

The combination of the previous equation results in the PB equation describing the ion distribution in an electrolyte solution next to a charged interface.

$$\varepsilon_0 \varepsilon_r \vec{\nabla}^2 \Phi = -e \sum_i z_i c_{i0}(r)\, exp(\frac{-z_i e\phi}{kT}) \qquad (9)$$

In a real electrolyte solution, outside a charged surface, the ions constantly change their positions. In each moment, there is a certain position of all ions and we could, in principle, solve the Poisson equation for that particular charge configuration. In the next moment, ions have changed places slightly and we can solve for the new spatial variation of the potential. If we follow the system in this way over a molecularly long time, we get a distribution of values for the potential at each position in space. The average value of this potential is called the mean potential, and this is the relevant potential that enters the PB equation. Thus, in deriving the PB equation we have made a so-called mean field approximation replacing true ion distributions by their distribution in the mean, and the electrostatic potential by its mean value. This is a very useful and convenient approximation, but there are circumstances of practical importance where it gives quantitatively incorrect results and it can even fail qualitatively.

## 2. Thermodynamical properties at the solid-liquid interface

Differences in energy between molecules located at the surface and in the bulk phase of a material manifest themselves as surface tension. The surface tension γ and surface free energy concepts provide a basis for understanding a number of practically important phenomena such as capillary condensation of a liquid on a rough surface, growth of colloidal precipitates through Ostwald ripening, and the nucleation of a new phase under supersaturated conditions.

Since molecules at a surface are bonded differently (coordination numbers) than molecules in the bulk phase, the generation of interfaces requires energy. This energy is called surface tension and contribute to the Gibbs energy for surfaces and interfaces:

$$dG = Vdp - SdT + \sum_i \mu_i dn_i + \gamma dA \qquad (10)$$

If we consider now particles formed by precipitation from solution, all molecules of the precipitate and in solution are in equilibrium. Assuming constant temperature and pressure, the free energy of a particle *i* with n molecules has a bulk term $\mu_i n_i$ and a surface term $\gamma dA$. Nucleation means taking a molecule from the solution and add it to the colloidal particle. The free energy of forming a particle of radius *R* is expressed by:

$$dG = -nkTln\left(\frac{p}{p_0}\right) + 4\pi R^2\gamma = -\frac{4}{3}\pi\frac{R^3}{V_m}kTln\left(\frac{p}{p_0}\right) + 4\pi R^2\gamma \qquad (11)$$

Where $V_m$ represents the volume of particle. From this relation, the Kelvin equation is obtained describing the maximum possible vapor pressure in the presence of particle having a critical radius $R_c$ before the bulk liquid phase is necessarily formed.

$$kTln\left(\frac{p}{p_0}\right) = \frac{2\gamma V_m}{R_c} \qquad (12)$$

This nucleation theory can be found in several other phenomena like crystallization of a pure liquid, Ostwald ripening or heating above the boiling point. This means that crystallization of water can be significantly suppressed at the solid-liquid interface.

## 3. Structural properties

Sum frequency generation (SFG) spectroscopy is very effective to probe the solid-liquid interface and to give a detailed picture of interfacial water. Since the symmetry for surface-near molecules is different, bulk contribution to the SFG signal are eliminated and neat information of the interface are accessible. *Shen et al.* first carried out SFG measurements on the quartz/water interface distinguishing two major contributions: i) a disordered liquid-like contribution at 3400 $cm^{-1}$ and ii) a ordered ice-like contribution at 3200 $cm^{-1}$.[60,61] In addition, they found that the contribution of tetrahedrally coordinated water molecules, related to the band at 3200 $cm^{-1}$, are decreasing with pH. The strong effect of the surface charge on the water orientation and the corresponding hydrogen bond network was confirmed by *Ostroverkhov and coworkers.*[62,63] Above the point-of-zero-charge of silica (PZC ≈ 2 - 3)[64], the mainly negatively charged surface can interact with the water molecules in order to change the orientation significantly from the bulk phase. Recently, several studies have shown that not only the surface charge, but also the ion species[65,66] and their ionic strength[67] play a dominant role on the interfacial hydrogen bonding. Cations were found to have a less pronounced effect on the dissociation constants of surface silanol groups than anions. Moreover, for sufficiently high ion concentrations, the decrease of the SFG signal is related to a disruption of the hydrogen bond network. [68,69] *Pezzotti et al.* defined in their SFG study two interfacial regions depending on the water orientation: the interfacial layer and diffuse layer.[70] By deconvolution of the two contributions, the SFG analysis leads to a specific water structure in the interfacial layer, whereas the local hydrogen bonding in the diffuse layer is comparable to bulk water. Furthermore, they found that $K^+$ ions adsorb in the interfacial layer where $Cl^-$ ions are located in the diffuse layer.

### 4. Dynamical properties

The dynamical properties of water molecules in aqueous solutions in contact with a solid phase were predominantly studied by MD simulations of water in parallel plane nanochannels. The walls are modeled as flat surfaces interacting with the fluid molecules via a continuous potential varying only with perpendicular distance from the wall[71–75]. The simulations have revealed that the diffusion of water molecules in interfacial layers is significantly affected by the surface. The viscosity of water was found to increase dramatically in the near wall region where the ion concentration is high. Such a dramatic increase in viscosity seems to be related to the high electric field strength, layering of the fluid molecules and the high concentration of ions near the channel wall.[76,77] Dynamical properties obtained from simulations can be distinguished in two different diffusion coefficients: diffusion perpendicular to the surface and diffusion parallel to the surface. The diffusion perpendicular to the surface was found to be drastically reduced with respect to the bulk values whereas the change of the parallel diffusion coefficients are not so pronounced.[78]

## C. Aqueous solutions at a curved surface

Going away from planar solid-liquid interfaces, the curvature of the surface is expected to have further effects on the structure and dynamics of aqueous solutions.

### 1. Extended conceptual models

It is important here to bear in mind that the previously mentioned concepts are established for plane surfaces in contact with aqueous solutions. For cylindrical surfaces the electric double layer of concave shape, the ion distribution is comparable; cations are accumulated near the charged surface while anions are depleted from this region. In the case of charged porous media, the PB approach is also particularly significant because it yields the equilibrium electrostatic properties of

the materials and it can be easily coupled to further equations in order to provide a global model of the system.[79] Assuming an extended Poisson-Boltzmann theory, *Bohinc and coworkers* have calculated the ion concentration profiles for several geometries.[80]

Particularly, in highly ordered mesoporous silica the confinement effect is expressed by the reduced number of accessible surface sites and the corresponding OH-OH distance between the sites. The Cd(II) adsorption isothermes on SBA-15 and on nonporous silica Spherosil carried out by *Prelot et al.* have revealed that the average OH-OH distance between the surface sites in mesoporous silica is 2.6 times bigger than for plane surfaces.[81] Furthermore, they have concluded that the number of accessible surface sites is decreasing in the confinement. The increasing distance is directly related to the entropy-driven ion adsorption and lowers the possibility of ions to interact with them.

Considering these models, our confined system may indeed be described as follows: a bulk-like part in the pore center and an interfacial layer at the pore surface presenting an excess of ions due to their sorption at the pore surface. Generally, this interfacial layer can be described by double-layer or a triple-layer models such as the Gouy-Chapman-Stern-Grahame model. According to the pH values in solutions, solvent molecules and hydrated cations are adsorbed in the inner and outer Helmholtz layer to compensate and reduce the surface potential $\psi_{surface}$ to an effective potential $\psi_{eff}$. The remaining counterions feel a much reduced "external" potential and form the "diffuse" part of the double layer until electroneutrality is reached. Regarding the existence of such interfacial layer in confinement, it is reasonable to assume that the observed changes of water structure and dynamics may be mainly associated with the modification of the water properties within a layer having a thickness of few water molecules.[7]

## 2. Thermodynamic properties in nanopores

### 2.1 Thermodynamic properties of water in nanopores

Since the late 19th century, the melting and freezing behavior in spatially restricted systems has been of considerable interest. In 1888, *J. J. Thompson* suggested that the freezing temperature of a small finite particle is depending on the physical and chemical properties of the surface. Later in the 1950s, *Defay and Prigogine* have discussed these properties in relation to surface equilibrium thermodynamics.[82] The properties of solutions confined in nanometric pores can be significantly different from those in the bulk phase due to higher surface contributions to the free energy of the fluid. Such confinement effects can result in a shift of the phase transitions, condensation of vapor at pressures well below the bulk vapor/liquid transition and the lowering of the freezing temperature of liquids. The lowering of the freezing temperature can be explained using the Gibbs-Duhem equation of a two-phase system of a spherical droplet coexisting in equilibrium with its vapor:

$$s_i dT - v_i dP_i + d\mu_i = 0 \qquad (13)$$

where $s_i$ and $v_i$ are the molar entropy and volume of phase $i$. $P_i$ and $\mu_i$ represent the pressure and the chemical potential of each phase $i$. Since the system is in equilibrium, the pressure $P_l$ of a liquid droplet having a radius $r_l$ and the pressure of its vapor has to fulfill the Laplace equation: $P_l - P_v = 2\gamma_{lv}/r_l$ , where $\gamma_{sl}$ is the surface energy of the droplet.

Assuming an ideal gas approximation for the vapor in Gibbs-Duhem and Laplace equations, neglecting the volume of the liquid relative to the volume of the vapor, one obtain the Kelvin

equation, giving the droplet temperature in equilibrium with its vapor (often expressed by the vaporization temperature) in equilibrium with a liquid droplet of radius $r_l$:

$$ln\frac{T^*}{T_0} = -\frac{2\gamma_{lv}}{r_l}\frac{v_l}{\Delta H_{lv}} \quad (14)$$

where $\Delta H_{lv}$ represents the transition enthalpy, $T_0$ is the bulk transition temperature and $T^*$ is the droplet temperature in equilibrium with its vapor (often expressed by the vaporization temperature). During the freezing process, there is a coexistence of solid and liquid phases inside the pores. Since the pore radius and the pressure remain the same during the phase transition and considering open cylindrical pores, the shift of the phase transition temperature can be expressed by the Gibbs-Thomson equation[83,84]:

$$T_p(R) - T_0 = -\frac{C_{GT}}{r} \; with \; C_{GT} = \frac{2T_0(\gamma_{sv} - \gamma_{lv})V}{\Delta h_{sl}} \quad (15)$$

where $T_p$ and $T_0$ denotes the solid-liquid coexistence temperature in the pore and in the bulk solution, respectively, and $C_{GT}$ is the Gibbs-Thomson constant, $r$ stands for the pore radius, $\gamma_{sv}$ and $\gamma_{lv}$ represent the surface energies per unit area of the interface solid/vapor and solid/liquid, $\Delta h_{sl}$ is the melting enthalpy and $V$ is the volume of the liquid phase or the solid phase. The last contribution is depending whether the solid or the liquid has the lower surface free energies with respect to the wall. Eq. 15 shows a linear relationship between the temperature shift and the inverse pore radius, meaning the smaller the pores the higher the temperature shift.

A combination of NMR line-shape analysis and differential scanning calorimetry (DSC) can provide detailed information on thermal events inside the samples. NMR experiments are able

to detect processes that lead to interaction changes, such as crystallization or melting. Moreover, the determination of phase transition are possible, whereas DSC present phase changes over a broad range of temperatures. Indeed, several authors have shown, using NMR[85–90] and DSC[91–93], that the decrease of the freezing temperature of water confined in mesoporous silica materials is consistent with the Gibbs-Thompson equation. The melting and freezing point depression of water in several sizes of confinement are illustrated in Figure 8. It is evident that the shift of the melting and freezing temperature increases with the inverse pore radius. This behavior suggests two different types of water within confinement: bulk-like water in the pore center and water influenced by the surface.

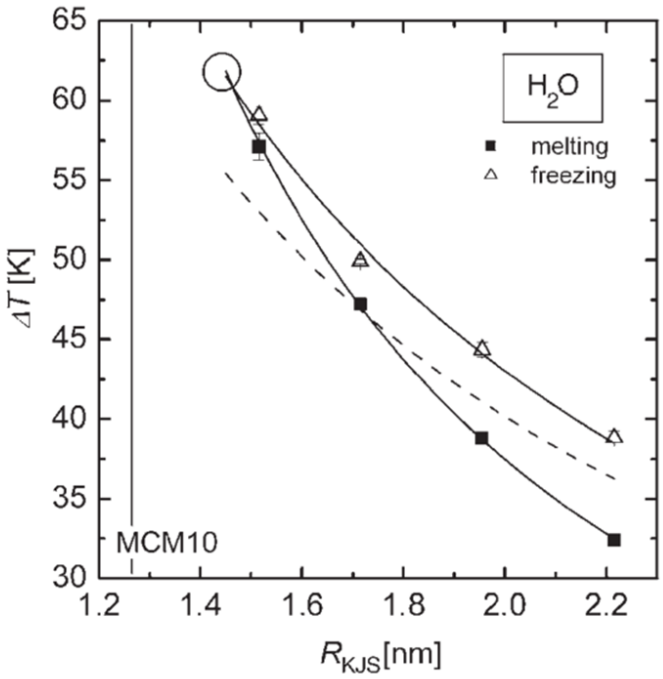


*Figure 8 Melting point depression and freezing point depression for $H_2O$ in pores of highly ordered mesoporous silica represented by MCM-41 using differential scanning calorimetry (DSC). The circle indicated the point at which the hysteresis disappears. Figure taken from ref* 83.

The experimental data can be fitted using an adapted Gibbs-Thompson relation considering a liquid-like layer next to the pore surface of thickness *t*:

$$\Delta T_p(R) = \frac{C_{GT}}{R - t} \qquad (16)$$

This behavior suggests that the hydrogen bond network of water is perturbed by the interaction with a hydrophilic substrate, and these structural changes have a pronounced effect on the thermodynamical properties of water. The thickness of this surface-bound non-freezable layer has been estimated to be approximately three monolayer of water molecules.

2.2 Thermodynamic properties of water in nanopores

From the basic thermodynamic relations for the surface we can define a surface excess of adsorbents related to the surface tension and the chemical potential of the solute. The Gibbs adsorption isotherm (at constant temperature) can be expressed as[59]:

$$-d\gamma = \sum_i \frac{n_i^\sigma}{A}\, d\mu_i = \sum_i \Gamma_i\, d\mu_i \qquad (17)$$

which relates the change in surface tension $d\gamma$, to changes in the chemical potential $d\mu_i$, through the surface excess. By defining an arbitrary plane dividing the two phases and expressing the chemical potential in terms of concentration: $\mu_2 = \mu_2^\theta + RTlnc_i$, we obtain a relationship between the surface tension, the chemical potential and the surface excess:

$$\Gamma_2 = -\frac{1}{RT}\frac{d\gamma}{dlnc_2} \qquad (18)$$

Therefore, in the case of solutes decreasing the surface tension (chaotropic ions), the concentration increase correspond to an increase of the chemical potential. Consequently, the surface excess increases, which means that ions favor sorption on the surface.

## 3. Water structure in nanopores

There have been many experimental reports on the structure of water confined in porous media investigated by NMR, DSC and X-Ray / neutron diffraction (XRD and ND) measurements. X-Rays are very appropriate to study solid-water interfaces. The surface-sensitivity arises from the interference of X-Rays scattered from the surface and interfaces.[56] Based on the XRD studies, *Morishige and coworkers* have shown that water confined in MCM-41 having a pore size of 4.2 nm freezes rather into cubic ice ($I_c$) than into hexagonal ice ($I_h$). Furthermore, the diffraction peak profile after freezing does not show diffusive scattering like in free water with short-range order. This can be explained by assuming an interfacial water layer with randomly displaced water molecules, confined between the crystalline ice in the pore center and the amorphous pore wall. The peak position analysis results in Scherrer lengths smaller than the corresponding pore sizes indicating a nonfreezable layer adjacent to the pore surface.[94] In another study, *Morishige et al.* investigated the freezing and melting behavior of water confined in SBA-15 (3.9 nm) depending on the pore filling. At low pore filling, they concluded that there is a nonfreezable layer at the pore surface of SBA-15. The formation of tetrahedral hydrogen bonds is hindered in this layer and may be less distinctive at higher pore filling.[95]

These results were confirmed by X-Ray and neutron diffraction experiments on hydrophilic and hydrophobic mesoporous silica. The different hydrophilic properties of the surface gave a detailed insight in the interaction pore wall – water molecules. For hydrophilic surfaces, like in

MCM-41 and SBA-15, the surface silanol groups modify the water structure due to interfacial hydrogen bonding. In contrast to hydrophobic surfaces, the surface groups will influence the orientation and configuration of water molecules adjacent to the pore wall.[96] The hydroxyl groups can act as either hydrogen bond donor or acceptor atoms for a hydrogen bond with water and will distort the hydrogen-bond network and its dynamics. These experimental results were confirmed by MD simulations in Vycor glass.[97]

In addition to that, the pore size is expected to have a significant impact on the structural properties of confined water. *Smirnov et al.* revealed in their diffraction study that decreasing pore size of MCM-41 (2.1 nm and 2.8 nm) leads to increasing distortion and breaking down the hydrogen bond network of water next to the pore wall.[98] Considering the hysteresis effect between freezing and melting of confined water, *Morishige et al.* found that this effect arises from the supercooling of water. However, the hysteresis is strongly size-dependent being negligible for small pores and becoming more significant for larger pores.[99]

While XRD provides information about long- and short-range ordering and periodicities, NMR spectroscopy is a powerful technique to get information about the local environment of the nuclei. Concerning NMR spectroscopy, both $^{1}H$ and $^{29}Si$ solid state NMR are used to characterize the porosity and the water structure within. In spatially restricted geometries, water can interact with surface molecules via hydrophilic and hydrogen bond interactions. These two interactions lead to a competition between surface-liquid and liquid-liquid interactions resulting in interesting new structures of water. NMR studies have revealed that different water environments existing within the mesopores of silica represented by their individual chemical shifts. *Grünberg et al.* have shown that at low filling level, water in SBA-15 is stronger bound than in MCM-41. The

water molecules at the surface of SBA-15 are enclosed to surface defects and more energy is needed to shed them off.[100]

Moreover, at higher pore filling, *Buntkowsky and coworkers* determined two different filling mechanisms for MCM-41 and SBA-15. The wide pores in SBA-15 are filled starting at the pore wall followed by a gradual increase of the thickness of the adsorbed layer until pore condensation takes place. In contrast, the smaller pores of MCM-41 are filled by pore condensation (axial-pore-filling). Due to dynamic exchange effects between water molecules and surface silanol groups, $^{1}$H-MAS spectra exhibit averages of the line positions. By a combination of $^{1}$H and $^{2}$H NMR, *Sattig and coworkers* have found fractions of liquid and solid water coexisting below 220 K. The fractions of water in diameter of 2 - 3 nm were assigned to interfacial and bulk-like water.[101]

Moreover, spectroscopic experiments can give a more detailed insight about the water properties. An incident electromagnetic wave (here Infrared light) will excite molecular vibrations providing information about the sample composition and their structure. As shown in the work of *Brubach et al.*, the frequency of the O-H stretching band (νOH) depends on the strength of the hydrogen bonding between the water molecules. The observed substructures in the νOH were assigned to different water populations having different coordination numbers. A shift of νOH band to the low-frequency region of the spectrum corresponds to an increase of the number of hydrogen bonds that a water molecule can establish with its neighbors. The frequency downshift can be related to a weaker OH oscillation strength.[102] *Le Caer and coworkers* have studied the structural properties of water enclosed within mesoporous glasses (8 – 320 nm) using FTIR-ATR. The distortion of the hydrogen bond network of water molecules is induced by the confinement.[103] Depending on the average number of hydrogen bonds with its surrounding neighbors, they

proposed three different types of water: fully bonded water ("network water") at low frequencies at 3310 $cm^{-1}$, water with an average hydrogen bond number below network water ("intermediate water") in the frequency range around 3450 $cm^{-1,}$ and poorly bonded water ("multimer water") at high frequencies at 3590 $cm^{-1}$. This perturbation was also found in the nanoconfinement of micelles and for Raman measurements in Vycor glass.[102,104]

SFG measurements have revealed, that interfacial water molecules form a hydrogen-bonding network with ordered (ice-like) and disordered (liquid-like) structures. *Zhang and coworkers* have studied self-assembled nanoporous silica films with 2 nm pores at several pH using SFG. At high pH, the negatively charged surface orients the interfacial water molecules to decrease the ice-like contributions and to increase the net polar orientations of liquid-like bands.[105] Comparable results were found for the water/quartz interface.[106]

*Gupta et al.* used classical molecular dynamics simulations to show water molecules optimize their orientation with respect to the surface silanol groups resulting in a less ordered structure for water adjacent to the surface.[6] Moreover, the combination of MD simulation and SFG show how the solid material surface perturbs the local structure and hydrogen bond dynamics of water until 1.0 nm away from the surface.

Eventually, the structure of interfacial water can be examined by measuring the relative permittivity of the system by applying an alternating electrical potential. Using Dielectric relaxation spectroscopy (DRS), the obtained dielectric constant κ leads to the dielectric relaxation time τ giving information about the local water structure. *Banys et al.* revealed three diverse dispersion regions for water enclosed in MCM-41. These regions correspond to three types of water more or less affected by the pore surface: liquid-like water in the pore center, intermediate water

layer with reduced mobility and interfacial water layer at the inner surface of the mesopores.[107] In the same system of MCM-41 having a pore size of 3.7 nm, *Kinka and coworkers* found strongly pore surface dependent freezing-melting dynamics. The analysis of the dielectric response and the conductivity depicts a formation of a highly disordered network of hydrogen bonds.[108] The same tendency for disordered orientation within the interface was shown in silica glasses, yet having higher pore sizes between 50 – 70 nm. The measured relaxation processes were significantly affected by the confined geometry and the water interaction with the pore wall.[109]

The combination of scattering and spectroscopy techniques allows one to obtain a detailed and advanced image of water confined in highly ordered mesoporous silica. It is well-established that water molecules in the immediate vicinity to the pore wall are strongly influenced by interactions with the surface groups.

## 4. Dynamical properties in nanopores

### *4.1.1 Water confined in mesoporous silica*

As already mentioned for bulk solutions, molecular motion in confinement can be effectively examined by neutron scattering techniques and especially at a pico-second time scale using quasi-elastic neutron scattering (QENS). From the elastic peak broadening at several values of the scattering vector, information about the sample dynamics can be obtained. In this context, *Teixeira and coworkers* studied the water dynamics in a temperature-range from room temperature to -20 °C in the supercooled state.[110] Two different times scales and their temperature dependence were determined by cooling down water from room temperature to – 20 °C. These two different time scales can be related to the short time and intermediate time scale of water motions. The different time scales of microscopic water motions within the mesoporous confinement are shown in Figure 9. At short time scales (pico-second time scale), where not all hydrogen bonds are broken,

the motion of the hydrogen atoms can be considered as a spherical rotation around the oxygen atom with a characteristic relaxation time $\tau_r$. Regarding the intermediate-time scales (nano-second time scale), when more bonds are broken, the proton can jump to the nearest site connected with a second relaxation time $\tau_0$. Vibrational motions (< pico-second time scale) are too fast for the time scale of the QENS experiment.

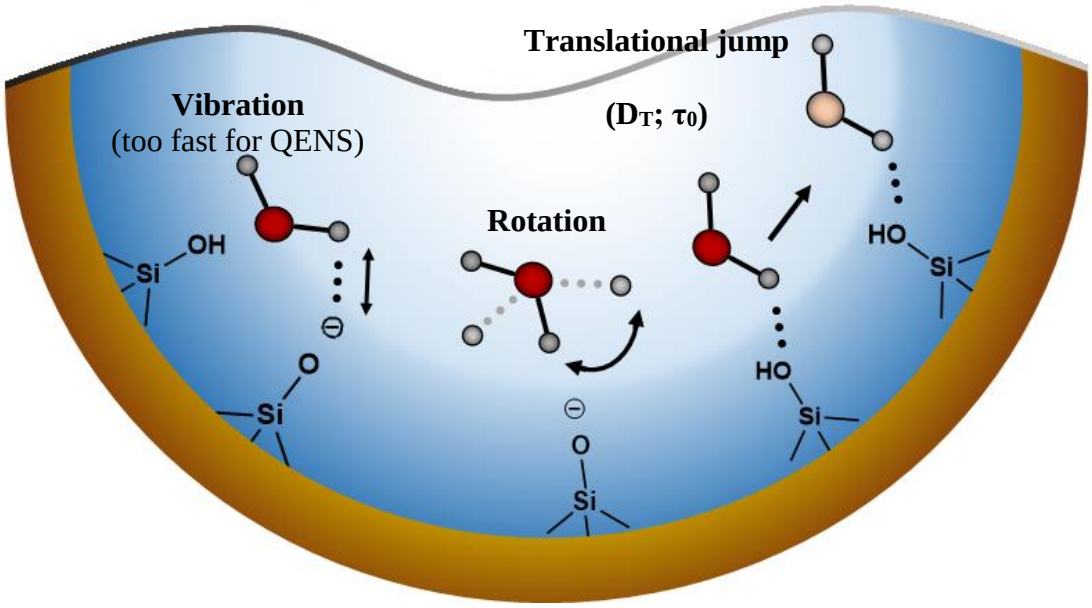


*Figure 9: Different water motions at various time scales within the nanoconfinement. The two different relaxation times found experimentally can be related to reorientation and translational jumps of water molecules. Vibrational motions are too fast for the QENS time scale.*

Previous studies have shown that dynamics of water molecules confined within mesoporous silica is perceptibly altered by decreasing the confinement size. *Takahara et al.* have used MCM-41 samples with different pore sizes in the temperature range from 200-300 K and measured the diffusion properties of water. Assuming the same time-scale model for the water motions, they found a decreasing translational diffusions coefficient $D_T$ with narrowing pore size from 1.9 nm to 1.1 nm.[111] Furthermore, the relaxation time $\tau_R$ for rotational diffusion and the residence time $\tau_T$

for translational diffusion both showed an Arrhenius temperature dependence, indicating a growth inhibition of hydrogen bond network. Generally, one can say that with a decreasing pore size the values for $\tau_R$ and $\tau_T$ are increased (slowed) due to an increasing amount of water molecules at the vicinity of the surface.

*Osti et al.* tried to quantify the water diffusion dynamics in confinement regarding the temperature and the pore size using a more general equation, assuming a sum of contributions from molecules acting like bulk water and molecules that are strongly influenced by the confinement[112]:

$$D_r(T) = \theta D_C + (1 - \theta) D_{bulk}(T) \tag{19}$$

where $D_{bulk}(T)$ is the bulk water translational diffusion at temperature $T$ and $D_C$ the temperature independent translational diffusion coefficient of the water molecules that are solely affected by the surface. The factor $\theta$, having values between 0 (bulk water case) and 1 (totally confined water) is representing a scaling parameter $\theta = \frac{V_{in}}{V_W}$ giving the volume ratio of water molecule within the influence of confinement $V_{in}$ and the total volume of water $V_W$. Figure 10 depicts the diffusion coefficients as a function of the temperature and pore size in MCM-41.

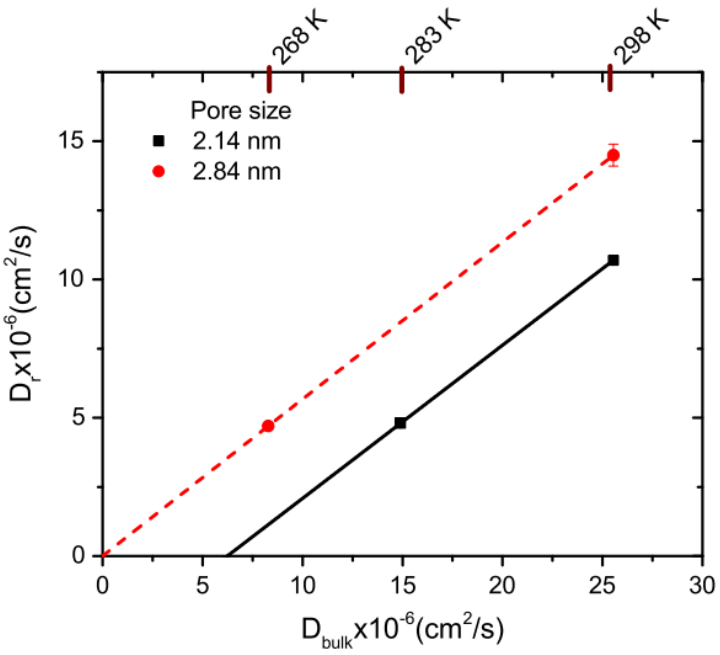


*Figure 10: Water diffusion coefficient $D_r$ vs $D_{bulk}$ in mesoporous silica MCM-41 for 2.1 and 2.8 nm. The lines are showing the best fits for equation 2. Figure adapted from ref* 112.

Generally, an increase of $\theta$, meaning more water molecules are influenced by the confinement, is related with a decrease of the pore size and the diffusion dynamics. Moreover, equation 19 was applied to data obtained from different materials of confinement (Vycor, carbon fibers, etc.) and concluded that size trend is a generic feature of water enclosed in spatially environment.

*Chiavazzo et al.* extended this general feature of confinement dynamics to over 60 different cases, confirming that the evolution of the diffusion coefficients can be described sufficiently accurate by introducing a scaling parameter.[7] Figure 11 presents the evolution of the self-diffusion coefficient of water within various types of restricted areas as a function of the scaling parameter.

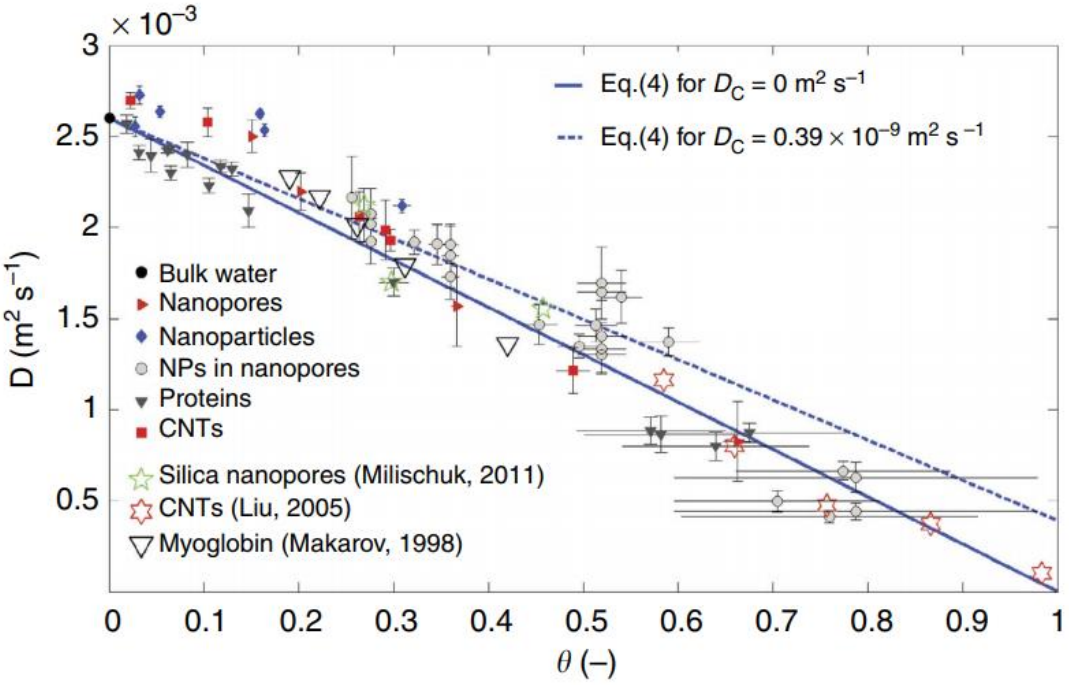


*Figure 11: The self-diffusion coefficient of water D for 60 different confinement cases including water confined in nanopores, proteins and carbon nanotubes. Figure adapted from ref 7.*

Indeed, it is possible to fit the data precisely using a simple relationship:

$$D(\theta) = D_B[1 + \left(\frac{D_c}{D_B} - 1\right)\theta] \qquad (20)$$

where $D_B$ is the self-diffusion coefficient of bulk water and $D_c$ is representing the self-diffusion coefficient of totally confined water. Table 2 presents a general overview about various values for the self-diffusion coefficient $D_T$ of water confined in several types of confinements at given temperature $T$. As highlighted, the diffusion coefficients decrease distinctively below confinement sizes of 5 nm and by decreasing the temperature $T$.[110,111,113–119] Self-diffusion coefficients obtained

by NMR field gradient and NMR dispersion measurements in Vycor glass having a confinement size of 4 and 7.5 nm are in good agreement with the values obtained by neutron scattering.[120,121]

*Table 2: Different values for self-diffusion coefficients $D_T$ of water confined in various types of confinements at the given temperature T.*

| Sample | Pore size (nm) | $D_T$ ($10^{-9}$ $m^2/s$) | Temperature (K) | $\tau_T$ (ps) | References |
|---|---|---|---|---|---|
| Bulk water | - | 2.5 | 298 | 1.1 | *Zanotti Bellissent 1995* |
| | - | 1.1 | 268 | 4.6 | *Teixiera 1985* |
| Vycor | 5.0 | 1.1 | 293 | - | *Zanotti Bellissent 1999* |
| | 5.0 | 0.8 | 258 | 4.3 | *Zanotti Bellissent 1995* |
| MCM-41 | 2.8 | 1.5 | 298 | 3.2 | *Takahara Yamaguchi 2005* |
| | 2.1 | 1.0 | 298 | 5.6 | |
| | 1.4 | 1.6 | 300 | 3.1 | *Takahara Yamaguchi 1999* |
| | 1.0 | 1.0 | 273 | 9.4 | |
| MCM-41 | 2.7 | 3.4 | 260 | 1.1 | *Matar Briman 2013* |
| | 2.3 | 2.4 | 260 | 1.4 | |
| | 2.0 | 2.1 | 260 | 1.3 | |
| Porous alumina | 5.0 | 1.7 | 270 | 8.8 | *Mitra 2001* |
| Single-wall nanotubes | 1.4 | 0.5 | 260 | 125 | *Mamontov 2006* |

Not only the confinement size and the temperature have an impact on the water properties, but also the composition of the confining surface. In this context, *Briman and coworkers* studied the impact of surface composition and confinement size on the dynamics of water molecules in highly ordered porous silica materials. Water properties were studied in mesoporous pores, having a size between 2.0 to 2.7 nm and possessing a modified surface by replacing the surface silanol groups with Al-OH and Zr-OH groups. At ambient temperature, a decrease of the mobile protons was observed when Si-OH groups were replaced with Al-OH and Zr-OH. This slow-down may be related with the stronger interaction between the more Lewis acidic Al-OH and Zr-OH groups and water molecules. It is worth to note, that the impact of surface composition was found to be more dominant on the water dynamics than the decrease of the confinement.[119]

In the recent past, much effort was put to confirm the experimental data by using theoretical calculations. Molecular Dynamic simulation (MD) is a very powerful tool to provide the most fundamental and flexible platform for analysis of molecular interaction. The trajectories of these particles are determined by solving different numerically Newton's equations of motion for the system. Inter-particle forces and their potential energies are calculated using interatomic potentials and molecular force fields. Therefore, MD simulations performed in realistic environments can be a great help for a better understanding and interpreting of the experimental data.

Generally, computer simulations performed on water properties confined in nanopores of MCM-41 and Vycor have revealed that the water behavior is strongly dependent on the hydration level inside the pore. In our context, we will only focus on the full hydration simulations. *Gallo et al.* presented in their calculations a formation of a double layer of water molecules close to the surface of the confinement. The density profiles of water oxygens along the pores, reported in Figure 12, exhibits clearly the formation of this double layer for MCM-41 and Vycor.

Furthermore, it is obvious that the density profile of Vycor is more homogeneous than for MCM-41 and the first shell of water is shifted towards the pore center.[122]

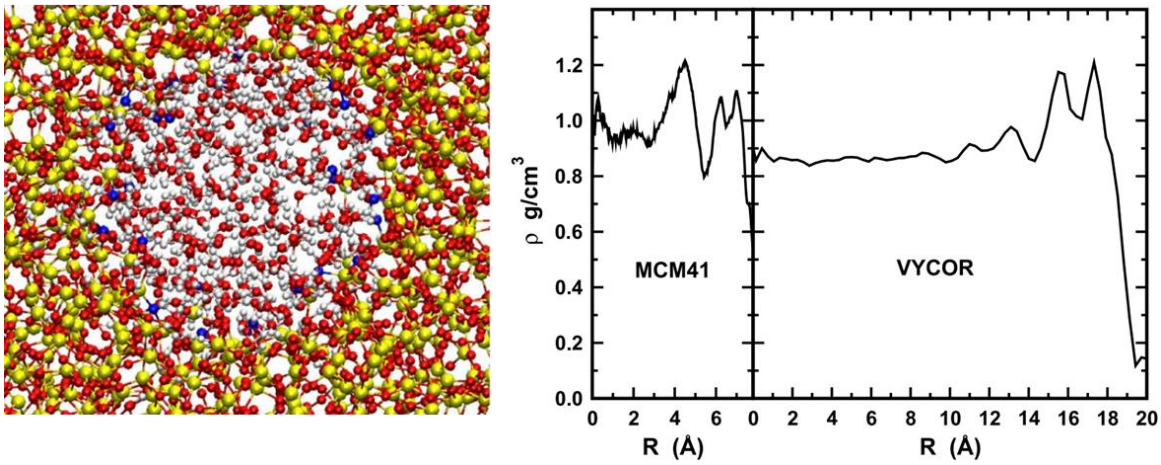


*Figure 12: Snapshot of MD simulation of water configuration within inside a silica pore of MCM-41 having a pore size of 1.5 nm at T = 300 K. The panel on the right: Density profiles of water oxygen along the pores of MCM-41 and Vycor (2.0 nm). R = 0 Å represents the silica surface. Figure adapted from ref* 122.

Due to strong interactions with the surface, calculation of hydrogen bonds of water confined in Vycor showed that the number of hydrogen bonds rapidly decreases inside the layer closer to the substrate. In this near-surface layer, the water molecules tend to form hydrogen bonds with the surface atoms. Bourg et al. have confirmed this behavior by modelling several pore diameter sizes. The diffusion coefficient was found to decrease significantly near the surface.[14]

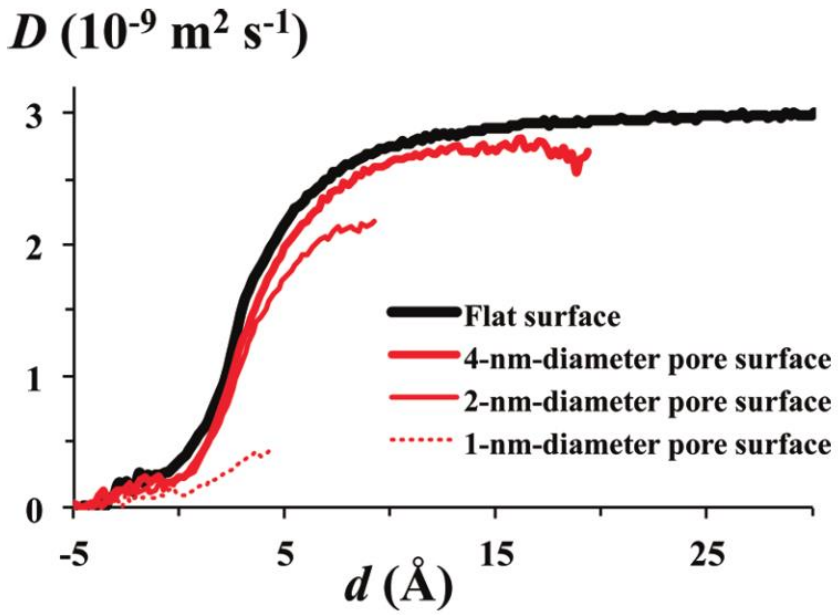


*Figure 13: Molecular-scale diffusion coefficient of water molecules plotted as a function of distance from the silica surface, on flat surfaces. Figure adapted from ref* 14.

Regarding the computer simulations made on water confined in nanopores of MCM-41 and Vycor, it is indeed possible to model satisfactorily the water properties in mesoporous silica. Both the structural and dynamical changes obtained from various experimental approaches, can be proven using MD simulations.

### *4.1.2 Aqueous solutions confined in mesoporous silica*

Despite substantial research efforts on pure water in confinement, understanding the structural and dynamic properties of confined aqueous solutions remain limited. This is largely because the properties of pure water, which represents the limiting, and, presumably, the simplest case of an infinitely dilute solution, are not completely understood. Moreover, the presence of ions would add another parameter to the complexity. However, *Mamontov and coworkers* investigated the effect of adding salts on the diffusion dynamics on the nano-second time scale of water in Vycor

glass using QENS.[123] In their study, the dynamical properties of a 2.3 M $CaCl_2$ solution confined in the nano-sized voids of porous Vycor glass were analyzed in the temperature range of 220 to 260 K. Furthermore, they compared the results with QENS data on the dynamics of pure water confined in Vycor glass to show the salt impact. Indeed, they found a cumulative effect. Adding salt to water confined in Vycor, suppresses its translational dynamics to a much greater extent than expected. At comparable temperatures, the differences for the results of local diffusion coefficients between pure water and aqueous solution were quite tremendous. While the dissolved ions had only a little effect on the spatial aspects of the diffusion process, they alter greatly the water dynamics. Explanation for this could be the stabilization of $Ca^{2+}$-$H_2O$ and perhaps $Cl^-$-$H_2O$ hydration complexes on this time scale. Such stabilization in confined solutions would result in a no longer fast exchange and the binding time of the first hydration layer becomes longer and the concerning water molecules appear immobile for time scale of the experiment.

Later the same group studied the impact of other confined aqueous solutions of $LiCl_2$ and $CaCl_2$ with a pore size of 2.7, 1.9 and 1.4 nm.[2] In agreement with their previous study, they found the combined effect of confinement and adding a salt to decelerate the water motion in a greater extent that one expects from either confining pure water or from a solution in bulk form.

## D. Water reactivity and dissolution driven by interfacial processes

### 1. Dissolution of dense silica

Since water molecules strongly change their structural and dynamical properties in the proximity of the surface and in the presence of ions, the reactivity is expected to change significantly.[124–126] In the absence of ions, it is well-established that decomposition of $SiO_2$ surfaces takes place by a nucleophilic attack of the solvent through reactions of the general form:

$$> Si - O - Si < + H_2O = (> Si - O - Si <) \cdot (OH_2)^{\ddagger} = H_4SiO_4$$

$$> Si - O - Si < + OH^- = (> Si - O - Si <) \cdot (OH^-)^{\ddagger} = H_4SiO_4$$

Where > or < represents a surface-bound species and ‡ an activated complex of unknown composition that decomposes to $H_4SiO_4$ species.

As mentioned before, it is well-known that cations in the electrolyte solutions are drawn by electrostatic attraction to the negatively charged silica surface in order to compensate the surface charge. The partially hydrated ions can form complexes with the surface sites in the following way:

$$> SiO^- + Mg^{2+} = > SiO - Mg^+ \quad K_{ad,Mg}$$

$$> SiO^- + Ca^{2+} = > SiO - Ca^+ \quad K_{ad,Ca}$$

$$> SiO^- + Ba^{2+} = > SiO - Ba^+ \quad K_{ad,Ba}$$

where $K_{ad,i}$ is the interaction constant, depending on the average number of deprotonated surface sites. Thus it appears, that the silica hydrolysis rate is directly proportional to the cation affected fraction of surface sites and the macroscopic dissolution rate *r* can be expressed as following:

$$r = k_{mx,i}\theta_i \qquad (21)$$

with *r* represents the experimentally determined reaction rate, $k_{mx,i}$ indicates the rate constant for dissolution of quartz in solution containing cation i and $\theta_i$ is the fraction of surface sites affected by the cation.

Assuming these reaction constants, *Dove and coworkers* have shown that the dissolution kinetics of quartz are enhanced in the presence of electrolyte solutions. Quartz dissolution rates were found to increase by a factor of 100 to 400x in the presence of potassium and sodium[127,128] as

well as magnesium and calcium.[129] General ion properties and model parameters are summarized in Table 3. For example, magnesium exhibits the lowest $k_{mx,i,}$ (smallest rate-enhancing effect) while also possessing the largest $K_{ad,I}$ (largest adsorption strength).

*Table 3: Summary of cation physical properties, hydration number, adsorption model constants, and experimental estimates of cation-quartz adsorption constants (at 200 °C).*

| **Cation** | **$R_{ionic}$ (Å)** | **$z/r_{ionic}$** | **Hydration number** | **$R_{hydr}$** | **$k_{mx,i}$ (mol/m/s)** | **$K_{ad,i}$** |
|---|---|---|---|---|---|---|
| $Mg^{2+}$ | 0.7 | 2.9 | 6.0 | 4.3 | $10^{-6.7}$ | $10^{3.7}$ |
| $Ca^{2+}$ | 1.0 | 2.0 | 7.0 | 4.1 | $10^{-6.4}$ | $10^{3.4}$ |
| $Ba^{2+}$ | 1.4 | 1.4 | 9.5 | 4.0 | $10^{-6.0}$ | $10^{2.7}$ |

Generally, at near-neutral pH, the dissolution rate-enhancing tendency was found to increase in the order: pure water < $Mg^{2+}$ < $Ca^{2+}$ ≈ $Li^{+}$ ≈ $K^{+}$ < $Ba^{2+}$. Furthermore, *Jollivet et al.* have revealed the favorable effect of ions on the forward dissolution of silicate glasses in clay-equilibrated groundwater.[130]

These conceptual models and experimental results suggest the complex interplay between ion sorption on the surface and the changes in water reactivity. The interaction of cations with the surface silanol groups leads to an enhanced bulk silica dissolution rate.

This was confirmed using SFG spectroscopy and the results revealed that salt influences the molecular arrangement of water at the silica/water interface depending on the bulk pH and hence the surface charge density of silica. The maximum perturbation by salt occurs at near-neutral pH, consistent with "surface charge sensitivity" obtained by *Dove et al.* and validating the

hypothesis that changes in water structure close to the silica surface directly increase the surface hydrolysis rate.[129,131,132]

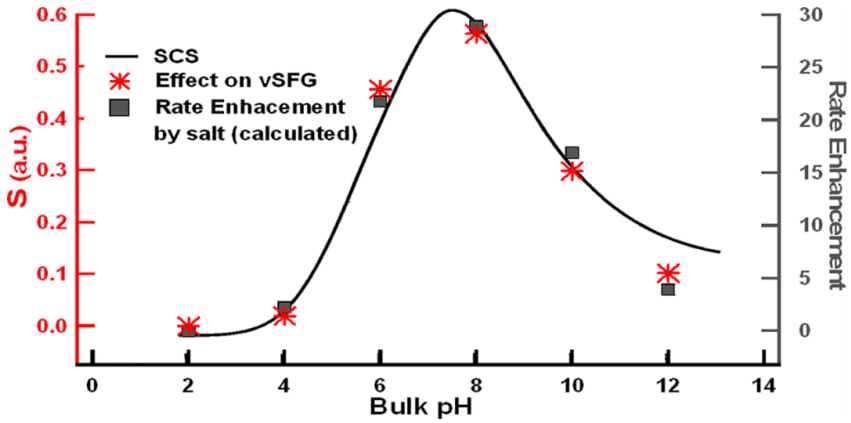


*Figure 14: Comparison between the effect of salt on the vSFG response of the silica-water interface and effect of salt on silica dissolution, as a function of pH. Red crosses: salt effect (S); Black squares: calculated quartz dissolution rate enhancement on adding 0.1 M NaCl salt. Figure adapted from ref* 131.

However, previous studies have only taken into account the dissolution rate of bulk silica materials. The confinement of highly ordered mesoporous silica is expected to have a further impact on the Electric double layer and therefore on the ion distribution.

## 2. Dissolution behavior of porous silica

The dissolution behavior regarding highly ordered mesoporous silica was studied by *Gouze et al.* The results revealed two different evolutions for dense pore walls of MCM-41 and the microporous walls of SBA-15 in contact with water. In the case of MCM-41, the loss of the hexagonal pore order has been attributed to a change of the pore shape probably due to the dissolution of silica wall and to the recondensation of hydrolyzed silica on the pore surface.

In contrast to that, in the case of SBA-15, the alteration is driven by an equilibrium between the reactive diffusion of water and the dissolution of the altered silica wall. The differences of evolution between the two silica are explained by their different pore diameter and the presence of microporosity.[4]

Furthermore, *El Mourabit et al.* have performed stability measurements on various structured mesoporous materials (SBA-1, SBA-3, SBA-15, MCM-41 and MCM-48) in contact with acidic solutions.[133] They concluded that the degradation of silica during the alteration results in the loss of their textural and structural properties. The dissolution rate depends on the nature of acidic media and on the type of silica. Besides, the formation of an alteration gel is proposed which recondenses into a thermodynamically stable matrix. The overall stability is driven by the wall thickness and the pore size of silica confinement.

Until now, there are no studies dealing with the dissolution mechanism in electrolyte solutions. Therefore, the question arises whether ions in confinement alter the dissolution of SBA-15 and MCM-41 in the same way than ions in bulk silica materials.

## E. Conclusion

Summing up all the relevant studies regarding water properties in the presence of ions and confined in highly ordered mesoporous silica, the following aspects can be concluded:

- Ions exert a strong electric field on surrounding water molecules perturbing the water structure and decrease the dynamics
- Water confined in nanopores results in a non-freezable liquid in the interfacial. The thickness of this liquid-like layer can be successfully described using the adapted Gibbs-Thompson relation.
- The molecular-scale structure of this interfacial layer can be described using electric double layer models and/or Poisson-Boltzmann theory
- Confinement decreases the water dynamics and perturbs the water structure. Via hydrophilic and hydrogen bonding interaction the surface-near water layer (interfacial layer) exhibits significantly different properties than the bulk-like liquid in the pore center.
- The presence of ions in nanoconfinement change drastically the water properties. These dynamical and structural changes are predominantly related to the interfacial layer
- MD simulations confirmed the confinement effect on the water structure and the deceleration of water dynamics
- Bulk dissolution rates of silica are significantly altered in the presence of ions, following the order: pure water < $Mg^{2+}$ < $Ca^{2+}$ ≈ $Li^{+}$ ≈ $K^{+}$ < $Ba^{2+}$.
- Degradation of silica results in the loss of their textural and structural properties. The alteration rate depends on the wall thickness and the pore size of silica confinement.

# *Chapter II - Transport of electrolyte solutions and interfacial layer in silica nanoconfinement - case of two plane and parallel surfaces*

Because geochemical processes such as dissolution and precipitation are mainly driven by an interfacial layer and the solution transport, the first step of our approach was to determine the impact of the confinement size on the transport at a large scale, i.e. few mm, and on the interfacial layer between two parallel and plane silica surfaces spaced of few nm. These model systems made of nanochannels were filled with salt solutions $XCl_2$ having cations with various kosmotropic properties (X = Ba, Ca, Mg). These nanochannels were characterized during their filling using hard X-Ray reflectivity for the determination of the electron density profiles perpendicular to the surface. From these results, the solution density inside the nanochannels was determined and the ions surface excess at $SiO_2$ surface were calculated. These experimental results were compared with the results obtained from molecular dynamics simulations.

## A. Introduction

A strong interest exists to use model system such as nanochannels defined as two planar and parallel plane surfaces spaced of few nm. Indeed, the planar model systems can provide an attractive configuration for fundamental studies like filling kinetics (wetting dynamics), diffusion, and for molecular separation processes.[134] Channels with heights in the range of 2-100 nm usually still contain several hundreds of molecules in the height dimension, and typical effects are related to the interfacial layer or the extreme surface to volume ratio. As the channel dimension is scaled down to the nanometer range, fluids inside the channels exhibit properties which can be significantly different from the bulk properties, such as reduced electroosmotic flow and increased viscosity.[135] As already studied, channels below 10 nm can be very interesting to investigate the dynamics of confined solutions[136] and the ion sorption in confinement.

In the present chapter, we propose a method to determine the filling kinetics of nanochannels with a height of 3 and 5 nm using X-Ray reflectivity (XRR). This technique allows the determination of the electron density profiles perpendicular to the surface[137] leading to the determination of the density evolution in the nanochannels and to the characterization of the interfacial layer in confined media. Furthermore, the effect of confinement size and the nature of ions on the interfacial layer were studied. To reach this goal, we used two types of $SiO_2$ nanochannels, ones from the University of Twente and ones fabricated by the CEA/LETI (Laboratoire d'Electronique et de Technologie de l'Information). These nanochannels were both filled with electrolyte solution $XCl_2$ (X = Ba, Ca, Mg) at 1 M.

## B. Experimental section

In this study, two different types of nanochannels obtained from two institutes were used. The preliminary investigations were done using nanochannels obtained from the Institute of Nanotechnology, Twente, fabricated by the group of *N. Tas* in a collaboration with *L. Mercury* (University of Orleans). The 5 nm nanochannels were investigated during short times scales. The second studies were performed with nanochannels provided by the CEA/LETI. Two nanochannels sizes were used in order to study the impact of confinement size: 3 and 5 nm. The filling kinetics of various electrolyte solutions were probed during several months.

### 1. Nanochannels from the University of Twente

These model systems are described in Figure 15. Before the experiments, an $O_2$ plasma cleaner was performed on the samples to clean and create –OH groups at the surface of silica. Then, nanochannels were placed in experimental set-up dedicated to the X-ray reflectivity measurement of samples. At both sides of this cube, two compartments were screwed providing a constant supply of solution on the one side and an empty one on the other side. Hard X-ray reflectivity measurements at 27 keV (= 0.4592 Å) were performed at the ESRF, BM32 beamline to limit the absorption of X-rays through sample crossing.

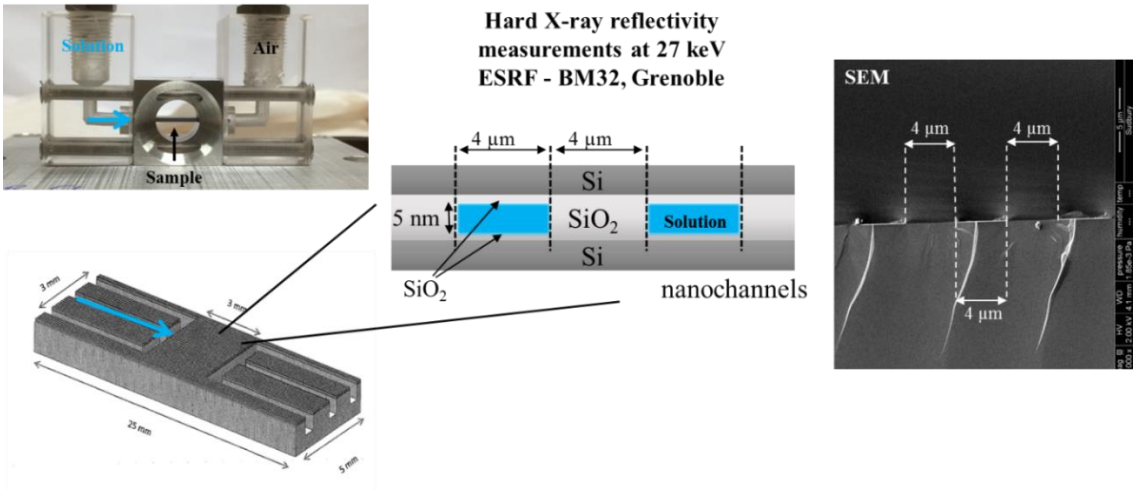


*Figure 15: Schematic overview of the 5 nm nanochannels from the University of Twente. The sample was placed between two compartments providing at one side, a constant supply of solution. XRR was measured after various times in order to characterize the filling kinetics.*

Two types of experiments were performed. In the first experiment, the filling kinetics of nanochannels dried at 250 °C under vacuum during 2 hours with a $BaCl_2$ solution at 1 M were investigated in order to determine the time required to reach the equilibrium. In the second experiment, samples were analyzed after their immersion during 24 hours in water and in solutions of $CaCl_2$ and $MgCl_2$ first at 0.1 M and then at 1 M. The pH (20 °C) of the electrolyte solutions were comprised between 5.2 and 5.7.

## 2. Nanochannels from CEA/LETI

Nanochannels used in the second part were fabricated by CEA/LETI (Vincent Larrey, Claudine Bridoux and Frank Fournel) using lithography and direct wafer bonding technologies. After the growth of a thermal oxide layer of 3 and 5 nm on the surface of a silicon wafer having a 200 mm diameter, the samples were patterned (lithography and etching) in order to obtain an alternation of silica nanochannels and voids of 250 nm width, as described in Figure 16.

Subsequently, a second substrate of silicon with a native oxide layer was bonded onto the other by a thermal treatment at 1100 °C.

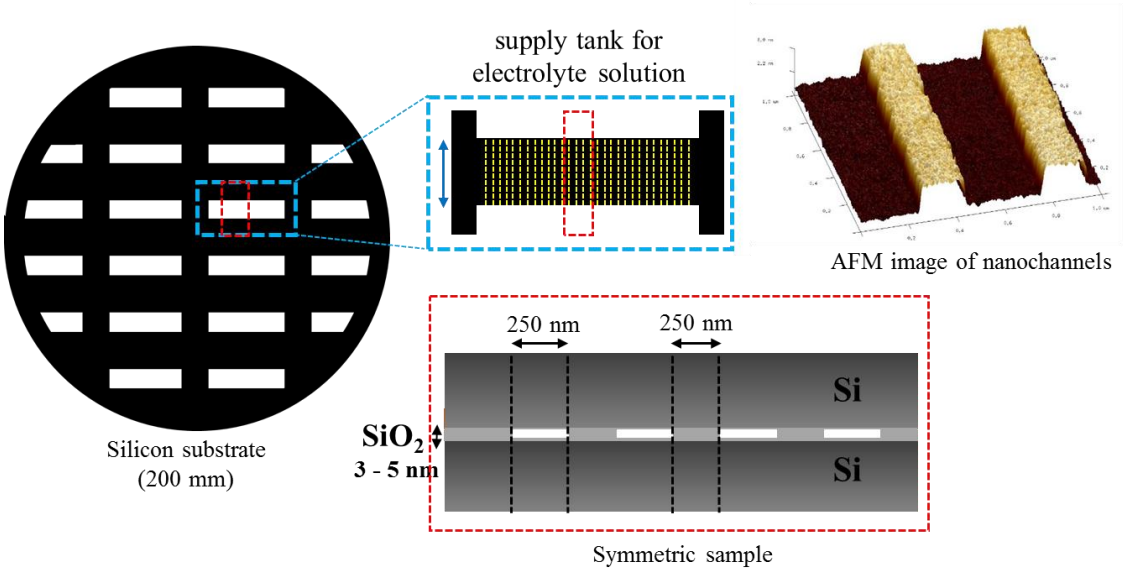


*Figure 16: Schematic overview of the nanochannels of 5 nm supplied by CEA/LETI. The AFM image shows the well-defined channels having a height of 5 nm. The electrolyte solutions are provided by the tanks at both sides of the channels.*

First, the nanochannels were dried at 200 °C for 4 days under vacuum and characterized by X-ray reflectometry. Then, samples were immersed in various electrolyte solutions $XCl_2$ (X = Ba, Ca, Mg) at 1 M. After 1 weeks, 4 months and 8 months the same samples were placed in experimental set-up dedicated to the in-situ X-ray reflectivity measurement and characterized.

## C. X-Ray reflectivity analysis

X-ray reflectivity (XRR) is a surface-sensitive analytical technique to characterize surfaces, thin films and multilayers. In the following part, we present the general principle of this technique and the data treatment to obtain information about the interfacial layer within the nanochannels. For a more detailed description of this technique the reader is referred to ref 138.

## 1. General principle

The basic idea of the XRR technique is to reflect a beam of X-rays from a flat surface or interfaces having different electron densities and to measure then the intensity of X-rays reflected in the specular direction (reflected angle equal to incident angle), as presented in Figure 17. In order to get surface and interface related information, measurements are usually performed at low angles from $\theta < 3°$. If the interface is not perfectly sharp and smooth, then the reflected intensity will deviate from that predicted by the law of Fresnel reflectivity.

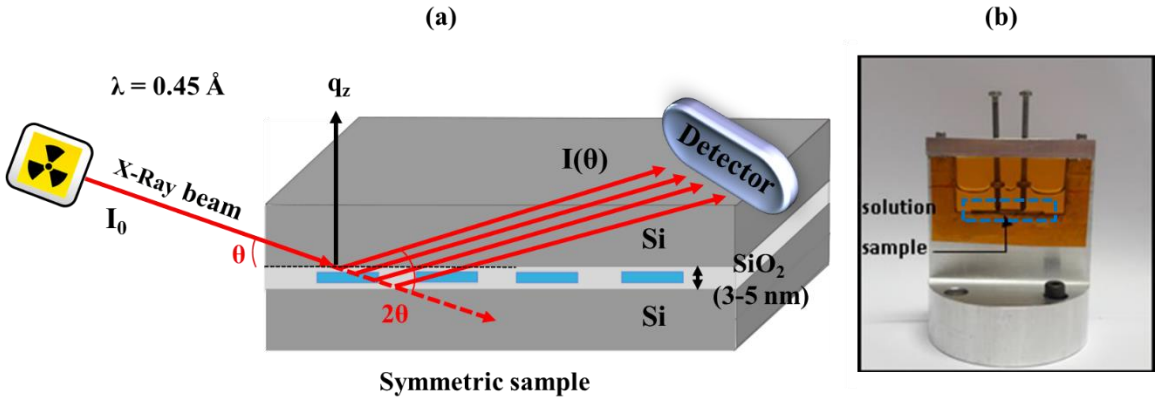


*Figure 17:Principle of hard X-ray reflectivity measurement on the nanochannels (a) X-Rays are reflected at each interface and can interfere constructive or destructive providing information about the electron density profile and ion distribution. Cell used for XRR measurements at BM32, ESRF Grenoble (b). The nanochannels were fixed using two screws and filled with the corresponding electrolyte solutions.*

The deviations can then be analyzed to obtain the density profile of the interface normal to the surface. The reflectivity of the substrate $R(\theta)$ is given by the ratio of the measured reflectivity at a given angle $I(\theta)$ and the intensity of the direct beam $I_0$:

$$R(\theta) = \frac{I(\theta)}{I_0} \qquad (22)$$

The reflectivity is often expressed using the wave vector $\vec{q}$ which is defined as the difference between the vector of the reflected wave and the vector of the incident wave $\vec{q} = \overrightarrow{k_r} - \overrightarrow{k_{in}}$. Since the reflection of the X-Rays is an elastic process, the wave vectors are equal (eq. 23) and can be expressed as a function of the angle θ (eq. 24):

$$\left|\overrightarrow{k_{in}}\right| = \left|\overrightarrow{k_{in}}\right| = \frac{2\pi}{\lambda} \qquad (23)$$

$$q_z = 2k_z = \frac{4\pi sin\theta}{\lambda} \qquad (24)$$

## 2. XRR data treatment

From X-ray reflectivity curves, electron density profiles were extracted directly by inverse Fourier transform assuming the symmetry of the profile and using the following equation:

$$R(q) = \frac{(4\pi r_e)^2}{q^2}\left|\int \rho_{el}(z)\, exp(iqz)\, dz\right|^2 \qquad (25)$$

where $R(q)$ represents the reflectivity as a function of the scattering vector, $r_e$ denotes the electron radius and $\rho_{el}(z)$ the electron density at a given distance *z*.

Direct inversion is only possible because of the assumption of a symmetric profile: when $\rho(z)$ is an even function, the Fourier transform inside eq. 25 is a real function. The phase problem is hence limited to a sign problem, which can be solved from a continuity argument. The reflected amplitude can only change sign when it comes to zero, i.e. close to minima of interference fringes.

The reflectivity curves were plotted in the standard $I.q^4$ vs. q ($q = 4\pi\sin(\Theta)/\lambda$, with the incident angle $\Theta$) mode to remove the Fresnel decay with q the wave vector transfer. They display large fringes associated to the interference between the waves reflected at both bottom and top surfaces of the channels. Their spacing is thus directly related to the gaps.

## 3. Molecular dynamics solutions

Molecular dynamics (MD) simulations were performed by the Laboratory for mesoscopic modelling and theoretical chemistry LMCT/ICSM for an aqueous $BaCl_2$ solution confined between two charged amorphous silica walls (Figure 18). A charged silica surface was created following the approach detailed in ref 139. The surface contains 48 charge sites and 192 silanol groups, with

charge sites resulting from deprotonation of a silanol group. Considering the frontal surface area of $5.7042^2$ nm$^2$, the charge and surface group density are 0.74 charges and 2.95 silanol groups per nm$^2$, respectively, which is representative of amorphous silica. A slot was created by mirroring and rotating the surface by 90° around the axis normal to the surface.

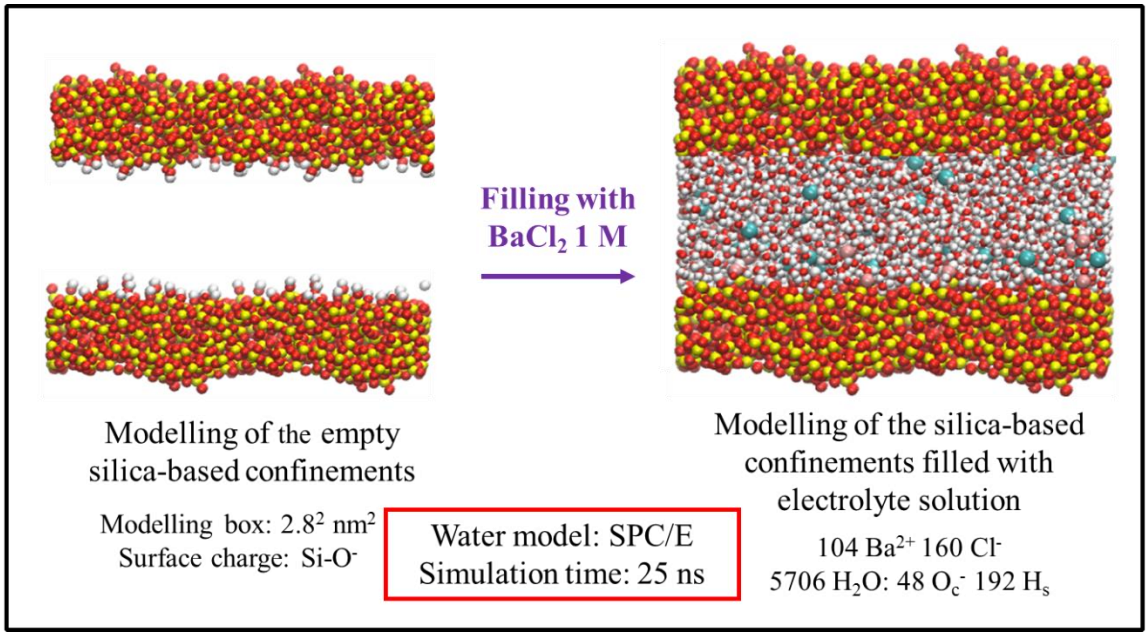


*Figure 18: MD simulations of silica-based nanoconfinement. First, the periodic simulation box was empty and afterwards the equilibrium state of a 1 M $BaCl_2$ solution was simulated during a simulation time of 25 ns.*

The surfaces were separated by approximately 4.7 nm, which is sufficient to avoid an overlap of the electrical double layer (EDL) in the center of the slot for the ion concentration ($c_0$ = 1 mol·L$^{-1}$) considered here. The hydrophilic silica surfaces were obtained by distributing the partial charges on the surface atoms such that a deprotonated silanol group has a net charge of −1.0 *e*, where *e* is the elementary charge. The charge distribution on the silanol groups is an equivalent version of published values.[140] The force field therefore distinguishes between the charge on a silicon atom corresponding to a protonated (SiOH) and a charged (SiO) group. No

distinction is made here between geminal, vicinal, and isolated atoms, since differences between these types of groups are small[140] and not directly relevant for this methodological study. Each charge site was compensated by a divalent excess counterion to produce an overall charge-neutral simulation system, containing a total of 104 counterions ($Ba^{2+}$) and 160 coions ($Cl^{-}$). Anomalies of divergent electrostatic energy caused by a non-neutral simulation system can, in theory, be corrected in the case of homogeneous systems by imposing a neutralizing background plasma,[141] but spurious effects arise when this method is applied to inhomogeneous systems.[142] Apart from spurious effects, a charge-neutral simulation system is needed to ensure that cation and anion charge densities are equal in the center of the slot. This type of simulation produces a sound image of the EDL, which includes an adsorbed Stern layer and a diffuse Gouy-Chapman layer. The amount of ions in the diffuse layer result from the surface charge and the adsorption of ions, both cations and anions. The silica was kept frozen in the course of the simulations. 5076 water molecules were modeled via the rigid three-point SPC/E (simple point charge / extended) model.[143] The number of water molecules in the system was chosen such that the water density in the center of the box was very close to the bulk density of SPC/E water. The simulation was performed with DL_POLY[144] using Verlet's algorithm with a simulation time step of 1 fs. The PN-TrAZ potential[145] for water--surface interaction was fitted against an "nm" potential.[146] All other interaction potentials are Lennard−Jones potentials with the cross terms obtained using the Lorentz−Berthelot mixing rules. The parameters are listed in ref 139. Interactions are truncated at 1.4 nm. Long-range electrostatics are treated with the Ewald method. The temperature of the fluid is controlled using a Berendsen thermostat with the target temperature of 300 K and a coupling time of 0.5 ps. The simulation was equilibrated for 1 ns, followed by a 25 ns production run.

## D. Results and discussion

In this part, we present the XRR results obtained for the nanochannels from the University of Twente and from the CEA/LETI. The reflectivity was measured for various electrolyte solutions as a function of the filling time.

### 1. Nanochannels from the University of Twente

#### 1.1 Filling kinetics of nanochannels with $BaCl_2$ at 1 M

The evolution of the X-ray reflectivity curves as a function of time during the filling of nanochannels with a $BaCl_2$ solution at 1 M and the corresponding electron density profiles are presented in Figure 19 (a) and (b).

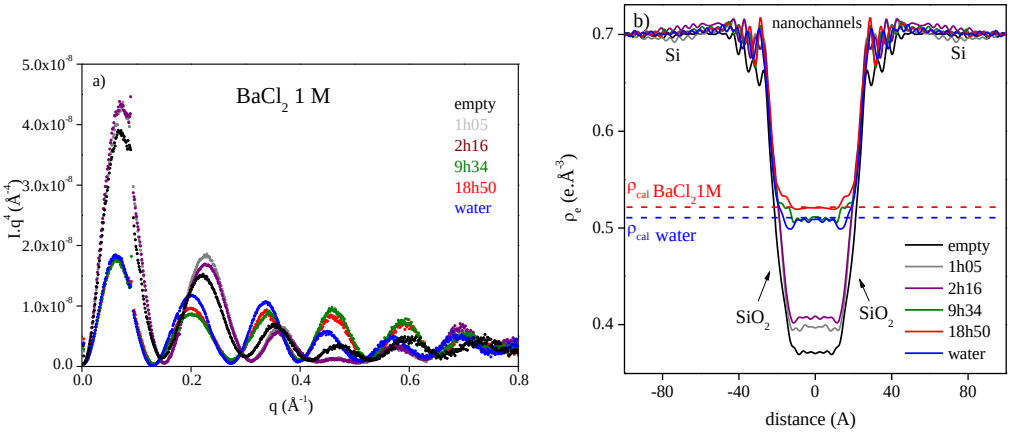


*Figure 19: (a) Reflectivity curves obtained from the measurements of nanochannels during their filling with an electrolyte solution of $BaCl_2$ at 1 M for different times and (b) the corresponding electron density profiles.*

The results show some modifications of the contrast (intensity) of the fringes as a function of time until 18h50. This highlights an evolution of the densities inside the nanochannels and at the $SiO_2$/solution interface. After 18h50, we observe no evolution of the reflectivity signal showing that the equilibrium is reached. The corresponding electron density profiles presented in Figure

19 (b) reveal an increase of the density inside the nanochannels with the filling time. After 9h34, the density in the center of the nanochannels is equal to the one of bulk water and the density close to the $SiO_2$ surface exhibits a higher density than in the center. This phenomenon can be explained by an adsorption process of ions after filling the channels with a electrolyte solution. Since the pH of the point of zero charge for silica is about 2 to 3, the silica surface in our study ($5.4 < pH < 6.4$) is mainly negatively charged.[64] Thus, surface $–SiO^-$ groups can interact with the cations $X^{2+}$ and to a lower extent with $H_3O^+$, via electrostatic interactions to decrease the surface potential. Even anions are expected to sorb within the interfacial layer to compensate the cation sorption and to reach the electroneutrality in the bulk-like solution. After 18h50, the density in the center increases until a density close to the one of a bulk solution at $BaCl_2$ 1 M is reached.

Regarding this first approach, the electrolyte solution behavior inside the nanochannels can be described as follows: First, the density inside the nanochannels is close to the one of bulk water until the saturation of the $Si\text{-}O^-$ is reached. Thus, the ion adsorption can probably explain the depletion of the electrolyte solution inside the nanochannels. Afterwards, when the surface sites are saturated, the density of the solution in the center of the nanochannels ($\rho_{eCenter}$) increases up to the density of the bulk electrolyte solution.

### 1.2 Filling kinetics of nanochannels with $CaCl_2$ and $MgCl_2$ at 0.1 and 1 M

The XRR curves obtained for $MgCl_2$ and $CaCl_2$ at 0.1 and 1 M after 24 h of filling are presented in Figure 20 (a). The graph shows a shift of the fringes at high q values, characteristic for a modification of the $SiO_2$/solution interface. The density profiles presented in Figure 20 (b) depict an electron density increase at the $SiO_2$ surface of the nanochannels for all solutions.

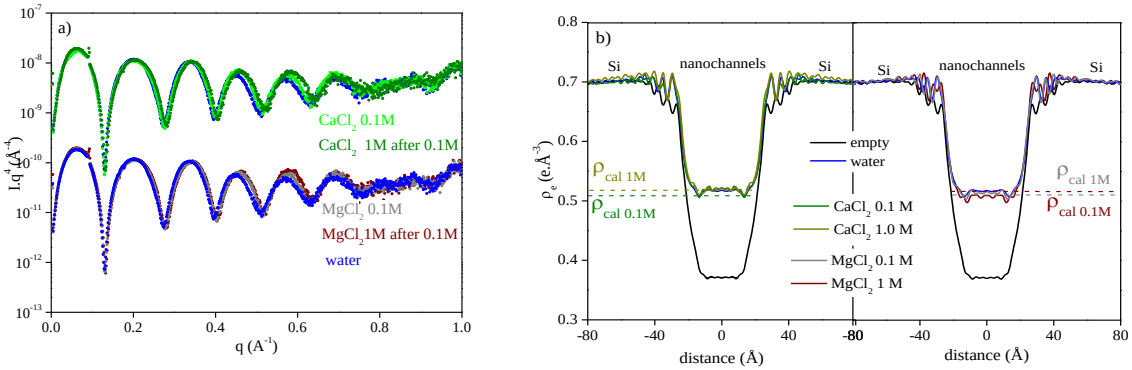


*Figure 20: (a) Reflectivity curves of nanochannels after 24 h of filling with the electrolyte solutions $CaCl_2$ and $MgCl_2$ at 0.1 M and 1 M and (b) the corresponding electron density profiles.*

1.3 Determination of the surface ion excess

In order to get information about the interfacial layer at $SiO_2$ surfaces in the confinement, the surface ion excesses were calculated considering a diffuse Gibbs distribution of ions (eq. 27). In a first approach, we assumed that the electron density increase is related to X and Cl species (stoichiometric ratio 1:2).

$$d_i = \frac{\int_0^l (\rho_{eXRR} - \rho_{eXRRCenter}) dz}{0.33Z_X + 0.66Z_{Cl}} \qquad (26)$$

with $d_i$ is the surface ion excess, $\rho_{eSurf}$ the electron density at the surface of $SiO_2$, $\rho_{eCenter}$ the electron density in the center of the filled nanochannels, $l$ the distance for the ion distribution from the surface and $Z_X, Z_{Cl}$ the atomic number of X and Cl, respectively.

The results are presented in Table 4. As highlighted, the values for the electron densities in the nanochannel center are in good agreement with the theoretically calculated values, assuming the following parameters obtained from the sample filled with water: i) the interfacial central zone (projection of the silica nanochannels) is composed from 41 % channels voids and 59 % silica

oxide and ii) the electron density of silica oxide is 0.628 e/Å$^3$. The results show that the surface ion excess is dependent on the nature of the sorbed ion and follows the order: $Ba^{2+} < Ca^{2+} < Mg^{2+}$.

*Table 4: Calculated electron densities $\rho_{ecalSol}$ of solution and $\rho_{ecalSample}$ inside the sample, and electron densities determined from the electron density profiles $\rho_{ecenter}$ in the center of the filled nanochannels $\rho_{ecalSample}$ have been calculated with a $\rho_{eSiO2}$ = 0.628 e.Å$^{-3}$ and $\rho_e$ = 0.372 e.Å$^{-3}$ measured in the water filled sample.*

| Aqueous solution | $\rho_{ecalSol}$ (e.Å$^{-3}$) | $\rho_{ecalSample}$ (e.Å$^{-3}$) | $\rho_{eCenter}$ (e.Å$^{-3}$) | $d_i$ (nm$^{-2}$) |
|---|---|---|---|---|
| $BaCl_2$ 1 M | 0.378 | 0.526 | 0.521 | 0.2 |
| $CaCl_2$ 0.1 M | 0.336 | 0.509 | 0.520 | 0.3 |
| $CaCl_2$ 1 M | 0.358 | 0.518 | 0.520 | 0.3 |
| $MgCl_2$ 0.1 M | 0.336 | 0.509 | 0.515 | 0.6 |
| $MgCl_2$ 1 M | 0.355 | 0.516 | 0.508 | 0.6 |

In order to obtain the ion distributions in the nanochannels, the filling nanochannels were modelled using MD simulations. *Hocine-Mehtari et al.* performed MD simulations for an aqueous 1 M $BaCl_2$ solution confined between two charged amorphous silica walls. From these simulations, the ion distribution and the electron density profile of the electrolyte solution were obtained and are shown in Figure 21. The profile depicts an increase of the electron density at the silica surface related to ion sorption processes. From the ion distributions, the surface ion excesses for cation and anion can be calculated and are about 0.1 $Ba^{2+}.nm^{-2}$ and 0.2 $Cl^{-}.nm^{-2}$. These values are about the same order of magnitude than the ones obtained by XRR.

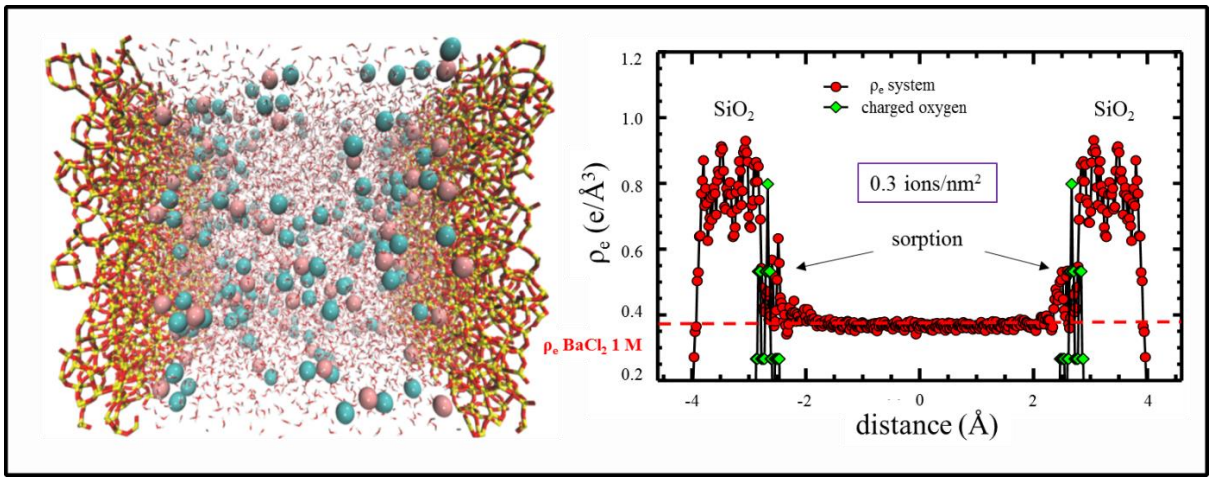


*Figure 21: (a) Snap-shot from atomistic modelling of a 1 M $BaCl_2$ solution in $SiO_2$ nanochannels having a gap size of 5 nm. $Ba^{2+}$ ions are presented in red spheres and $Cl^-$ in blue. (b) Electron density profile obtained from atomistic modelling. As shown, an increase of the electron density $\rho_e$ can be observed due to the ion sorption on the silica surface.*

Applying a Fourier transform to the electron density profile obtained by modelling, X-ray reflectivity curves were obtained. The comparison of the experimental data and the data obtained from the modelling as a function of the scattering vector q are presented in Figure 22.

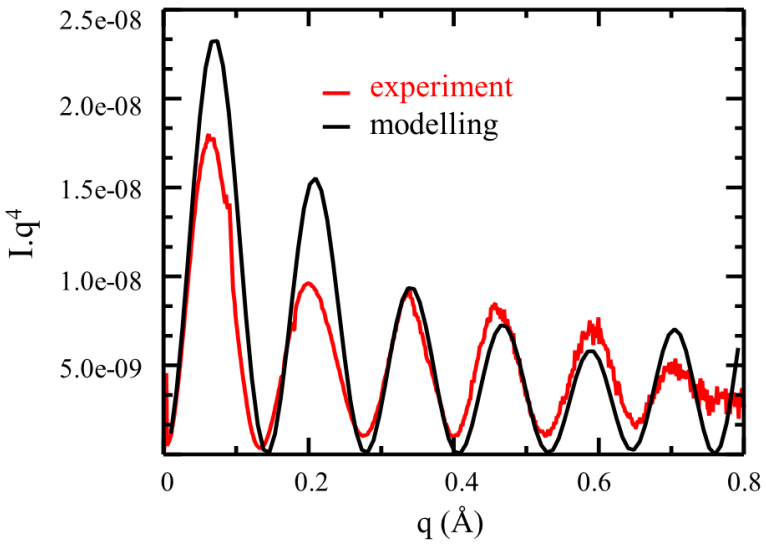


*Figure 22: Comparison of the $I.q^4$ obtained from the experiment and atomistic modelling as a function of the scattering vector q.*

First, at small q values, attributed to larger length scales, we observe discrepancies between modelled and experimental curve. This may be explained with the variation of the nanochannels thickness at a larger scale. While atomistic modelling takes only one channel size into account for the simulation, the thicknesses of the nanochannels in the experiments can vary and deviate slightly. Second, at high q ($0.3 < q < 0.6$ Å), which are related to the interface, a good correlation between both curves is obtained. This good agreement enhances the ions surface excesses obtained experimentally and shows the quality feature of the method.

For the first time, the ion distributions in nanoconfinement were measured experimentally by X-ray reflectometry and modelled by MD simulations.

## 2. Nanochannels from CEA/LETI

Figure 23 - 27 present the reflectivity curves and the corresponding electron density profiles as a function of the filling time for $XCl_2$ solution at 1 M in 5 and 3 nm, respectively.

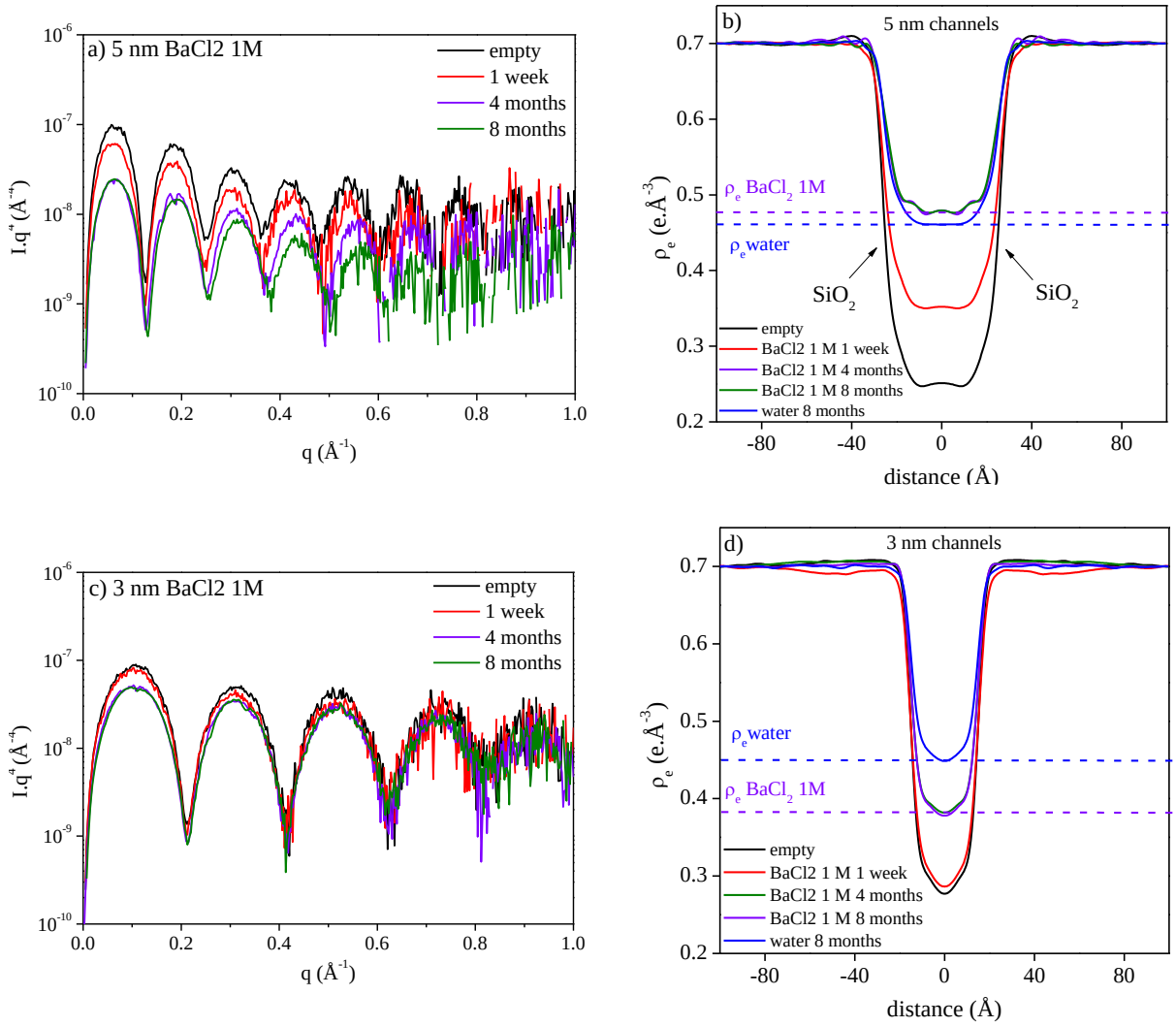


*Figure 23: Experimental reflectivity curves (NB: log scale) and associated electron density profiles obtained from the measurements of 5 nm and 3 nm nanochannels filled with $BaCl_2$ at 1 M.*

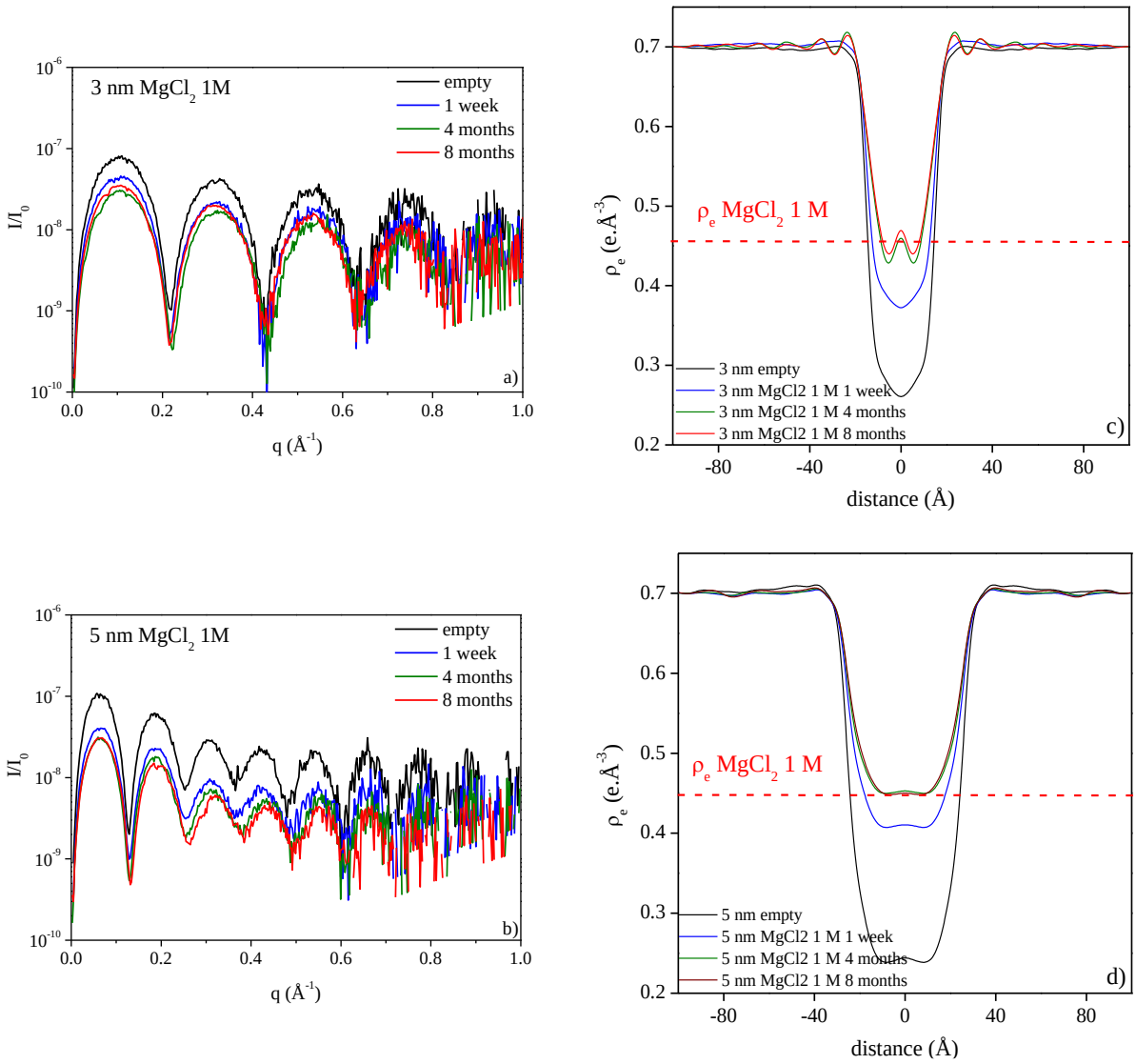


*Figure 24: Experimental reflectivity curves (NB: log scale) and associated electron density profiles obtained from the measurements of 5 nm and 3 nm nanochannels filled with $MgCl_2$ at 1 M.*

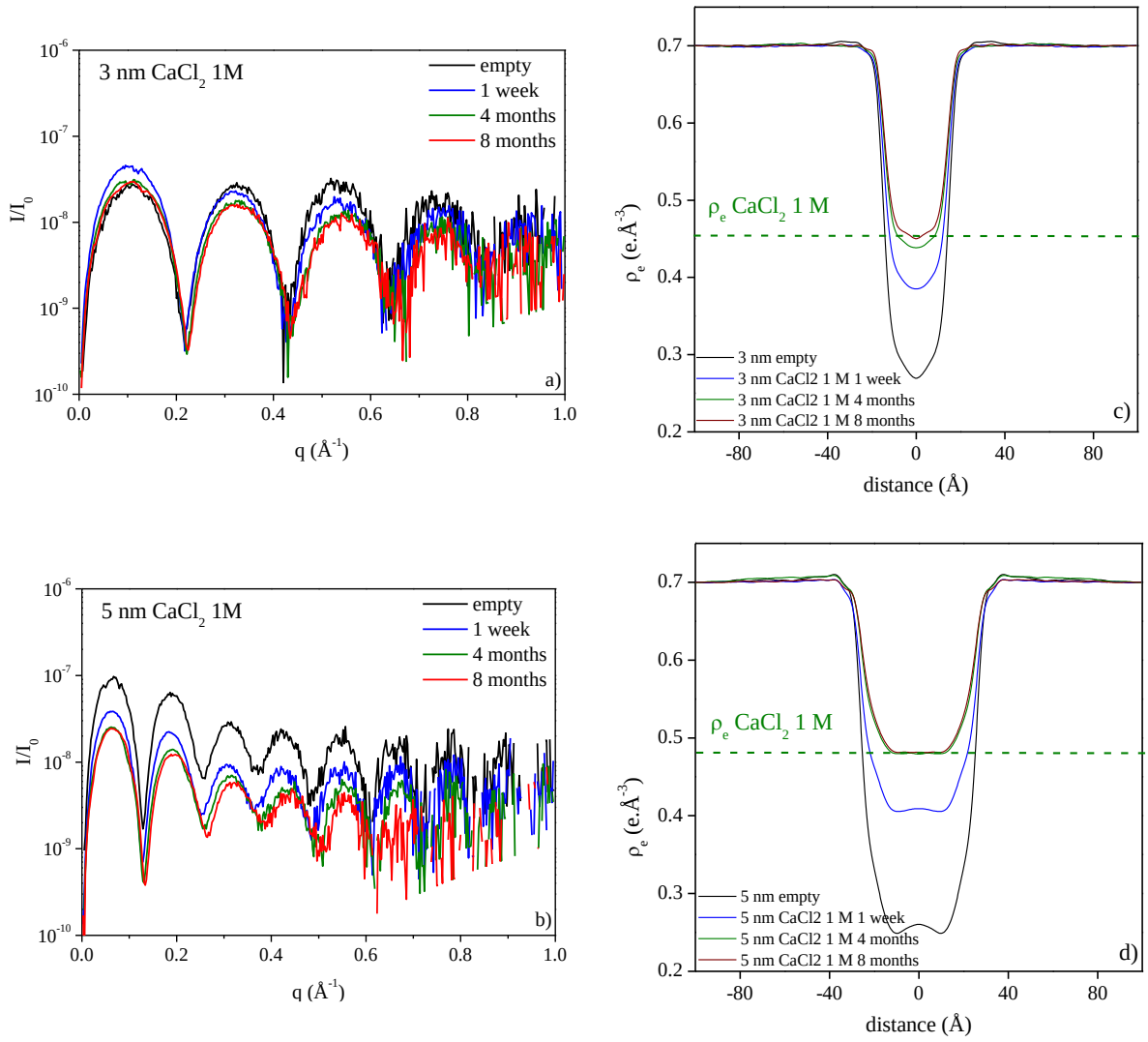


*Figure 25: Experimental reflectivity curves (NB: log scale) and associated electron density profiles obtained from the measurements of 5 nm and 3 nm nanochannels filled with $CaCl_2$ at 1 M.*

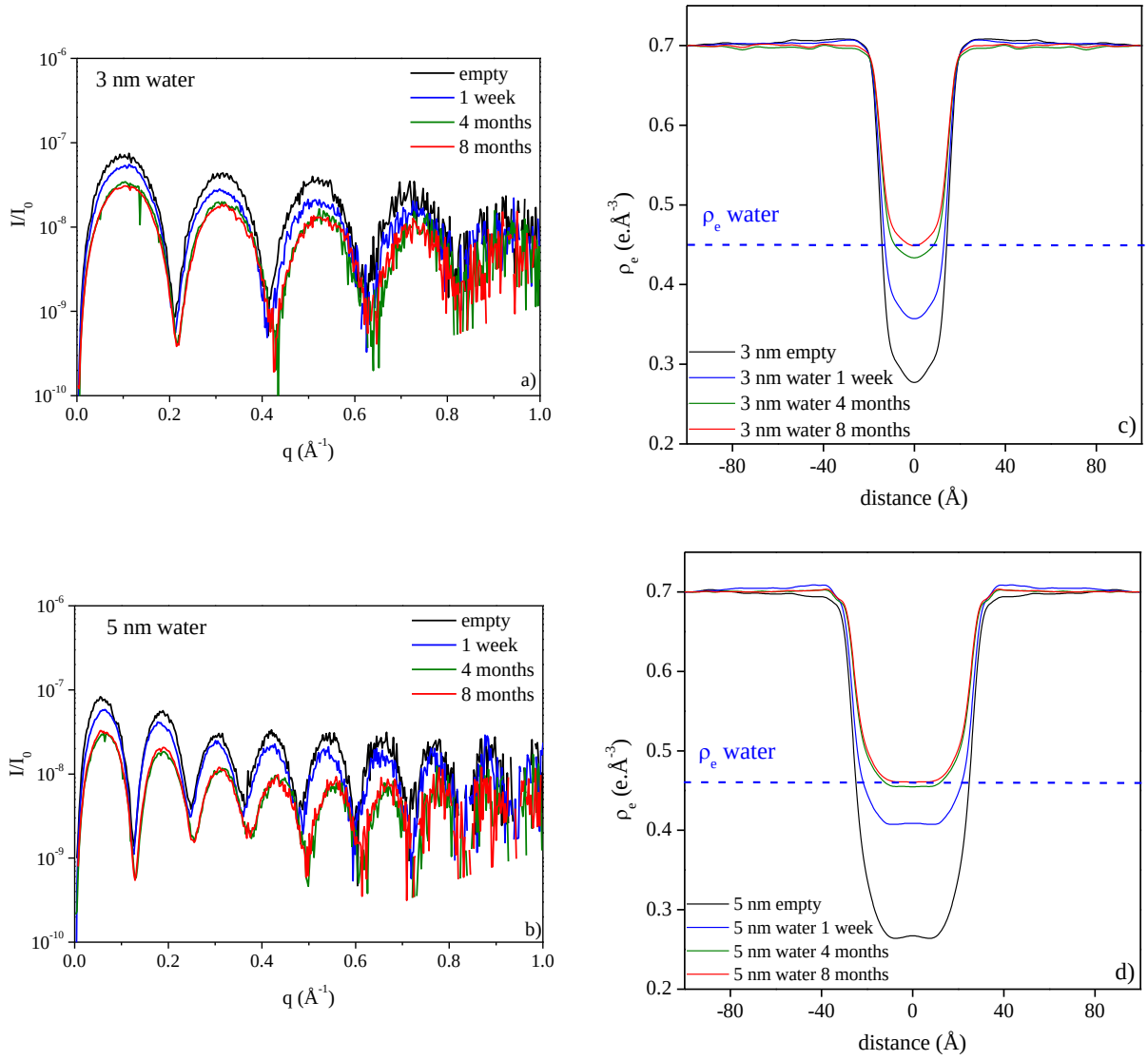


*Figure 26: Experimental reflectivity curves (NB: log scale) and associated electron density profiles obtained from the measurements of 5 nm and 3 nm nanochannels filled with water.*

The filling kinetics of the CEA/LETI nanochannels differ from the kinetics obtained in the nanochannels obtained from the University of Twente. Owing to the annealing step at 1100 °C in the elaboration process, we expect that the surface in the CEA/LETI nanochannels is almost completely dehydrated and that there are almost no free silanol groups available on the surface (see Figure 27).[64]

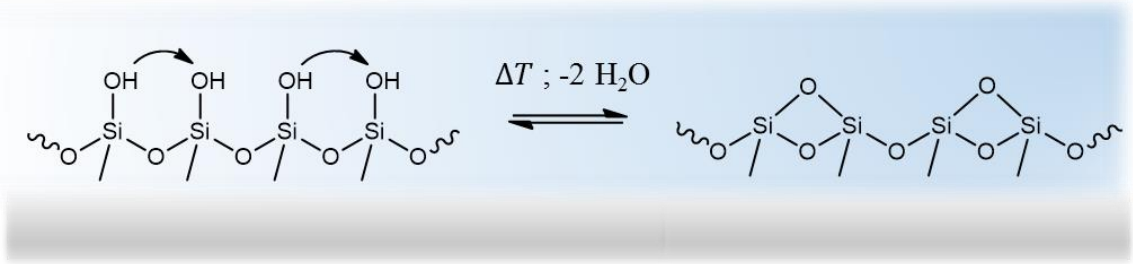


*Figure 27: Dehydration of silanol groups on a silica surface at high temperature. The initial hydrophilic surface tends to become more hydrophobic.*

This dehydration of the surface silanol groups tends to make the silica surface more hydrophobic than in the case of the silica of the nanochannels from Twente. Consequently, the kinetics rates for the filling of electrolyte solutions are much slower than for more hydrophilic channels. Therefore, the measurement of X-Ray reflectivity curves at several times step during 8 months were necessary.

### 2.1 Filling kinetics of nanochannels

As presented on Figure 23 (a) and (c) the intensity of the reflectivity decreases with the filling duration. This intensity decrease is related to the progressive filling of the nanochannels as indicated by the electron density profiles. To highlight this phenomenon, the evolutions of the electron density in the center of the nanochannels as a function of the duration of filling with the various electrolytes are presented in Figure 28.

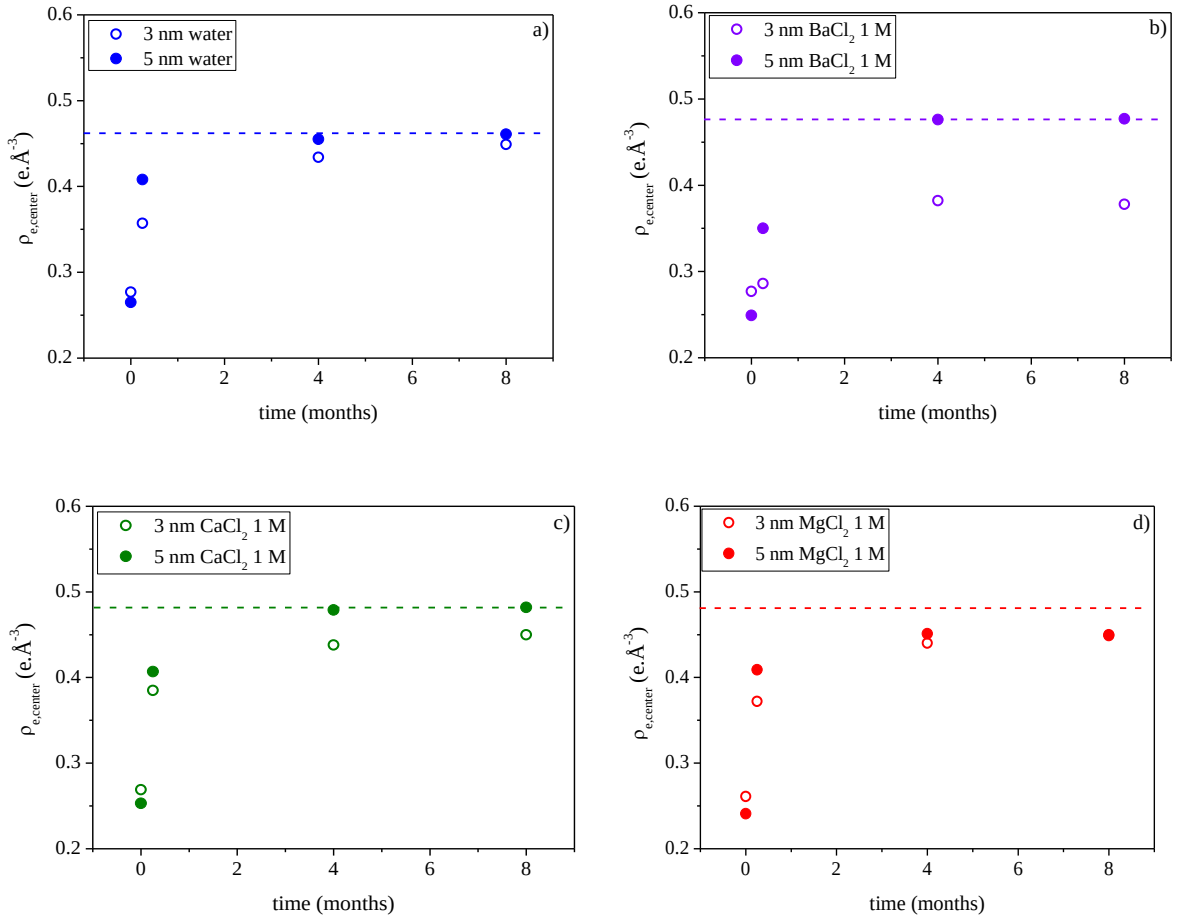


*Figure 28: Evolutions of the electron density in the center of the 3 and 5 nm nanochannels filled with water (a) and electrolyte solutions $XCl_2$ at 1 M (b-d)) as a function of the filling time.*

As highlighted in Figure 28, the evolution of the density in the center of the nanochannels depends on the nanochannels size and on the nature of the electrolyte. These differences are observed for the penetration rate of the solution and the level of filling of the nanochannels at the equilibrium, i.e. at 8 months.

First, whatever the electrolyte, the penetration rates of the solutions are lower in the 3 nm than in the 5 nm nanochannels. As we will present and discuss more detailed in chapter III, the water dynamics at a pico-second time scale strongly decreases with the pore size and the presence

of ions (Chapter III Figure 26). This could explain the transport rate of the solutions in the 3 nm nanochannels. Moreover, the penetration rate increases following this order: $BaCl_2 < CaCl_2 \approx MgCl_2 \approx H_2O$. This result cannot be explained by the dynamics at a pico-second time scale of water confined in highly ordered mesoporous silica in presence of these ions since the tendencies are different and follow the kosmotropic properties of the ions ($MgCl_2 < CaCl_2 < BaCl_2 <$ water). This will be presented and discussed in detail in chapter III. Furthermore, the penetration rate of the electrolyte solutions may be explained by the silica surface hydrophilicity driven by the ability of water to hydrolyze the silica surface and form hydroxyl groups. However, the catalytic effect of ions present in solution on the silica hydrolysis ($BaCl_2 > CaCl_2 > MgCl_2 >>$ water)[127,129,132,147] cannot explain the obtained tendencies either.

By comparing the filling kinetics of CEA/LETI nanochannels with the nanochannels from the University of Twente, it is important to note that the confinement sizes of 3 and 5 nm do not follow the same relationship obtained for the kinetics of a $BaCl_2$ solution in the Twente nanochannels. In this case of the Twente nanochannels, we assume a non-classical diffusion process during the filling of electrolyte solutions that could be attributed to a reactive diffusion process driven by the hydrolysis of the $SiO_2$ surface. However, the catalytic ion effect on the silica hydrolysis (($BaCl_2 > CaCl_2 > MgCl_2 >>$ water) [127,129,132,147] cannot explain the obtained tendencies either.

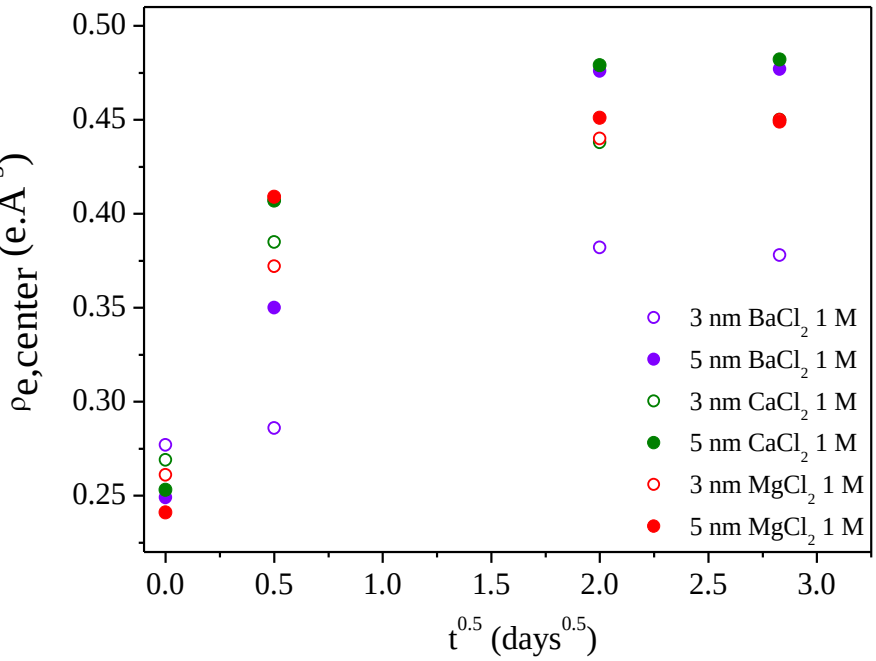


*Figure 29: Evolutions of the electron density in the center of the nanochannels (3 and 5 nm) as a function of the square root of time for the filling with electrolyte solutions at 1 M.*

Second, considering that the complete filling of the nanochannels is reached when the electron density in the center of the nanochannels is equal to the one of the bulk solutions, we observed a complete filling of the 5 nm nanochannels whatever the solutions, except with the $MgCl_2$ solution, and the following tendency in the 3 nm nanochannels: $BaCl_2 < CaCl_2 < MgCl_2 < H_2O$.

### 2.2 Determination of the surface ion excess

The surface ion excess $d_i$ were calculated using eq. 27. Figure 30 presents the surface ion excess $d_i$ for the electrolyte solutions in 3 and 5 nm nanochannels. First, the total $d_i$ obtained for the CEA/LETI nanochannels are in the same order of magnitude that the one obtained for the nanochannels of the University of Twente. Second, whatever the electrolyte solution, $d_i$ is lower in

the smaller nanochannels. Furthermore, $d_i$ follows independently from the confinement size the order: $BaCl_2 < CaCl_2 < MgCl_2$.

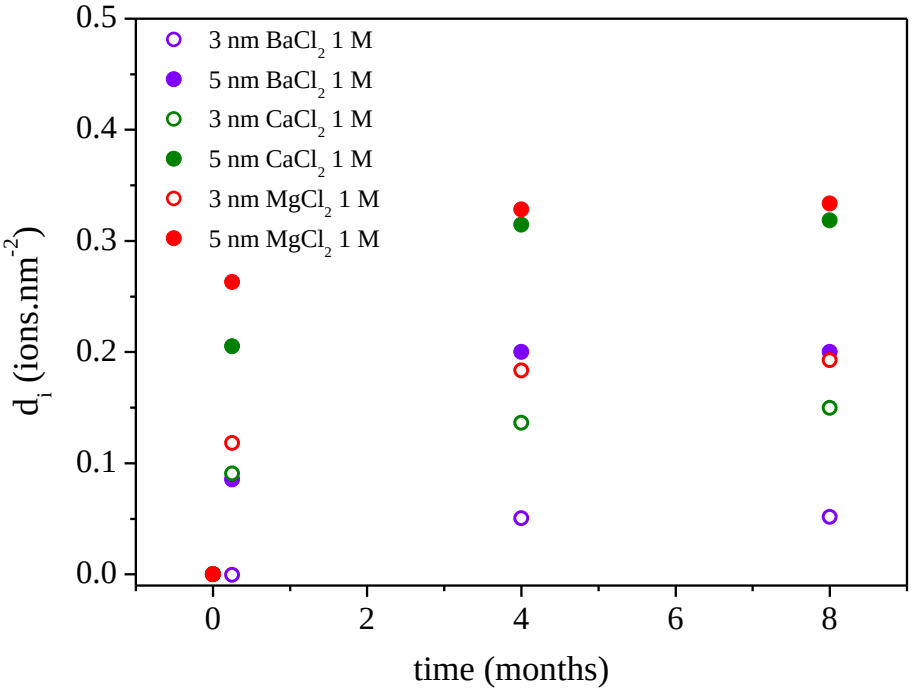


*Figure 30: Evolutions of the surface ion excess $d_i$ at the silica surface of the nanochannels as a function of the filling time with electrolyte solutions at 1 M.*

We have to precise that such determination of the surface ion excess depends on the electron density in the nanochannels center. When the nanochannels are not completely filled, the value of $d_i$ is not exact and can be underestimated.

## 2.3 MD simulations

As shown in the preceding section, MD simulations provide a more detailed insight on the ion sorption processes and therefore, in the interfacial layer. Since it is not possible from the experimental XRR to distinguish between sorbed cations and anions, Tristan Wang and Bertrand Siboulet modelled two charged silica walls having 2, 3 and 5 nm, filled with an aqueous $BaCl_2$ solution. From this MD simulation (Figure 31), the distributions of ion densities were obtained and are presented in Figure 32.

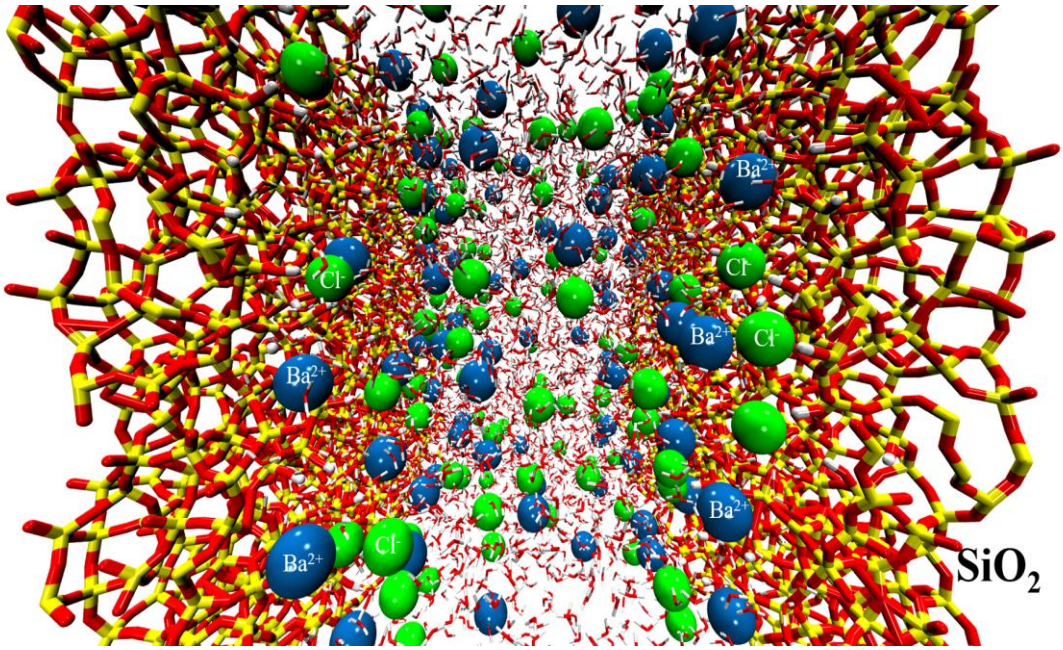


*Figure 31: Snap-shot from atomistic modelling of a 1 M $BaCl_2$ solution within $SiO_2$ nanochannels having a gap size of 5 nm. $Ba^{2+}$ ions are presented in red spheres and $Cl^-$ in blue.*

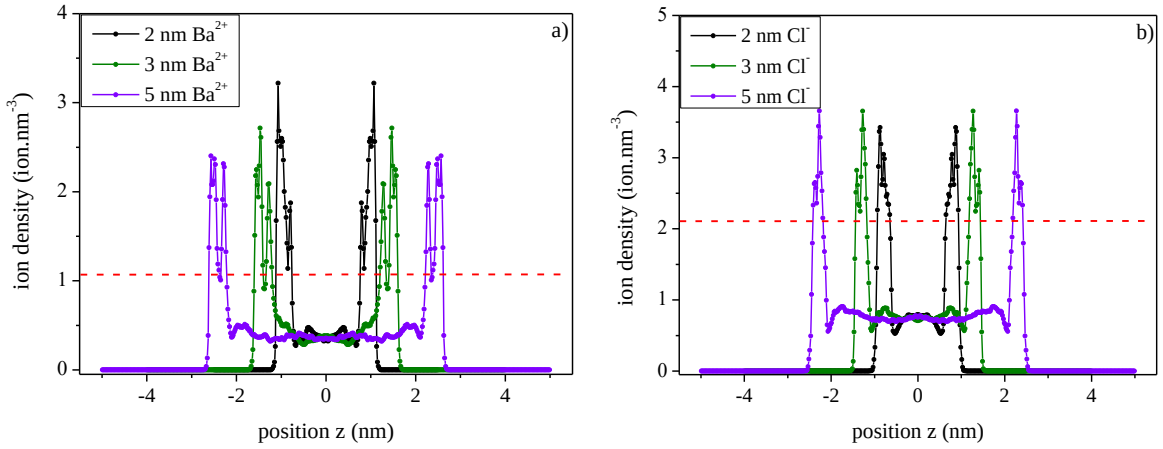


*Figure 32: Electron density profiles for $BaCl_2$ solutions at 1 M in 3 and 5 nm nanochannels obtained from MD simulations. On the top, the profiles for $Ba^{2+}$ and $Cl^-$ are shown. The dashed red line denotes the limit of $BaCl_2$ solubility at 25 °C.*

As highlighted with the red dashed line in Figure 32, the number of sorbed ions in the interfacial layer can exceed the limit of solubility of $BaCl_2$ at 25 °C. The solubility of various salts can be found in Table 5.[148]

*Table 5: Salt solubility at 25 °C for $XCl_2$ (X = Ba, Ca, Mg).*

| salts | $BaCl_2$ ($g.L^{-1}$) | $CaCl_2$ ($g.L^{-1}$) | $MgCl_2$ ($g.L^{-1}$) |
|---|---|---|---|
| solubility at 25 °C | 360 | 745 | 542 |

Therefore, in the case of $BaCl_2$, the supersaturation in the interfacial layer can lead to a precipitation of a phase in the nanochannels. This precipitation may induce a nanochannels clogging and result in an incomplete filling of the nanochannels. This is observed with the $BaCl_2$ solution in the 3 nm nanochannels and also with the $MgCl_2$ in the 3 and 5 nm nanochannels. However, the solubility of the $MgCl_2$ salt is higher than the one of $BaCl_2$ and the incomplete filling

is observed, whatever the size of the confinement. This means that the salt solubility would not be the only reason. Indeed, if we take into account the water dynamics at the picosecond timescale in presence of these electrolytes, as presented in the chapter III, the presence of $Mg^{2+}$ in solution lead to the strongest decrease of water motions. Thus, the combination of slowed dynamics related to the size of the confinement and/or the nature of the ions, and a low salt solubility, may mainly drive the solution transport in the silica confined media.

### 2.4 Possible precipitation in nanochannels

In order to estimate if our previous hypothesis about the salt precipitation is valid, we calculated the critical size of crystallites as a function of the supersaturation. As *Stack et al.*[3], we have used the following equation, based on the Young-Laplace equation:

$$r = \frac{V_m \gamma_{sl}}{RTln(a/a_0)} \qquad (27)$$

with $\gamma_{sl}$ the interfacial tension between the solid-liquid interface, with $V_m$ the molar volume of the corresponding precipitating salt $XCl_2$ (see Table 5; $\gamma_{sl}$ estimated to 0.100 $J.m^{-2}$)[149], a the actual concentration activity in solution, $a_0$ the actual concentration activity of the solid phase, R the ideal gas constant, and T the temperature. Solving this equation, we are able to calculate the size of the critical radius ($r_c$) for nucleation in bulk solution (i.e., homogeneous nucleation). Figure 33 presents the evolution of the critical nucleation radius as a function of the supersaturation. To enable $MgCl_2$ crystallites to precipitate in nanoconfinement below 5 nm, a supersaturation above 20 is required. Above this threshold, the formation of crystallites in the nanochannels is possible. At high degree of supersaturation, the nucleation rate is so high that the precipitate formed consist mostly of extremely small crystallites. The first formed crystallite might be of different polymorphous forms

than the final crystals. If the nucleus is smaller than a one-unit cell, the growing crystallite produced initially is most likely amorphous.

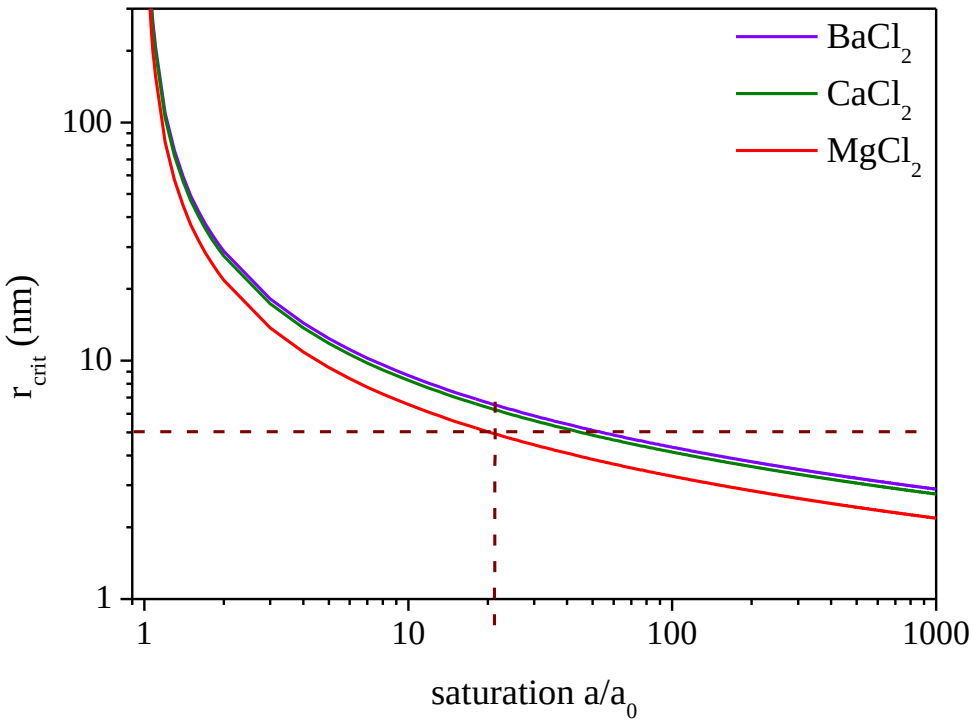


*Figure 33: Evolution of the critical nucleation radius as a function of the supersaturation concentration.*

Taking into account the values of Ba ions in the interfacial obtained by MD simulations and if our hypothesis in (3) are consistent, we assume that this threshold is not reached. Previous experiments to investigate the confinement effect of silica gels on the crystallization of salts have shown that the crystallization within the pores can be inhibited by several reasons.[150] *Nindiyasari et al*. revealed that the suppression of nucleation is related to the reduced ion diffusion in small pores.[151] Furthermore, the pore size can be a limiting factor for the crystal growth.[152–154] For nanometer-sized pores, NMR results suggest that the pressure in a growing crystal can lead to a higher solubility than in bulk solution.[155,156] However, X-Ray scattering experiments performed by *Stack et al.* have reported the that the pore size distribution (8.1 nm) in which a precipitation

reaction preferentially occurs depends on the favorability of interaction between the substrate and precipitate.[157] Nevertheless, a recent study by *Zeng et al.* has shown that aragonite, a metastable calcium carbonate, is promoted in confinement (25 nm) and in presence of Mg ions to the detriment of calcite the thermodynamically stable calcium carbonate. This would confirm the possible precipitation of metastable phase in nanoconfinement.[158]

Other nanoporous materials such as gels formed during glass alteration in presence of ions (Mg Ca and Fe) present some nanophases in the gel porosity.[159–163]

## E. Conclusion

In this study, we presented a powerful method coupling X-ray reflectivity and MD simulations to obtain the kinetics of electrolyte solution filling a confined media having plane and parallel surfaces and the surface ion excess in the interfacial layer.

The results obtained with plane silica surfaces and electrolytes having more or less kosmotropic ions have shown that the water dynamics and the salts solubility may be the main driving force for the filling of the confinement. If the supersaturation regarding the ions is reached in the interfacial layer, then the hydrated salt species may precipitate and lead to a complete or a partial channel clogging resulting in an incomplete confinement filling. In this case, the calculation of the surface ion excess in the interfacial layer is not correct. Such experiment should be performed again with lower electrolyte concentration and other electrolyte solutions.

In the following chapter, we study the ion sorption and the water properties in highly ordered mesoporous silica (SBA-15 and MCM-41).

# Chapter III - Study of water properties in highly ordered mesoporous silica filled with various electrolytes

*After the investigation of the transport of aqueous solutions and the interfacial layer in nanoconfinement made of two parallel and plane silica surfaces, we studied the water properties in nanoconfinement made of silica concave surface such as cylinders. In the following chapter, we intend to relate the properties of water in presence of various electrolytes confined in several mesoporous silica, such as its structure and its diffusion at a picosecond time scale, to the pore size and the electrolyte nature. To reach this goal, several highly organized mesoporous silica presenting different pore sizes and walls (dense and microporous) were used as model materials: SBA-15 (pore size around 6.6 nm and microporous silica wall), MCM-41 and grafted MCM-41 (pore size varying from 2.9 to 2.4 nm and dense silica wall). These properties were extrapolated to the properties of water molecules located in the interfacial layer.*

## A. Introduction

In this chapter, we pinpoint the structural and dynamical properties of water confined in highly ordered mesoporous silica in the presence of ions. Therefore, in the beginning of this chapter, we present the synthesis route and the experimental method followed by the characterization of the model materials. Second, we provide the sorption isotherms of several electrolytes in the silica materials in order to determine the ions surface excess as a function of the pore size and electrolyte nature. Third, the overall properties of water in these model materials in the presence of electrolytes solutions were characterized. The thermal behavior, the water structure and water dynamics at a picosecond timescale were determined and finally extrapolated - if possible -, to the water properties in the interfacial layer. Finally, we summarize and discuss the effects of the size of the confinement and nature of the electrolytes on the water properties.

## B. Experimental section

### 1. Synthesis of model materials

In this study, the soft-templating method was chosen to synthetize the silica model materials in order to have a control pore size and organized pore arrangement. Mesoporous silica which are defined in ref 164 as materials having pore sizes comprised between 2 and 50 nm, are generally prepared under “hydrothermal” conditions (Figure 34). The typical sol - gel process is involved in the “hydrothermal” process. However, the synthesis temperature is relatively low, ranging from room temperature to 150 °C. Mesoporous materials can be synthesized either under basic or acidic conditions. A general procedure includes several steps. First, a homogeneous solution is elaborated by dissolving the surfactants in water. Inorganic precursors (alkoxysilane) are then added into the

solution where they undergo the hydrolysis catalyzed by an acid or a base and transform to a sol and then a gel. A hydrothermal treatment is then carried out to induce the complete condensation and solidification. The resultant product is cooled to room temperature, filtered, washed and dried. Mesoporous material is finally obtained after the removal of organic templates by calcination or extraction. Here, SBA-15, MCM-41 and grafted MCM-41 silica were elaborated.

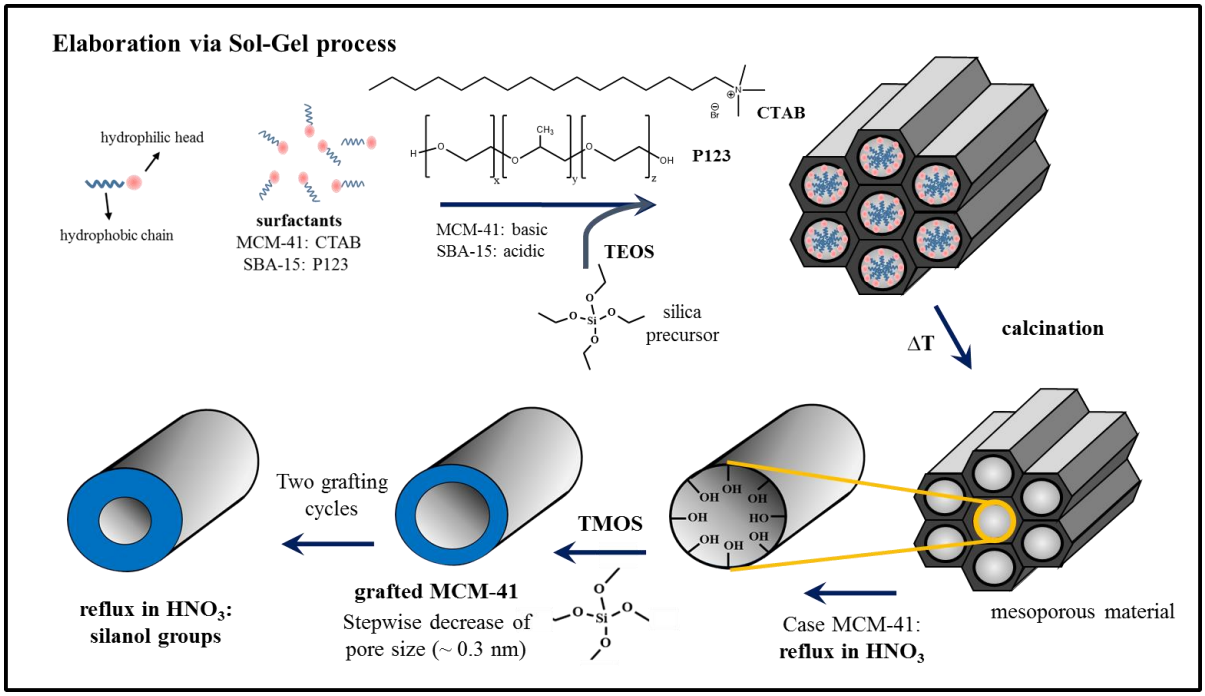


*Figure 34: Synthesis route for highly ordered mesoporous silica SBA-15 and MCM-41.*

1.1 SBA-15

SBA-15 was prepared using the hydrothermal method described by *Zhao et al.*[165] A mass of 6.0 g of Pluronic P123 ($EO_{20}$-$PO_{70}$-$EO_{20}$ MW = 5800, Aldrich,) was dissolved in a mixture of 45 mL of ultrapure water and 180 mL of 2 M HCl (37 wt%, Merck) solution under stirring at 35 °C. Then, 13.5 mL of TEOS (99 wt%, Sigma–Aldrich) was added dropwise to this solution under stirring at 35 °C for 20 h. The sol was aged at 80 °C in an oven during 8 h. The obtained precipitate

was filtered, washed with ultrapure water, and dried at laboratory atmosphere. Finally, powder calcination was carried out at 500 °C for 6 h (heating rate 1 °C/min). White powder was obtained in a yield of 98 %.

### 1.2 MCM-41

MCM-41 was first prepared using the hydrothermal method described by *Chen et al.*[166] Amounts of 1.01 g of cetyltrimethylammonium bromide (CTAB 99 wt %, Sigma−Aldrich), used as template, and 5.78 g of TEOS (99 wt %, Sigma−Aldrich) were added to 30 mL of water and 0.34 g of NaOH (99 wt %, VWR). The latter was used as catalyst to enhance condensation reactions. The mixture was stirred for 60 min at room temperature. Then, the sol was heated at 110 °C for 96 h in an oven. After 96 h, the resulting white precipitate was filtered and washed with 1 L of deionized water and 50 mL of ethanol (99.9 wt %, Merck). The resulting powder was dried for 2 h at 80 °C. To remove the CTAB template, 1.06 g of resulting powder was mixed with 0.25 mL of HCl (37 wt %, Merck) and 20 mL of ethanol. The mixture was stirred at 60 °C for 90 min, washed with deionized water, dried at 80 °C for 2 h, and then calcined at 540 °C for 2 h (heating rate of 4 °C/min).

### 1.3 Grafted MCM-41

To decrease stepwise the pore size, MCM-41 was grafted using the Hydrolytic Surface Sol−Gel method (HSS) according to the protocol of *Ichinose and co-workers*.[167] The HSS method used to functionalize the surface layer by layer, was performed in two steps: a first step consists of an acid treatment to hydrolyze the surface and form reactive hydroxyl groups, and a second step consists of the reaction of these hydroxyl functions with metal-alkoxides in an anhydrous solvent. Tetramethoxysilane (TMOS) was used to decrease the pore size. MCM-41 (3 g) was refluxed in 50 mL of nitric acid (10 wt %, Merck) for 2 h to generate silanol groups at the material surface. After acidic hydrolysis, MCM-41 was filtered and washed with 3 L of deionized water and then

dried for 4 h at 120 °C to remove physisorbed water. Hydrolysed MCM-41 was mixed and refluxed with a solution of 1.88 mL of TMOS dissolved in 50 mL of anhydrous toluene (99.8 wt %, Sigma−Aldrich). This step was repeated to obtain samples of MCM-41 grafted with one (MCM-41-1) and two layers (MCM-41-2). In a final step, grafted mesoporous silica were refluxed in 50 mL of nitric acid (10 wt %, Merck) for 2 h to regenerate the silanol groups at the surface.

## 2. Solid characterizations

The porous structure of SBA-15 and MCM-41 was characterized using small-angle X-Ray scattering (SAXS) in the transmission geometry with a molybdenum anode, delivering a wavelength of 0.71 Å. Focusing and wavelength selection are achieved using a Xenocs Fox 2D multilayer mirror. Two sets of scatterless slits allow the beam to be collimated and to have a squared shape of side 0.8 mm. SAXS patterns were recorded on a MAR345 2D image plate which enables the simultaneous detection over scattering vectors q ranging from 0.3 to 20 $nm^{-1}$. Samples were analyzed in glass capillaries of around 2 mm diameter. The detailed treatment of the raw SAXS data can be found in annex III.

Nitrogen adsorption-desorption analyses were carried out using a Micromeritics apparatus. Before analysis, all samples were outgassed at 350 °C during 8 h under high vacuum ($10^{-5}$ Pa). Specific surface area, pore volume and pore size distribution were obtained using the Brunauer−Emmett−Teller (BET) method and the Barret−Joyner−Halenda (BJH) model, respectively.

## 3. Sorption isotherms and preparation of filled material

The sorption isotherms of ions were performed at 20 °C by immersing 0.2 g of SBA-15 powder or 0.15 g of MCM-41 in 4.2 mL of $XCl_2$ solution in a polytetrafluoroethylene reactor

(see Figure 35) during 24 h. In these experimental conditions, the silica powder surface area to solution volume ratio (S/V) was $4.10^7$ $m^{-1}$ for SBA-15 and MCM-41. This high S/V allows the minimization of the silica dissolution. Electrolytes solutions of $XCl_2$ (X = Ba, Ca, Mg) at $[XCl_2]_0$ = 0.01, 0.2 and 1 M were prepared using hydrated salts of barium chloride dihydrate ($BaCl_2$, $2H_2O \leq 99$ %, Sigma-Aldrich), calcium chloride dihydrate ($CaCl_2$, $2H_2O \leq 99$ %, Sigma-Aldrich) and magnesium chloride hexahydrate ($MgCl_2$, $6H_2O \leq 99$ %, Sigma-Aldrich). The final pH values of the solutions measured at the laboratory atmosphere are summarized in Table 6.

*Table 6: pH values of electrolyte solutions $XCl_2$ (X = Ba, Ca, Mg) measured at the laboratory atmosphere. The uncertainties do not exceed ± 0.05.*

| $[XCl_2]_0$ | 0.01 M | 0.2 M | 1 M |
|---|---|---|---|
| $BaCl_2$ | 5.79 | 5.47 | 5.38 |
| $CaCl_2$ | 6.22 | 6.31 | 6.37 |
| $MgCl_2$ | 6.35 | 6.07 | 5.77 |

At the sorption isotherms equilibrium (24 h), the remaining solutions were filtered using a membrane filter having 0.25 µm pore size. The filtered solutions were acidified to 2 vol % of $HNO_3$ (65 wt% Suprapur Merck). Then, diluted and acidified solutions were analyzed using ICP-AES to determine the atomic concentrations of Ba, Ca and Mg before and after immersion of silica powder. Chloride concentrations were measured using an ICS 5000 Capillary Ionic chromatography equipped with an AS11 Capillary. A 20 mM KOH solution was used as eluent maintaining the flow at 0.012 $ml.min^{-1}$ in isocratic mode. Each run was performed at least three times to ensure a sufficiently high accuracy. The concentration uncertainties were calculated taking into account all the experimental and analytical uncertainties.

The powder was removed from the reactor after 24 h. Subsequently, the powder was freeze-dried with a LABCONO FreeZone 2.5 Freeze Dry System for 48 h to remove the water molecules adsorbed around the silica grains and a maximum of water located into the nanopores. This method allows the preservation of the material porosity and ensures that the ions remain present inside the pores.[88,168] After this process, the powder was placed in a desiccator in the presence of a beaker containing a saturated solution of KCl, fixing a relative humidity (RH) of 82 % at 25 °C in order to reach rapidly the desired humidity. At this humidity, water only fills the nanopores and does not adsorb around the powder grains.[119] Samples were stored in this condition between one week and one month until their characterization.

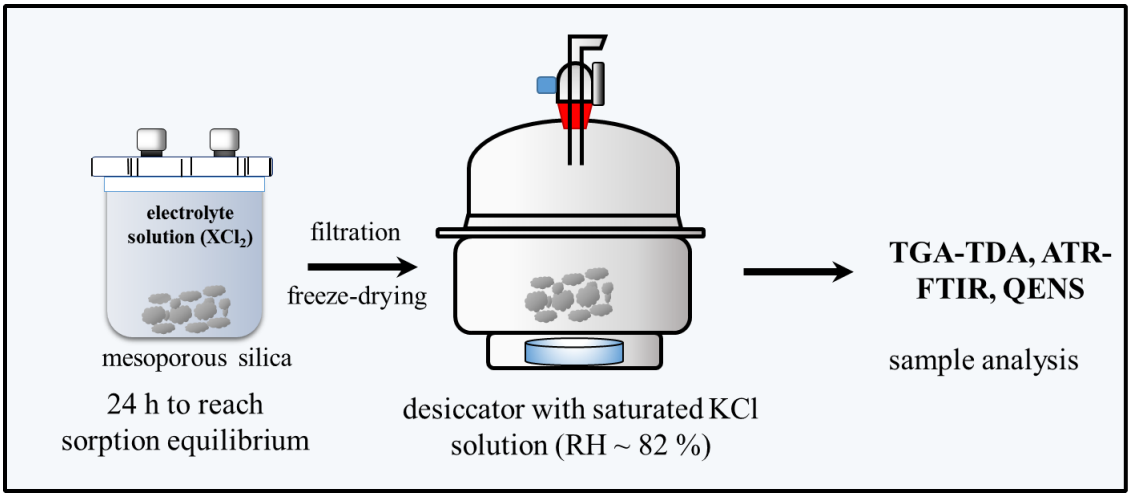


*Figure 35: Schematic overview of the preparation of the silica model materials filled with various electrolytes.*

## 4. Water characterization

The properties of confined water and electrolyte solutions were studied performing the same protocol. In order to ensure the mesoporous filling as long as possible, the stored samples were taken out of the desiccator before the corresponding analysis.

The thermal behavior of water confined in mesoporous silica was characterized using a SETARAM Setsys 60 thermogravimetric apparatus. Thermogravimetric analysis (TGA) and differential thermal analysis (DTA) data were collected under an air stream (20 $cm^3.min^{-1}$), without further drying, running from room temperature up to 700 °C with an heating rate of 10 $°C.min^{-1}$. Buoyancy effects were corrected by a blank run with an empty alumina crucible. Data treatments were done using the Calisto Processing software v.1.065.

Water structure was analyzed using Fourier transform infrared spectroscopy in attenuated total reflection mode (ATR-FTIR). Spectra were recorded using a PerkinElmer Spectrum 100 spectrometer, operating with a Globar MIR source, in combination with a Cesium Iodide (CsI) beamsplitter and a deuterated triglycine sulphate DTGS detector, through CsI transmission windows. The samples were placed at the surface of a 2 mm diameter top-plate diamond crystal, stacked on a KRS-5 (Thallium Bromide-Iodide) bottom-plate micro focus condenser. A high pressure was generated on the small amount of sample, and was adjusted until stabilization of the spectra was achieved, allowing good signal-to-noise ratio and highly reproducible measurements. Spectra were recorded from 500 to 4000 $cm^{-1}$, adding 4 scans, using 4 $cm^{-1}$ nominal resolution, and operating background correction (atmospheric bands) for each substrate. Data treatments like baseline adjustments, normalization of spectrum and bands decomposition were performed using the ORIGIN software. The O-H stretching band was decomposed with several Gaussian functions

adjusting the intensity and the width of the fitting curves. The "best fit" was considered when the statistical parameter R was the lowest.

Water dynamics at pico-second time scale in hydrated samples was analyzed by quasi-elastic neutron scattering (QENS). Experiments were performed on the time-of-flight spectrometer FOCUS for cold neutrons at SINQ at the Paul Scherrer Institute (Villigen, Switzerland). Samples were placed into aluminum cells sealed with an indium wire to avoid water loss and ensure a constant hydration level during neutron scattering experiments. The QENS measurements of samples were carried out at 300 K with an incident wavelength of 4.32 Å and a resolution of 90 μeV in order to cover a correlation time ranging from 0.1 to 10 ps. The QENS signal was treated and analyzed with the DAVE software provided by PSI and designed to treat such data.[169] A more detailed description of this scattering method can be found in the annex III.

## C. Characterization of filled materials

### 1. Model materials characterization

The removal efficiency of surfactants after the SBA-15 and the MCM-41 thermal treatment and the efficiency of the last step of the HSS grafting process (hydrolysis of O–$CH_3$) were controlled by ATR-FTIR. Figure 36 exhibits the removal of surfactants after the calcination step and the presence of silanol groups on the surface after the HSS step. The presence of $\nu_s$C-H and $\nu_{as}$C-H bands can be related to the contamination of the ATR crystal, as already observed in previous studies.[162,170] Moreover, the presence of $CH_2$ low intensity band for the MCM-41-2 could come from an incomplete hydrolysis of O–$CH_3$ groups.

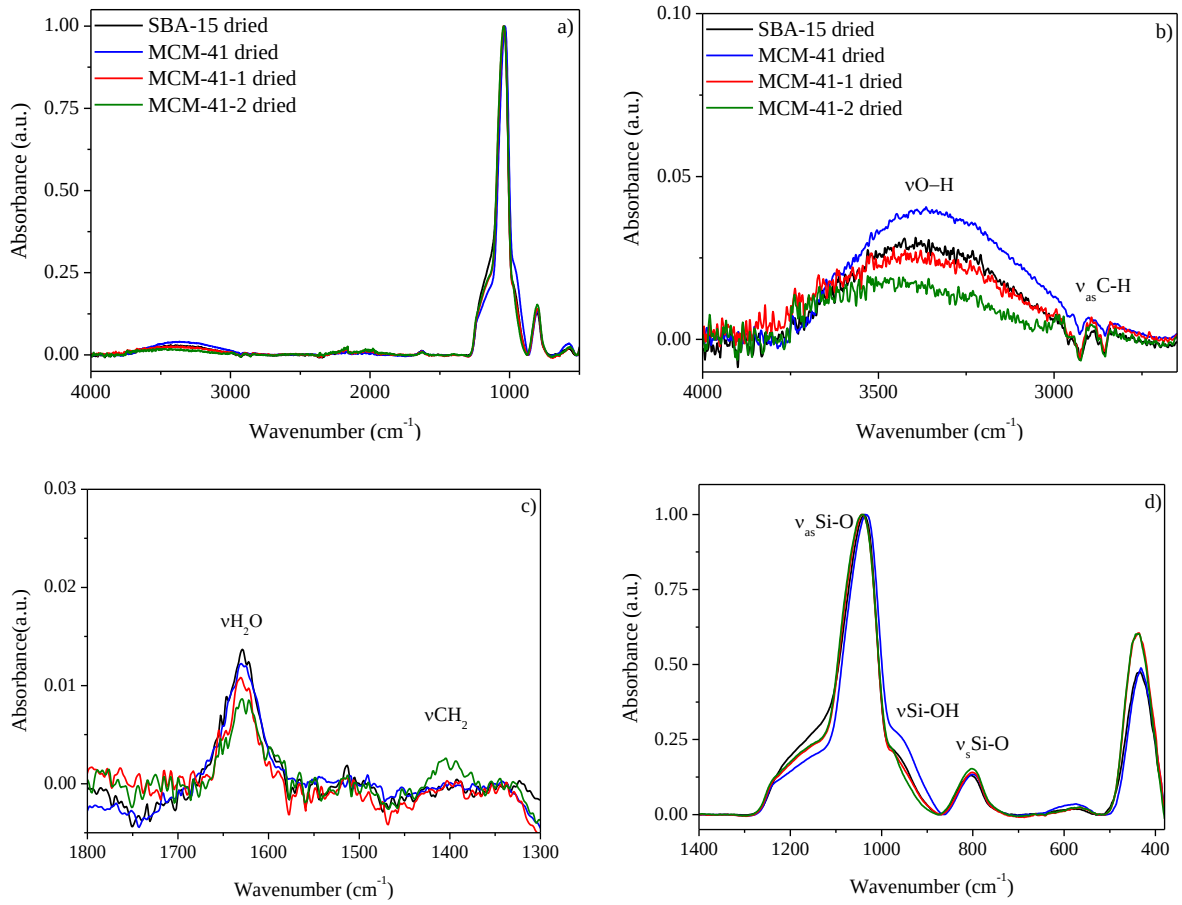


*Figure 36: a) FTIR-ATR spectra of dried SBA-15, MCM-41 and grafted MCM-41. Figure b) to d) show the characteristic vOH, vCH and vSiO bands in the corresponding frequency range.*

The porosity and the characteristics of the materials were analyzed by SAXS and nitrogen adsorption-desorption. Figure 37 presents the SAXS pattern of SBA-15, MCM-41 and grafted MCM-41 samples. The pattern of SBA-15 presents a strong and well-defined peak at $q = 0.62\ nm^{-1}$ and three peaks of weaker intensity at around $1.08\ nm^{-1}$ and $1.25\ nm^{-1}$ and at $q = 1.88\ nm^{-1}$. Since MCM-41 has a smaller confinement than SBA-15, the Bragg peaks are shifted to higher q values. As highlighted at the bottom of Figure 37, these peaks correspond to the (100), $(1\bar{1}0)$, (200) and (300) lattice planes of the hexagonal arranged pores. These peaks are shifted to

the higher q values with the number of grafting processes. From these data, inter-reticular distances *d* were calculated by using eq. 29:

$$d = \frac{\lambda}{2\ sin\theta} \qquad (28)$$

where $\lambda$ is the wavelength of incident wave; *d* is the spacing between the planes in the mesoporous lattice; and $\theta$ is the angle between the incident beam and the scattering planes. The unit cell parameter $a_0$ was also deduced from eq. 30:

$$a_0 = \frac{2d_{100}}{\sqrt{3}} \qquad (29)$$

These parameters are illustrated in Figure 37 (c).

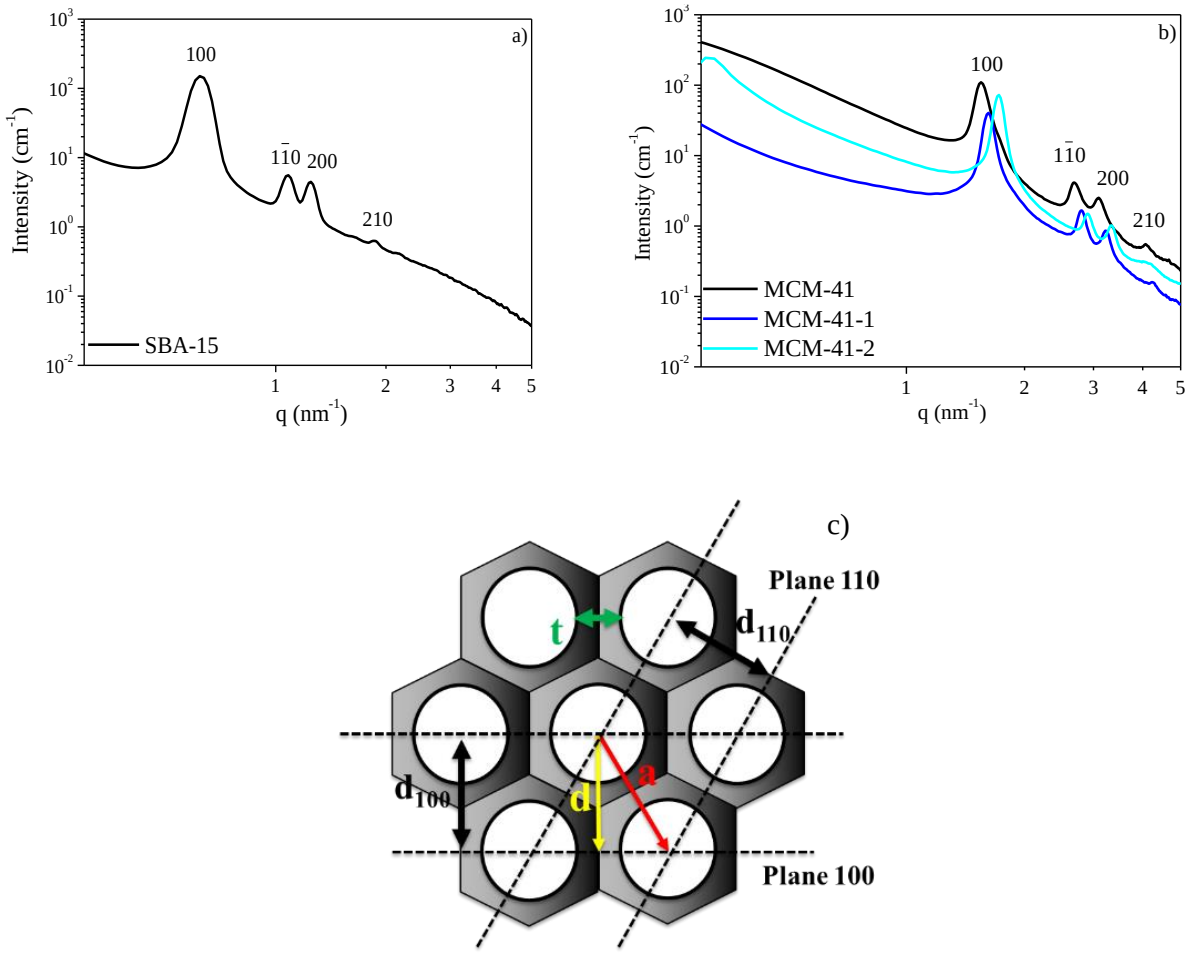


*Figure 37: SAXS pattern of SBA-15 (a) and MCM-41 and grafted MCM-41 (b) showing the Bragg peaks. The scheme (c) presents the various parameters defining the hexagonal arrangement of the mesopores: cell unit parameter a, wall thickness t and interreticular distance d.*

From the adsorption-desorption isotherms of the various silica presented in Figure 38 (a), characteristics of mesoporous materials, such as the specific surface areas and the pore volumes were determined and are presented in Table 7. The curves for the materials correspond to typical type IV (IUPAC) isotherms where the adsorption-desorption of SBA-15 exhibits a hysteresis of

type H1. This hysteresis loop is associated with the capillary condensation in mesoporous structures. In this case, the parallel desorption and adsorption branches are related to a narrow pore size distribution. In contrast to that, the isotherms of MCM-41 and grafted MCM-41samples show no hysteresis. This can be explained by the small pore sizes of MCM-41 and grafted MCM-41 samples.

Only SBA-15 presents a microporosity resulting from the penetration of PEO chains into the silica wall, surfactant used during its synthesis.[171,172] The mean pore sizes of each materials were deduced from the pore size distribution obtained from the BJH model (Figure 38 (b)). As showed by these results, the pore size of grafted MCM-41 are reduced step-by-step after each grafting cycle from 0.2 to 0.3 nm.

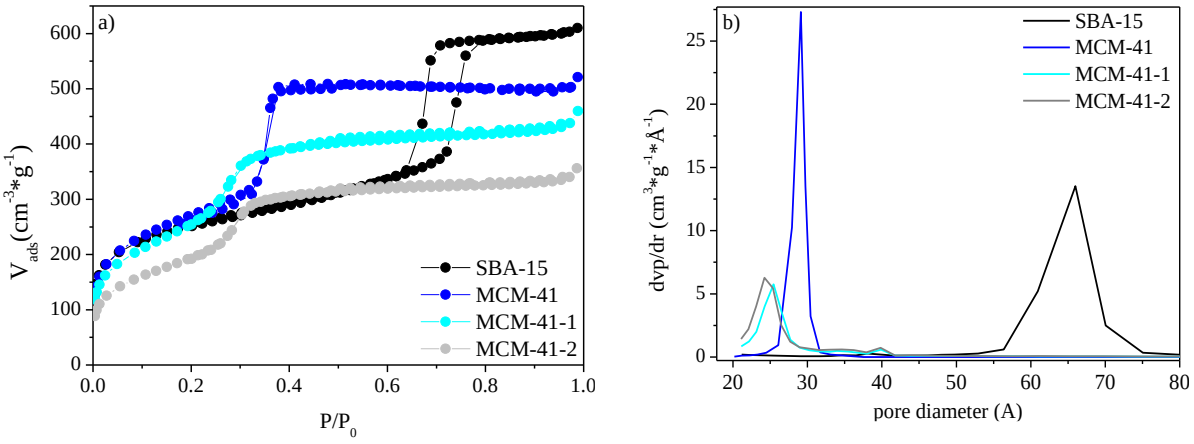


*Figure 38: (a) Nitrogen adsorption-desorption isotherms and (b) pore size distributions of SBA-15, MCM-41 and grafted MCM-41.*

*Table 7: Properties of the structure and of the porosity of SBA-15, MCM-41 and grafted MCM-41. d: inter-reticular distance, $a_0$ unit cell parameter, $V_p$: porous volume, $V_{micros}$: microporous volume, $S_{BET}$: Specific surface area.*

| Sample | d (nm) | $a_0$ (nm) | Mean pore diameter (nm) | $V_p$ ($cm^3/g$) | $V_{micro}$ ($cm^3/g$) | $S_{BET}$ ($m^2/g$) |
|---|---|---|---|---|---|---|
| **SBA-15** | 10.1 | 11.7 | 6.6 ± 0.1 | 0.94 ± 0.02 | 0.46 ± 0.01 | 842.1 ± 17 |
| **MCM-41** | 4.1 | 4.7 | 2.9 ± 0.1 | 0.81 ± 0.02 | - | 954.3 ± 19 |
| **MCM-41-1** | 3.9 | 4.5 | 2.6 ± 0.1 | 0.75 ± 0.01 | - | 810.6 ± 16 |
| **MCM-41-2** | 3.7 | 4.2 | 2.4 ± 0.1 | 0.51 ± 0.01 | - | 796.1 ± 12 |

## 2. Sorption isotherms and surface ion excess

The sorption behavior of the selected ions within mesoporous silica was the first characteristic property we studied. From the concentrations of the element *i* measured in solutions before ($C_{i0}$, $mol.L^{-1}$) and after ($C_{ieq}$, $mol.L^{-1}$) the sorption isotherm experiments, the surface ion excess $d_i$ ($nm^{-2}$) at the surface of the nanopores were calculated assuming that at the equilibrium, the concentration of the ions in the center of the nanopores is equal to the ions concentration $C_{ieq}$ of the bulk solution (eq. 31).

$$d_i = \frac{(C_{i0} - C_{ieq}).V_p.N_A}{S_{BET}.m_p} \qquad (30)$$

with $N_A$ the Avogadro number and $m_p$ (g) the mass of SBA-15.

Figure 39 presents the evolution of $d_i$ as a function of $C_{i0}$ for the four different ions. The obtained values for the different materials are presented in Table 8. In addition to that, the concentration of Si in the bulk electrolyte solutions after 24 h of immersion are also shown.

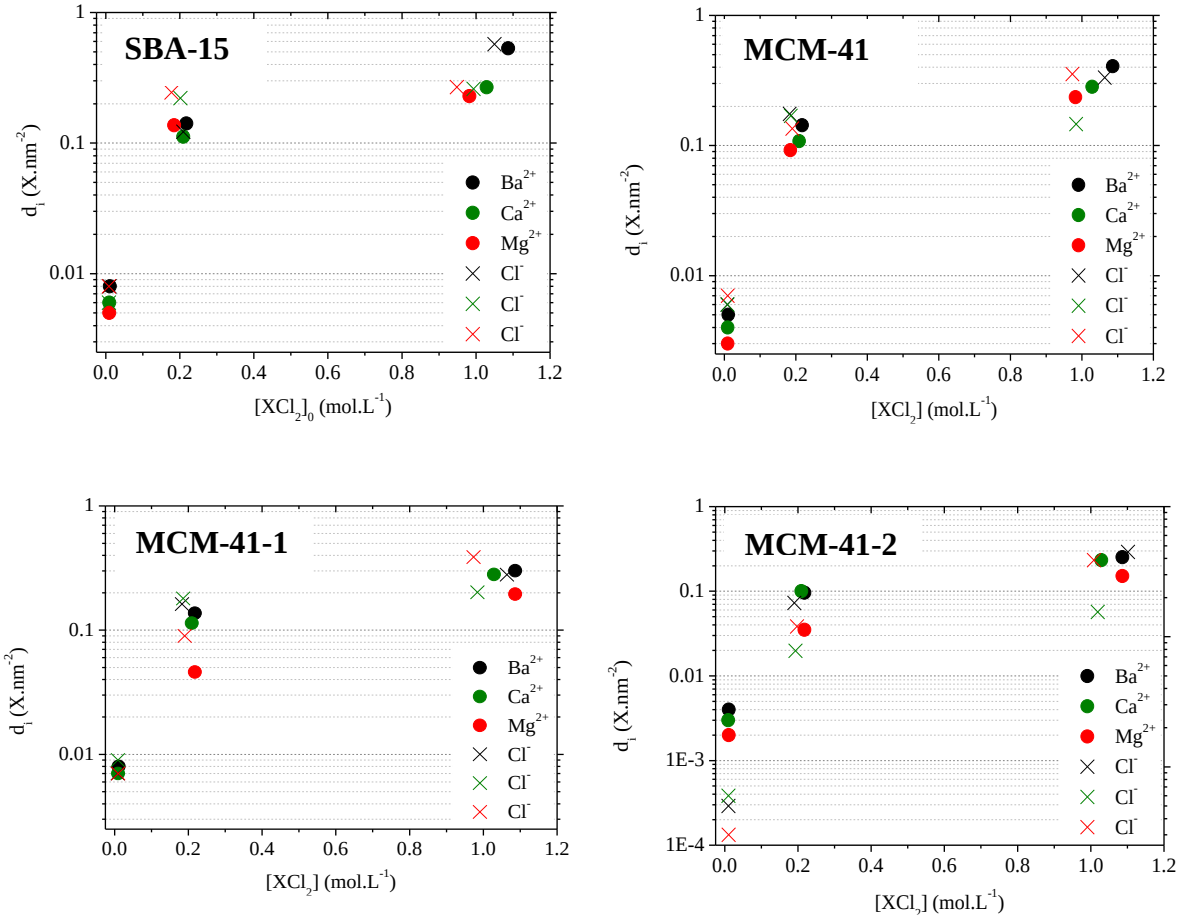


*Figure 39: Surface ion excess $d_i$ in SBA-15, MCM-41 and grafted MCM-41 as a function of the initial electrolyte concentration.*

*Table 8: Surface ion excess* $\boldsymbol{d_i}$ *on SBA-15, MCM-41 and grafted MCM-41 and concentration of Si in the bulk electrolyte solutions measured by ICP-AES. Uncertainties do not exceed ± 5.5 %.*

| $d_i$ (.nm$^{-2}$) | **SBA-15** | | | **MCM-41** | | | **MCM-41-1** | | | **MCM-41-2** | | |
|---|---|---|---|---|---|---|---|---|---|---|---|---|
| $[XCl_2]_0$ | *0.01* | *0.2 M* | *1 M* | *0.01 M* | *0.2 M* | *1 M* | *0.01 M* | *0.2 M* | *1 M* | *0.01 M* | *0.2 M* | *1 M* |
| $d_{Ba}$ | 0.00 | 0.141 | 0.535 | 0.005 | 0.143 | 0.407 | 0.008 | 0.137 | 0.301 | 0.004 | 0.096 | 0.253 |
| $d_{Cl}$ | 0.00 | 0.122 | 0.572 | 0.006 | 0.175 | 0.333 | 0.007 | 0.162 | 0.280 | 0.005 | 0.182 | 0.348 |
| $d_{Tot}$ | 0.01 | 0.263 | 1.107 | 0.011 | 0.318 | 0.740 | 0.015 | 0.299 | 0.581 | 0.009 | 0.278 | 0.601 |
| *[Si] (mg.L$^{-1}$)* | 6.9 | 31.6 | 190.8 | 9.6 | 19.8 | 203.1 | 4.0 | 26.2 | 174.1 | 3.2 | 29.6 | 195.2 |
| $d_{Ca}$ | 0.00 | 0.112 | 0.267 | 0.004 | 0.108 | 0.283 | 0.007 | 0.114 | 0.281 | 0.003 | 0.100 | 0.233 |
| $d_{Cl}$ | 0.00 | 0.221 | 0.260 | 0.006 | 0.169 | 0.146 | 0.009 | 0.180 | 0.202 | 0.006 | 0.078 | 0.155 |
| $d_{Tot}$ | 0.01 | 0.333 | 0.527 | 0.010 | 0.277 | 0.429 | 0.016 | 0.294 | 0.483 | 0.009 | 0.178 | 0.388 |
| *[Si] (mg.L$^{-1}$)* | 1.2 | 26.8 | 135.8 | 1.4 | 25.5 | 142.1 | 1.4 | 32.5 | 141.0 | 1.5 | 33.1 | 144.3 |
| $d_{Mg}$ | 0.00 | 0.137 | 0.281 | 0.003 | 0.092 | 0.235 | 0.001 | 0.046 | 0.195 | 0.002 | 0.035 | 0.151 |
| $d_{Cl}$ | 0.00 | 0.244 | 0.268 | 0.007 | 0.135 | 0.354 | 0.007 | 0.009 | 0.388 | 0.003 | 0.120 | 0.387 |
| $d_{Tot}$ | 0.01 | 0.381 | 0.549 | 0.010 | 0.227 | 0.589 | 0.008 | 0.136 | 0.583 | 0.005 | 0.155 | 0.538 |
| *[Si] (mg.L$^{-1}$)* | 2.0 | 15.2 | 71.8 | 4.2 | 12.4 | 86.5 | 4.1 | 11.9 | 99.5 | 1.3 | 17.3 | 85.3 |

As presented in Figure 39, the slopes of the sorption isotherms decrease with the initial element concentration, suggesting an asymptotic plateau achieved for element concentration higher than 0.2 M, and resulting in a limited sorption capacity.[173] Since the pH of the point of zero charge for silica is about 2 to 3, the silica surface in our study ($5.4 < pH < 6.4$) is mainly negatively charged.[64] Thus, surface $–SiO^-$ groups can interact with cations $X^{2+}$ and in less extent with $H_3O^+$, via electrostatic interactions and decrease the surface potential via sorption. As shown, even anions sorb within the interfacial layer to compensate the cation sorption and to reach the electroneutrality in the bulk-like solution.

Moreover, these results depict that the surface ion excess $d_i$ is about the same order of magnitude than the one calculated in silica nanochannels and depends on the mesoporous material, the size of the confinement and on the nature of ions. To clarify this phenomenon, the evolution of the electron density $d_X$ as a function of the pore size is presented on the Figure 40 and shows that the surface ion excess is higher in SBA-15 than in MCM-41 and it decreases with the pore size (MCM-41 > MCM-41-1 > MCM-41-2), whatever the electrolyte. This result is globally similar to the one experimentally obtained in nanochannels (chapter II). However, for this calculation, we assumed that the concentration of the ions in the center of the pores is equal to the ions concentration $C_{ieq}$ of the bulk solution. For SBA-15, as presented in the paragraph (4.), bulk-like solutions are present in the center of the pore and, except for a filling of the nanochannels with $MgCl_2$ at 1 M, the density of the solution in the center of nanochannels at the equilibrium is equal to the bulk one. This is not the case for MCM-41 and grafted MCM-41 and not the case for nanochannels of 3 nm which are not completely filled due to a probable $XCl_2$ precipitation. This may lead to a

modification of the $d_i$ values for the MCM-41 and grafted MCM-41 due to the decrease of the accessible surface and porous volume.

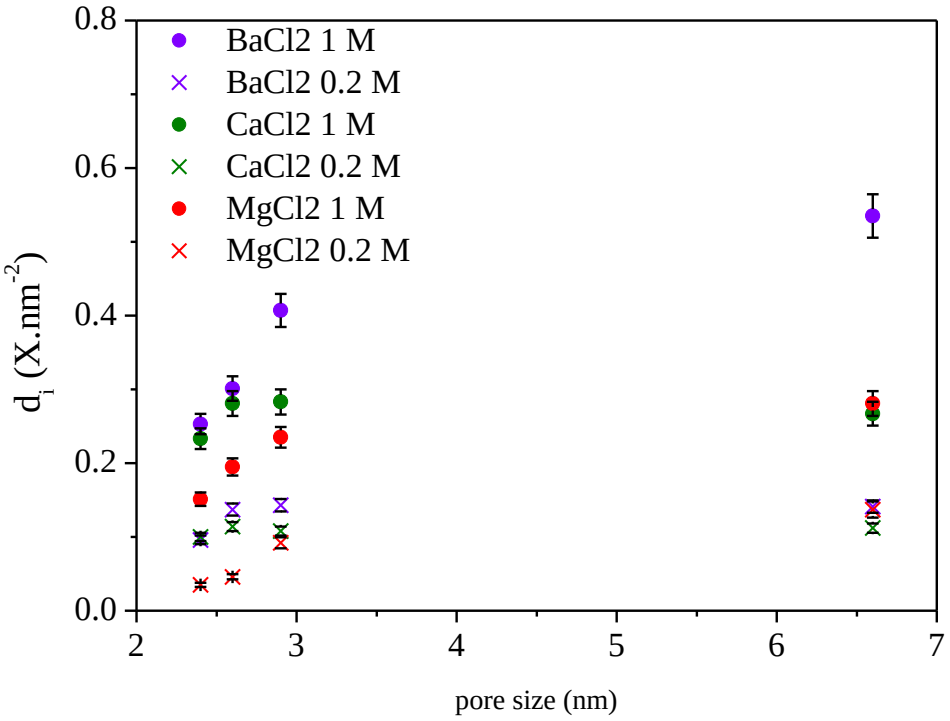


*Figure 40: Evolutions of surface cation excess $d_X$ at the equilibrium for various electrolyte solutions as a function of the pore size.*

At the equilibrium, $d_X$ depends on the nature of the element. As illustrated in Figure 40, whatever the silica confinement and $[XCl_2]_0$, $d_X$ follows $d_{Ba} > d_{Ca} > d_{Mg}$. Moreover, the highest $d_X$ is obtained for Ba at the initial salt concentration $[XCl_2]_0$ = 1 M. Generally, $d_X$ is higher than $d_{cl}$ except for MCM-41 and grafted MCM-41 filled with $MgCl_2$ solutions and MCM-41-2 filled with $BaCl_2$ 1 M where $d_X$ is higher than $d_{cl}$. The higher $d_{Ba}$ in SBA-15 may be related to the diffusion of Ba and Cl into the microporosity. The hydrated radius of $Ba^{2+}$ ($r_{hyd}$ = 4.0 Å) is smaller than $Ca^{2+}$ ($r_{hyd}$ = 4.1 Å) and $Mg^{2+}$ ($r_{hyd}$ = 4.3 Å) and therefore, $Ba^{2+}$ may penetrate the smaller micropores.[50]

The concentration of dissolved silica in the bulk electrolyte solution after 24 h depends on the initial electrolyte concentration. Generally, we found that [Si] is the highest for $[XCl_2]_0$ = 1 M, following the order $BaCl_2 > CaCl_2 > MgCl_2$, reaching the maximum for $BaCl_2$ in MCM-41. This is classically observed for the silica.[174] Since the dissolved concentration of silica is an important parameter to characterize the materials evolution, we will return to this point in the last chapter of the manuscript. In this chapter, we analyze the material dissolution using in-situ SAXS to quantify the impact of various electrolyte solutions on the stability of mesoporous silica.

## 3. Overall properties in the silica nanoconfinement

In the following section, we have a closer look on the water properties confined in mesoporous silica filled with various electrolytes. Both the thermal behavior of water and the water structure were analyzed using TDA, TGA and FTIR-ATR. Water dynamics at a pico-second time scale was determined using QENS.

### 3.1 Thermal behavior of water

#### *3.1.1 SBA-15*

The thermal behavior of the dried SBA-15, SBA-15 filled with water and various electrolyte solutions at different concentrations was determined by TGA and DTA analysis. The results are given in Figure 41 (a) and (b).

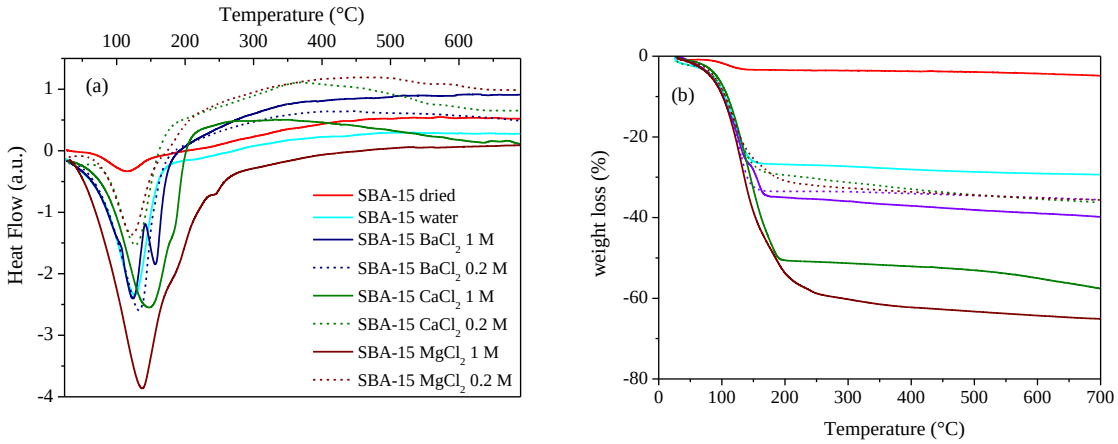


*Figure 41: TDA (a) and TGA (b) curves of SBA-15 filled with electrolytes $XCl_2$ under airflow.*

The TDA curves show several endothermic peaks for all samples. The first ones having a characteristic minima between 115 °C and 148 °C (peak I) and can be attributed to the desorption of physically adsorbed water in the micro- and mesoporosity.[175] These minima depend on the confined solution as indicated in Table 9. Furthermore, samples filled with the electrolyte solution at 1 M show a supplementary, more or less intense (peak II) between 150 °C and 200 °C. This peak can be attributed to water molecules located in the interfacial layer and/or to the water molecules belonging to the hydration shells of the ions. This peak is more obvious for SBA-15 $BaCl_2$ 1 M sample than for SBA-15 $CaCl_2$ 1 M and SBA-15 $MgCl_2$ 1 M samples, and present a temperature increase following this order: SBA-15 $BaCl_2$1 M < SBA-15 $CaCl_2$ 1 M < SBA-15 $MgCl_2$ 1 M. This means that the water molecules are more strongly bonded in SBA-15 $MgCl_2$ 1 M sample than in the other samples. It is also remarkable that the percentage of water inside the material is strongly dependent on the electrolytes nature and concentration. When $[XCl_2]_0$ = 1 M, the amount of water for samples filled with $MgCl_2$ and $CaCl_2$ is higher than for $BaCl_2$. This was also observed in 5 nm nanochannels after one week of filling (chapter II). The differences in water amount

are less distinctive for $[XCl2]_0$ = 0.2 M. Above 250 °C, the weight losses attributed to the silanol at the pore surface and/or embedded into the pore wall, are lower than 7 %.

*Table 9: Temperatures of endothermic peaks I and II and their corresponding weight loss percentages of SBA-15 samples obtained by DTA/DGA measurements.*

| sample | $[XCl_2]_0$ (M) | Peak I (°C) | Peak II (°C) | Mass loss (%) |
|---|---|---|---|---|
| SBA-15 dried | | 115.0 | - | 4.8 |
| SBA-15 water | | 127.3 | - | 29.3 |
| SBA-$BaCl_2$ | 0.2M | 134.2 | - | 35.6 |
| | 1 M | 125.1 | 157.6 | 39.9 |
| SBA-$CaCl_2$ | 0.2M | 127.6 | - | 35.8 |
| | 1 M | 148.3 | 184.3 | 57.6 |
| SBA-$MgCl_2$ | 0.2M | 123.5 | - | 35.9 |
| | 1 M | 137.8 | 191.6 | 65.2 |

### *3.1.2 MCM-41 and grafted MCM-41*

The results for the dried MCM-41 and MCM-41-1, as well as the corresponding solutions in confinement are shown in Figure 42 (a) - (d).

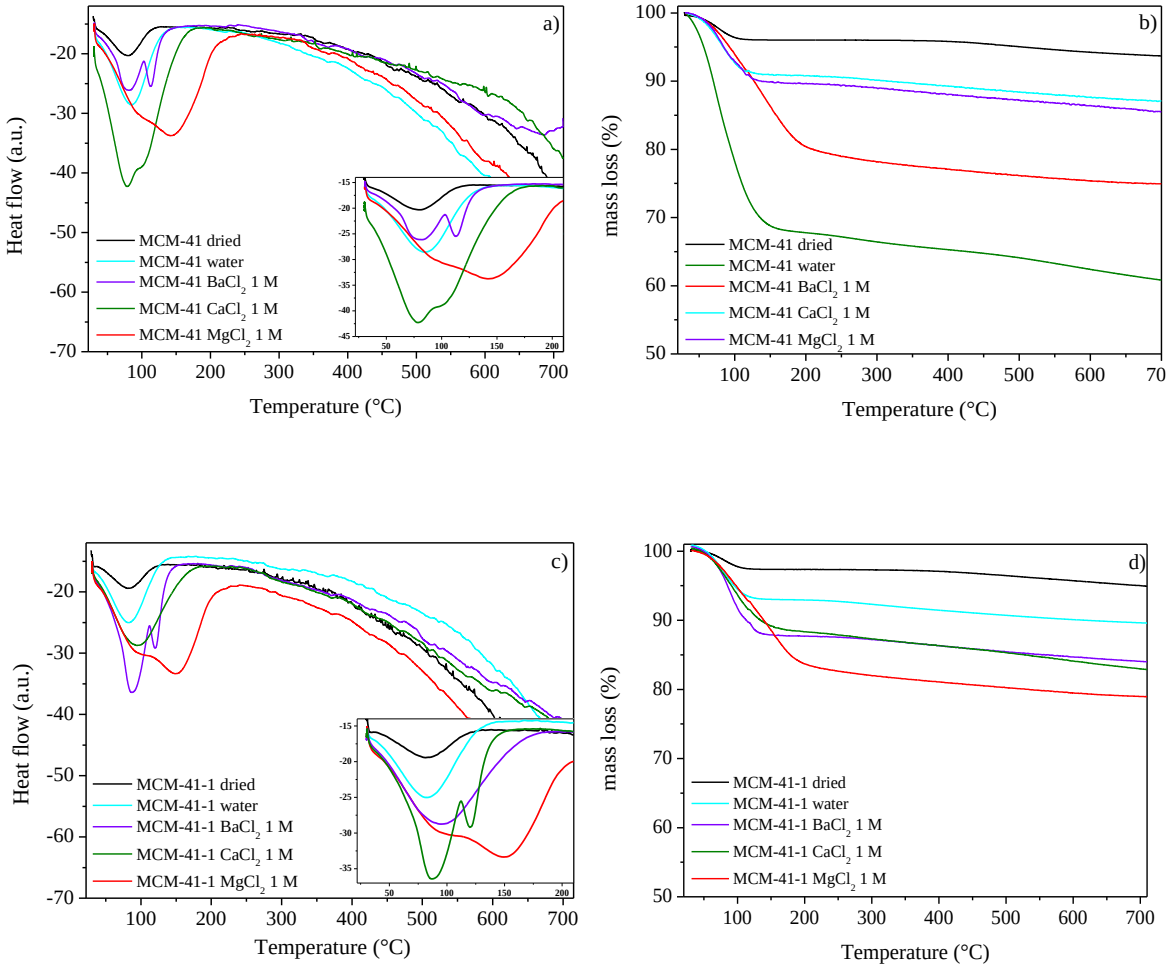


*Figure 42: TDA (left panels) and TGA (right panels) curves of samples confined in MCM-41 and MCM-41-1 under airflow.*

As already seen for SBA-15, the solutions confined in MCM-41 show several endothermic peaks (see Table 10). The first peaks having a characteristic minima between 81 °C and 110 °C (peak I) and cannot be related unambiguously to the desorption of physically adsorbed water in the mesoporosity. Supposing that water confined in MCM-41 shows higher evaporation temperatures, we expect that there is residual water around the grains of MCM-41. Thus, we focus on the samples filled with the electrolyte solution at 1 M and $MgCl_2$ at 0.2 M, showing a supplementary peak (peak II) between 112 °C and 150 °C.

This peak corresponds to water molecules in the interfacial layer and/or in the hydration shell of ions. Moreover, the mass loss of water during the TG measurements reveals that the pores in SBA-15 are completely filled and the pores in MCM-41 are filled more than 90 %.

*Table 10: Temperatures of endothermic peaks I and II and their corresponding weight loss percentages of SBA-15 samples obtained by DTA/DGA measurements.*

| Sample | $[XCl_2]_0$ (M) | Peak I (°C) | Peak II (°C) | Mass loss |
|---|---|---|---|---|
| MCM-41 dried | - | 78.3 | - | 6.4 |
| MCM-41-1 dried | - | 82.0 | - | 5.1 |
| MCM-41 water | - | 84.8 | - | 15.1 |
| MCM-41-1 water | - | 82.0 | - | 13.4 |
| MCM-41 $BaCl_2$ | 1 M | 81.7 | 112.6 | 16.6 |
| MCM-41 $CaCl_2$ | 1 M | 78.4 | 104.6 | 49.9 |
| MCM-41 $MgCl_2$ | 1 M | 90.2 | 144.1 | 26.8 |
| MCM-41-1 $BaCl_2$ | 1 M | 87.0 | 119.7 | 19.0 |
| MCM-41-1 $CaCl_2$ | 1 M | 96.7 | 137.3 | 23.1 |
| MCM-41-1 $MgCl_2$ | 1 M | 97.9 | 150.5 | 20.2 |

### *3.1.3 Discussion*

To highlight the confinement effect, the effect of the ion nature and the impact of the silica, the evaporation temperatures of the second peak as a function of the confinement size are presented in Figure 43.

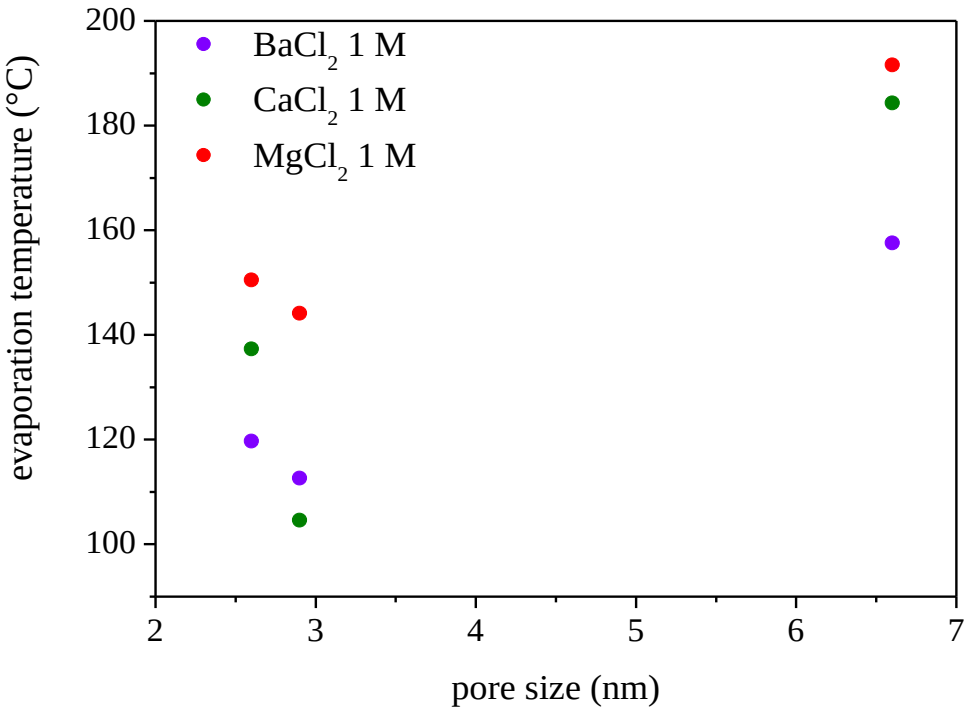


*Figure 43: Evaporation temperatures of peak II attributed to water molecules in the interfacial layer and/or in the hydration shell of ions.*

Whatever the confined electrolyte solution, we found that the evaporation temperature in SBA-15 is higher than in MCM-41. Generally, the evaporation temperature in MCM-41 is expected to be higher than in SBA-15 because of smaller pore size in MCM-41. This phenomenon can be explained by the presence of the microporosity in SBA-15 silica pore wall, which consists of a supplementary confinement smaller than 1 nm in which the solution can diffuse.[4] With dense pore wall, the solutions confined in MCM-41, we observed an increase of the evaporation temperature with decreasing the pore size. This is due to the stronger water-surface interactions existing in small pore related to a higher surface-to-bulk-ratio. Concerning the electrolyte solutions in MCM-41 and MCM-41-1, we observe an increase of the evaporation temperatures for solutions in the smaller confinement. In addition to that, the temperature shift of peak II in MCM-41 follows the order:

$BaCl_2$ 1 M < $CaCl_2$ 1 M < $MgCl_2$ 1 M, except for MCM-41 $CaCl_2$ 1 M. This temperature shift can be explained by the charge density of ions. While kosmotropic ions ($Mg^{2+}$) have a high charge density and therefore a strongly attached hydration shell, chaotropic ions ($Ba^{2+}$) carry a low charge density and a weakly attached hydration shell. Thus, more energy is required to evaporate water molecules near kosmotropic ions.

Concerning the TGA measurements, we conclude that the percentage of water inside the material is dependent on the electrolytes nature and concentration. The mass loss in SBA-15 (pore size 6.6 nm) and MCM-41 (2.9 nm) reveals the same tendencies observed during the filling kinetics of the CEA/LETI nanochannels presented in chapter II. The electron density after one week of filling in 3 and 5 nm nanochannels have shown the same order: $BaCl_2 < CaCl_2 \leq MgCl_2$. The differences in MCM-41-1 samples are less pronounced, whereas the order changes to $BaCl_2$ 1 M ≤ $CaCl_2$ 1 M ≤ $MgCl_2$ 1 M. The mass loss is related to the different penetration rates of the solutions into the porosity of the silica.

Generally, to summarize the thermal behavior of water and electrolyte solutions in mesoporous silica, we found two different types of bonded water in the porosity of SBA-15 and MCM-41. While the first peak is related to physically adsorbed water molecules, the second peak can be attributed to water molecules in the hydration shells of ions and/or in the interfacial layer. The quantity of water in the silica confinement follows the same tendencies observed during the filling kinetics of nanochannels having a height of 3 and 5 nm.

### 3.2 Water structure

To better understand the effect of the confinement, the ions and their concentrations on the water structure, the solutions and the samples were characterized using FTIR-ATR. The spectra are presented in the appendix (Figure 78 and Figure 79). Figure 45 (a) to (f) and Figure 46 (a) to (f) display the FTIR spectra focusing on the large band corresponding to the stretching vibration of the O-H bond (νOH), between 2650 and 3800 $cm^{-1}$. These results highlight that the νOH bands are modified with the electrolyte concentration and when the solutions are confined in SBA-15 and MCM-41. In confinement, the absorbance of the νOH band is not as intense as in bulk solutions but increases with the electrolytes concentration. The absorbance for SBA-15, MCM-41 and MCM-41-1 are in the same order of magnitude. However, the integrated area of the νOH band depends on the electrolyte solutions and on the confinement size (see Figure 44). This is in accordance with the percentages of electrolyte solutions within SBA-15 and MCM-41 obtained by TGA. In the smaller confinements of MCM-41, the amount of water for $BaCl_2$ is lower than the corresponding values for $MgCl_2$ and $CaCl_2$, as in the 3 nm nanochannels. In the bigger pores of SBA-15, the ion effect on the water amount are less pronounced. The tendency observed at 1 M $BaCl_2$ < $CaCl_2$ << $MgCl_2$, could be explained by the presence of microporosity, where water can penetrate.

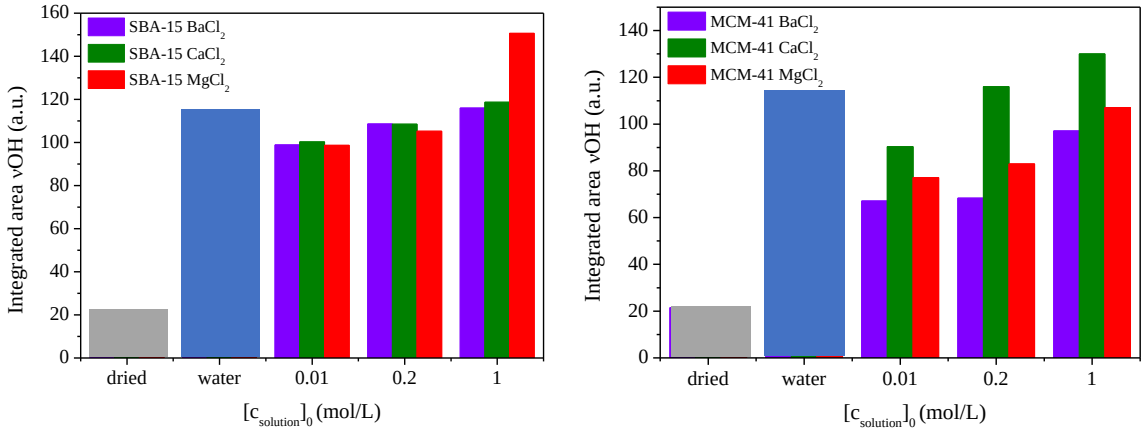


*Figure 44: Integrate areas of the νOH band for various electrolyte solutions at different concentrations confined in SBA-15 and MCM-41.*

As shown in the work of *Brubach et al.*[176], the frequency of the νOH band depends on the strength of the hydrogen bonding between the water molecules. The observed substructures in the νOH were assigned to different water populations having different coordination numbers. A shift of νOH band to the low-frequency region of the spectrum corresponds to an increase of the number of hydrogen bonds that a water molecule can establish with its neighbors. The frequency downshift can be related to a weaker OH oscillation strength. Then, comparing the evolution of the νOH band of solutions and samples and considering that the νOH band mainly corresponds to water molecules (for dried samples the weight loss which could be related to Si-OH embedded in the silica matrix is only about 4 wt%), it allows the determination of the evolution of the water network structure in solution and in confinement.

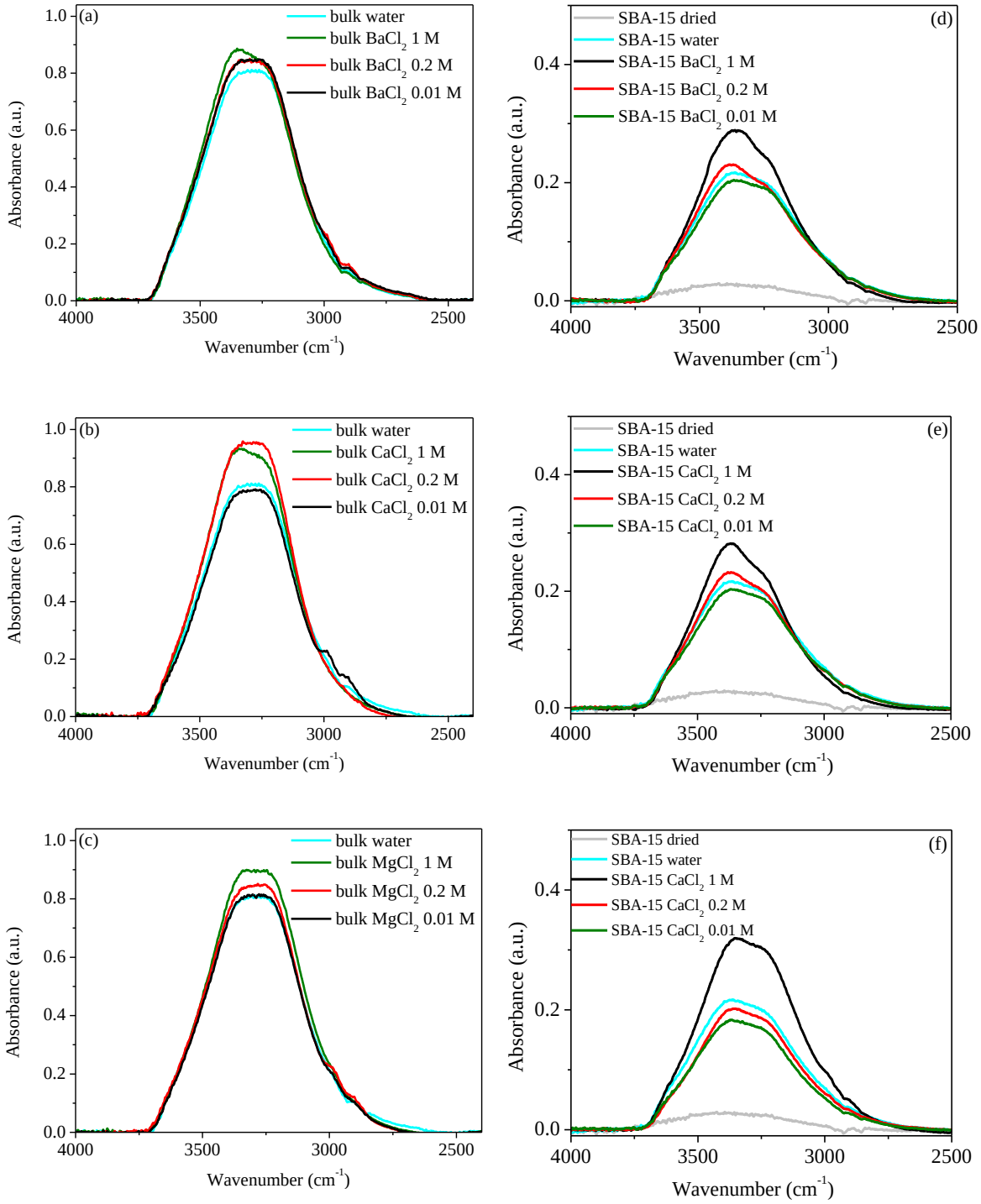


*Figure 45 (a) to (f): Experimental ATR-FTIR spectra of vOH band between 2650 and 3800 $cm^{-1}$ of bulk electrolyte solutions and SBA-15 filled with water and electrolyte solutions at various concentrations.*

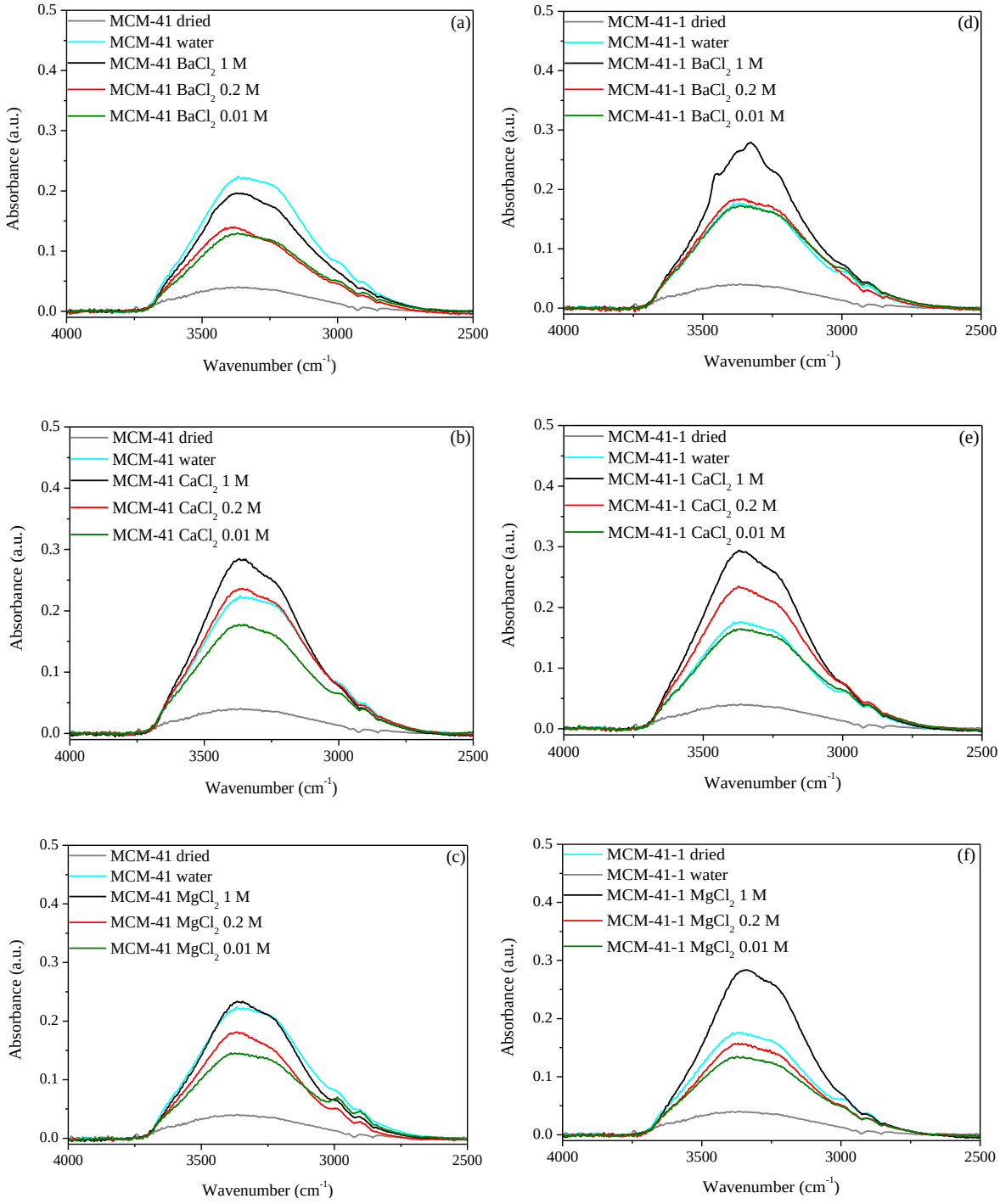


*Figure 46 (a) to (f): Experimental ATR-FTIR spectra of the vOH band between 2650 and 3800 $cm^{-1}$ of MCM-41, MCM-41-1 and MCM-41-2 filled with water and electrolyte solutions at various concentrations.*

In order to quantify the evolution of the various types of water molecules in electrolyte solutions and in confined electrolyte solutions, we referred on two previous works. First, we based on the work of *Le Caer and coworkers* showing that the network of water molecules confined in nanopores is perturbed by the confinement.[103] Depending on the average number of hydrogen bonds with its surrounding neighbors, they proposed three different types of water: fully bonded water ("network water") at low frequencies at 3310 $cm^{-1}$, water with an average hydrogen bond number below network water ("intermediate water") in the frequency range around 3450 $cm^{-1,}$ and poorly bonded water ("multimer water") at high frequencies at 3590 $cm^{-1}$. Second, following the work of *Crupi et al.* with zeolithes, we considered the interaction between ions and water molecules through the existence of an extra contribution at around 3000 $cm^{-1}$.[177] Then, the ν*OH band was resolved in four contributions using four Gaussian curves ascribed to different populations of water: a first subband between 3080 – 3110 $cm^{-1}$ attributed to ion bonded water (IBW), a second subband assigned to "fully bonded" water molecules between 3220 - 3250 $cm^{-1}$ having four coordination neighbors (FBW), a third one corresponding to "intermediate bonded water" at 3385 - 3400 $cm^{-1}$ (INBW) and the last one between 3520 - 3550 $cm^{-1}$, related to "low bonded water" hardly building up a hydrogen bond network with other water molecules (LBW). In some cases, we added two peaks at 2900 and 2990 $cm^{-1}$ to include the C-H vibrations coming from contamination of the spectrometer diamond. The contributions of these two peaks do not exceed 5 % and 4 % of the relative band area, respectively.

To enhance the band decomposition of the ν*OH band of the various electrolyte solutions, we have taken into account the percentage of water molecules in the hydration

shells of the ions in solution and fixed the percentage of the relative peak area at 3070 - 3100 $cm^{-1}$ at the calculated values presented in Table 11. In addition, to optimize the band decomposition of the SBA-15 water spectrum, we fixed the percentage of bulk water, obtained from differential-scanning calorimetry, at 53 % (see appendix). The widely used Gibbs-Thompson equation to determine the amount of water molecules under the influence of the pore surface is only applicable for pores having a size bigger than 3 nm. Previous studies have shown that the shift of the melting temperature depression for pores below 3 nm cannot be satisfactorily be fitted using the GT equation.[91,178–180] Therefore, in the case of MCM-41 and MCM-41-1, we assumed three monolayers of water in the interfacial layer, resulting to 15 % and 10 % of bulk water, respectively. Since the decomposition with these values of bulk water lead to non-satisfying results, we assumed two layers of water molecules resulting in 35 % and 30 % of bulk water, which is still in good agreement with the values found in the literature.[92,181]

*Table 11: Percentage of water in the hydration shell of ions present in electrolyte solutions.*

| Electrolytes | Hydration number[52] | 0.01 M (%) | 0.2 M (%) | 1 M (%) |
|---|---|---|---|---|
| $Mg^{2+}$ | 6.0 | 0.01 | 2.2 | 11.3 |
| $Ca^{2+}$ | 7.0 | 0.01 | 2.5 | 13.1 |
| $Ba^{2+}$ | 9.5 | 0.02 | 3.4 | 17.2 |
| $Cl^{-}$ | 5.6 | 0.01 | 2.0 | 10.2 |

The decomposition of the νOH bands obtained for the bulk electrolyte solutions and for the SBA-15 and MCM-41 samples filled with water and electrolyte solutions are presented in the annex II. From the decompositions, the percentages of the various types of water (IBW, FBW, INBW and LBW) as a function of electrolyte solutions and their concentrations in bulk solution and in confinement were determined and are shown in Figure 47 and Figure 48 (a) to (f).

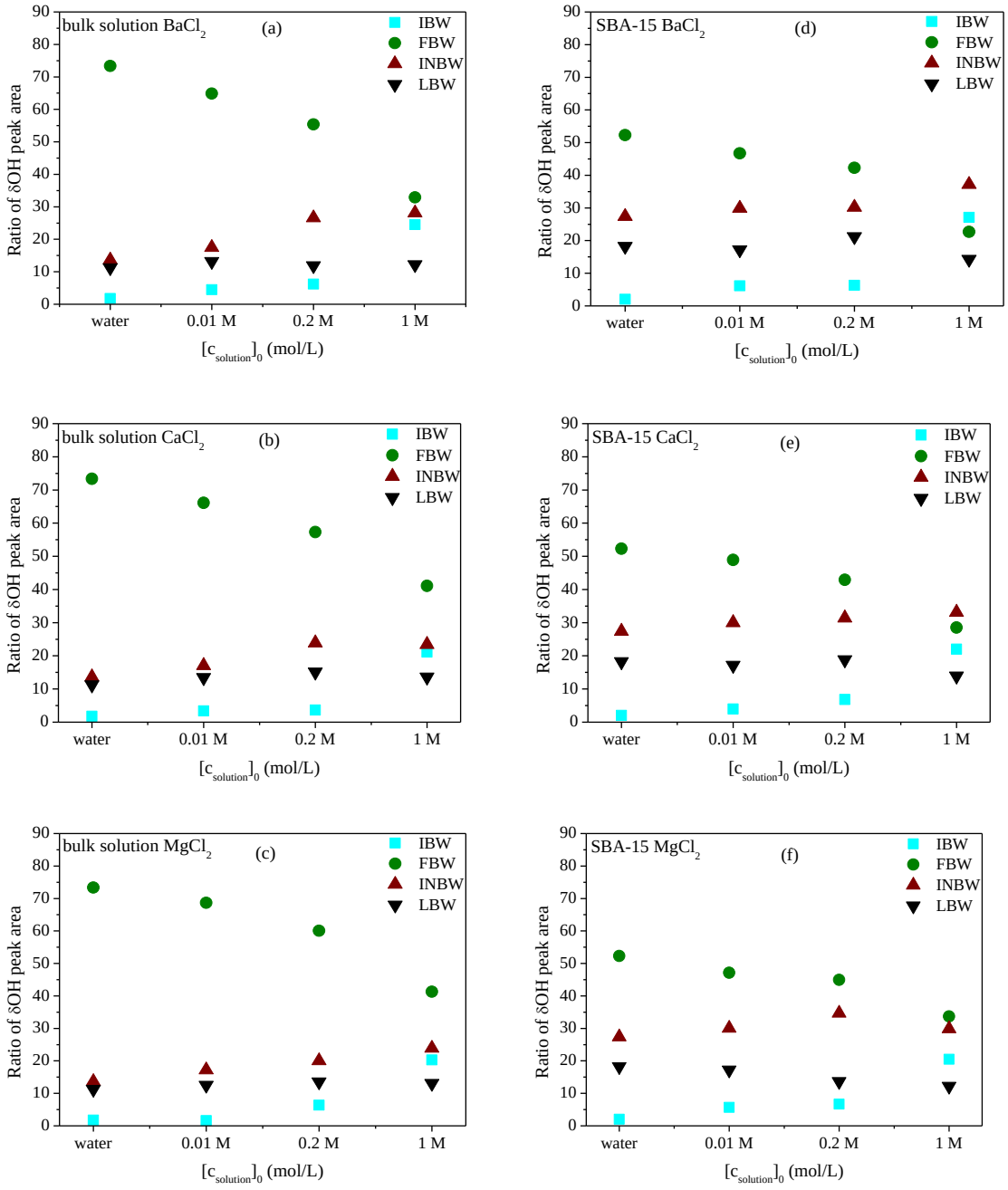


*Figure 47 (a) to (f): Evolutions of the percentages of the areas of the various vOH bands as a function of electrolyte concentration for bulk water, electrolyte solutions, water and electrolyte solutions confined in SBA-15.*

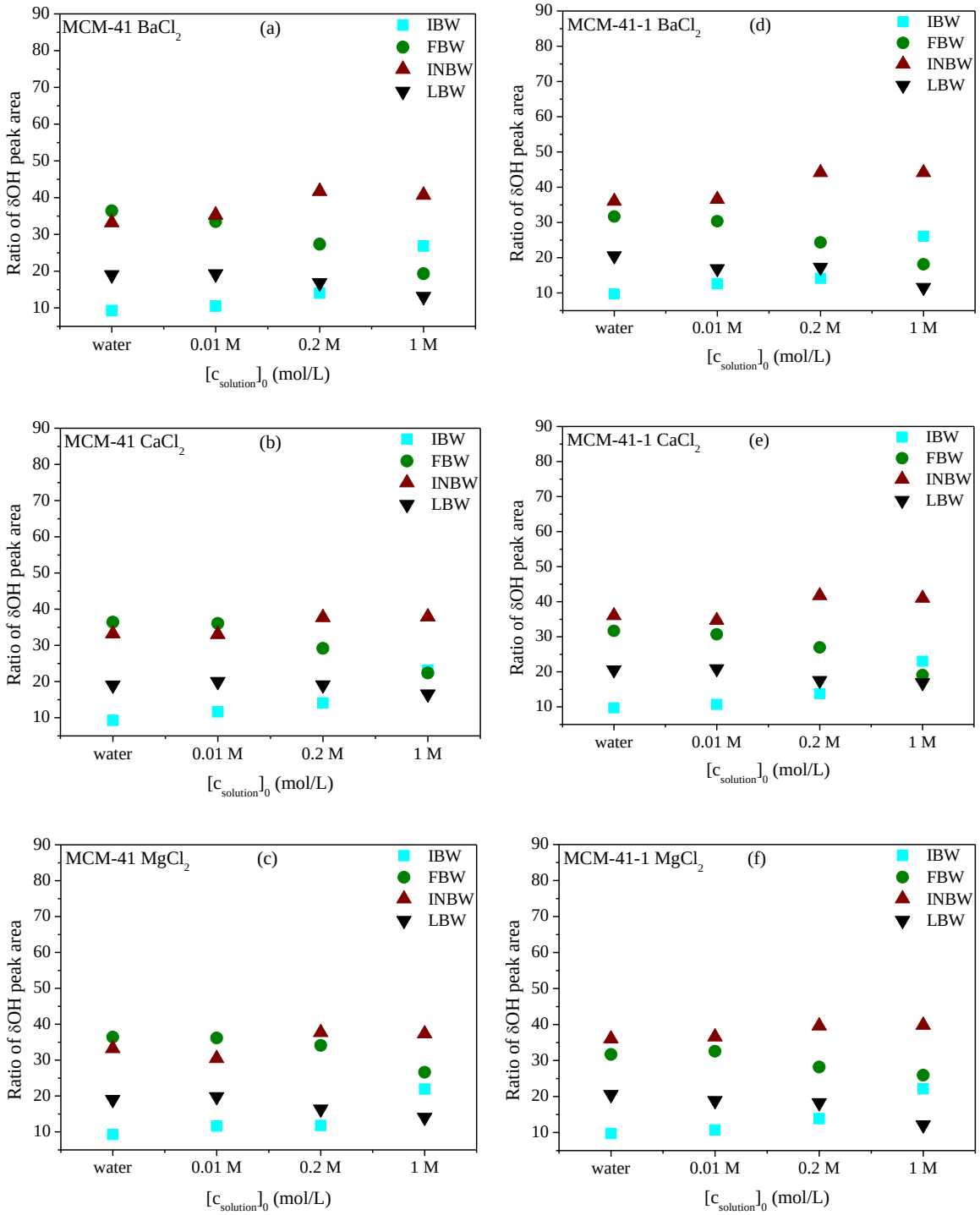


*Figure 48 (a) to (f): Evolutions of the percentages of the areas of the various vOH bands as a function of electrolyte concentration for water and electrolyte solutions confined in MCM-41 and MCM-41-1.*

The decomposition of the νOH bands highlights several results. First, for all bulk electrolyte solutions and electrolyte solutions confined both in SBA-15, MCM-41 and grafted MCM-41, we observe a contribution decrease of fully bonded water FBW and the sum of the less bonded water populations increases with the electrolyte solutions (see Figure 49). Such perturbation of the hydrogen bond network was already observed in several previous studies[26,43,65,68,98,182,183] and in molecular dynamics simulations.[35,36,184,185]

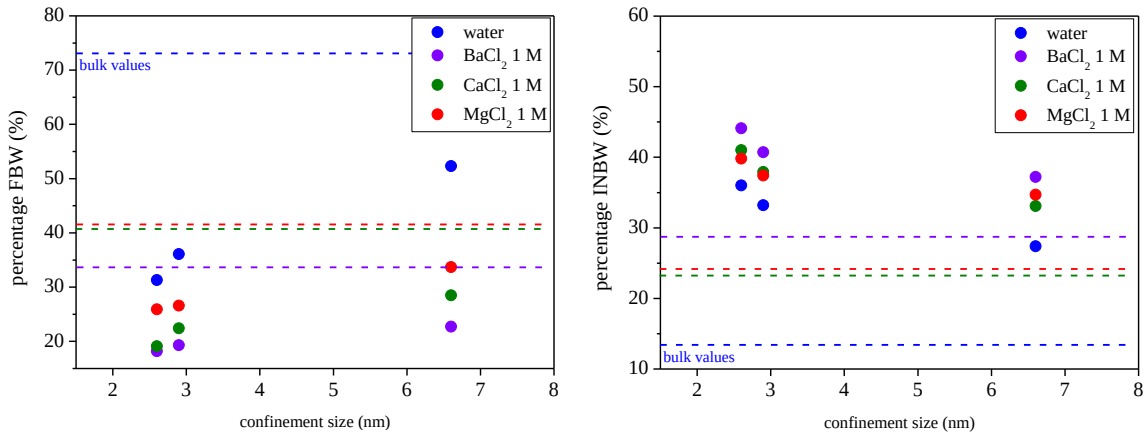


*Figure 49: Percentages of fully bonded water (FBW) in confined solutions as a function of the confinement size of SBA-15, MCM-41 and MCM-41-1. The dashed line represent the bulk solution values.*

Second, the water network in SBA-15, MCM-41 and MCM-41-1, is distorted due to the strong interactions of water molecules with the pore surface. This is represented by the decrease of FBW with the decrease of the pore size. This confinement effect was observed both in experimental studies and MD simulations.[102,186–188]

Third, the presence of electrolytes in the confined solution adds a supplementary perturbation through the excess of ions at the pore surface due to the sorption process and the

ions solvation. As the concentrations of electrolytes in the solution increase, we find a corresponding increase for the contribution of ion-bonded water. Furthermore, by comparing the electrolyte solutions and the confined electrolyte solutions, several statements can be made:

(i) the percentage of FBW water are lower in confined electrolyte solutions than in bulk electrolyte solutions and decrease with the increase of electrolyte concentration (minimum for MCM-41-1 $BaCl_2$ at 1 M);

(ii) the percentages of INBW are higher in confined electrolyte solutions confined in MCM-41 and MCM-41-1 than in bulk electrolyte solutions;

(iii) the percentage of INBW in confined electrolyte solutions increase with the electrolyte concentration until $[XCl_2]_0$ = 0.2 M. At $[XCl_2]_0$ = 1 M solutions confined in MCM-41 remain constant, while the percentage in solutions of $BaCl_2$ ($MgCl_2$) in SBA-15 increase (decrease);

(iv) regarding the nature of ions, we observe that the perturbation of the hydrogen bonding network follows the order $BaCl_2 > CaCl_2 > MgCl_2$.

To summarize this part, we can conclude that the hydrogen bonding network of water confined in SBA-15 and MCM-41 is distorted by confinement and by the presence of ions. The evolutions of the FBW percentages contribution to the νOH bands in Figure 49 suggests, that the ion effect on the water structure is more distinctive than the confinement effect for pores having a size bigger than 2 nm. In addition to that, the perturbation is related to the surface ion excess and to the specific ion effects. Kosmotropic ions ($Mg^{2+}$) with a strongly

attached hydration shell are found to increase the structure of surrounding water molecules by strengthen the water-water interaction. In contrast to that, chaotropic ions with a barely attached hydration shell decrease the water-water interaction and therefore, the contribution of less coordinated water molecules increases with the electrolyte concentration.

### 3.3 Water dynamics at pico-second time scale

In order to characterize the water dynamics on a pico-second time scale, quasi-elastic neutron scattering (QENS) experiments were performed probing the protons motions. Neutron scattering is a spectroscopic technique measuring the energy and/or the momentum of neutrons scattered by the atomic nuclei in a given sample. The wavelength of the incoming neutrons is well adapted to condensed materials and thus in the range of interatomic distances. In addition to that, the energy of neutrons are comparable to the particle motions and molecular excitations. For a more detailed description of the QENS method, we draw the reader's attention to the annex III. We present a basic overview over the QENS experiment and a step-by-step explanation how we can obtain information about the dynamical properties.

QENS spectra were collected for dried, hydrated SBA-15 and MCM-41, and the corresponding mesoporous silica filled with electrolytes. The sum over Q spectra are presented in Figure 50 (a) to (k). A vanadium foil was measured and used as a reference to determine the instrumental resolution.

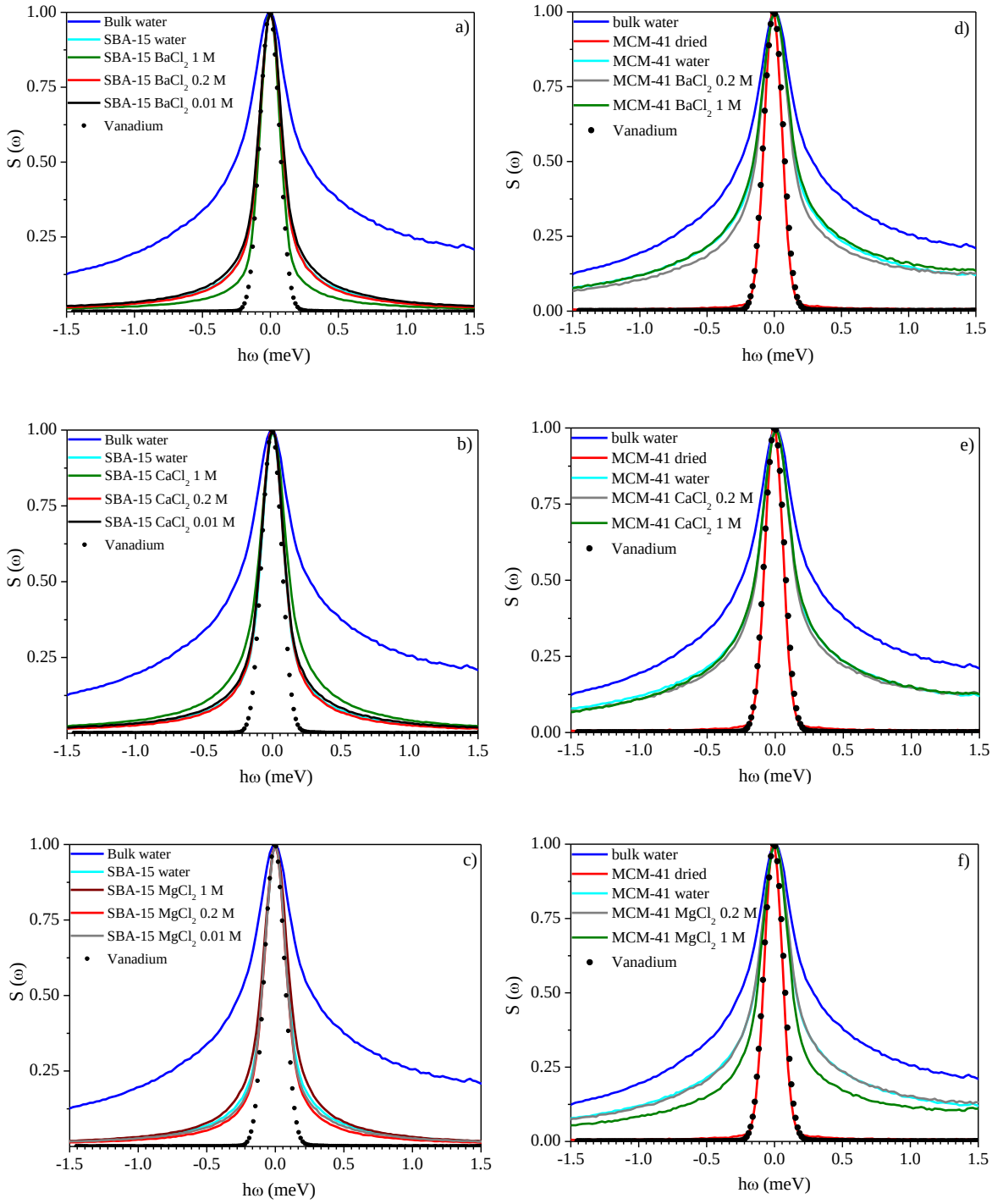
a)
Bulk water
SBA-15 water
SBA-15 BaCl2 1 M
SBA-15 BaCl2 0.2 M
SBA-15 BaCl2 0.01 M
Vanadium
b)
Bulk water
SBA-15 water
SBA-15 CaCl2 1 M
SBA-15 CaCl2 0.2 M
SBA-15 CaCl2 0.01 M
Vanadium
c)
Bulk water
SBA-15 water
SBA-15 MgCl2 1 M
SBA-15 MgCl2 0.2 M
SBA-15 MgCl2 0.01 M
Vanadium
d)
bulk water
MCM-41 dried
MCM-41 water
MCM-41 BaCl2 0.2 M
MCM-41 BaCl2 1 M
Vanadium
e)
bulk water
MCM-41 dried
MCM-41 water
MCM-41 CaCl2 0.2 M
MCM-41 CaCl2 1 M
Vanadium
f)
bulk water
MCM-41 dried
MCM-41 water
MCM-41 MgCl2 0.2 M
MCM-41 MgCl2 1 M
Vanadium
S (ω)
hω (meV)

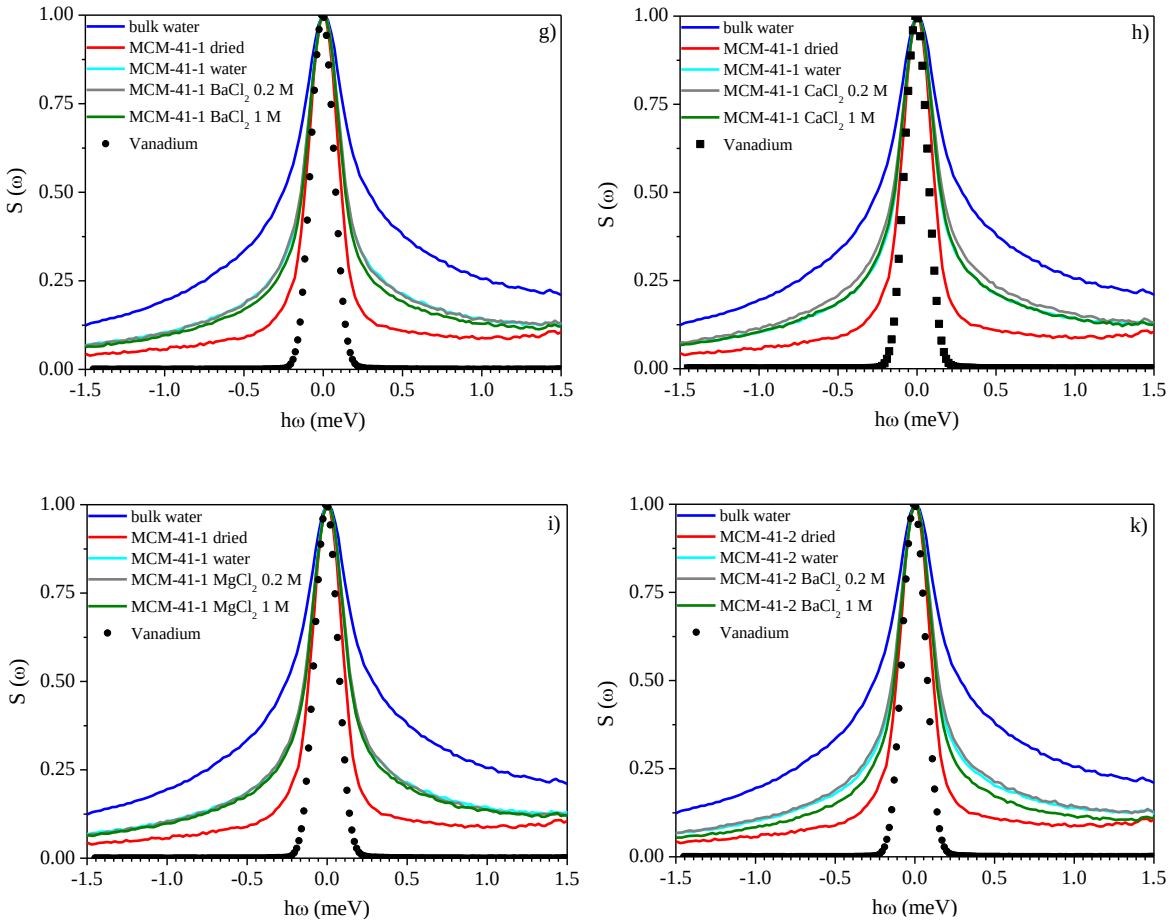


*Figure 50 (a) - (k): Sum over Q of QENS spectra of bulk, SBA-15, MCM-41 and grafted MCM-41 filled with water and the various electrolytes at room temperature and λ = 5.2 Å. QENS spectra of vanadium is also shown as reference for instrument resolution.*

The QENS spectra presented in Figure 50 (a) to (k) consist of several contributions: the confined electrolyte, the hydroxyl groups of the pore surface, the silica matrix of SBA-15 and various MCM-41 and the sample cell. Samples measured in a dried state, consist of the two last contributions. Since the incoherent scattering cross section of hydrogen is huge, it can be assumed that the main contribution to the scattering intensity comes from hydrogen, meaning the spectra is proportional to the probability, at which neutrons are scattered by the protons in the sample.[189]

The spectra of the samples show a much broader signal compared with vanadium but less intense than the one for bulk water. This signal broadening comes from the small energy transfer, typically a few meV, between incoming neutrons and the mobile protons of confined water. Moreover, this broadening depends on the cations and decreases with the increasing salt concentration. This highlights that the effect of the confinement, the nature of the ions and their concentrations in solution affect the protons dynamics.

In the quasielastic region, the obtained QENS signals correspond to the dynamic structure factor of total confined water $S(Q,\omega)$ defined as follows[190]:

$$S(Q,\omega) = exp(-Q^2\langle u^2\rangle/3)[C\delta(\omega) + (1-C)S_T(Q,\omega)\otimes S_{rot}(Q,\omega)] + B(Q) \qquad (31)$$

with Q and ω represent momentum and energy transfers, respectively. $\langle u^2\rangle$ is the mean-square vibrational amplitude of water molecules. $\delta(\omega)$ is a δ-function and corresponds to the elastic component. $(1-C)S_T(Q,\omega)\otimes S_{rot}(Q,\omega)$ represents the quasi-elastic component. C is the fraction of the elastic component. ⊗ indicates a convolution in ω. $S_T(Q,\omega)$ and $S_{rot}(Q,\omega)$ are contributions from translational and rotational diffusions of water molecules confined within the pores of MCM-41, respectively. The two different water motions are outlined in Figure 9.

$B(Q)$ is the ω-independent background due to the vibrational motions. The elastic term in the equation above is related to the contribution of atoms that are immobile on the experimental time scale. For $S_T(Q,\omega)$ and $S_{rot}(Q,\omega)$ the following functions were used[111]:

$$S_T(Q,\omega) = L(\omega, \Gamma_T) \quad (32)$$

$$S_{rot}(Q,\omega) = j_0^2(Qa)\delta(\omega) + 3j_1^2(Qa)L\left(\omega, \frac{1}{3\tau_{rot}}\right) + 5(Qa)L\left(\omega, \frac{1}{\tau_{rot}}\right) \quad (33)$$

where $L(\omega, \Gamma)$ is a Lorentzian function depending on ω and characterized by a half-width at half-maximum (HWHM) $\Gamma_T$. $j_l$(x) is the spherical Bessel functions and *a* stands for the radius of rotation ($a$ = 0.98 Å, the O-H distance in the water molecule). $\tau_{rot}$ denotes a relaxation time of rotational diffusion. The second and third terms in the well-known Sears formalism (eq. 34), assuming a decoupling of rotational and translational motion, are negligible in our experimental Q range.[191]

The details of the fitting procedure of the QENS spectra are as follows: First, eighteen spectra measured at different Q values between 0.65 Å$^{-1}$ to 2.25 Å$^{-1}$ were fitted simultaneously using the eq. (32) – (34) in order to obtain the fitting parameter of $\Gamma_T$. Figure 51 displays a fitting example obtained for a $BaCl_2$ solution at 1 M confined in SBA-15. Second, the resulting $\Gamma_T$ as a function of $Q^2$ for bulk water and water confined in mesoporous silica are presented in Figure 52. Figure 53 highlights the evolution of $\Gamma_T$ in the presence of various electrolytes.

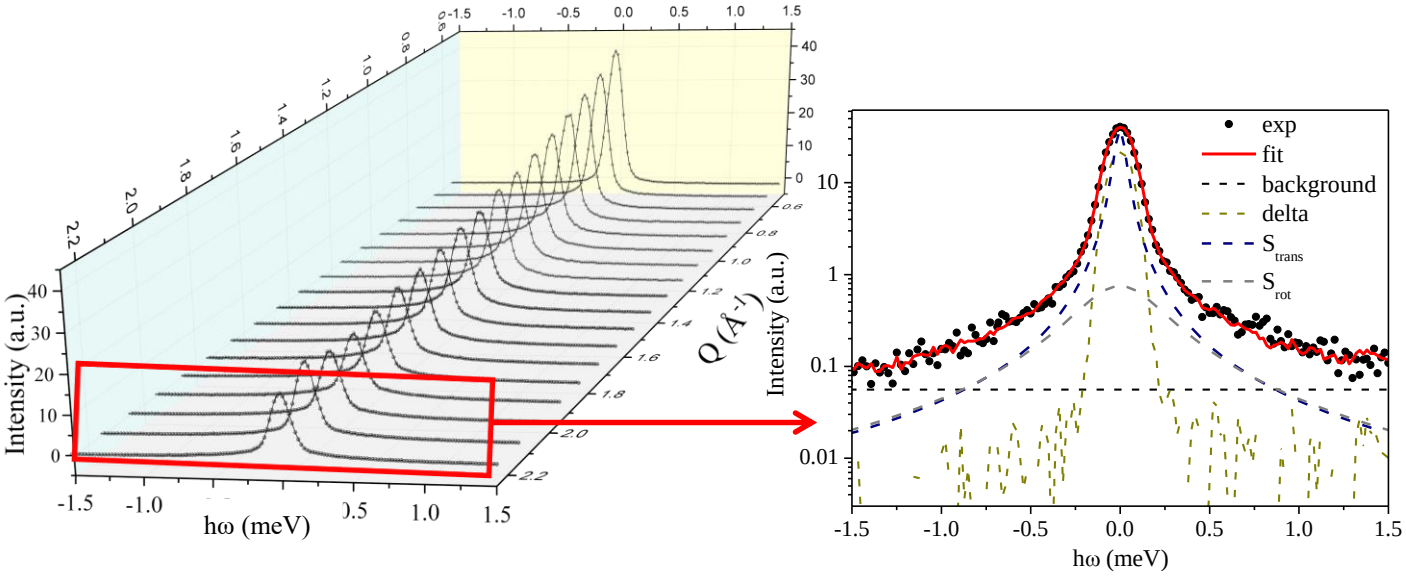


*Figure 51: Example of experimental and fitted curves S (Q, ω) using two Lorentzian functions from Q = 0.65 Å$^{-1}$ to 2.25 Å$^{-1}$ for SBA-15 $BaCl_2$ at 1 M.*

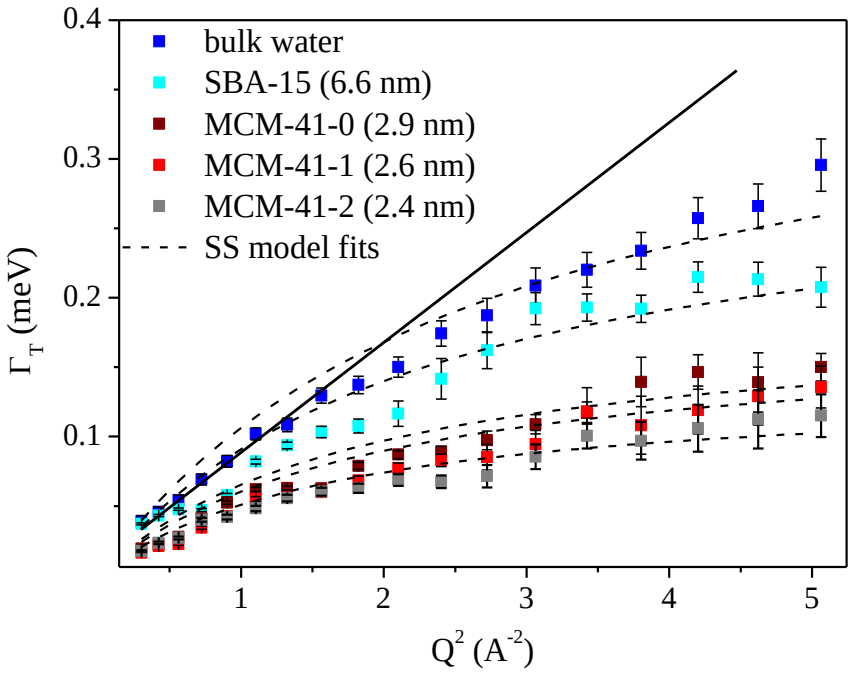


*Figure 52: Evolutions of the half width at half-maximum $\Gamma_T$ of the first Lorentzian as a function of $Q^2$ obtained from the fitting of QENS spectra for bulk water and water confined in SBA-15, MCM-41 and grafted MCM-41.*

$\Gamma_T(Q^2)$ of bulk water shows an initial linear evolution with $Q^2$ and a deviation at higher values of $Q^2$ as already found by *Teixeira et al.*[190] Compared to bulk water, $\Gamma_T(Q)$ of the confined solution, shows a stronger deviation from this linear evolution at high Q values. Indeed, $\Gamma_T(Q)$ asymptotically reaches a plateau having an intensity decreasing with the increase of the electrolyte concentration. This plateau can be described by a jump-diffusion model.[192]

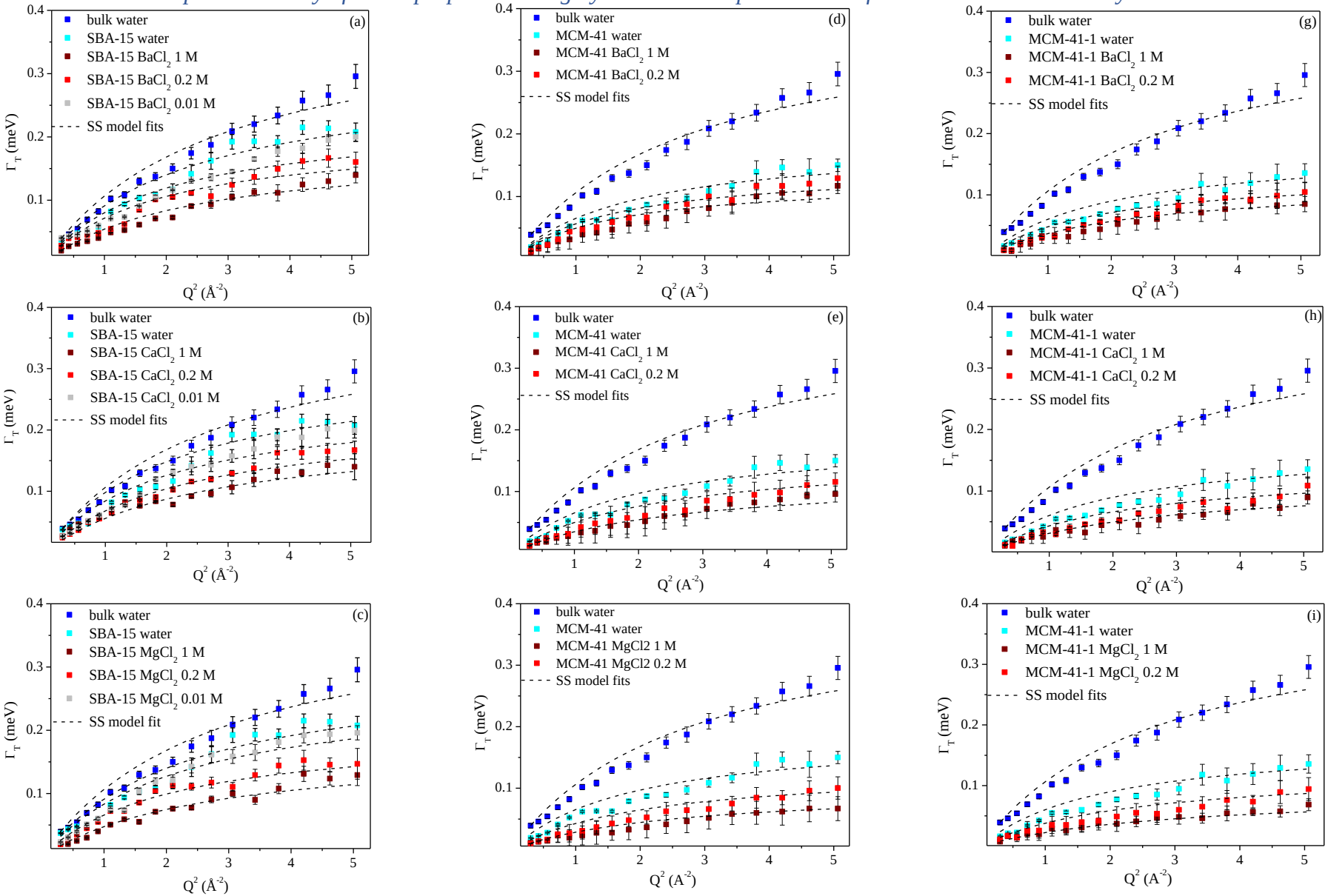


*Figure 53:* ***(a) to (i):*** *Evolutions of the half width at half-maximum $\Gamma_T$ of the first Lorentzian as a function of Q² obtained from the fitting of QENS spectra for bulk water, samples filled with water and samples filled with electrolyte solutions at various concentrations at 300 K. Fits were done using the first Fick's Law for bulk water and the jump-diffusion model for the confined solutions.*

Concerning the confined solution, $\Gamma_T(Q)$ is different at high Q values, showing a deviation from this linear evolution. At high Q values, $\Gamma_T(Q)$ asymptotically reaches a plateau having an intensity decreasing with the increase of the electrolyte concentration. This plateau can be described by a jump-diffusion model, assuming that the mobility of water is limited in a restricted geometry. $\Gamma_T(Q)$ was fitted using the Singwi and Sjolander (SS) model based on an exponential distribution of jump lengths.[193] According to this random-jump-diffusion model, the Q-dependence of $\Gamma_T$ is given by eq. 35:

$$\Gamma_T = \frac{D_T Q^2}{1 + D_T Q^2 \tau_T} \qquad (34)$$

Where $\tau_T$ the residence time of the translational diffusion between two consecutive jumps and $D_T$ is the translational diffusion coefficient of confined water defined by $D_T = \langle l^2 \rangle / 6\tau_T$, with $\langle l^2 \rangle$ being the mean jump length.[48] The parameters obtained from the fits are presented in Table 12. The determined $L$ values are in the same order as the molecular size of water and thus, reasonable for the employed model. Diffusion coefficients of water in bulk electrolyte solutions obtained from NMR and spin echo measurements were added.[44,46,55,113,194] The values obtained for bulk water $D_T = 2.2.10^{-9}$ m².s$^{-1}$ and $\tau_T$=2.5 ps, are consistent with the experimental values in ref 190 and with the MD simulations in ref 195.

*Table 12: Fitting parameters $D_T$ and $\tau_T$ obtained by fitting of $\Gamma_T(Q)$ using the jump diffusion model of Singwi and Sjolander model. The relative self-diffusion coefficient of water in electrolyte obtained by NMR and spin echo from various references were also added for comparison.*

| sample | $D_T \cdot 10^{-9}$ ($m^2s^{-1}$) | $D_{bulk} \cdot 10^{-9}$ ($m^2s^{-1}$) electrolyte solutions from literature | $T_T$ (ps) | L (Å) |
|---|---|---|---|---|
| bulk water | 2.2 (± 0.1) | 2.5[59,60] | 2.5 (± 0.2) | 1.8 (± 0.3) |
| SBA-15 water | 2.0 (± 0.2) | 2.5[59,60] | 3.3 (± 0.2) | 1.9 (± 0.3) |
| SBA-15 $BaCl_2$ 0.01 M | 1.9 (± 0.1) | 2.5[61,62] | 4.3 (± 0.1) | 2.2 (± 0.1) |
| SBA-15 $BaCl_2$ 0.2 M | 1.7 (± 0.3) | 2.4[61,62] | 4.9 (± 0.3) | 2.2 (± 0.2) |
| SBA-15 $BaCl_2$ 1 M | 1.2 (± 0.2) | 2.1[61,62] | 5.7 (± 0.3) | 2.0 (± 0.3) |
| SBA-15 $CaCl_2$ 0.01 M | 1.9 (± 0.1) | 2.4[61,63] | 4.0 (± 0.2) | 2.1 (± 0.2) |
| SBA-15 $CaCl_2$ 0.2 M | 1.5 (± 0.1) | 2.4[61,63] | 4.5 (± 0.3) | 2.0 (± 0.2) |
| SBA-15 $CaCl_2$ 1 M | 1.2 (± 0.3) | 2.0[61,63] | 5.0 (± 0.3) | 1.9 (± 0.3) |
| SBA-15 $MgCl_2$ 0.01 M | 1.9 (± 0.1) | 2.5[61,62] | 4.1 (± 0.2) | 2.2 (± 0.1) |
| SBA-15 $MgCl_2$ 0.2 M | 1.5 (± 0.1) | 2.3[61,62] | 4.9 (± 0.2) | 2.1 (± 0.2) |
| SBA-15 $MgCl_2$ 1 M | 1.0 (± 0.2) | 1.8[61,62] | 5.7 (± 0.3) | 1.8 (± 0.2) |
| MCM-41 water | 1.5 (± 0.1) | - | 5.3 (± 0.1) | 2.2 (± 0.1) |
| MCM-41 $BaCl_2$ 0.2 M | 1.4 (± 0.2) | - | 6.8 (± 0.3) | 2.4 (± 0.3) |
| MCM-41 $BaCl_2$ 1 M | 1.2 (± 0.2) | - | 7.8 (± 0.2) | 2.4 (± 0.2) |
| MCM-41 $CaCl_2$ 0.2 M | 1.1 (± 0.3) | - | 6.2 (± 0.3) | 2.0 (± 0.3) |
| MCM-41 $CaCl_2$ 1 M | 0.7 (± 0.2) | - | 8.0 (± 0.2) | 1.8 (± 0.1) |
| MCM-41 $MgCl_2$ 0.2 M | 1.0 (± 0.1) | - | 7.5 (± 0.3) | 2.1 (± 0.2) |
| MCM-41 $MgCl_2$ 1 M | 0.6 (± 0.1) | - | 10.0 (± 0.3) | 1.9 (± 0.2) |
| MCM-41-1 water | 1.4 (± 0.3) | - | 5.7 (± 0.1) | 2.2 (± 0.1) |
| MCM-41-1 BaCl2 0.2 M | 1.1 (± 0.2) | - | 7.3 (± 0.3) | 2.2 (± 0.3) |
| MCM-41-1 BaCl2 1 M | 0.8 (± 0.1) | - | 8.2 (± 0.2) | 2.0 (± 0.2) |
| MCM-41-1 CaCl2 0.2 M | 1.0 (± 0.3) | - | 7.2 (± 0.3) | 2.1 (± 0.3) |
| MCM-41-1 CaCl2 1 M | 0.6 (± 0.1) | - | 8.5 (± 0.2) | 1.7 (± 0.1) |
| MCM-41-1 MgCl2 0.2 M | 0.8 (± 0.2) | - | 7.8 (± 0.3) | 1.9 (± 0.2) |
| MCM-41-1 MgCl2 1 M | 0.5 (± 0.2) | - | 11.1 (± 0.3) | 1.8 (± 0.2) |
| MCM-41-2 water | 1.2 (± 0.1) | - | 7.3 (± 0.1) | 2.3 (± 0.1) |

These results reveal that the water dynamics is affected by several parameters such as the size of the confinement, the electrolyte concentration and the nature of the ions. The results rise the question whether the dynamics are more affected by the confinement and therefore by the interaction with the pore surface, or by the presence of ions. In the following section, we want to pinpoint the confinement and ion effect on the water dynamics. In a next attempt, we try to highlight the two effects separately, to know which one is more predominant and affects the dynamical properties the most.

### *3.3.1 Impact of confinement effect*

The evolutions of the $D_T$ and $\tau_T$ as a function of the pore size of the confinement are shown in Figure 54. First, the value of $D_T$ for water confined in SBA-15 is close to that of bulk water measured in the same conditions ($2.0 \times 10^{-9}$ m$^2$ s$^{-1}$ vs. $2.2 \times 10^{-9}$ m$^2$ s$^{-1}$) but $\tau_T$ (3.3 ps) is slightly higher than the one of bulk water (2.5 ps) and the one found in the literature (1.1 ps).[190] This means that the size of the SBA-15 confinement has a minor impact on water dynamics. Similar results were found in mesoporous silica materials having a pore size close to the SBA-15 used in this study such as Vycor glass[196] and several types of highly ordered mesoporous silica.[111] Moreover, the results are consistent with the values obtained by MD simulations.[14,188] The confinement effect is more obvious for water confined in MCM-41 and grafted MCM-41. The $D_T$ decreases with the pore size and the residence time $\tau_T$ increases with the pore size. The values obtained in the present study are in the same order of magnitude than for various types of MCM-type silica. [111,116]

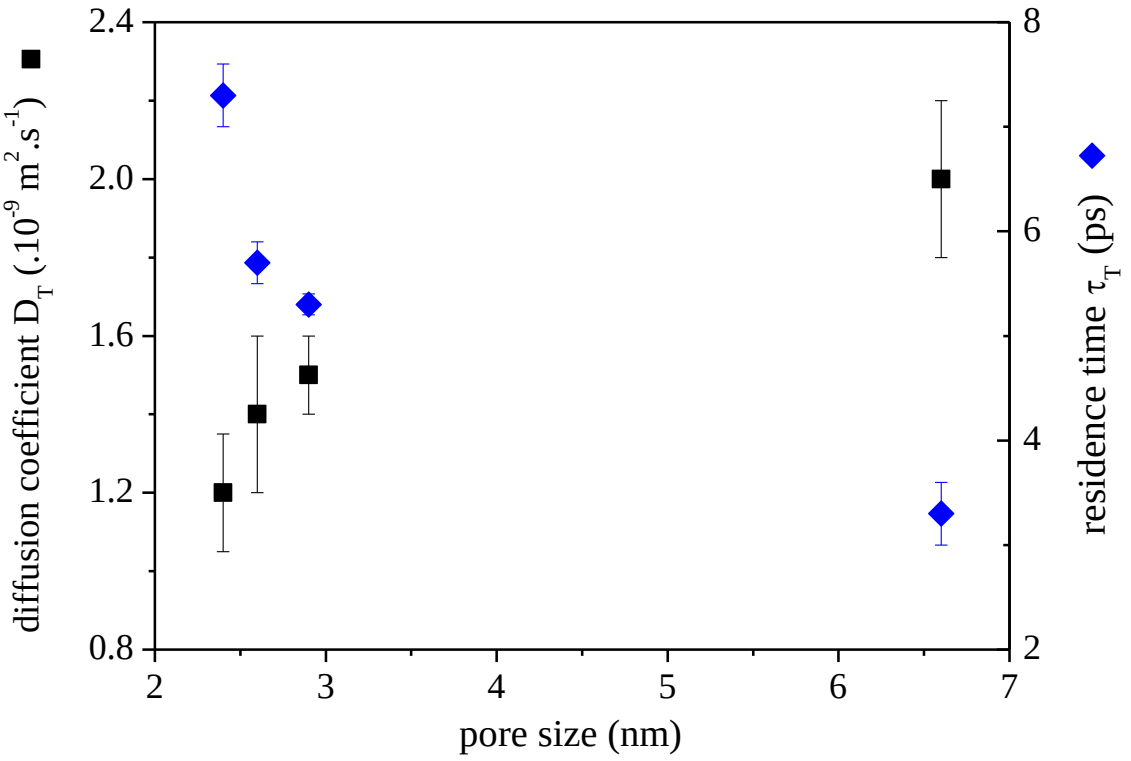


*Figure 54: Evolutions of the translational diffusion coefficient $D_T$ and residence time $\tau_T$ of water confined in SBA-15, MCM-41 and grafted MCM-41.*

The XRD study[197] and the ATR-FTIR analysis showed that water confined in MCM-41 interacts strongly with the surface hydroxyls and that the hydrogen bond network in confined water is gradually distorted in smaller pore sizes. Despite the distortion of the water structure, the present QENS study confirms the decrease of translational diffusion of water molecules within confinement. The decrease of $D_T$ goes with the decrease of the amount of fully bonded water due to the increase of the interactions of water with the silica surface.

### *3.3.2 Impact of ion effect*

In addition to the confinement, the concentration of the electrolyte and its nature influence the water dynamics. Figure 55 presents the evolution of the $D_T$ of water as a function of initial

electrolyte concentration in the corresponding silica confinements. Indeed, as for bulk electrolyte solutions, $D_T$ of confined water decreases with the increase of the electrolyte concentration. Such decrease of the dynamics of confined water in presence of ions in silica mesoporous materials was already observed in ref 2,123. In addition, $\tau_T$ of water increases globally with the electrolyte concentration.

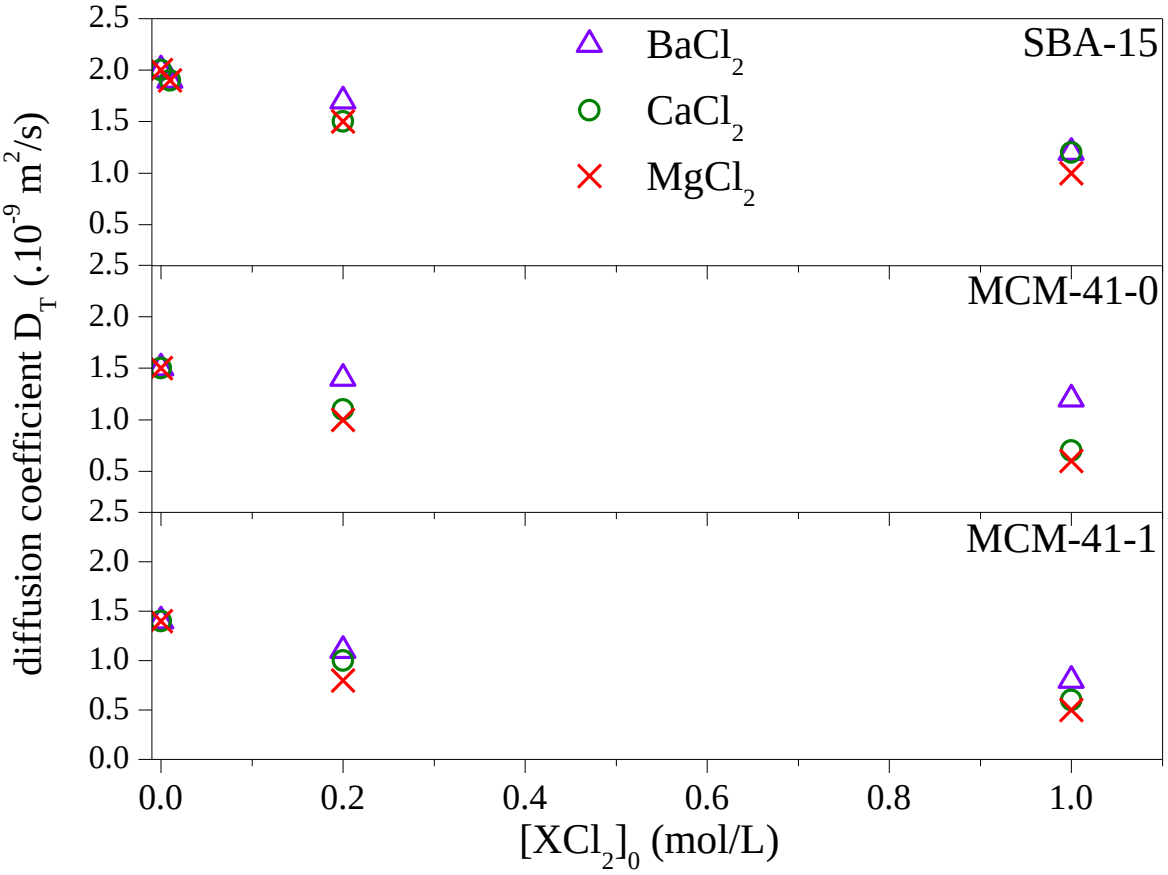


*Figure 55: Evolutions of the $D_T$ as a function of the initial electrolyte concentration $[XCl_2]_0$ within SBA-15, MCM-41 and MCM-41-1.*

As displayed in Figure 55, for electrolyte solutions at $[XCl_2]_0 = 0.01$ M there is a similar and slight impact of the concentration of the electrolyte and the nature of ions on the water dynamics. This is different for $[XCl_2]_0 \geq 0.2$ M. Indeed, for $[XCl_2]_0 = 0.2$ M the dynamics of water confined in SBA-15 is slowed according to the order: $MgCl_2 = CaCl_2 > BaCl_2$. For $[XCl_2]_0 = 1$ M,

the order changes to $MgCl_2 > CaCl_2 = BaCl_2$. $D_T$ of water in MCM-41 and MCM-41-1 decreases with $[XCl_2]_0$ in the order: $MgCl_2 > CaCl_2 > BaCl_2$.

As for the electrolyte solutions, this order can be explained by the kosmotropic character of the ions: kosmotropic ions diffuse slower than chaotropic ions due to their properties to strengthen the water network.[18] In addition to this evolution, the sorption of ions may have a slight effect on the dynamics of water. Indeed, the difference between the self-diffusion coefficient of electrolyte solutions and $D_T$ of confined water in presence of electrolyte increases with the kosmotropic properties of ions. This phenomenon may be due to the effect of the ions sorption at the pore surface changing the electrostatic interaction in the media.

### *3.3.3 Predominant effect: confinement or ion nature?*

Because the confinement and the nature of electrolytes and their concentration have an impact on the water properties, the question arises: what is the predominant factor driving the water dynamics? To assess this, intending to remove the effect of the confinement on water diffusion, the factor $\Delta$ representing the difference between the diffusion coefficient of the confined water $D_{T,water,conf}$ and the diffusion coefficient of the confined electrolyte $D_{Telec,conf}$ was calculated. The evolutions of this difference $\Delta$ as a function of the pore size and the concentration are presented in Figure 56.

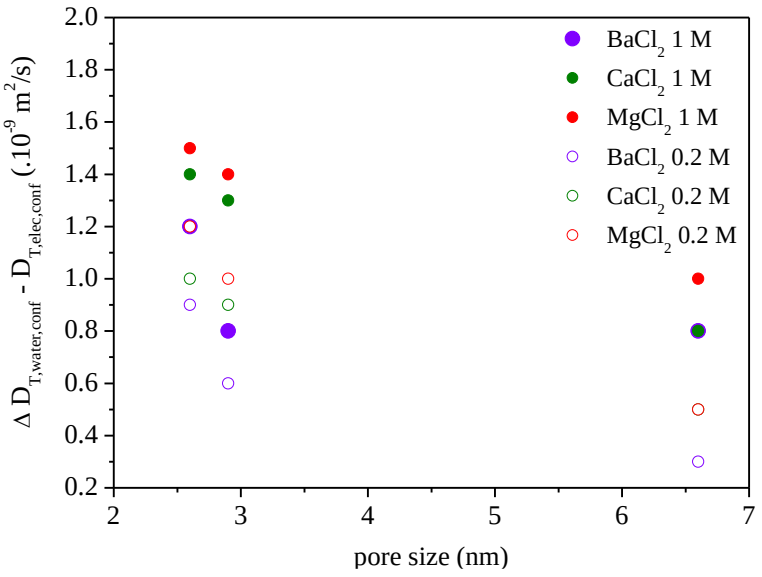


*Figure 56: Differences Δ between $D_{T,bulk,\ conf}$ and $D_{T,elec,\ conf}$ as a function of the pore size to remove the confinement effect on $D_T$.*

Figure 56 reveals that the differences of Δ between the various electrolytes is more intense for MCM-41 and MCM-41-1 compared to Δ obtained for SBA-15. This could mean that for pore size lower than 3 nm, the nature of ions impact more the water dynamics whatever the concentration. For such pore size, the amount of bulk electrolyte in the pore center is very reduced since water is predominantly located in the interfacial layer where ions are highly concentrated (thickness interfacial layer).

These observations and the fact that modifications of the water properties within confinement are predominately linked to the changes in the interfacial layer, lead to the assumption that ions sorbed in the interfacial layer are in charge of the water properties modification in the nanoconfinement. The measured structure and dynamics of the water consists in average properties and not the properties of the interfacial layer. This is the object of the following section.

## D. Water properties in the interfacial layer in silica nanoconfinement

In the following subchapter, we tried to estimate the water dynamics and the changes in the water structure within the interfacial layer. In this context, we extrapolate the overall water properties to the properties of water molecules that are located in the interfacial layer. Since ions are preferentially sorb to the surface, we assume modified properties for the water molecules in the hydration sphere and in the interaction range of the surface. We distinguish two cases: i) the SBA-15 case where we expect a lower confinement effect due to the bigger pore sizes and ii) the MCM-41 case where the confinement effect is more pronounced since in the smaller pores the surface-to-volume ratio is higher. We try to establish a link between the surface ion excess and the modifications of the structure and the dynamics of water.

### 1. Low confinement effect - case SBA-15

The characterization of the network structure and the dynamics of water in confined mesoporous silica SBA-15 (6.6 nm) in presence of ions, showed that the water network is perturbed and the water dynamics is slowed. These changes are induced by the confinement and mainly by the presence of ions, depending on their nature and their concentrations. While a pore size of 6.6 nm has an important impact on the structure of water network by strongly decreasing the highly coordinated water fraction (FBW) compared to bulk water, the dynamical properties are only slightly influenced by this confinement. The confinement effect slows the water dynamics significantly for pore sizes smaller than 3 nm. The perturbation of the water properties is reinforced when ions are added to the solutions decreasing the highly coordinated water fraction and slowing the water dynamics with respect to ions and their concentration.[2,18,198] Consequently, our system may be described as follow: a bulk-like part in the pore center and an interfacial layer at the pore surface presenting an excess of ions due to their sorption at the pore surface. Generally, this

interfacial layer is described by double-layer or a triple-layer models such as the Gouy-Chapman-Stern-Grahame model. According to these models and our pH values in solutions, hydrated cations are adsorbed in the first layer building up the compact electric double layer (Stern layer). The negative surface charge is further screened by excess cations in the diffusive layer until electroneutrality is reached.[57,58,199,200] Regarding the existence of such interfacial layer in confinement, it is reasonable to assume that the observed changes of water structure and dynamics may be mainly associated with the modification of the water properties within such layer having a thickness of few water molecules.[7]

In order to determine if the evolution of the water properties in the interfacial layer are related to the surface ion excess $d_{Tot}$ and/or to their kosmotropic character, we estimated the percentage of various types of water and the translational diffusion coefficient of water in the interfacial layer $D_{Tint}$. We assumed that the electrolyte solution in the center of the pore has the same properties as the bulk electrolyte solution. We also considered the percentage of water in the interfacial layer obtained by DSC measurements and the application of the adapted Gibbs-Thompson relation of approximately 50 % (see appendix). From eq. 36, the percentages of various types of water and $D_{Tint}$ were estimated:

$$X_{int} = 2 \cdot X_{conf} - X_{bulk} \qquad (35)$$

with $X_{int}$ is either the ratio of various types of water or $D_{Tint}$ in the interfacial layer next to the surface, $X_{bulk}$ is either the ratio of various types of water or the self-diffusion coefficient of water in bulk electrolyte solution and $X_{conf}$ is either the ratio of various types of water or $D_T$ obtained in SBA-15 filled of water or electrolyte solution. Figure 57 shows the evolutions of $D_{Tint}$

and the percentage of intermediate water INBW in the interfacial layer as a function of the total sorbed ion densities $d_{Tot}$. The calculated percentages of the various types of water in the interfacial layer (IBW, FBW, INBW and LBW) are summarized in the appendix (Figure 85).

Figure 57 highlights that whatever the electrolyte, $D_{Tint}$ is lower than the translational diffusion coefficient of bulk water and globally decreases with the increase of $d_{Tot}$ and this decrease depends on the concentration and the nature of the electrolyte. The tendencies presented here in the concentration range $[XCl_2]_0 > 0.2$ M are in agreement with *Ben Ishai et al*. studying the impact of ions in solution and their concentrations on water dynamics at a pico-second time scale.[18] $D_{Tint}$ of the water molecules in presence of kosmotropic ions such as $Ca^{2+}$ and $Mg^{2+}$ are dependent of $d_{Tot}$ and weakly dependent when chaotrope ions such as $Ba^{2+}$ are present even if $d_{Tot}$ is the highest.

However, the presence of $Ba^{2+}$ in the microporosity should decrease $d_{Tot}$ . In that case, the surface ion excess should not significantly influence $D_{Tint}$ and the INBW in the interfacial layer.

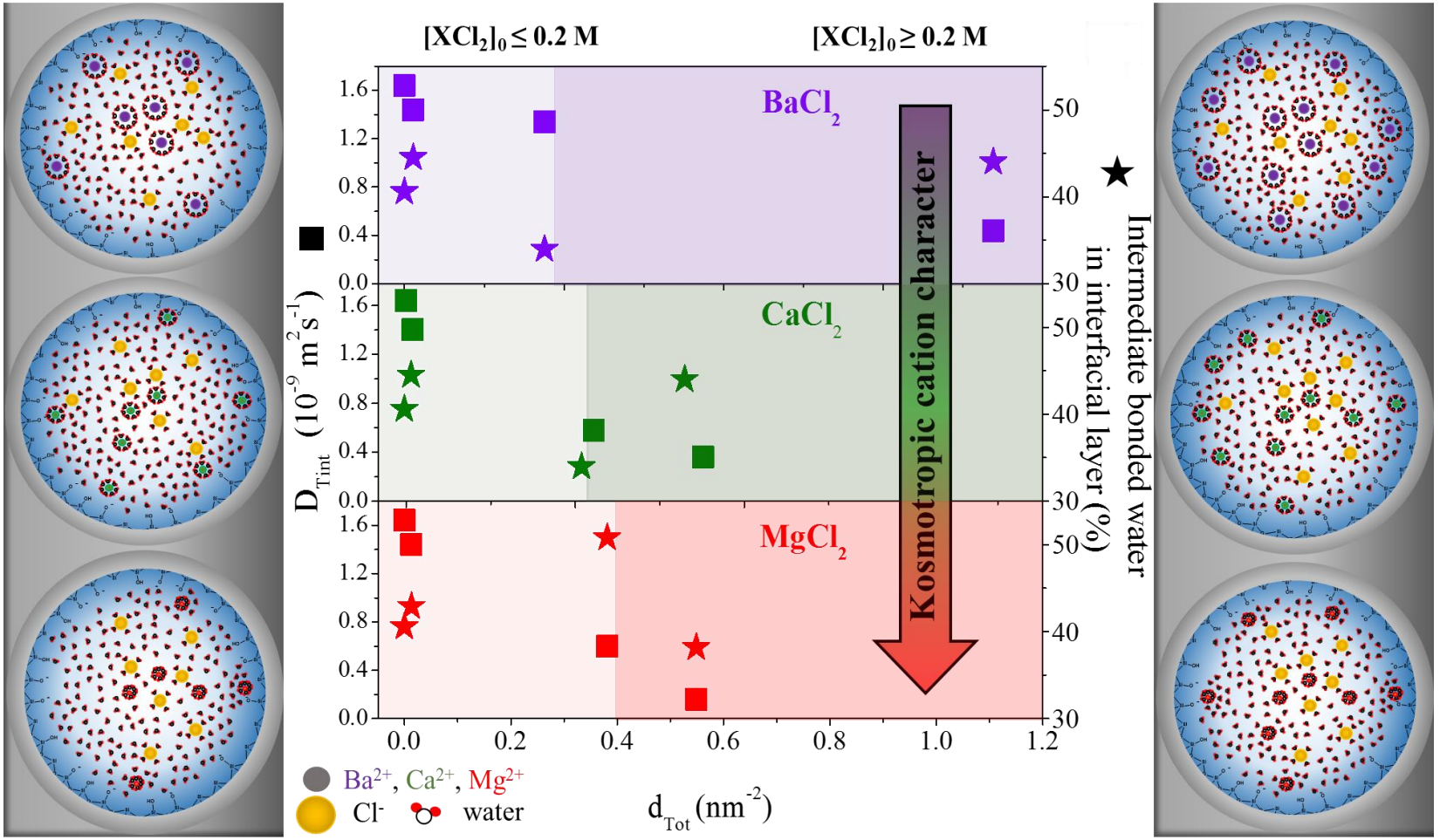


*Figure 57: Evolutions of the translational diffusion coefficient of water $D_{Tint}$ (■) and of the percentage of intermediate bonded water INBW (★) in the interfacial layer as a function of the surface ion excess $d_{tot}$. Schematic view of the ion distribution within the silica nanopores at $[XCl_2]_0 \leq 0.2$ M on the left and at $[XCl_2]_0 \geq 0.2$ M on the right.*

The evolution of the relative peak area of INBW in the interfacial layer with $d_{tot}$ is different than the $D_{Tint}$ one. It can be divided in two parts depending on $[XCl_2]_0$ and seems to be driven by the nature of ions present in the interfacial layer. For $[XCl_2]_0 \leq 0.2$ M, the percentage of INBW in the interfacial layer presents a decrease with $d_{Tot}$ for SBA-15 filled with $BaCl_2$ electrolytes, remains constant for SBA-15 filled with $CaCl_2$ electrolytes and increases for SBA-15 filled with $MgCl_2$ electrolytes. This may be due to the sorbed ion densities of $Cl^-$ in the case of SBA-15 samples filled with $BaCl_2$ solutions $d_{Cl^-} = d_{Ba^{2+}}$ (see Table 3). This is not the case for SBA-15 samples filled with $CaCl_2$ and $MgCl_2$ solutions having $d_{Cl^-} = 2d_{X^{2+}}$. An inversion of this trend occurs for $[XCl_2]_0 > 0.2$ M. In that case, the evolution of the relative peak area of INBW in the interfacial layer may be mainly driven by the nature of the electrolyte and more particularly by the kosmotropic properties of the cations since $d_{X2+} = d_{Cl^-}$.

Several studies showed this ions-induced perturbation of the hydrogen bond network using surface-sensitive in-situ vibrational sum frequency generation (SFG).[69,131,201–203] Probing the water structure at the silica/water interface, they revealed that accumulated cations at the silica surface due to their sorption, partially disrupt the hydrogen bonding between water molecules and lower their average coordination number. The authors observed also some differences of water network structure depending on the kosmotropic nature of the ions and the pH.[202,204] Even if SFG results are obtained on planar silica/water surface and that the surface curvature within the pore may also have an additional impact on the water ordering, we observed the same tendencies in our study. Indeed, the kosmotropic $Mg^{2+}$, having a high surface charge density and thus, a strongly attached hydration shell, is expected to reinforce the hydrogen bonding network of water molecules in its vicinity. At concentrations sufficiently high, $[MgCl_2]_0 > 0.2$ M, we observe a decrease of the percentage of INBW in the interfacial layer and of $D_{Tint}$ (43 % of $D_{Tbulk}$). The more chaotropic $Ba^{2+}$ with a less

attached water shell weakens the water-water interactions corresponding to an increase of the percentage of INBW. This is associated with a less distinctive deceleration of the water dynamics within the interfacial layer (65 % of $D_{Tbulk}$). The $Ca^{2+}$ features characteristics somewhere between kosmotropic and chaotropic properties (61 % of $D_{Tbulk}$).

## 2. Confinement effect on water dynamics - case MCM-41

Regarding the confinement effect in MCM-41, the extrapolation to the interfacial layer is more complicated. The widely used Gibbs-Thompson equation to determine the amount of water molecules under the influence of the pore surface is only applicable for pores having a size bigger than 3 nm. Previous studies have shown that the shift of the melting temperature depression for pores below 3 nm cannot be satisfactorily be fitted using the GT equation.[91,178–180] In the following, we assumed three monolayers of water in the interfacial layer to calculate the quantity of bulk water in the pores of MCM-41. Due to this fact the calculated diffusion coefficients in the interfacial layer for MCM-41 and MCM-41-1 lead to negative values and thus to non-rational results. Even the assumption of two layers of water molecules in the interfacial, does not lead to reasonable values for both diffusion coefficients and for the contribution of intermediate bonded water (INBW). This may lead to the assumption that no bulk-like electrolyte solution is present in the smaller pores of MCM-41 and MCM-41-1. Thus, the total amount of confined water is modified by the confinement and the presence of ions. This issue makes the comparison of the two silica materials difficult.

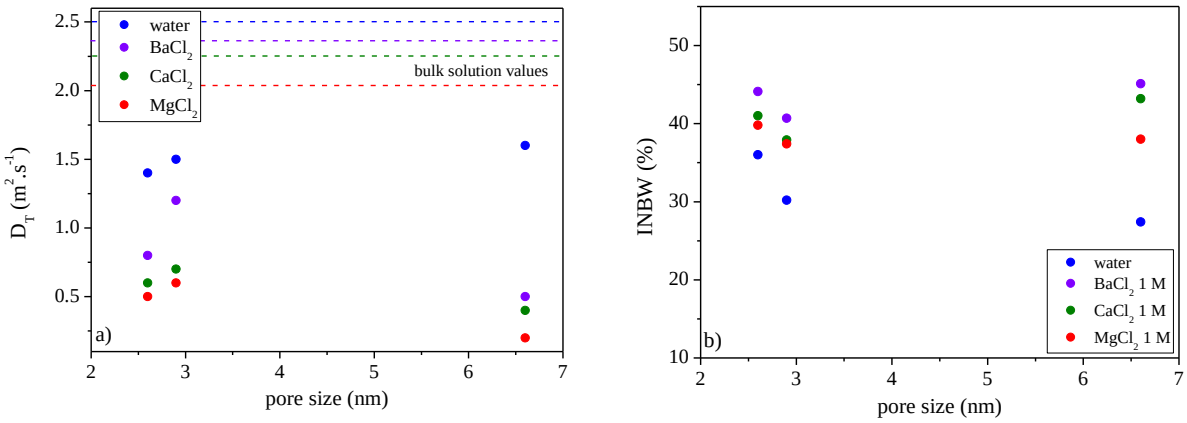


*Figure 58: Evolutions of the translational diffusion coefficients $D_T$ (a) and the contribution of intermediate bonded water (INBW) (b) for various electrolytes at 1 M as a function of the confinement. For SBA-15, the values of $D_T$ and INBW in the interfacial layer are depicted.*

However, the modified water dynamics and structure in the different mesopores of silica and in the presence of various electrolyte solutions at 1 M are illustrated in Figure 58. Comparing the water properties in the presence of ions in the interfacial layer, the results highlight that the water properties in MCM-41 and MCM-41-1 cannot be completely considered as interfacial water. However, due to previous calculation considering 2 to 3 water layers on the surface, almost no bulk-like solution may be present in MCM-41 and MCM-41-1. These results could suggest that in silica confinement lower than 3 nm, only interfacial water and modified water are present in the pores.

## E. Conclusion

For the first time, we present a complete study of the structural and dynamical properties of water in highly ordered mesoporous silica having various pore sizes and in the presence of ions having more or less kosmotropic properties. The modifications of the water properties were related to the pore size, and the nature of the electrolytes. The size of the silica nanoconfinement may have an additional effect on the surface ion excess and therefore, on the water properties. Generally, the ion effect on the structural and dynamical properties of water was attributed to the more or less kosmotropic ion properties. Kosmotropic (chaotropic) ions are found to increase (decrease) the water-water interactions and thus, reduce the water mobility more (less) pronounced. In a last part, the average water properties were extrapolated to the interfacial layer. In the case of SBA-15, the water properties were drastically modified in the interfacial layer whereas in the case of MCM-41, such an extrapolation was not possible probably due to the fact that no bulk-like solution is present.

In the following chapter, we present the evolution of the mesoporous silica alteration as a function of the electrolyte solutions. The modified water properties obtained in this chapter will help to better understand the alteration processes in the confinement.

# Chapter IV - Evolution of mesoporous silica in water and electrolyte solutions: The role of pore size and silica wall density

In this chapter, we have determined the evolution of the morphology and the structure of mesoporous silica, SBA-15 and MCM-41, during short-term alteration in water and the $XCl_2$ electrolyte solutions. Both silica materials were characterized by in-situ small angle X-ray scattering (SAXS) during their alteration at 50 °C. From the obtained results, we intend to relate the evolution of the confinement with the nature of the silica, the pore size and the electrolyte to *in fine* find a relation between the water properties and the silica evolution.

## A. Introduction

The objective of this study is to relate the structural and dynamical properties of water in electrolyte solutions with their impact on the mesoporous silica dissolution. As already shown in the material characterization section (chapter III), it is possible to relate the SAXS pattern and the corresponding Bragg peaks of mesoporous silica to the porosity and its arrangement. In order to characterize the evolution of the silica, we used a model to calculate SAXS scattering spectra to know their theoretical appearance as a function of different structural parameters. This comparison allows us to obtain information about the material evolution, the change of structural parameters at a short-term and the specific ion effect on the alteration.

## B. Experimental section

Several silica alteration experiments at high S/V were performed at 50 °C in pure water and in various electrolyte solutions $XCl_2$ (X = Ba, Ca, Mg) at $[XCl_2]$ = 1 M.

First, silica powders and the solutions were inserted in a 2 mm diameter glass capillary and afterwards sealed in order to avoid evaporation of the solutions. A surface area to solution volume ratio (S/V) around $4.10^7$ $m^{-1}$ was used to minimize the silica grain dissolution. In order to allow the solutions penetration through the pores and the ions sorption to the silica surface, the samples were stored during 24 hours before the scattering experiments. Second, the evolution of the silica powder porosity was determined using in-situ SAXS characterization. The sealed capillaries were placed in an oven at 50 °C, specifically dedicated to SAXS analyses. Scattering measurements were performed each 4 h during 60 h for MCM-41 and 88 h for SBA-15.

## C. Description of the model

The model used to perform these calculations has already been presented in full details in ref 205. In this model, arrays of cylindrical pores of infinite length are disposed on a hexagonal lattice, as shown in Figure 59. The hexagonal lattice can be described by three main parameters: the pore size $r_p$, the wall thickness $w$ and the unit cell parameter $a$. The mean lattice parameter is given by the distance from one pore center to another and this distance $d$ can be calculated using eq. 37:

$$d = \frac{2\pi}{q} \qquad (36)$$

where $d$ is the spacing between the {10} planes in the mesoporous lattice; and $q$ is the scattering vector. The unit cell parameter $a$ was also deduced from eq. 37 and 38:

$$a = \frac{2d_{100}}{\sqrt{3}} \qquad (37)$$

The unit cell parameter is accessible from the Bragg peak positions in the experimental spectra. The pore diameter and the cell parameter are adjusted in order to optimize the agreement between the experimental and the simulated SAXS pattern. It is important to note that a Gaussian distribution is considered for the pore diameters (pd). The full width at half maximum (FWHM) of this distribution is expressed as a percentage of the cell parameter.

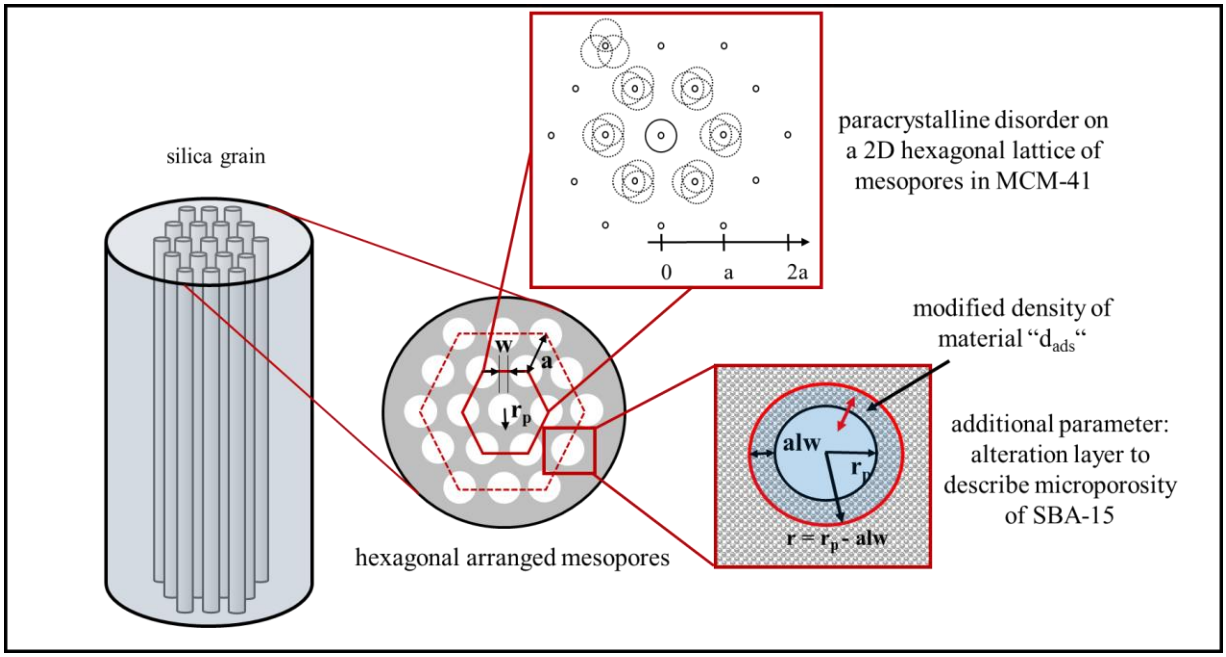


*Figure 59: Schematic representation of the structure used in the model adapted from ref 205. The silica grain is perforated with smaller cylinders of mesopores having three characteristic parameters: pore size $r_p$, lattice parameter a and wall width w.*

In addition to that, a paracrystalline disorder parameter (pcd) was introduced taking into account the imperfection of crystals.[138] This parameter considers the progressive loss of correlation between the positions of the pore centers in a hexagonal lattice, as illustrated in the inset of Figure 59.[206]

A paracrystalline degree (pcd) is therefore introduced and defined as the ratio between the FWHM of the Gaussian distribution, describing the dispersion of the position of the first neighbouring pore and the pore lattice parameter. A progressive increase of the pd and pcd parameters results in the progressive smoothing of all Bragg peaks as observed in the experimental data, obtained from the experiments with MCM-41. The pore centers are consequently shifted from their original positions of the hexagonal lattice.

Another possibility of this model is to take into account a layer of different density around the pore having a thickness altered layer width (alw). This layer is only considered for SBA-15 due to the presence of microporosity in the pore walls and was described by *Gouze et al*, as a zone around the pores where the solution has diffused through the microporosity.[4] In the calculations, the presence of microporosity was included through a density equal to that of microporous amorphous silica. As shown in annex IV, small variations in silica densities have no influence on the interpretation of the results. A descriptive scheme of the structure considered by the model is shown in the inset of Figure 59.

Adapting this model to the two silica MCM-41 and SBA-15, several SAXS spectra were calculated and the obtained parameters were used to propose some silica evolutions during their alteration.

## D. Evolution of MCM-41 in solution

The evolutions of the SAXS patterns of MCM-41 in water at 50 °C as function of the alteration time are reported in Figure 60. At the beginning of the alteration, the SAXS patterns show the Bragg peaks relative to the 2D hexagonal lattice of mesopores. These Bragg peaks correspond to the 10, 11, 20, and 21 reflections shown in 4.1 chapter III. From the positions of the Bragg peaks and using the equations (37) and (38), we obtained the unit cell parameter *a* of 4.7 nm.

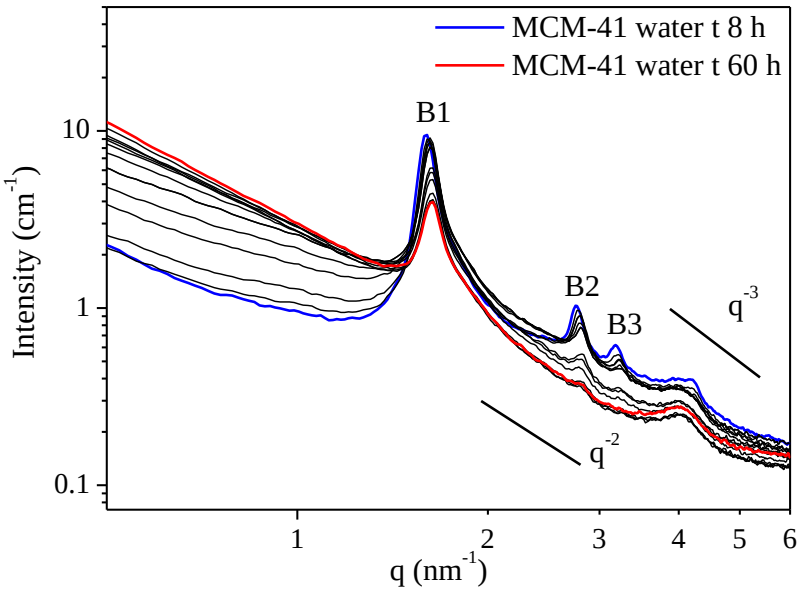


*Figure 60: Evolution of the experimental SAXS pattern of MCM-41 in pure water during 60 h at 50 °C. The characteristic Bragg peaks are denoted with B1, B2 and B3.*

During the alteration, the intensities of the Bragg peaks decrease and after approximately 60 h, the peaks I2 and I3 disappear. *Gouze et al.* found that this progressive loss of the structural Bragg peaks is related to the loss of the mesoporous order related to a randomization of the position correlation between pores.[4] As illustrated in Figure 61, the wall of each pore is partly deformed probably due to the dissolution of silica wall and to the recondensation/precipitation of hydrolyzed silica on the wall, resulting in a change of the pore shape.[133] This idea is supported by the solubility of amorphous silica at 50 °C (80 $mg.L^{-1}$).[64] As we observed in 3 nm nanochannels filled with $BaCl_2$ 1 M, the low amorphous silica solubility could lead to its precipitation inside the pore. The center of the pores is consequently shifted from the original position of the hexagonal lattice, leading to the smoothing of the Bragg peaks.[4,206]

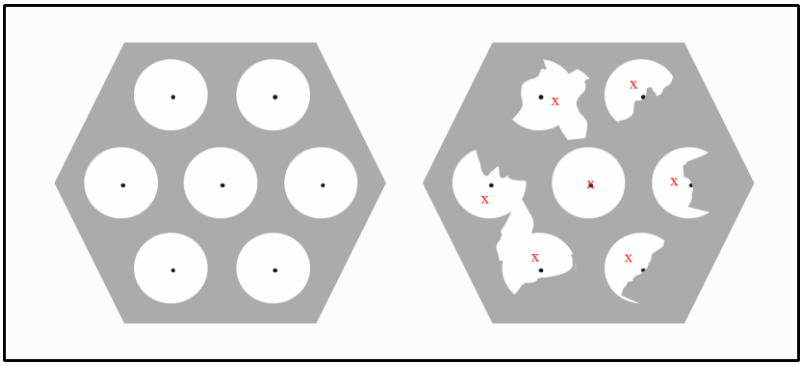

*Figure 61: Scheme of the possible evolution of the porous structure of MCM-41 sample before and after alteration in water and electrolyte solution. As the alteration duration increases, the position of the center of the hexagonal lattice(red crosses) are shifted due to dissolution and recondensation processes.*[4]

This is also supported by the fact that the overall intensity increases following a $q^{-3}$ to $q^{-2}$ power law, and this power law seems not to depend on the alteration time. The deviation from a Porod regime ($q^{-4}$ power law) were observed in similar SAXS measurements on mesoporous silica.[207] The deviation can be related to the roughness of the interface between the solution and the silica wall, and to the contribution of the structure factor coming from the amorphous structure of the silica tetrahedrons inside the walls.

To confirm the idea of a randomization of the position correlation between pores during alteration, several SAXS patterns were modelled taking into account a pore radius of 1.3 nm, a unit cell parameter of 4.7 nm and a FWHM of the pore size distribution and of the paracrystalline disorder parameter from 20% to 35 %. The electron densities used for water and electrolyte solutions are summarized in Table 13. The results are presented Figure 62 (a). As already observed by *Gouze et al.*, the cumulative increase of the pd and pcd parameters results in the progressive smoothing of all Bragg peaks as observed in the experimental data presented Figure 62 (b). While, the hypothesis of simultaneously increasing pd and pcd is a very coarse

approximation of the alteration mechanism that takes place in the sample, the calculated SAXS spectra are in a good agreement with the experimental ones.

*Table 13: pH values, mass volume $\rho_m$ and the electron densities $\rho_{el}$ for water and electrolyte solutions $XCl_2$ (X = Ba, Ca, Mg).*

| solution | pH | $\rho_m$ (g/L) | $\rho_{el}$ (g/Å$^3$) | $\rho_{el}.10^{-11}$ (cm/cm$^3$) |
|---|---|---|---|---|
| water | 5.8 | 1.0 | 0.334 | 0.94 |
| $BaCl_2$ 1 M | 5.8 | 1.2 | 0.379 | 1.08 |
| $CaCl_2$ 1 M | 6.2 | 1.1 | 0.356 | 1.00 |
| $MgCl_2$ 1 M | 6.4 | 1.1 | 0.358 | 1.01 |

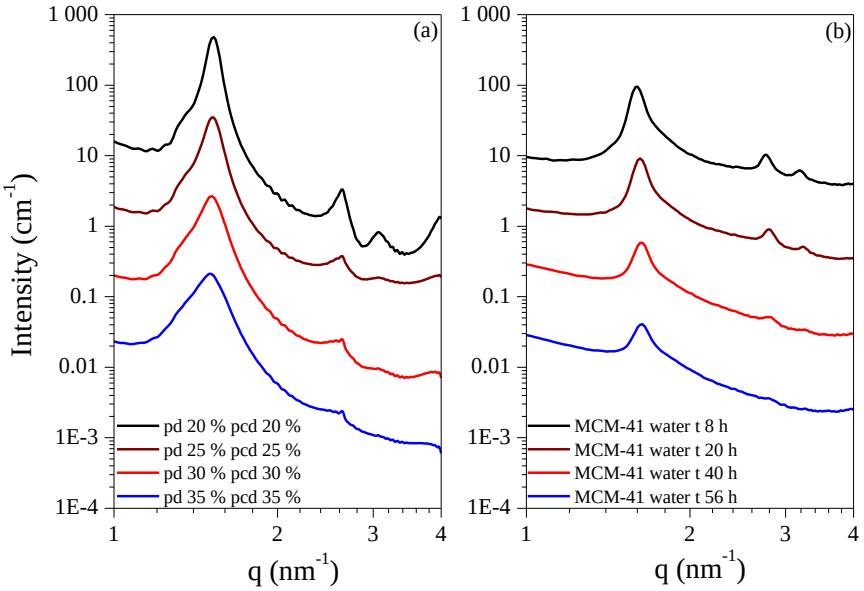


*Figure 62: (a) Modelled SAXS patterns of a mesoporous lattice with a unit cell parameter of 4.7 nm and a pore radius of 1.3 nm and (b) experimental SAXS patterns of MCM-41 in pure water. The FHWM of the pore diameter distribution (pd) and the parameter of the paracrystalline disorder (pcd) are equal to 20 %, 25 %, 30 % and 35 %. For the sake of readability, the curves have been shifted.*

The evolutions of the SAXS patterns of MCM-41 in electrolyte solutions as function of the time are reported in Figure 63.

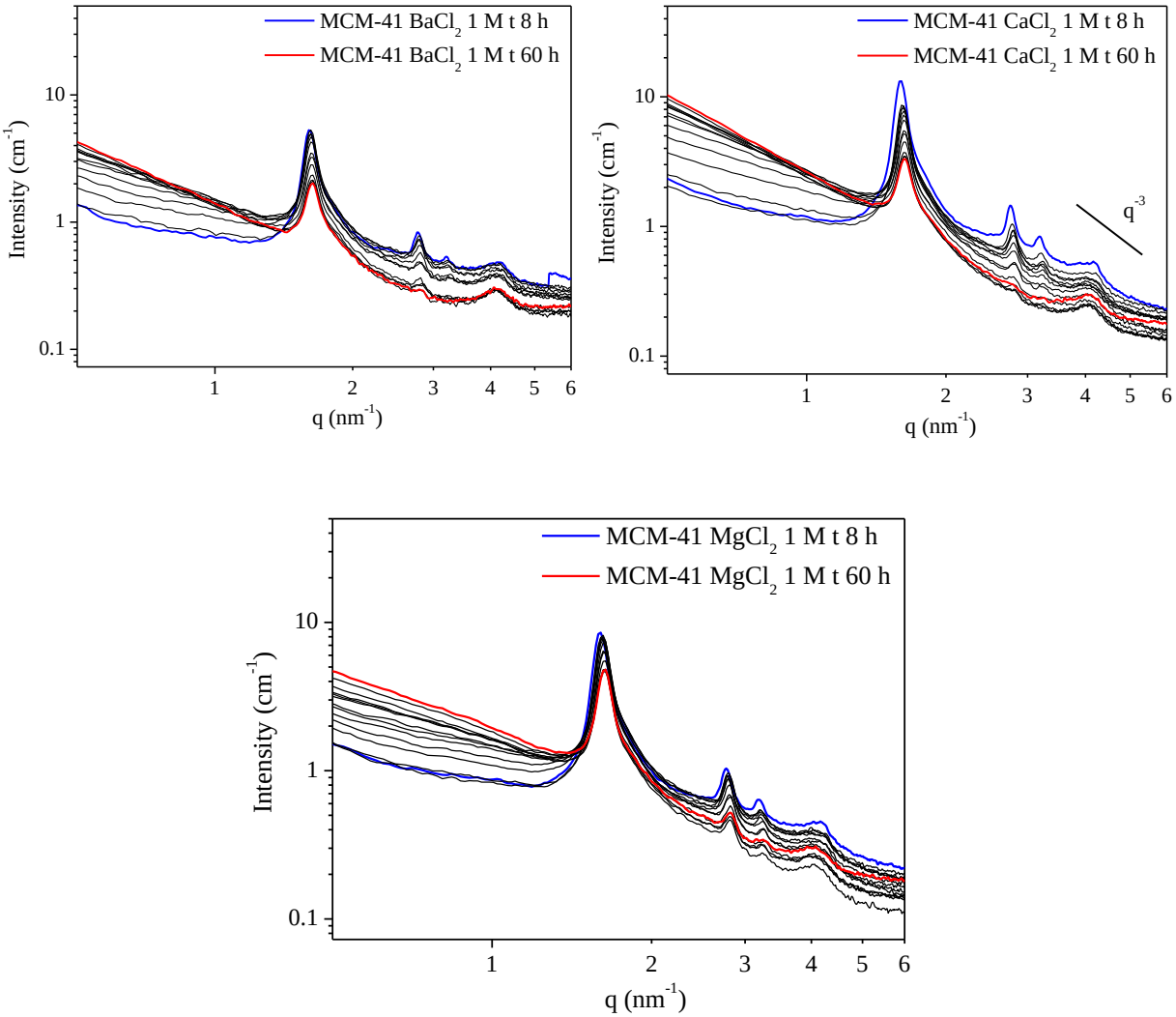


*Figure 63: Evolutions of the experimental SAXS pattern of MCM-41 in electrolyte solutions during 60 h at 50 °C.*

The same intensity decrease of Bragg peaks is also observed on the SAXS patterns of the MCM-41 in electrolyte solutions. However, the time required to decrease the intensity of B1 and to lose B2 and B3 depends on the electrolyte solution. Figure 64 highlights the evolutions of the different Bragg peaks in MCM-41 filled with water and various electrolyte solutions. The

difference of intensity between each series of experiments is due to the various electron density of the electrolyte solution modifying the contrast between the silica and the filled pores.

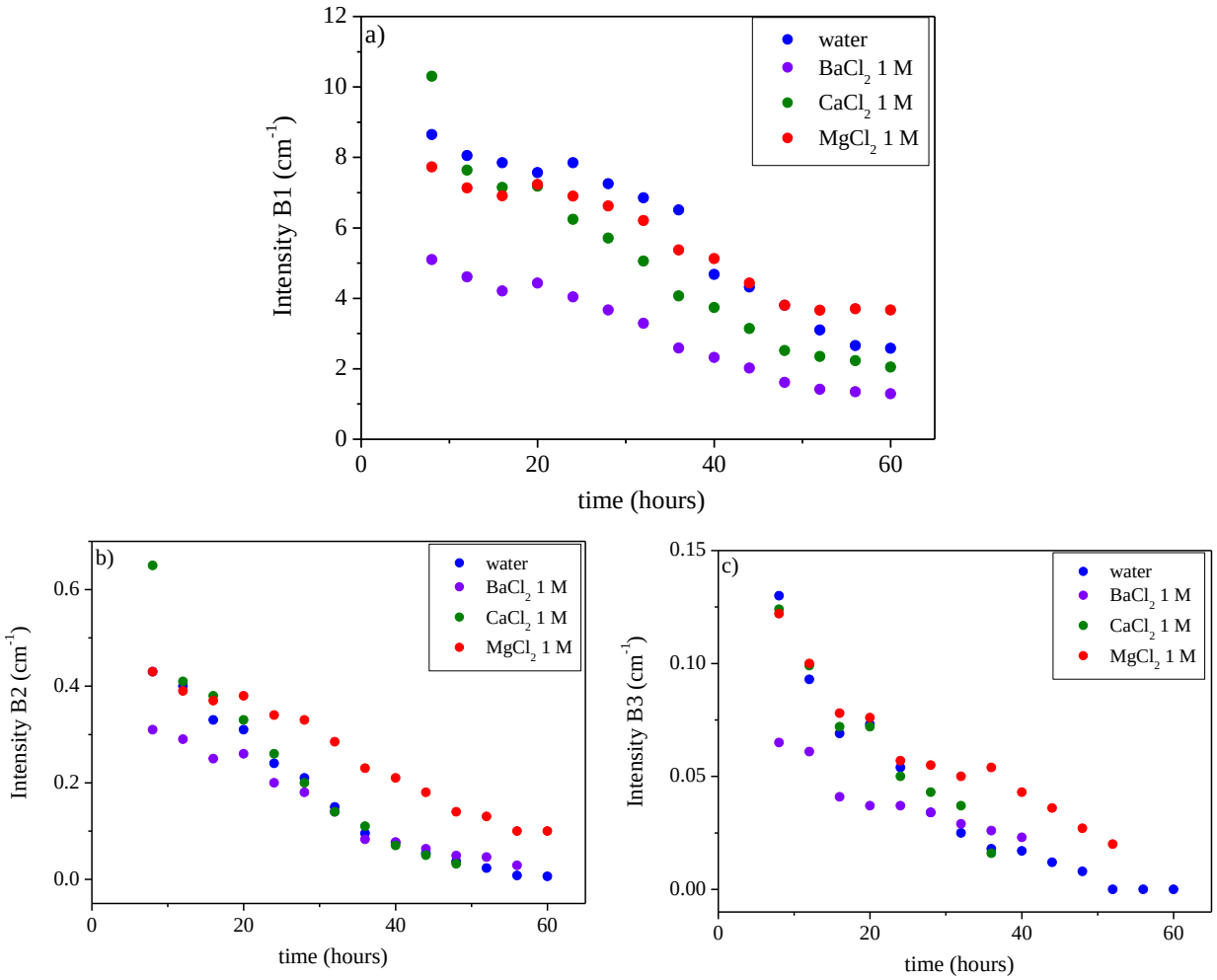


*Figure 64: Evolutions of the intensities of the Bragg peaks B1, B2 and B3 of the SAXS patterns of the MCM-41 in water and electrolyte solutions as a function of the alteration time.*

Figure 64 reveals that whatever the solutions and its concentration, the peak intensities continuously decrease with the alteration time and remain constant or null around 50 hours. In order to compare the impact of the various electrolyte on the MCM-41 alteration rate, the rates of

intensity decrease were estimated until the intensities remain null or constant and are presented in Table 14. The evolutions for the Bragg peaks B1, B2 and B3 are summarized in annex IV.

*Table 14: pH values of solutions, surface ion excesses of ions assuming their sorption in silica MCM-41 and the slopes of the loss of the Bragg peaks B1, B2 and B3 in MCM-41 immersed in water and electrolyte solutions.*

| Samples | pH | X.nm$^{-2}$ | Slope B1 | Slope B2 | Slope B3 |
|---|---|---|---|---|---|
| MCM-41 water | 5.8 | - | -0.109 | -0.011 | -0.003 |
| MCM-41 $BaCl_2$ 1 M | 5.8 | 0.407 | -0.084 | -0.007 | -0.001 |
| MCM-41 $CaCl_2$ 1 M | 6.2 | 0.283 | -0.173 | -0.013 | -0.004 |
| MCM-41 $MgCl_2$ 1 M | 6.4 | 0.235 | -0.084 | -0.007 | -0.002 |

As highlighted by the results presented in Table 14, at $[XCl_2] = 1$ M, the progressive rate decrease of B1 follows the order: $CaCl_2$ > water > $BaCl_2$ = $MgCl_2$. Regarding the Bragg peak B2, the results are comparable to B1, while the results for B3 are almost constant. The tendency of these results differ from the results obtained for the hydrolysis rate of quartz and amorphous silica micrometrics grains in similar electrolytes ($BaCl_2$ > $CaCl_2$ > $MgCl_2$).[129,132,147]

To summarize the alteration processes of MCM-41 in water and electrolyte solutions, we revealed that the progressive loss of the Bragg peaks of MCM-41 could be related to a dissolution-recondensation mechanism where the center of the initial pores are shifted. The loss of the ordered porosity depend on the electrolyte solutions in contact with MCM-41.

## E. Evolution of SBA-15 in solution

Figure 65 presents the evolution of the SAXS patterns obtained during the alteration of the SBA-15 in water and in electrolyte solutions. The experimental SAXS pattern of SBA-15 does not show a disappearance of the B2 and B3 Bragg peaks, as observed for MCM-41. While B1 remains almost constant, the relative intensities of I2 and I3 evolves continuously during the alteration time. The intensity of I2 increases progressively.

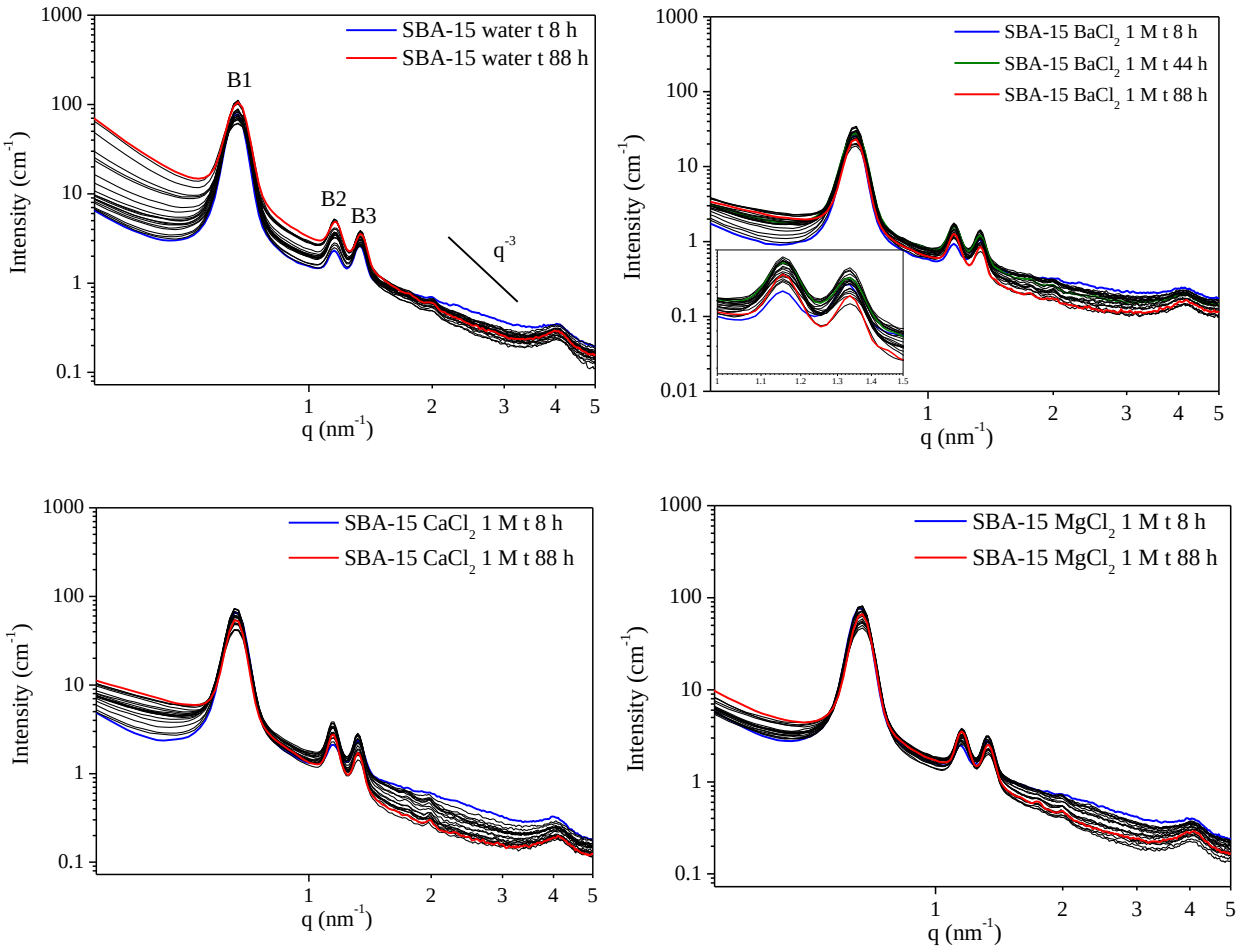


*Figure 65: Experimental SAXS pattern of SBA-15 filled with pure water and electrolyte solutions during 88 h at 50 °C. The spectra highlight the inversion of the Bragg peaks B2 and B3. The intensity of B1 remains almost constant.*

Since the peak positions remain constant during the alteration, we assume neither a contraction nor dilatation of the pore lattice in SBA-15. The unit cell parameter in SBA-15 was determined to be 10.8 nm. The change of the I2 / I3 ratio indicates that the pore shape is altered during the kinetics. *Gouze et al.* related this ratio evolution to the increase of the mean pore diameter and of a layer of altered silica in the vicinity of the pores edge using the model of *Cambedouzou et al.*, considering these two materials properties.[4] Indeed, due to the fact that the spectra results from a convolution of the form factor (cylindrical Bessel function with oscillation period inversely proportional to the pore diameter) with a structure factor that only depends on the unit cell parameter, the relative intensities of Bragg peaks B2 and B3 can be modified by the change of the pore diameter. Moreover, the existence of a microporosity in the pore walls of SBA-15 can lead to the formation of an alteration zone in which water can penetrate and diffuse (Figure 70).

To model the experimental ratio I2 / I3, we have used the same model, which includes a pore radius $r_p$, an alteration layer having a thickness *alw*. The electron density of the electrolyte solutions filling the pore were taking into account (Table 13), as well as the electron density within this alteration layer with respect to the value of amorphous silica (0.6 $e^-$/Å).[4] The previous parameters (unit cell parameter *a*, the solid fraction $f_s$, the paracrystalline disorder parameter *pcd* and the pore distribution *pd*) were defined in the same way than in the case of MCM-41.

Once the parameters *rp* and alw are set, simulated curves are calculated. The intensities of the Bragg peaks B2 and B3, I2 and I3, as well as the ratio I2 / I3, are then extracted from these curves, simulated and compared to the experimental values. Since the model takes into account certain hypotheses, such as infinite cylindrical pores, I2 and I3 experimental and modeled can be

different. The model is considered valid when experimental and simulated I2 and I3 follow the same tendency and the experimental and simulated I2 / I3 ratios have the same value.

Figure 66 presents the evolution of the experimental I2 / I3 ratio and the more consistent I2 / I3 ratio obtained by the modelling. The graph depicts the constant increase of the experimental I2 / I3 ratio for all experiments. As the alteration time is proceeded, the constant increase of the ratio flattens and reaches an equilibrium.

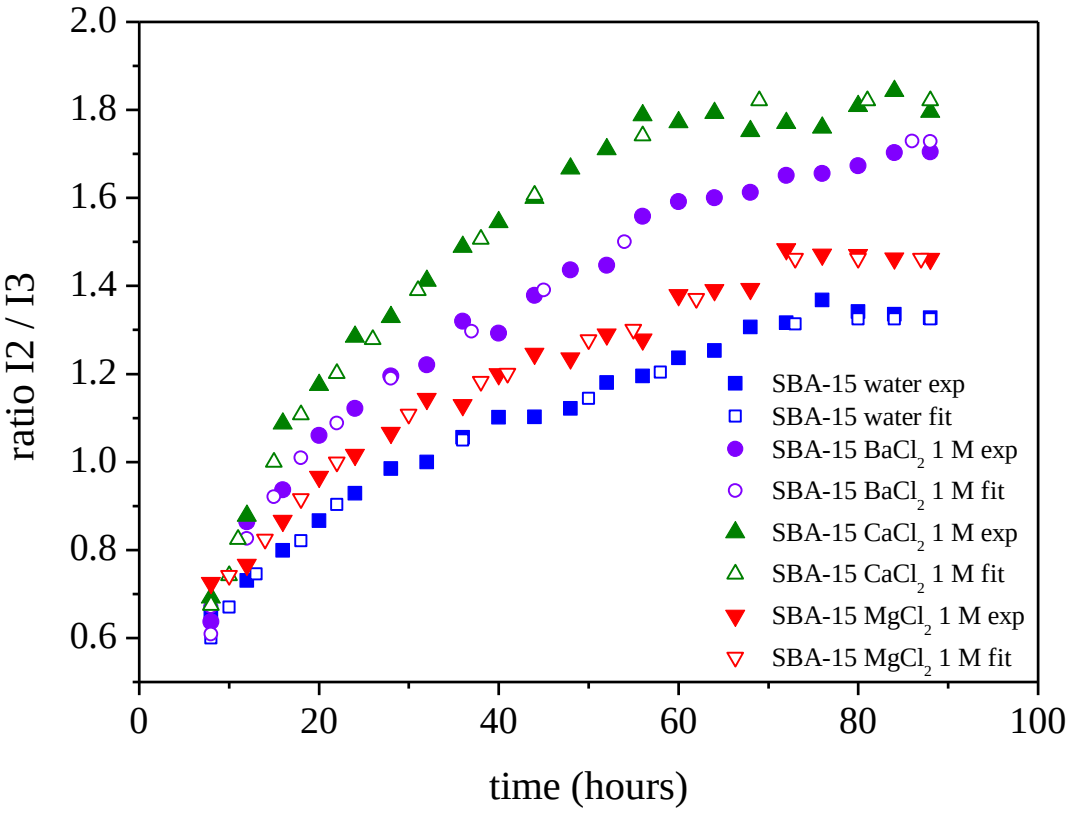


*Figure 66: Evolutions of the experimental I2 / I3 ratio (closed symbols) and the more consistent I2 / I3 ratio obtained from modelling (open symbols) as a function of alteration time.*

The evolutions of the parameters $r_p$ and *alw* used to obtain the most consistent I2 / I3 ratio are presented in Figure 67.

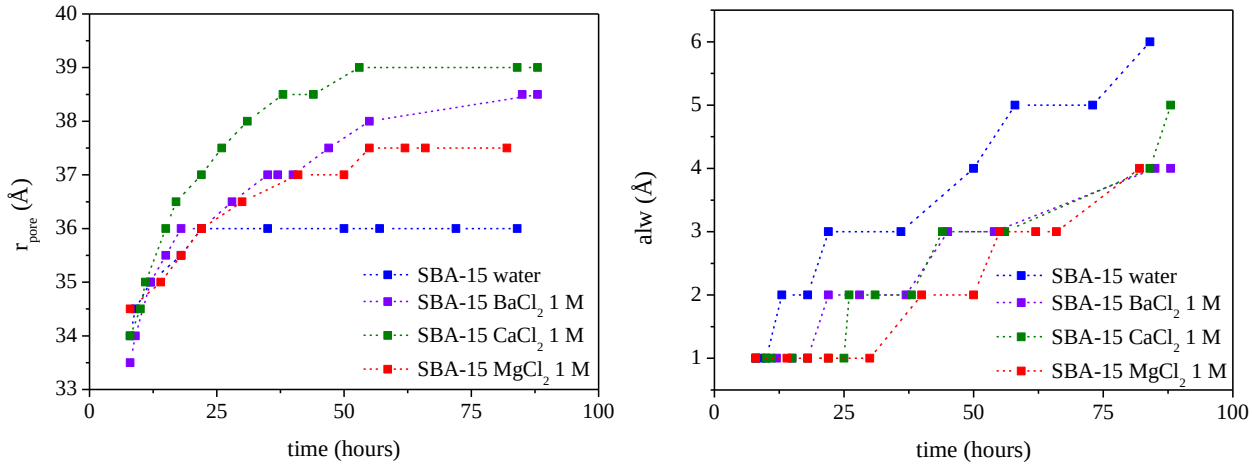


*Figure 67: Evolutions of the parameters (a) $r_p$ and (b) alw used to obtain the most consistent I2 / I3 ratio as a function of alteration time.*

The evolution of the pore size and the alteration layer presented in Figure 67 reveals two main dissolution stages of silica. First, at the beginning of the alteration, the thickness of the alteration layer and the radius of the pore increases. Second, the pore radius remains constant and the width of the alteration layer *alw* increases. From these results, the dissolution rate of the $SiO_2$ pore wall $r_{SiO2}$ was calculated as the difference between the initial pore size $r_0$ and the pore size at silica saturation divided by the time required to reach the equilibrium (Table 14).

Moreover, the $r_p$ + *alw* evolves with a power law of exponent 1/2, typical for a diffusion process, as highlighted in Figure 68. Assuming that diffusion is the limiting reaction, an apparent diffusion coefficient of microporous pore wall alteration $D_{alw}$ during the first 24 h of alteration was calculated from the eq. 39 based on the second Fick law. The results are presented in Table 15.

$$alw + rp = 2\sqrt{\frac{D}{\pi}}\sqrt{t} + r_{p0} \qquad (38)$$

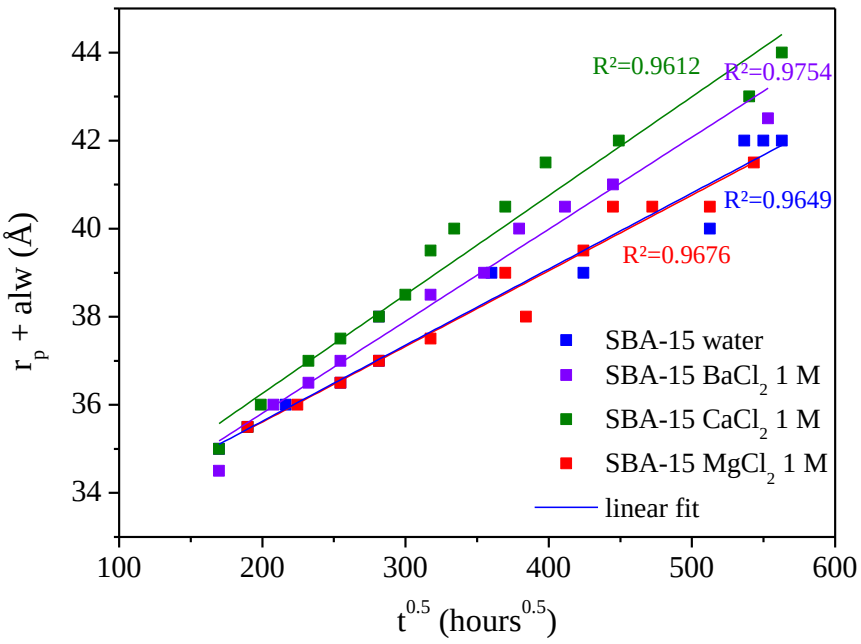


*Figure 68: Evolutions of the pore radius and the width of the alteration layer as a function of the square root of time. The linear evolution with a power law of exponent 1/2, is typical for a diffusive process.*

The dissolved silica concentration in the mesopores at the equilibrium was calculated using eq. 40:

$$[Si]_{eq} = \left(\frac{R_{eq}^2}{r_p^2} - 1\right) . \rho_{SiO2} . \frac{M_{Si}}{M_{SiO2}} \qquad (39)$$

where $R_{eq}$ is the sum of the pore radius of SBA-15 at the equilibrium and the width of the alteration layer *alw*, $r_p$ is the pore radius before the dissolution, $\rho_{SiO2}$ represents the density of silica oxide and *M* denotes the molar masses (Figure 70). These results were compared with the results obtained from bulk Si concentration measurements during the dissolution of SBA-15 using ICP-AES (Table

14). The concentrations of silica in bulk solution were analyzed after several times of alteration (Figure 69).

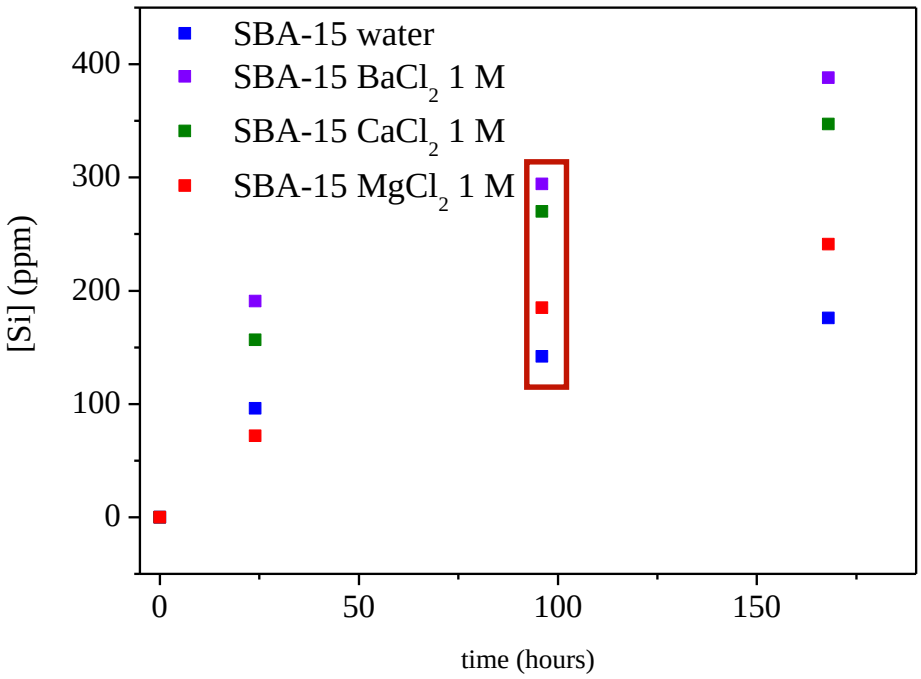


*Figure 69: Evolutions of the silica concentration measured in bulk solution during the alteration of SBA-15 in water and electrolyte solutions.*

*Table 15: pH values of solutions, surface densities of ions assuming their adsorption in silica SBA-15 in solution (X= $Ba^{2+}$ + 2 $Cl^-$), dissolved silica concentration $[Si]_{eq,}$ dissolution rates $r_{alw}$ of pore wall and apparent water diffusion coefficient $D_{alw}$ into the pore wall of silica SBA-15.*

| Samples | pH | X.nm$^{-2}$ | $[Si]_{eq, pores}$ (g.L$^{-1}$) | $r_{alw}$ (nm.d$^{-1}$) | $D_{alw}$ (. $10^{-24}$ m$^2$.s$^{-1}$) |
|---|---|---|---|---|---|
| SBA-15 water | 5.8 | - | 87 | 0.3 | 2.3 |
| SBA-15 $BaCl_2$ 1 M | 5.8 | 0.535 | 178 | 0.5 | 3.5 |
| SBA-15 $CaCl_2$ 1 M | 6.2 | 0.267 | 187 | 0.5 | 4.2 |
| SBA-15 $MgCl_2$ 1 M | 6.4 | 0.281 | 117 | 0.3 | 2.3 |

As summarized in Table 2, $D_{H2O}$ in the microporosity and $r_{SiO2}$ reveals the following order: $CaCl_2 \geq BaCl_2 > MgCl_2$ = water. Moreover, the results highlight that $[Si]_{eq}$ in the bulk solution are three orders of magnitude smaller than for $[Si]_{eq, pores}$ obtained in the mesopores of SBA-15 while no silica recondensation are observed by SAXS as in the case of MCM-41. The impact of the electrolyte is not similar to the one obtained for the quartz and amorphous silica micrometrics grains following this tendency: $BaCl_2 > CaCl_2 > MgCl_2$ > water.[127,132,147]

## F. Discussion

As the presented results highlight, the processes occurring in the pore of these mesoporous silica in solutions can be driven by several properties of the experimental system such as the pore wall (dense or microporous), the pore size (3 or 5.8 nm) of the silica and the nature of the electrolyte through the ions excess and their kosmotropic property.

## 1. Impact of the silica pore wall and pore size: case of silica in water

Generally, the evolution of mesoporous silica in contact with water depends both on the silica confinement and on the pore size.

In the case of dense pore walls, represented by MCM-41, the evolution of the Bragg peaks reveals a dissolution - reprecipitation process where the pore center are progressively randomized. This may be explained by two different phenomenon. First, in the smaller confinement of MCM-41, the alteration causes noticeable position shift of the pore center due to dissolution/recondensation.[133] This effect is less pronounced in the bigger pores of SBA-15. Second, the silica solubility (80 $mg.L^{-1}$ in water at 50 °C) and the low water dynamics in 3 nm pore size (chapter III) may induce a supersaturation of $H_4SiO_4$ in the interfacial layer and lead to a recondensation/precipitation of a more thermodynamically stable amorphous silica phase at the pore surface. Indeed, *Guthrie et al.*, have observed that MCM-41 was more soluble than amorphous silica and have supposed a precipitation of amorphous silica at the pore surface[208]. This recondensation/precipitation process can continue until the formation of a thermodynamically stable silica phase.

In the case of SBA-15, the bigger pore size of 5.8 nm and the presence of microporosity in the silica pore wall changes the material evolution. As highlighted in Figure 70, the alteration of SBA-15 presents two different stages: i) the radius of the pore and the alteration layer increase ii) the pore does not evolve probably due to the reaching of silica saturation and the alteration layer increases following a diffusive process. The higher water dynamics (chapter III) in the pores of SBA-15 (5.8 nm) size may not allow the silica recondensation/precipitation. However, this recondensation/precipitation could occur in the microporosity leading to an increase of the *alw*.

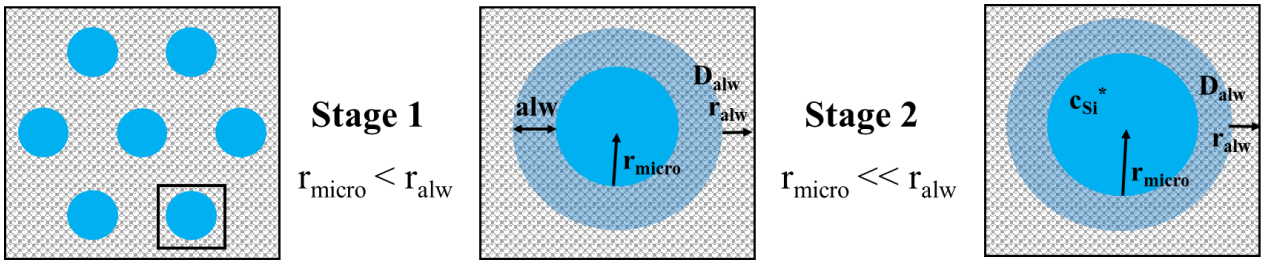


*Figure 70: Schematic representation of the proposed evolution of a pore of SBA-15 during its alteration at 50 °C in ultrapure water. $r_{micro}$: rate of microporous pore wall alteration $r_{alw}$: evolution rate of the altered silica layer, $C_{Si*}$: concentration of silica in the poral solution close or equal to the silica saturation concentration. $D_{alw}$: diffusion coefficient of microporous pore wall alteration.*

Even if MCM-41 and SBA-15 silica materials in water present two types of evolution, these mesoporous silica continue to evolve even in saturation condition. These results could be explained by the metastability of the silica materials.

## 2. Impact of aqueous solutions

In addition to the pore size and the silica pore wall, the various electrolyte solutions have a significant impact on the evolution of mesoporous silica materials. This enhanced material evolution was already observed in dense amorphous silica and quartz silica, as presented in the chapter I. [124–126] The catalytic ion effect on the dissolution was related to a distortion of the structure in the interfacial layer and at the silica surface resulting in an increased accessibility of the Si-O-Si bonds.[127]

For MCM-41, the impact follows the order: $CaCl_2$ > water > $BaCl_2$ = $MgCl_2$, which is quite different to the hydrolysis of microporous silica.[147] During the 24 h dedicated to reach the ions sorption equilibrium before the experiment at 50 °C, a precipitation of $MgCl_2$ and $BaCl_2$ may mainly explain these results. Indeed, in chapter II, we assumed that the low filling level of

3 nm nanochannels with $MgCl_2$ and $BaCl_2$ 1 M solutions can be explained by the low water dynamics due to the confinement and the kosmotropic property of the ions and with a low salt solubility. This $XCl_2$ salt precipitation may clog a fraction of the pores and lead to a less amount of water in the porosity, as we observed by ATR-FTIR (chapter III). Thus, the water amount, being directly related to the hydrolysis rate, may explain the lowest alteration rates of MCM-41 in $MgCl_2$ and $BaCl_2$ 1 M solutions. The dissolution of the silica and its recondensation/precipitation due to its low solubility (80 $mg.L^{-1}$ at 50 °C) could partially explain this result. In addition, some magnesium silicate phases could also precipitate.[161,209,210] In that case, the catalytic ion effect influences less the silica hydrolysis than the precipitation of salts. The evolution of SBA-15 in the various electrolyte solutions ($CaCl_2 \geq BaCl_2 > MgCl_2$ = water) is different from the one observed in MCM-41.

First, for SBA-15, we did not highlight a dissolution-recondensation/precipitation process probably related to the faster water dynamics in the pore of 5.8 nm (Figure 55 - chapter III). Furthermore, the bulk-like solutions in the pores center helps to renew the poral solution and therefore, to release ionic species to the bulk solutions outside the silica confinement. This would avoid the recondensation/precipitation of silica at the surface of the pores. However, salt precipitation could occur as observed in the 5 nm nanochannels for $MgCl_2$ (chapter II). As recently shown by *Dewan et al.*, the dissolution rate is directly linked to the water structure in the interfacial layer.[131] In order to determine if the ions enhance the $r_{alw}$, the water structure in the interfacial layer was related to the hydrolysis rate. Figure 71 shows an increase of $r_{alw}$ with the contribution of INBW. However, with $MgCl_2$ and $BaCl_2$ solutions, this increase is not significant probably due to salt precipitation modifying the water structure. This precipitation may lead to a limited hydrolysis rate.

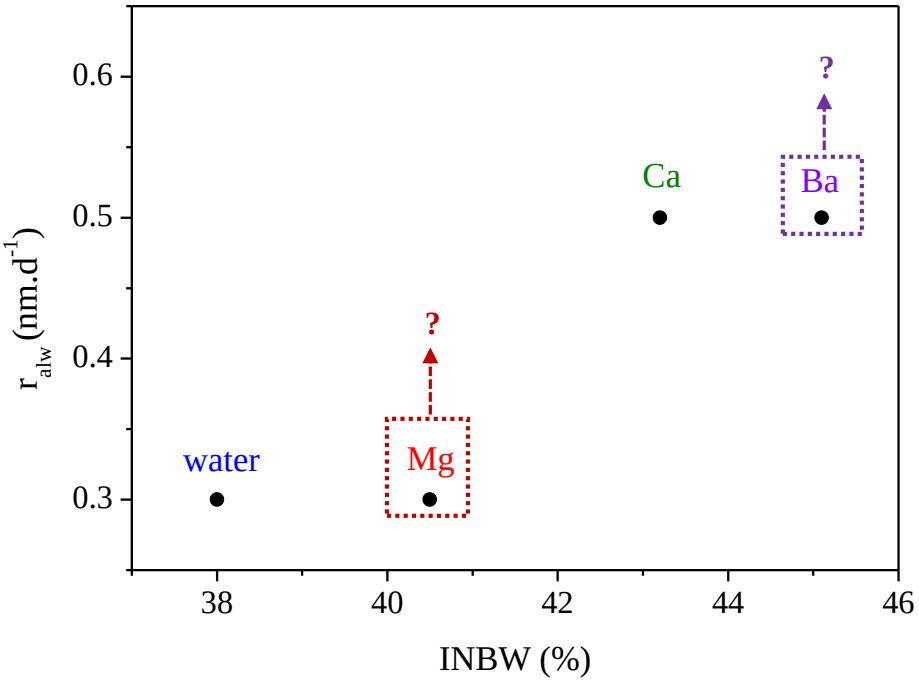


*Figure 71: Evolution of the hydrolysis rate of the alteration layer as a function of the amount of intermediate bonded water INBW.*

Second, this evolution goes hand in hand with a second alteration process in the microporosity, which is similar to the process observed in the smaller confinement of MCM-41 (dissolution-recondensation/precipitation process). Indeed, the existence of the microporosity inside the pore wall enables the diffusion of the solution including ions and dissolved silica. Due to the low water dynamics in such media, the silica recondensation/precipitation process and the salt precipitation may occur. This would explain the tendency observed for $D_{alw}$ ($CaCl_2$ > $BaCl_2$ > $MgCl_2$ = $H_2O$). In addition to that, this phenomenon can also explain the difference of silica concentration in bulk solution and in the mesopores. Indeed, the results highlight that $[Si]_{eq}$ in the bulk solution are three orders of magnitude smaller than for $[Si]_{eq,\ pore}$ calculated in the mesopores of SBA-15.

## G. Conclusion

The investigation of the evolution of highly ordered mesoporous silica in contact with water and various electrolyte solutions has shown different alteration behaviors which depend on the porosity and the structure of the silica. These two types of evolution are driven by the water dynamics which depends on the electrolyte and the salt solubility. For MCM-41 silica, having pores size around 3 nm and for which the water dynamics is slow, the alteration behavior is mainly driven by a silica dissolution – recondensation/precipitation process leading to a pore deformation and a possible precipitation of salts as observed in the 3 nm nanochannels. For SBA-15 silica, having a pore size around 6 nm and presenting microporous pore walls, the alteration is driven by the dissolution of the silica pore wall until silica saturation is reached and the dissolution-recondensation/ precipitation process due to the solution (ionic species) diffusion inside the microporosity. This alteration process may continue until a thermodynamically stable silica phase is formed.

# General conclusion and perspectives

The initial objective of this PhD thesis was to relate the properties of water confined in the presence of electrolytes to the evolution of silica mesoporous materials. To reach this goal, we have used an original approach, consisting to use electrolyte solutions containing ions with various kosmotropic properties $XCl_2$ (X = Ba, Ca, Mg) in model systems such as two parallel and plane silica surfaces (nanochannels) and highly ordered mesoporous silica materials (SBA-15 and MCM-41) to determine the impact of the curvature. This approach allowed the obtainment of several interesting results.

First, X-Ray reflectivity measurements of the filling kinetics of 3 and 5 nm silica nanochannels have brought information about the transport of the electrolyte solutions on few mm and the interfacial layer at the silica surface. The experimental approach was completed with molecular dynamic simulations to estimate the surface ion excess within this interfacial layer. Generally, we found that the penetration rate of the solutions in 3 nm nanochannels were significantly slower than in nanochannels having 5 nm. Furthermore, we highlight that the level of filling depends on the nature of ions and, in the case of $BaCl_2$ and $MgCl_2$, can be incomplete. To explain these results, we assumed that the water dynamics driven by the kosmotropic ion properties and the salts solubility might be the main driving force for the filling of the confinement. A combination of a supersaturation of ions in the interfacial layer and its low renewal probably lead to a salt precipitation and to a partial nanochannels clogging.

Second, we extended the investigations from parallel plane silica surface to highly ordered mesoporous silica, represented by MCM-41 (dense silica pore walls) and SBA-15 (microporosity around mesopores). Similar experiments with smaller nanoconfinement (MCM-41 and

grafted MCM-41) allowed to pinpoint of the critical pore size and electrolyte concentration at which the influence of the ion nature becomes the main factor affecting the water properties. The obtained results may show that the surface ion excess depends on the confinement size, the concentration and, on the density of the walls. In addition to that, we highlight that both the structure of the water network and the water dynamics at a pico-second time scale at the interface are influenced by the surface densities and the kosmotropic properties of ions. An increase of the kosmotropic properties of the ions leads to a decrease of the water dynamics. In the case of SBA-15 (pore size 6.6 nm), the average water properties were extrapolated to the interfacial layer. However, in the case of smaller confinement of MCM-41 (pore size 2.9 - 2.4 nm), the extrapolation did not lead to reasonable results. This was related to the fact, that in the pores of MCM-41 almost no bulk-like water is present in the center of the pores.

Third, we determined that the silica evolution in electrolyte solutions was driven by the density of the pore wall, the pore size and the nature of ions. The reduced dynamics at a pico-second time scale in smaller confinements may result in a supersaturation and can lead to a precipitation of phases, salts or silica phases. In the bigger mesopores of SBA-15 due to the microporosity, in a first step, an alteration layer is formed and the pore size increases when the material is in contact with water and electrolyte solutions, until the silica saturation is reached. This initial step is followed by a diffusive process into the microporosity, where similar recondensation/precipitation processes, as observed in MCM-41, could occur. Such evolutions could arise until the formation of a thermodynamic stable silica phase.

The schematic overview presented in Figure 72 summarizes the achieved tasks within the framework of this thesis and pinpoints the scientific issues that still need to be investigated.

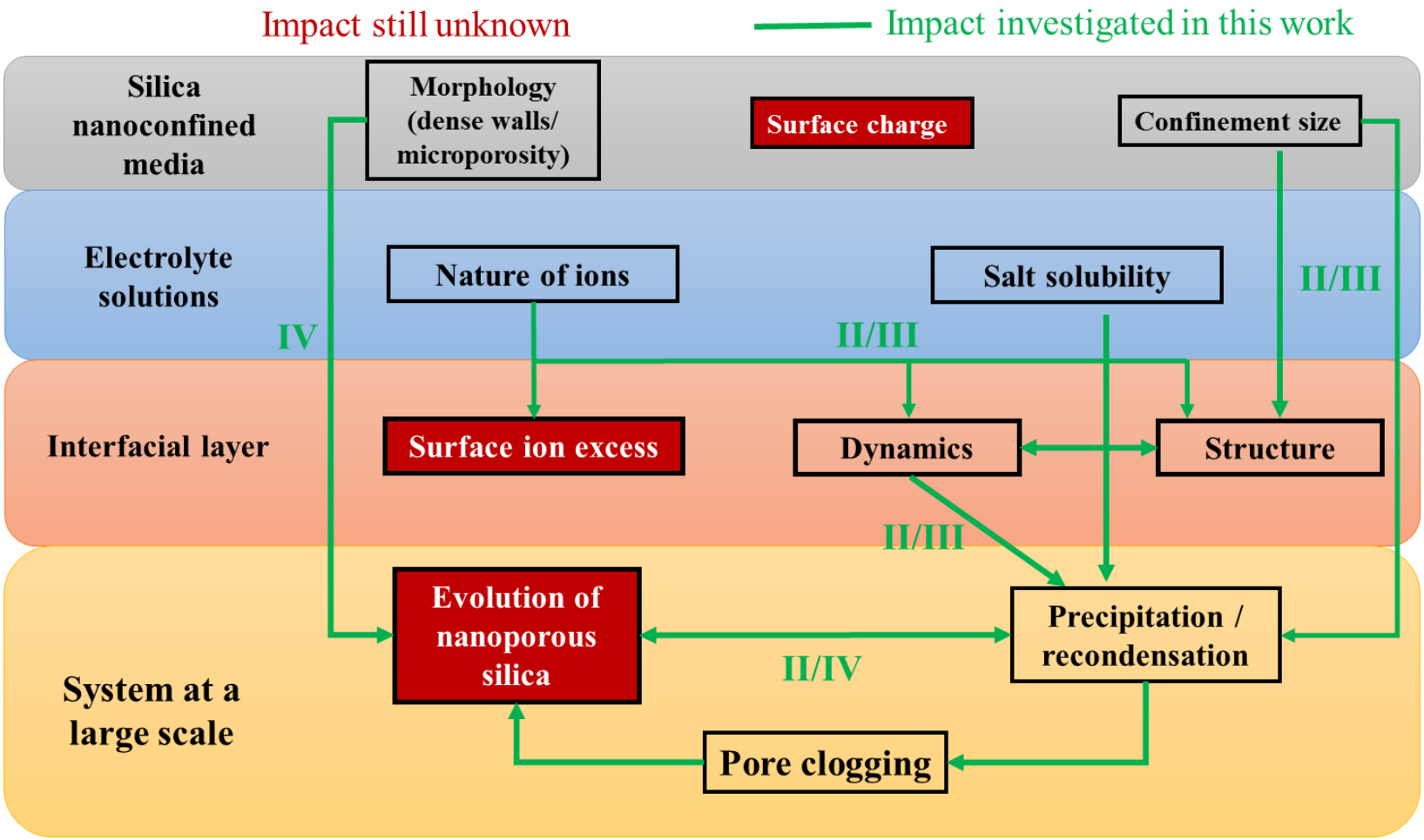


*Figure 72: Schematic overview of the desired tasks and goals in the framework of this PhD thesis. Several perspectives are proposed in order to gain a better understand of processes taking place in the nanoconfinement.*

Regarding the evolution of nanoporous silica at a large scale, several aspects remain unclear and were not studied in this work. First, it is important to clarify if the surface charge of the nanopores depends on the morphology and the density of the silica. The surface charge and therefore the pH value will, for sure, affect the surface ions excess. Since the surface ion excess is related to the water properties in the interfacial layer, this is expected to have a significant impact on the material evolution and the process occurring at the interface. Second, supplementary sizes of confinement (several grafting steps) could improve the understanding of the confinement effect on the water properties. Especially in terms of the properties in the interfacial layer, a stepwise decrease of the pore size can help to figure out how the amount of water in the interfacial layer influences the surface ion excess and therefore the corresponding structure and dynamics. Third, the investigations of various electrolyte solutions with a sufficiently high solubility and at various pH can improve the understanding of the kosmotropic and chaotropic ion effects on the water properties and on a possible precipitation. In this context, it would be interesting to study the impact of counterions and different cation charges (more pronounced effect with respect to the Hofmeister series). Since there is a catalytic ion effect on the dissolution, we expect significant changes on the material evolution. Furthermore, the use of different characterization techniques could be a powerful tool to extend the information on structure, dynamics, ion sorption and material evolution. In this context, nuclear magnetic resonance (NMR) can provide a deeper insight on the structure and interaction of water with the surface groups. $^{29}$Si CPMAS spectra can reveal the progressive dissolution of the silica network. In addition to that, surface-sensitive characterization techniques such as sum-frequency generation spectroscopy can highlight the water structure in the interfacial layer by removing the bulk contribution to the obtained signals. This would dramatically enhance the molecular picture of processes at the interface.

To be more general, similar study could be extended to others types of model nanoporous materials such as $Al_2O_3$, $TiO_2$, $ZrO_2$, $UO_2$ (for spent nuclear fuel dissolution application) and other mixed oxides in order to change the surface energy and determine the processes driving their evolutions in aqueous solutions.

The issues and tasks tackled in this thesis and the corresponding results may help also to enhance the understanding of processes in confinement and open new potentials of application in various fields. First, in the field of effluent decontamination (nuclear or not) using mesoporous materials as membranes, the protection of pore clogging through precipitation of phases could increase the lifetime of membranes and enhance the separation efficiency. Moreover, the results obtained during this work should help to gain a better understanding of the evolution of glass alteration layers and secondary minerals for long-term behavior of high-level nuclear waste. Indeed, the presence of various species in the geological repository (Fe, Ca, Mg, Si dissolved species…), able to penetrate into the glass alteration layer, could modify the processes occurring in the nanoporosity and then, its barrier properties regarding the solution at the equilibrium with the media.

Finally, these data should help to a lesser extend to improve the thermodynamics and rate laws used for the geochemical modelling.

# Annex

## Annex II

As illustrated in Figure 73, the nanochannels depict several layers (Si wafers, native $SiO_2$ layer and channels) and therefore, the measured reflectivity correspond to the reflectivity of all present layers. It is important to note that X-Rays cannot penetrate the surface material, if a certain angle is not exceeded. This angle is called critical angle $\theta_c$ and can be defined as:

$$\theta_c = \sqrt{\frac{\lambda^2 r_e}{\pi}} \rho_e \qquad (40)$$

where $\lambda$ is the wave length of the photons X ($Å^{-1}$), $r_e$ denotes the electron radius (Å) and $\rho_e$ represents the electron density of the layer ($e.Å^{-3}$). Knowing the layer composition, the electron density can be calculated with the following expression:

$$\rho_e = N_a \cdot \varphi_m \frac{\sum_k n_k Z_k}{\sum_k n_k A_k} \qquad (41)$$

where $N_a$ is the number of Avogadro, $\varphi_m$ denotes the mass volume (g. $Å^{-3}$) and $Z_k, A_k$ represent the atomic number and mass of atom *k*.

Figure 73 presents an example for the obtained reflectivity curves as a function of the scattering vector *q*. Before the critical angle $\theta_c$, X-Rays cannot penetrate the materials and the intensity of the reflected beam is equal to the incident beam. After exceeding the critical angle $\theta_c$, X-rays can penetrate the material and the reflected intensity drops with a $q^{-4}$ dependence. The fringes shown in the graph are called Kiessing fringes and correspond to the thickness of the

investigated layer. The decrease of the reflectivity intensity is also dependent on the layer absorption and on the interface roughness.

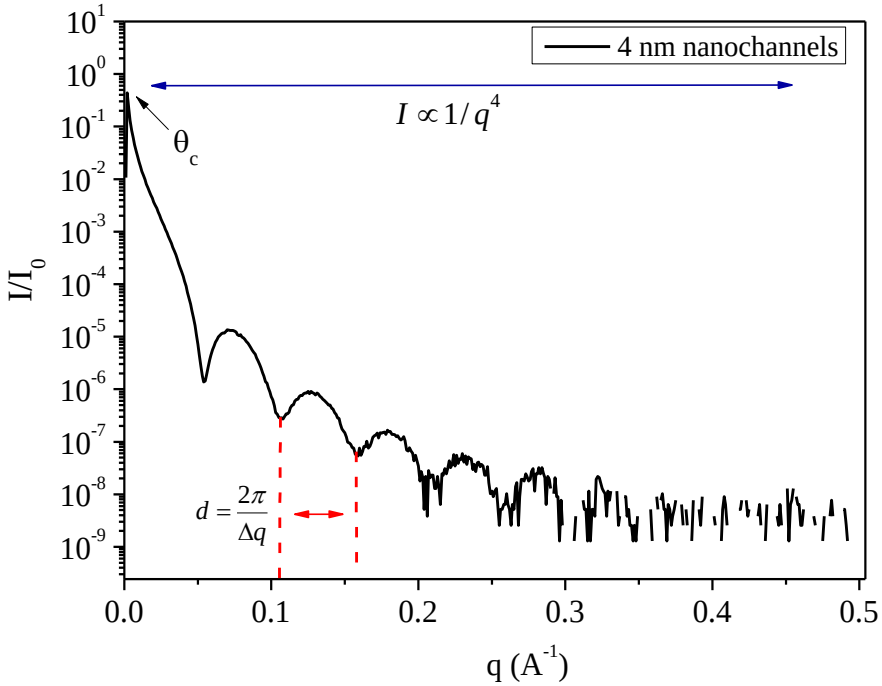


*Figure 73: The experimental measured XRR for 4 nm nanochannels showing the Kiessing fringes which correspond to the confinement size. At q values higher than the critical angle $\theta_c$, the reflected intensity decreases with a $q^{-4}$ dependence.*

The interest of nanochannels is that they provide confinement (i.e. the possibility of interaction between two surfaces) while remaining suitable for studies using surface techniques. The curvature effects are in principle absent in this geometry since the width of the channels is very large compared to their height and the double layer thickness.

The channel geometry is designed to have a top /down symmetry with same oxide on top and bottom. Using reflectometry techniques on such systems allows peculiar data analyses techniques

to be used, far better than the classical fitting procedures. We detail below how the procedure has been used in this thesis.

According to eq. 25 it is impossible from the reflected intensity to deduce the profile $\rho(z)$ since only the magnitude of the scattered amplitude is measured and not the phase.

Inverse Fourier transform cannot be performed since the phase of the scattered signal is unknown. This is a general statement in x-ray scattering, and solving the "phase problem" is at the heart of crystallography.

The assumption that the profile is symmetrical makes things different. The Fourier transform of an even function is real so that the unknown phase of the reflected intensity can take only the 0 or Pi value, the phase problem amounts to finding the sign of the amplitude signal. This sign can change at any point on the reflectivity curves, but the continuity of the reflectivity from experimental profiles ensures this sign can only change when the amplitude comes close to zero, i.e. close to interference minima. We show below how the procedure has been applied to real profiles, as e.g. the signal from water filled the 5 nm nanochannels (see Figure 74).

The reflectivity signal is shown below $Rq^4(q)$ as a function of $q$.

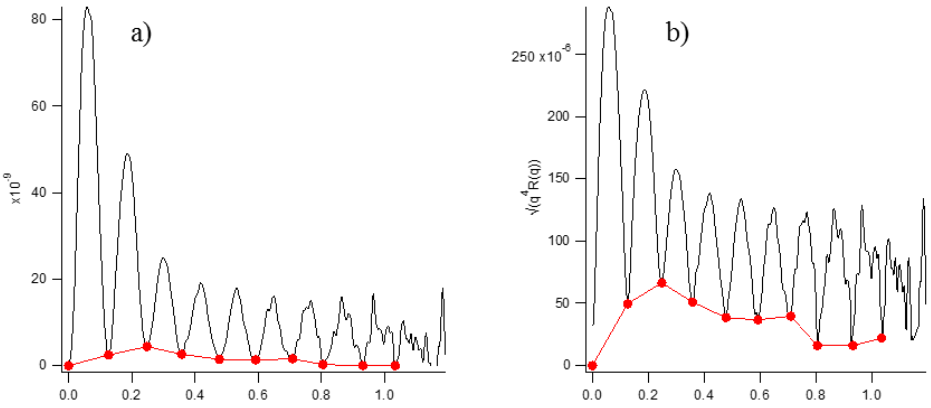


*Figure 74: XRR signal as a function of q. The continuity of the reflectivity from experimental profiles ensures this sign can only change when the amplitude comes close to zero. The minima intensity can differ slightly from zero and therefore, our assumption of symmetry is not strictly correct.*

Once the curve is obtained, possible points for sign inversion can only be fringe minima, which are easily and automatically located. We can see that the minima intensity can differ slightly from zero. This indicates probably that our assumption of a symmetric profile with cover and bottom of channels identical is not strictly correct and the bonding interface may be different from the bottom silicon/silicon oxide interface. However, let us assume the red point are close to zero and take the square root of the curve (Figure 74 b).

This non-zero background can be subtracted and then the sign allocation can be done changing sign at each oscillation. Finally, the reflected amplitude can be obtained, in the shape of a signed oscillating curve, as presented in Figure 75.

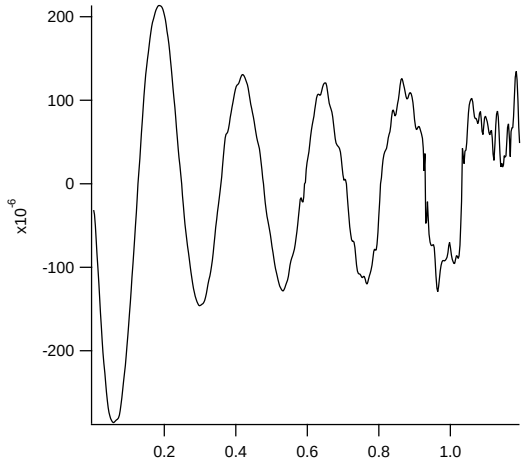


*Figure 75: The shape of a signed oscillating curve, which allows to obtain a reflected amplitude.*

This curve can be Inverse Fourier transformed to yield an electron density profile, with no other assumptions.

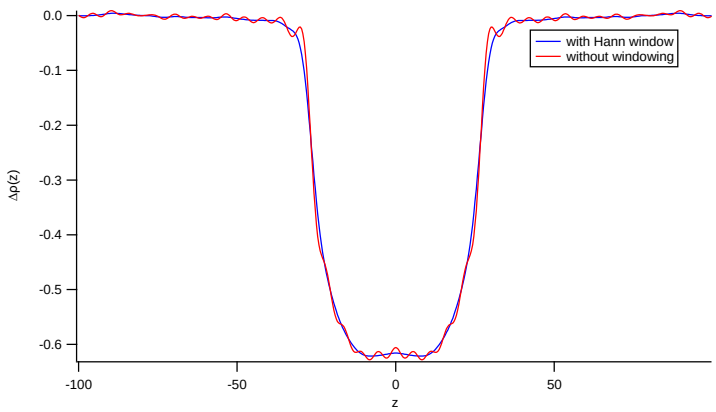


*Figure 76: The application of a Hann/Hamming windowing treatment on the obtained electron density profile to smoothen the oscillations.*

When performed directly, the inverse Fourier transform shows oscillations due to the finite sampling range up to q = 1.2 $Å^{-1}$, giving a $2\pi/q_{max}$ = 5 Å period. This period is not physical and can

classically be removed applying a windowing (for instance: Hann, Hamming) on the experimental data. As shown in Figure 76, with this treatment the windowing oscillations disappear.

Finally, similar results can be obtained using the classical trial and error procedure, describing the profile by a 2-box model. The model used can be inferred from the results of the direct inversion.

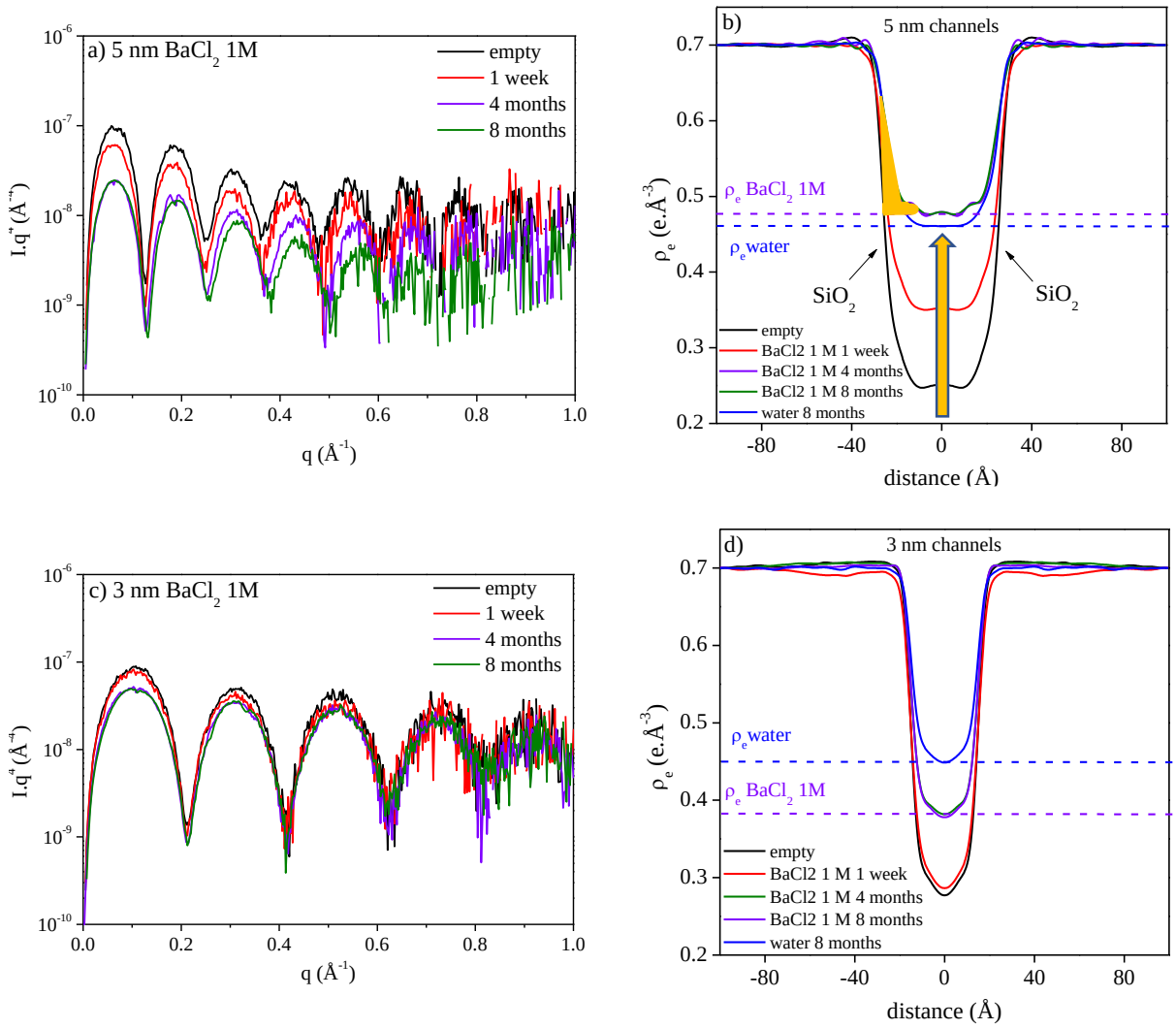


*Figure 77: Experimental reflectivity curves (NB: log scale) and associated electron density profiles obtained from the measurements of 5 nm and for 3 nm nanochannels filled with $XCl_2$ at 1 M.*

The yellow colored integral shown in Figure 4 (b) was determined and used to calculate the surface ion excess $d_i$ using the following equation:

$$d_i = \frac{\int_0^l (\rho_{eXRR} - \rho_{eXRRCenter}) dz}{0.33Z_X + 0.66Z_{Cl}} \quad (42)$$

# Annex III

FTIR-ATR spectra of bulk electrolyte solutions and solutions confined in SBA-15, MCM-41 and MCM-41-1.

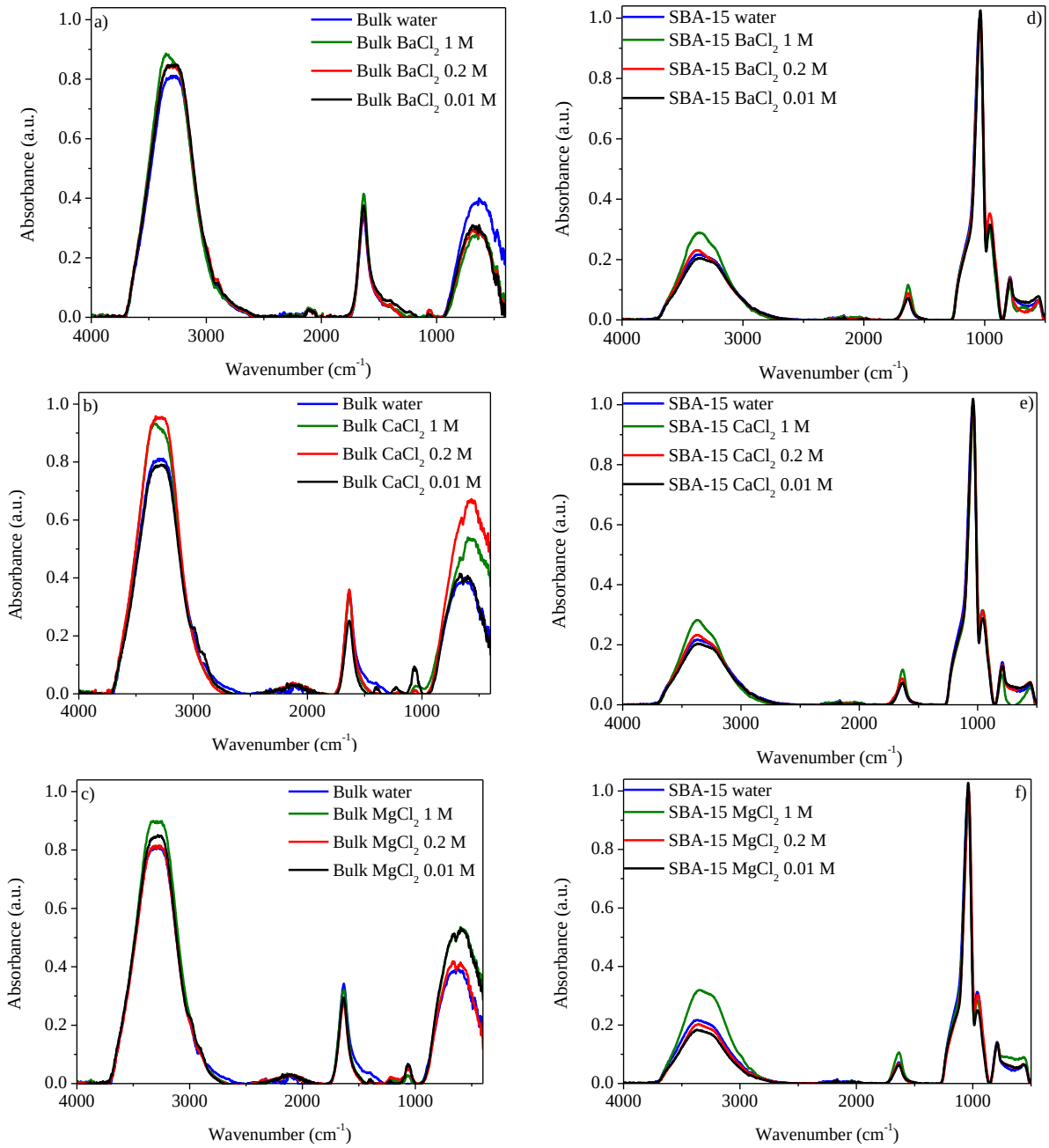


*Figure 78* ***(a) to (f):*** *Experimental ATR-FTIR spectra of bulk solutions and SBA-15 filled with water and electrolyte solution at various concentrations.*

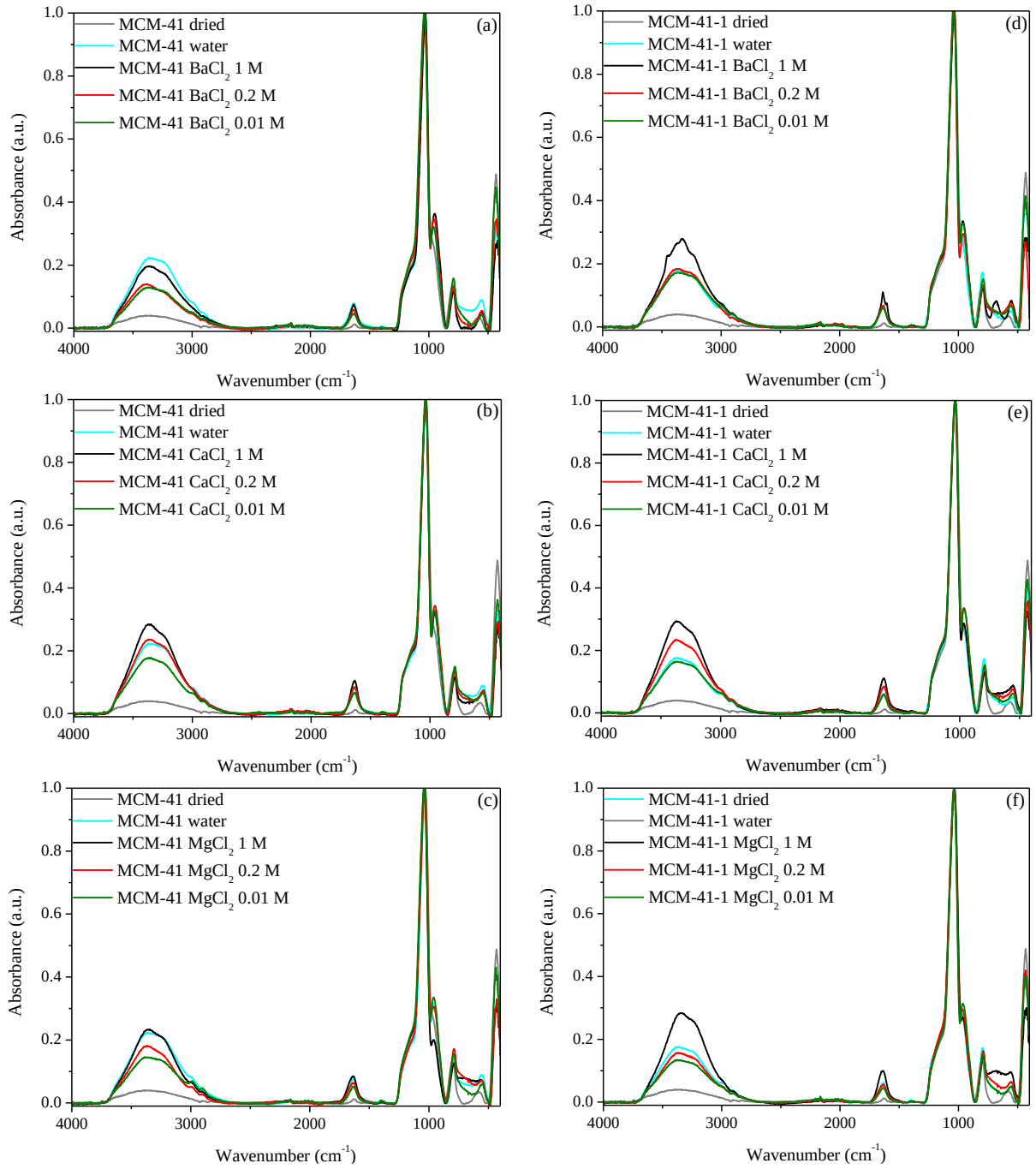


*Figure 79* ***(a) to (f):*** *Experimental ATR-FTIR spectra of MCM-41 and MCM-41-1 filled with water and electrolyte solution at various concentrations.*

**Preliminary approach to estimate the amount of interfacial water**

In order to estimate the amount of interfacial water inside the pore of highly ordered mesoporous silica we performed differential scanning calorimetry measurements. For this calculation, we start with the Kelvin equation describing the capillary condensation of a liquid from an under saturated vapor:

$$r = -\frac{\gamma_{LV} v_M}{kTln\left[\frac{p}{p_0}\right]} \qquad (43)$$

where $\gamma_{lv}$ represents the surface tension across a curved liquid-vapor interface, $\frac{p}{p_0}$ is the pressure difference, r is the radius of curvature and $v_M$ is the molecular volume of the liquid. It is worth to note that the radius of curvature is defined negative when the contact angle Θ of the liquid on the surface of the pores is less than 90°. For convex droplets (radius positive), there is a minimum size below which condensed droplets are unstable.

Using the Young equation $\gamma_{SV} = \gamma_{SL} + \gamma_{LV} cos\theta$

where $\gamma_{sv}$ is the surface tension of the solid-vapor interface and $\gamma_{sl}$ is the surface tension of the solid-liquid interface one derives[93]:

$$H = -\frac{2v_m[\gamma_{SV} - \gamma_{SL}]}{kTln[\frac{p}{p_0}]} \qquad (44)$$

with H being an infinite slit of width H. If the liquid wets the surface in the presence of a solid, the liquid is thermodynamically favored in confinement. Assuming that pressure effects are only small, we consider a reducing melting point.

The melting temperatures of water confined in different types of cylindrical mesopores (series of MCM-41 and SBA-15) were measured. Depending on the confinement and pore sizes (2.3 – 6.6 nm), we could observe a shift of the melting temperature of water. Figure 80 displays the peak minima for several materials as a function of temperature. Generally, one can state the smaller the pore size the lower the melting temperature of water and the smaller the pore size the lowering becomes greater.

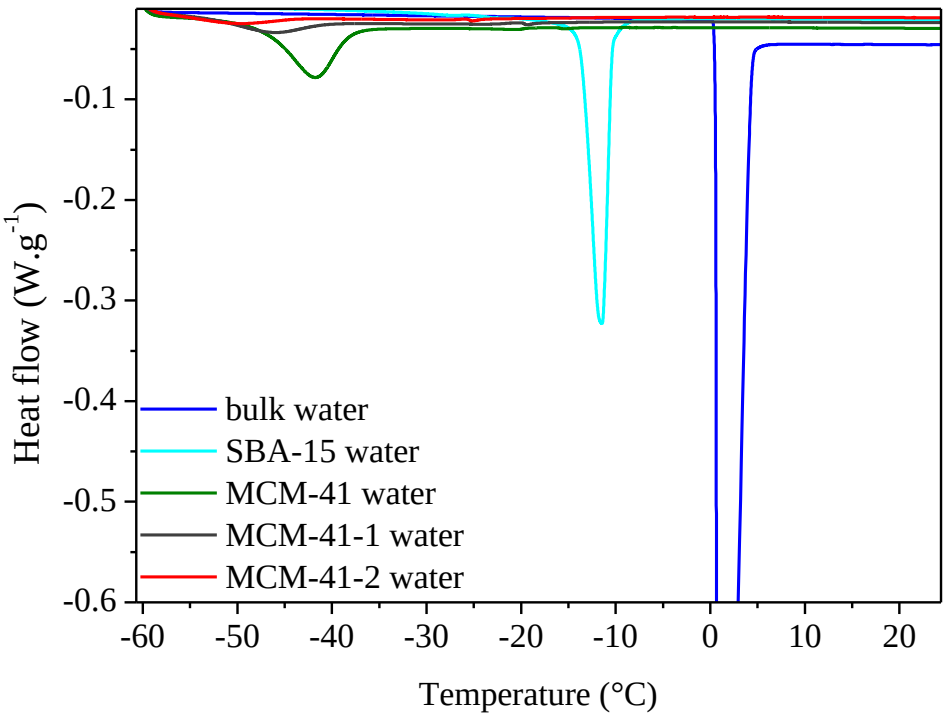


*Figure 80: The shift of the melting temperature of water confined in several types of MCM-41 and in SBA-15.*

The pore-size dependence of $\Delta T_m(R)$ is more pronounced for smaller pore sizes, but becomes much shallower for larger ones.

During the freezing process, there is a coexistence of solid and liquid phases inside the pores. Since the pore radius and the pressure remain the same during the phase transition the shift of the phase transition temperature can be expressed by the Gibbs-Thomson equation[84,92]:

$$T_p(R) - T_0 = -\frac{C_{GT}}{R} \; with \; C_{GT} = \frac{2T_0(\gamma_{sv} - \gamma_{lv})V}{\Delta h_{sl}} \qquad (45)$$

Where $T_p$ and $T_0$ denotes the solid-liquid coexistence temperature in the pore and in the bulk solution, respectively, and $C_{GT}$ is the Gibbs-Thomson constant, $R$ stands for the pore radius, $\gamma_{lv}$ and $\gamma_{sl}$ represent the surface energies per unit area of the interface wall/solid and wall/liquid, $\Delta h_{sl}$ is the melting enthalpy and $V$ is the volume of the liquid phase or the solid phase. The last contribution is depending whether the solid or the liquid has the lower surface free energies against the wall. The equation above can be rewritten using Young's equation:

$$\gamma_{WS} - \gamma_{WL} = \gamma_{SL} \cos\theta \qquad (46)$$

Where $\gamma_{SL}$ is the interfacial free energy of ice and water, and $\theta$ is the contact angle formed by water/ice interface with the wall. In the adapted equation there are rising two different cases for wetting the cylindrical pore. The contact angle can either be positive ($\theta < 90°$) leading to elevation of the melting temperature or negative ($\theta > 90°$) which would lead to a depression. Due to the fact, that liquids can adapt better to pore walls than solids the second case is more common.

Considering the wetting process inside the pore, one can distinguish two different cases. On the one hand, there can be a partial wetting process, which means there is a weak preference of the wall for the liquid ($\theta < 90°$). On the other hand, there can be a complete wetting case ($\theta = 0°$), in which the wall shows a strong preference for the liquid. In the second case, a liquid-like layer starts to form at the solid/wall interface at temperatures below $T_p$. In the Gibbs-Thomson relation, such a premelted layer is not accounted. Figure 81 shows the depression of the melting temperature as a function of the pore size.

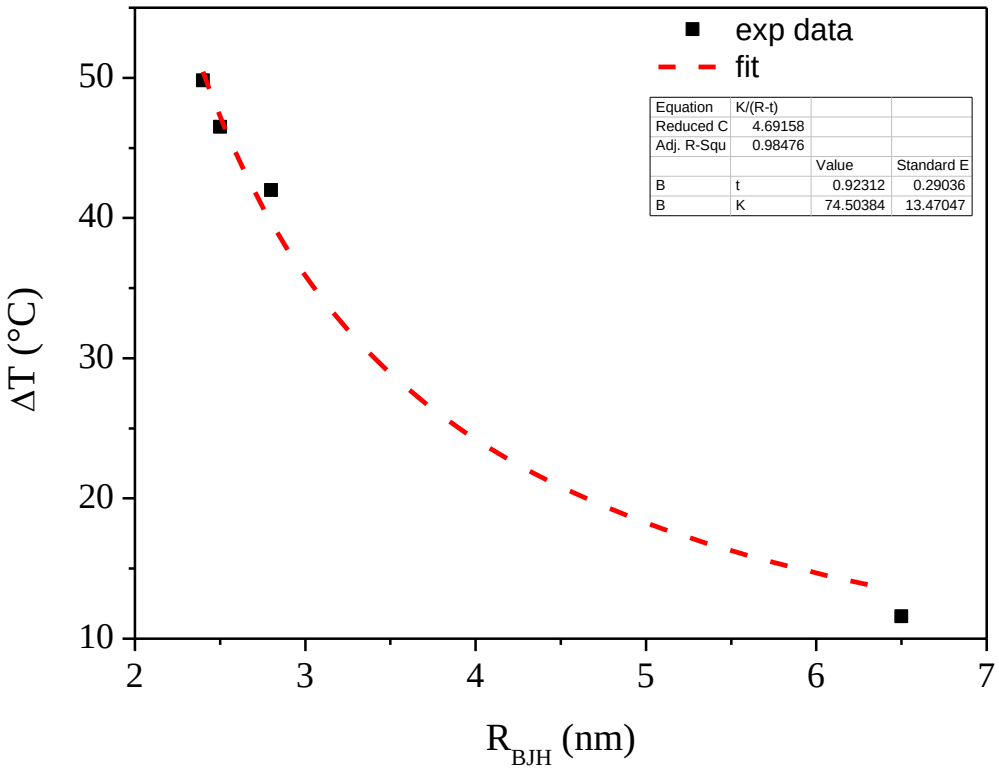


*Figure 81: Shift of melting temperature of water confined in several types of MCM-41 and in SBA-15 as a function of the pore size radius R. Melting temperatures in the pores are defined by the respective peak minimum temperature obtained by DSC measurements. Fitting was done using the adapted Gibbs-Thompson equation.*

The curve can be fitted using an adapted Gibbs-Thompson relation considering a liquid-like layer at the pore surface of thickness *t*:

$$\Delta T_p(R) = \frac{C_{GT}}{R - t} \qquad (47)$$

With $C$ = 74.5 K.nm and $t$ = 0.9 nm. The resulting value of $t$ corresponds to ca. three monolayer of water which is in good accordance with experimental and modelling values in the literature.[92] Due to the interaction with the pore surface, we can assume a liquid-like layer at the pore surface. The interactions perturb the water structure and hindering the crystallization. Knowing the thickness of the non-freezable water layer, we can estimate the amount of interfacial water in SBA-15 which was found to be around 47 %. This value was taken into account for the decomposition of the O-H stretching band of water confined in SBA-15. Moreover, we used the fraction for the calculation of the water properties within the interfacial water layer.

The widely used Gibbs-Thompson equation to determine the amount of water molecules under the influence of the pore surface is only applicable for pores having a size bigger than 3 nm. Previous studies have shown that the shift of the melting temperature depression for pores below 3 nm cannot be satisfactorily be fitted using the GT equation.[91,178–180] Therefore, in the case of MCM-41 and MCM-41-1, we assumed three monolayers of water in the interfacial layer, resulting to 15 % and 10 % of bulk water, respectively. Since the decomposition with these values of bulk water lead to non-satisfying results, we assumed two layers of water molecules resulting in 35 % and 30 % of bulk water, which is still in good agreement with the values found in the literature.[92,181]

## Decomposition of O-H stretching band in Infrared Spectroscopy

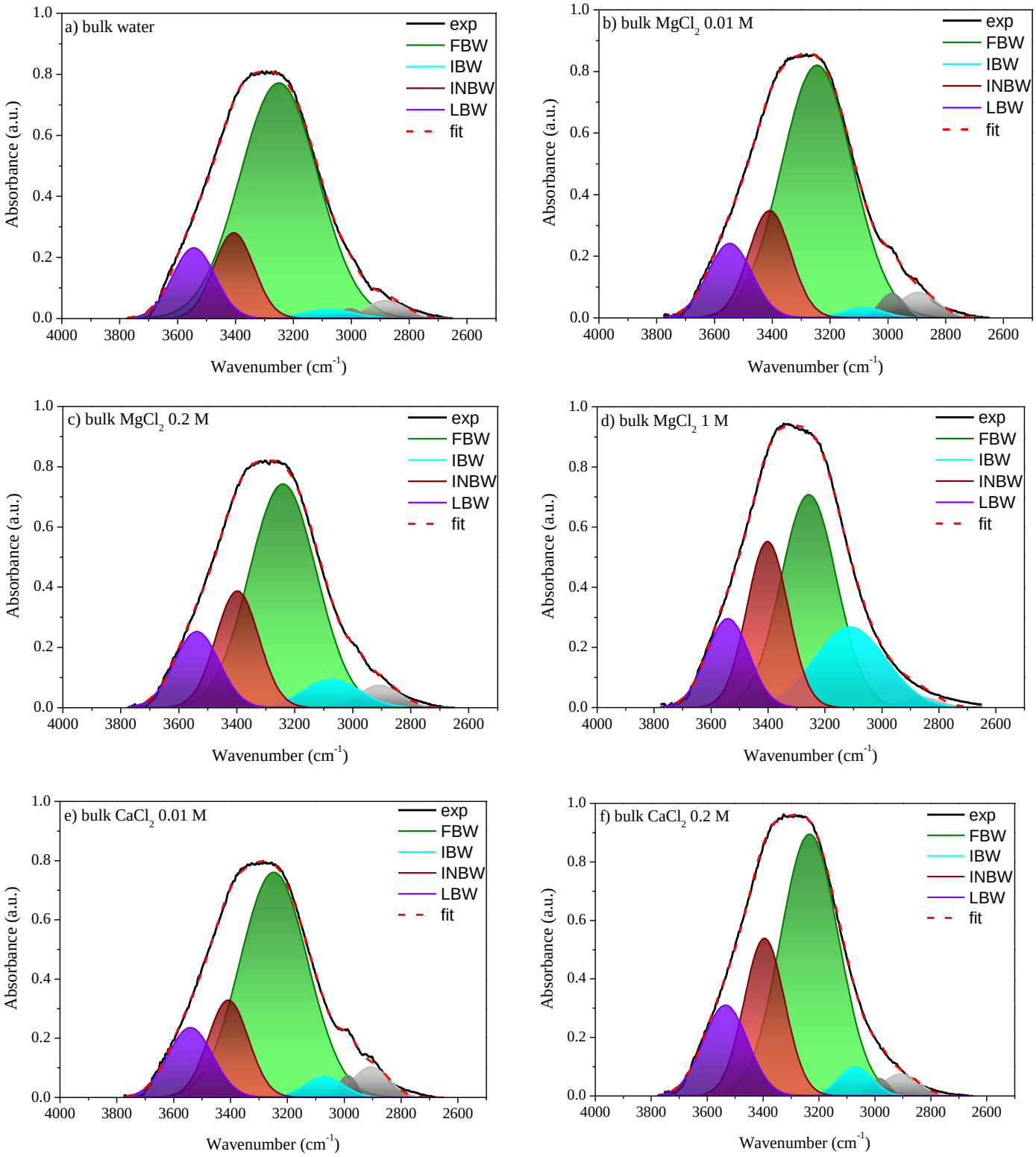

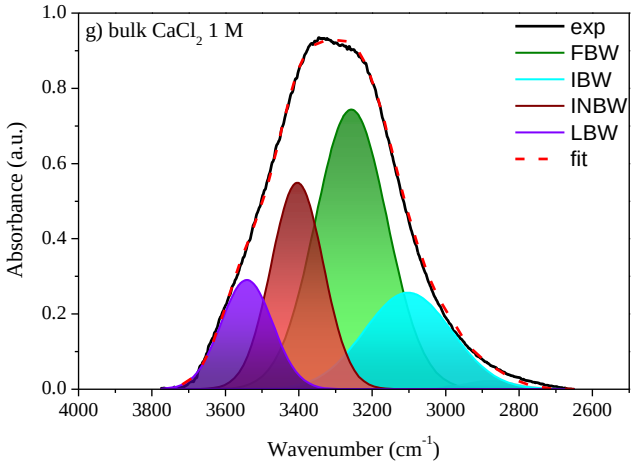
g) bulk CaCl2 1 M
exp
FBW
IBW
INBW
LBW
fit
Absorbance (a.u.)
Wavenumber (cm-1)

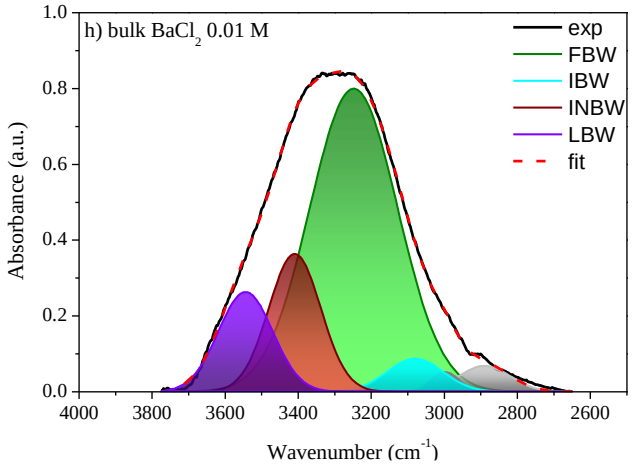
h) bulk BaCl2 0.01 M
exp
FBW
IBW
INBW
LBW
fit
Absorbance (a.u.)
Wavenumber (cm-1)

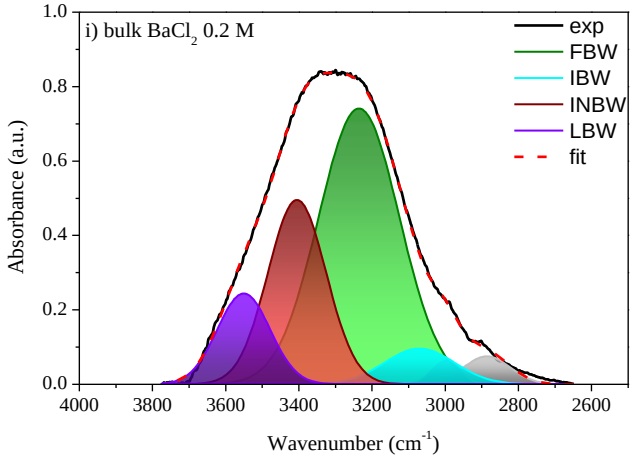
i) bulk BaCl2 0.2 M
exp
FBW
IBW
INBW
LBW
fit
Absorbance (a.u.)
Wavenumber (cm-1)

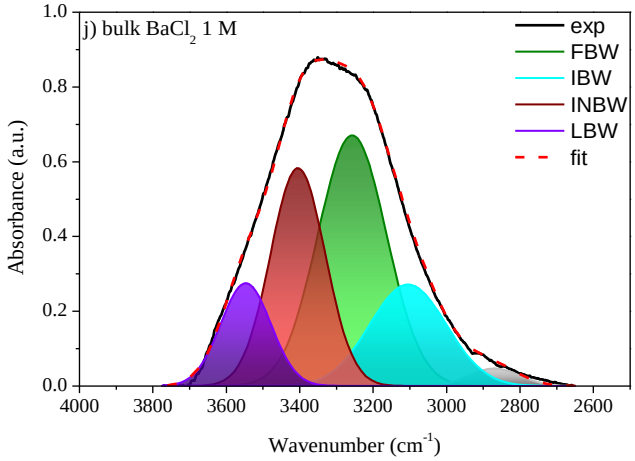
j) bulk BaCl2 1 M
exp
FBW
IBW
INBW
LBW
fit
Absorbance (a.u.)
Wavenumber (cm-1)

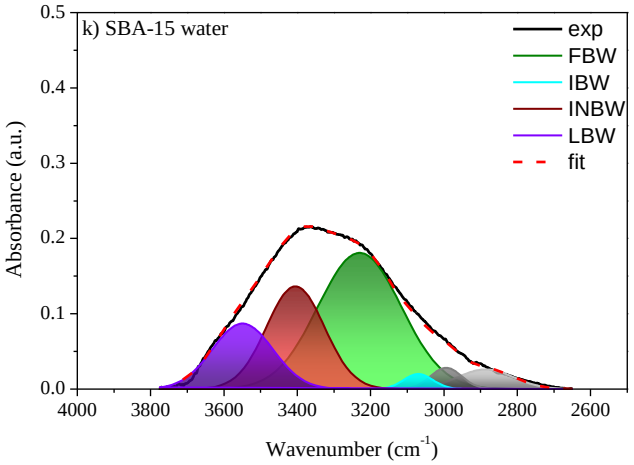
k) SBA-15 water
exp
FBW
IBW
INBW
LBW
fit
Absorbance (a.u.)
Wavenumber (cm-1)

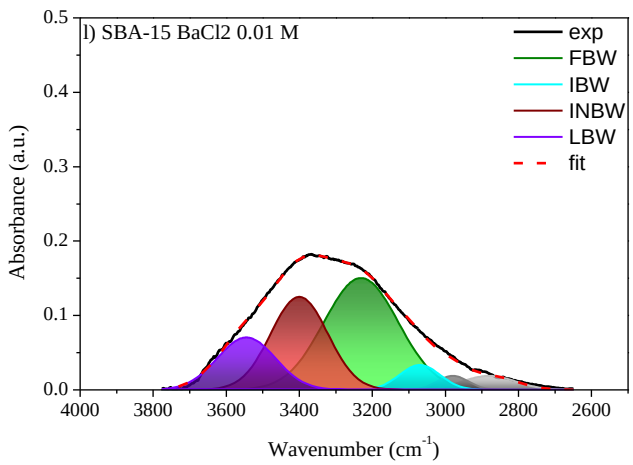
l) SBA-15 BaCl2 0.01 M
exp
FBW
IBW
INBW
LBW
fit
Absorbance (a.u.)
Wavenumber (cm-1)

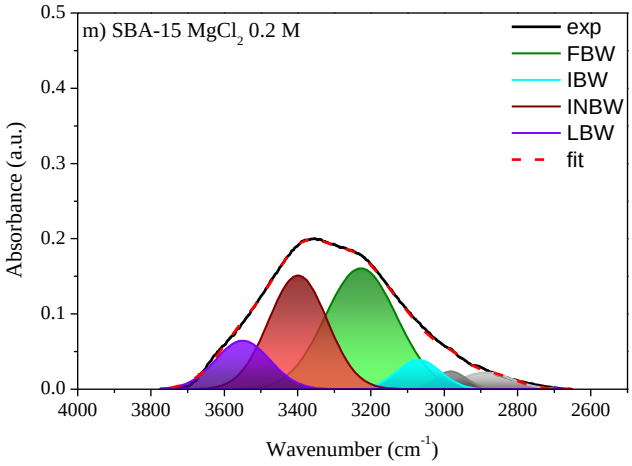
m) SBA-15 MgCl2 0.2 M
exp
FBW
IBW
INBW
LBW
fit
Absorbance (a.u.)
Wavenumber (cm-1)

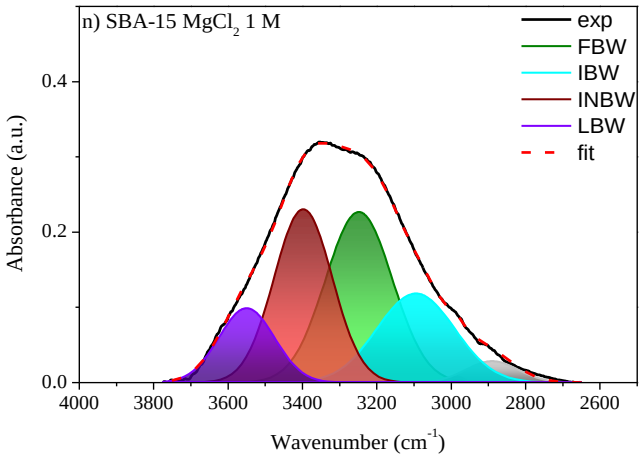
n) SBA-15 MgCl2 1 M
exp
FBW
IBW
INBW
LBW
fit
Absorbance (a.u.)
Wavenumber (cm-1)

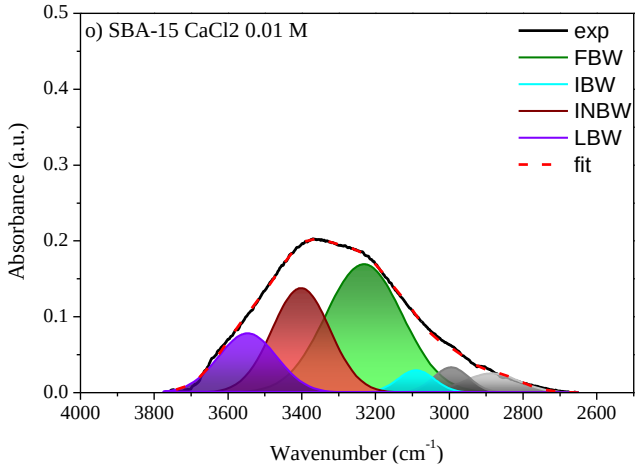
o) SBA-15 CaCl2 0.01 M
exp
FBW
IBW
INBW
LBW
fit
Absorbance (a.u.)
Wavenumber (cm-1)

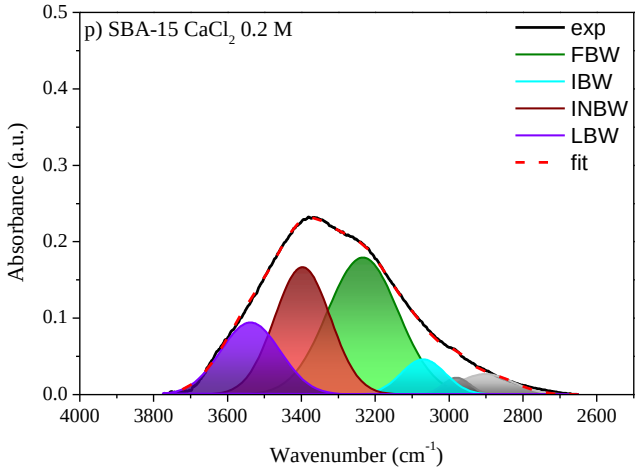
p) SBA-15 CaCl2 0.2 M
exp
FBW
IBW
INBW
LBW
fit
Absorbance (a.u.)
Wavenumber (cm-1)

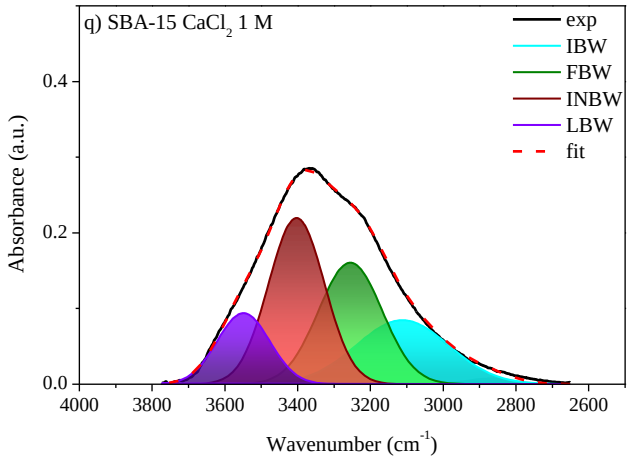
q) SBA-15 CaCl2 1 M
exp
IBW
FBW
INBW
LBW
fit
Absorbance (a.u.)
Wavenumber (cm-1)

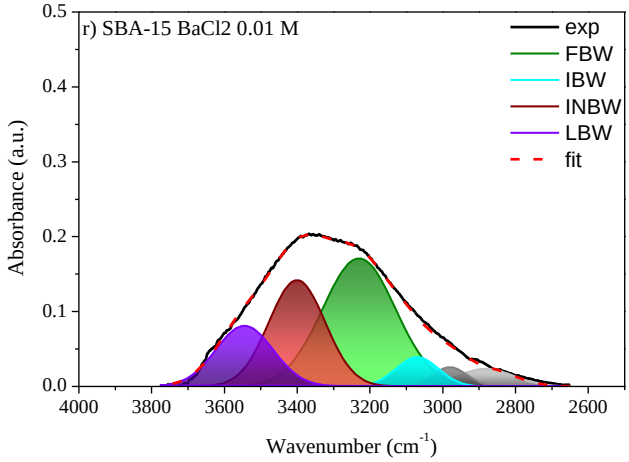
r) SBA-15 BaCl2 0.01 M
exp
FBW
IBW
INBW
LBW
fit
Absorbance (a.u.)
Wavenumber (cm-1)

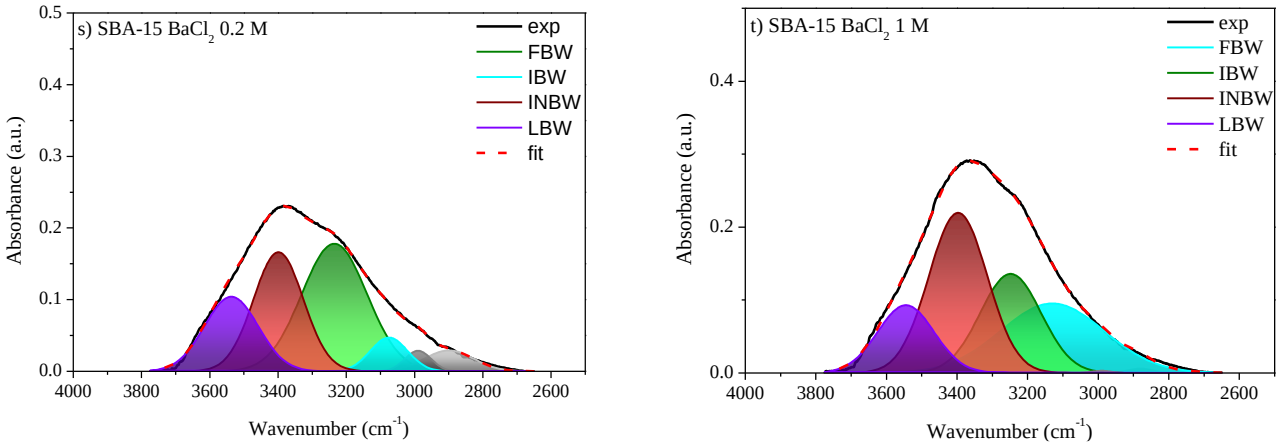


*Figure 82* ***(a) to (t):*** *Decomposition of the vOH band between 2650 and 3775 $cm^{-1}$ of bulk and electrolyte solutions confined in SBA-15.*

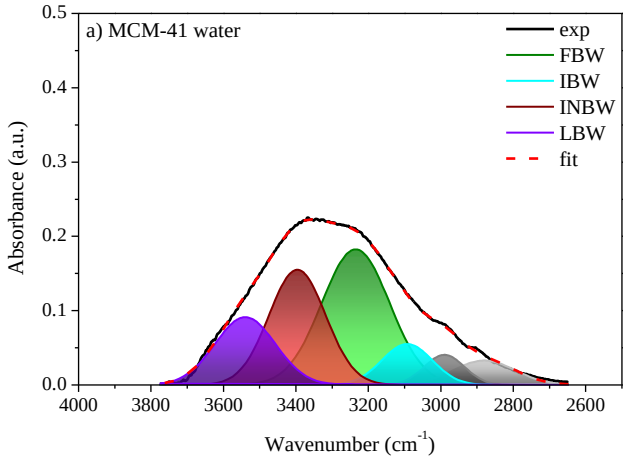
a) MCM-41 water
exp
FBW
IBW
INBW
LBW
fit
Absorbance (a.u.)
Wavenumber (cm-1)

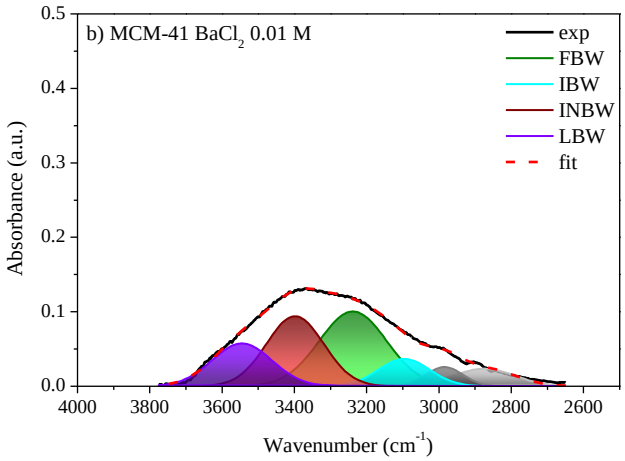
b) MCM-41 BaCl2 0.01 M
exp
FBW
IBW
INBW
LBW
fit
Absorbance (a.u.)
Wavenumber (cm-1)

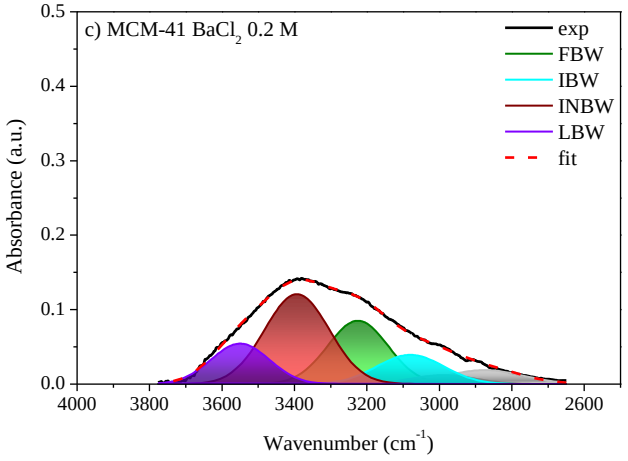
c) MCM-41 BaCl2 0.2 M
exp
FBW
IBW
INBW
LBW
fit
Absorbance (a.u.)
Wavenumber (cm-1)

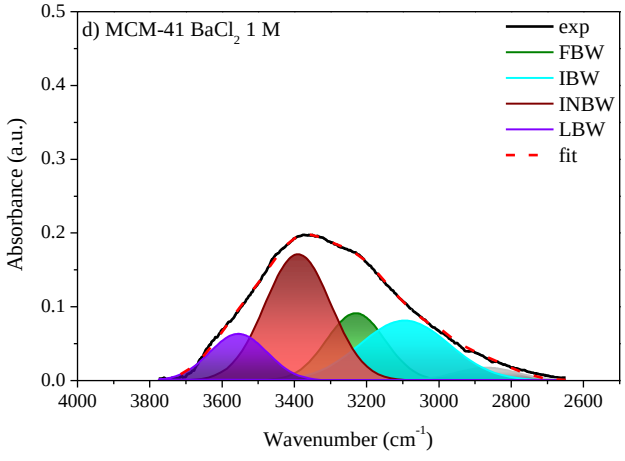
d) MCM-41 BaCl2 1 M
exp
FBW
IBW
INBW
LBW
fit
Absorbance (a.u.)
Wavenumber (cm-1)

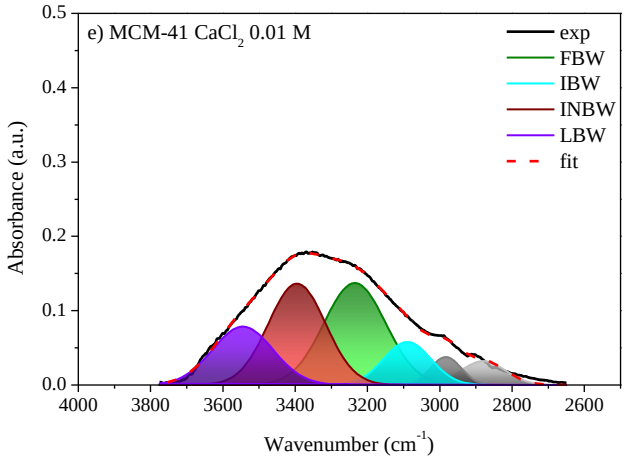
e) MCM-41 CaCl2 0.01 M
exp
FBW
IBW
INBW
LBW
fit
Absorbance (a.u.)
Wavenumber (cm-1)

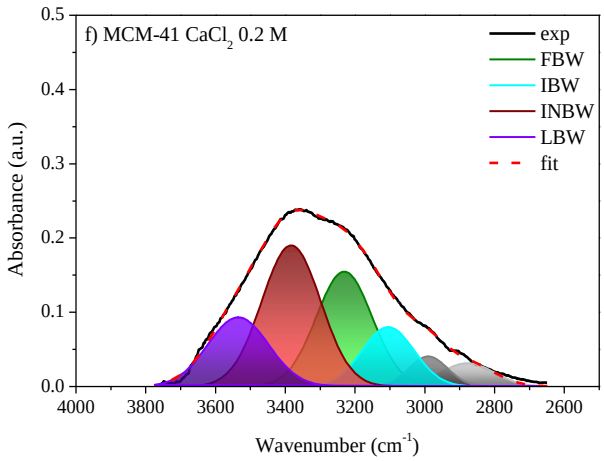
f) MCM-41 CaCl2 0.2 M
exp
FBW
IBW
INBW
LBW
fit
Absorbance (a.u.)
Wavenumber (cm-1)

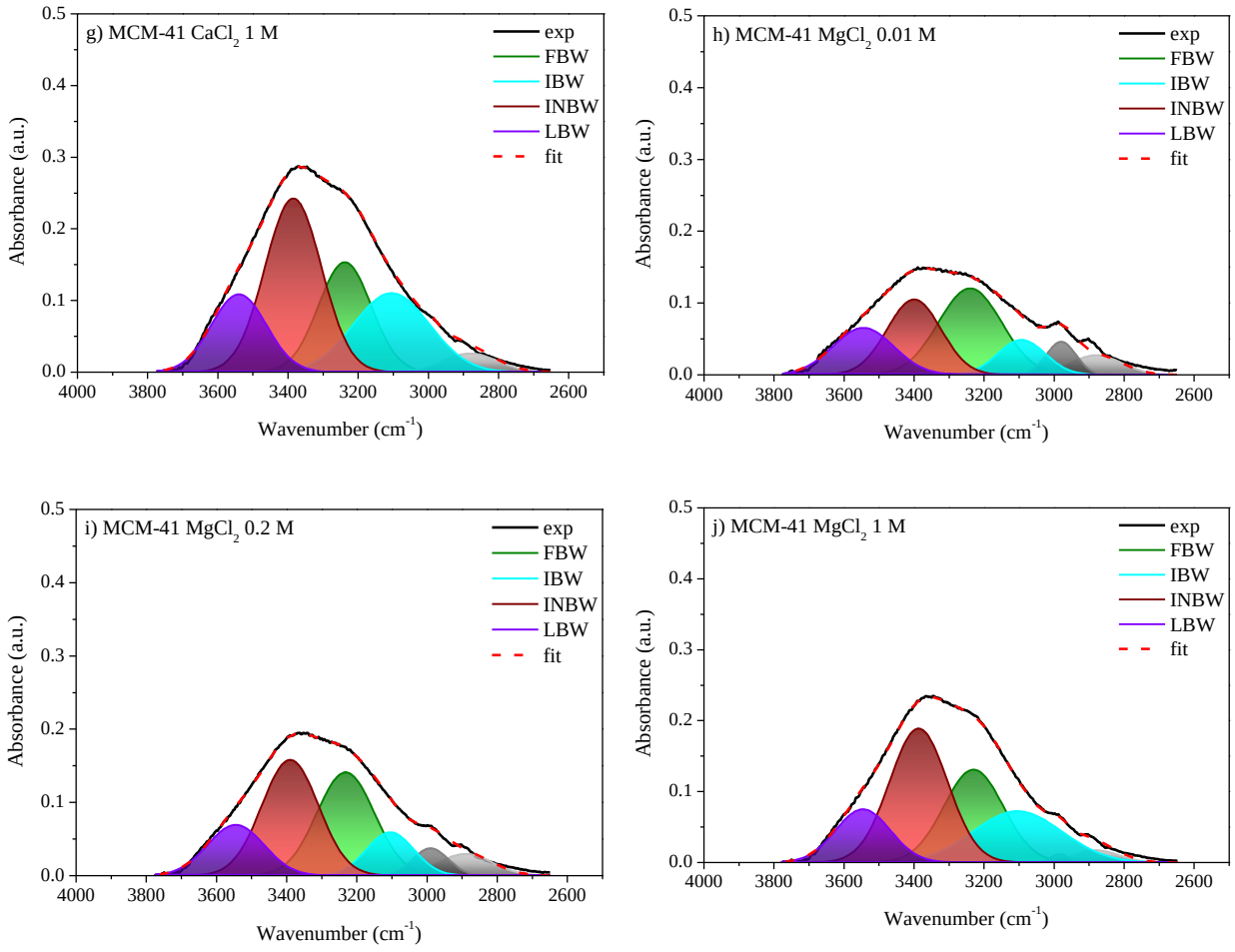


*Figure 83 (a)-(j): Decomposition of the vOH band between 2650 and 3775 $cm^{-1}$ of electrolyte solutions confined in MCM-41.*

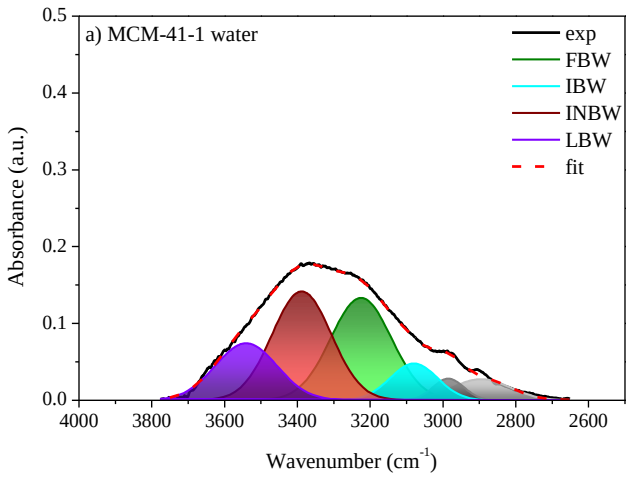
a) MCM-41-1 water
exp
FBW
IBW
INBW
LBW
fit
Absorbance (a.u.)
Wavenumber (cm-1)

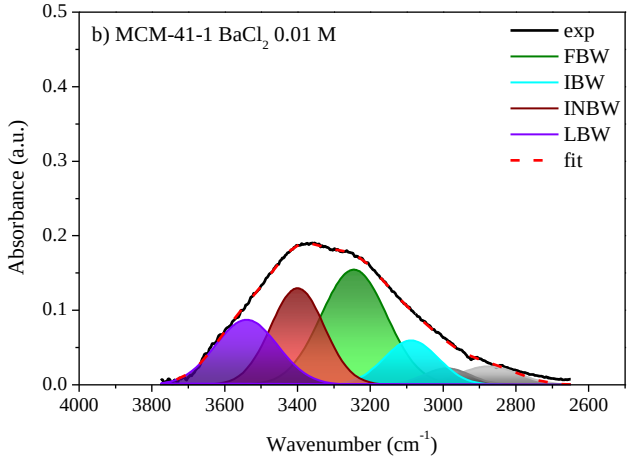
b) MCM-41-1 BaCl2 0.01 M
exp
FBW
IBW
INBW
LBW
fit
Absorbance (a.u.)
Wavenumber (cm-1)

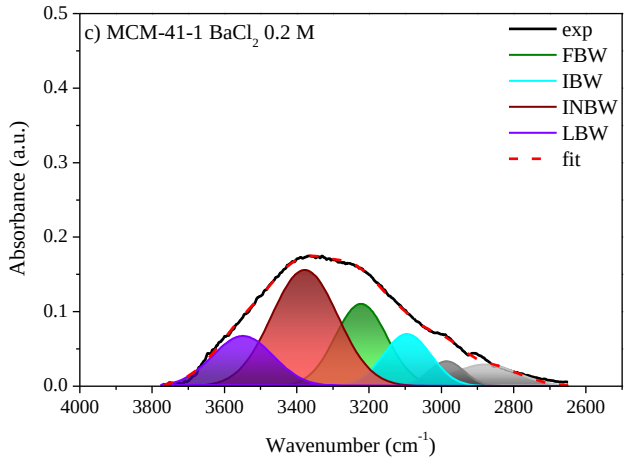
c) MCM-41-1 BaCl2 0.2 M
exp
FBW
IBW
INBW
LBW
fit
Absorbance (a.u.)
Wavenumber (cm-1)

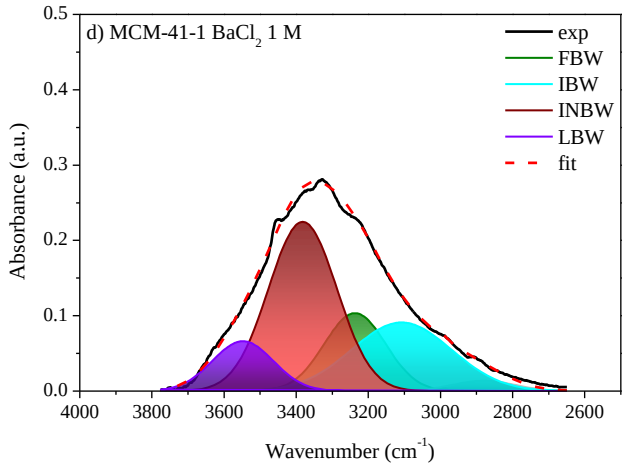
d) MCM-41-1 BaCl2 1 M
exp
FBW
IBW
INBW
LBW
fit
Absorbance (a.u.)
Wavenumber (cm-1)

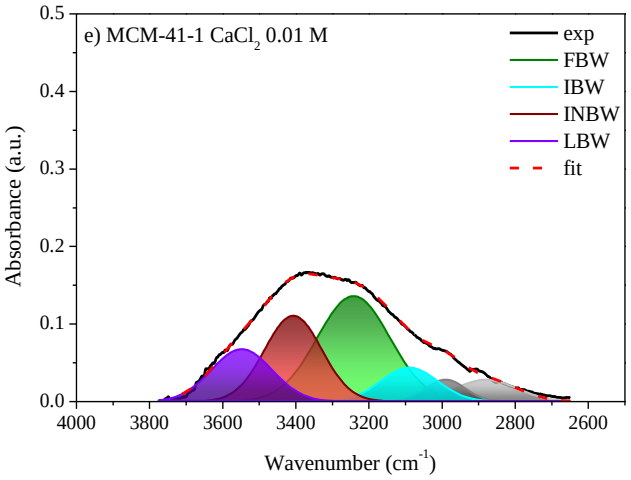
e) MCM-41-1 CaCl2 0.01 M
exp
FBW
IBW
INBW
LBW
fit
Absorbance (a.u.)
Wavenumber (cm-1)

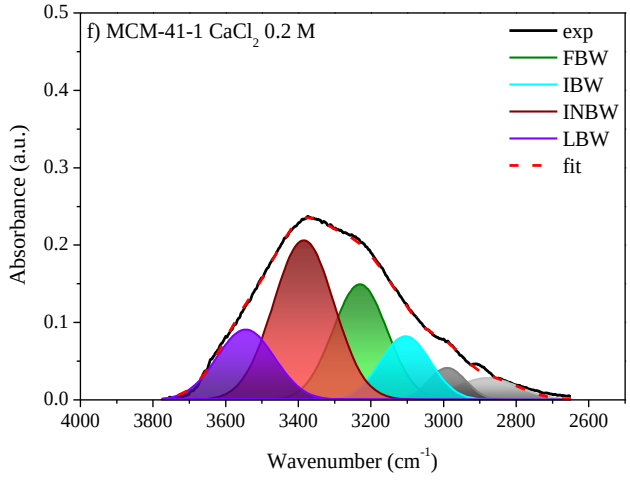
f) MCM-41-1 CaCl2 0.2 M
exp
FBW
IBW
INBW
LBW
fit
Absorbance (a.u.)
Wavenumber (cm-1)

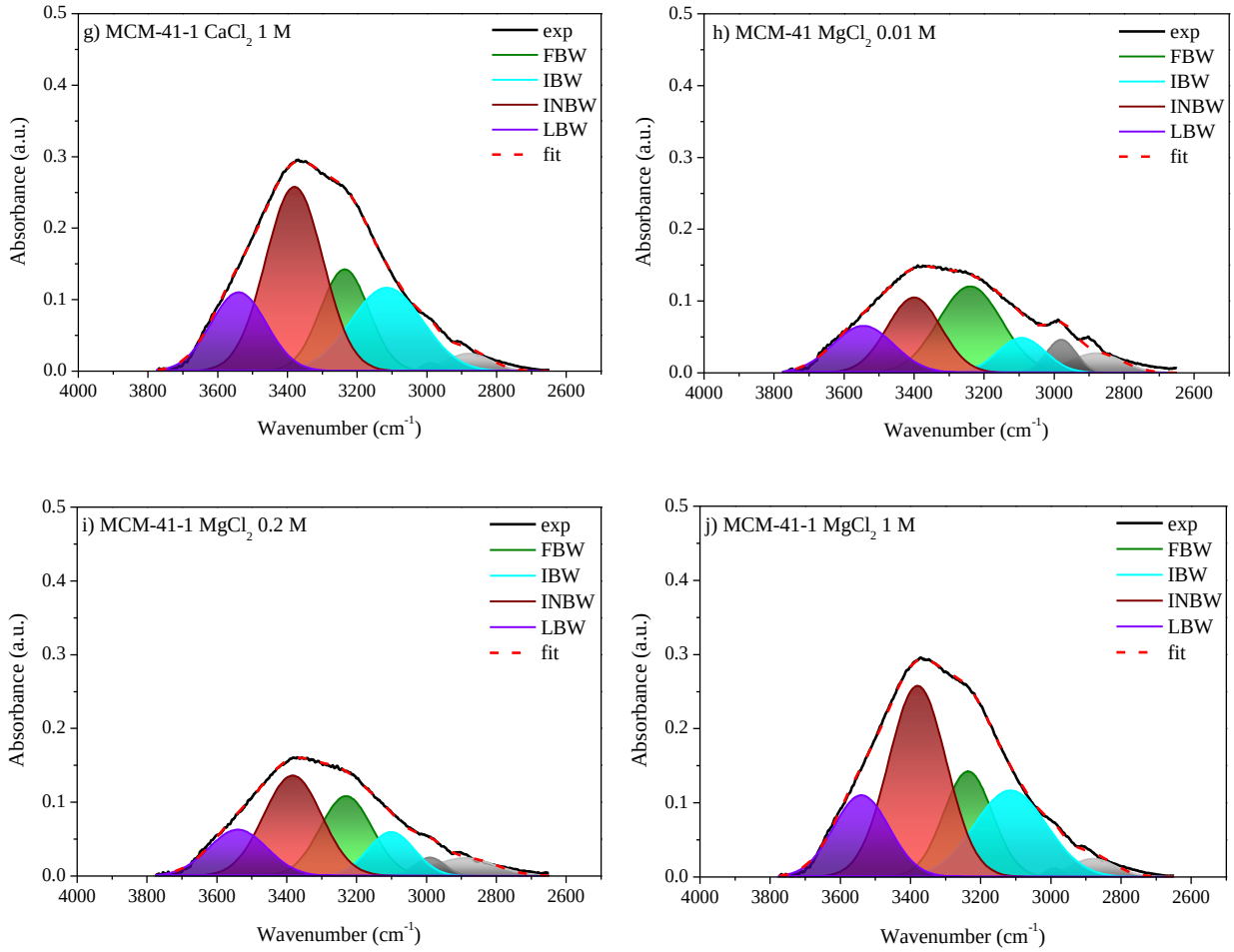


*Figure 84 (a)-(j): Decomposition of the vOH band between 2650 and 3775 $cm^{-1}$ of electrolyte solutions confined in MCM-41-1.*

In some cases, we added two peaks at 2900 and 2990 $cm^{-1}$ to include the C-H vibrations coming from contamination of the spectrometer diamond. The contributions of these two peaks do not exceed 5 % and 4 % of the relative band area, respectively.

The best-fit parameters (center frequencies ω, intensity I and half width at half maxima Γ) of O–H stretching band for bulk water, bulk electrolyte solutions and solutions confined in SBA-15 are summarized in Table SI2.

***Table SI2:*** Best-fit parameters (center frequencies ω, intensity I and half width at half maxima Γ) of O–H stretching band for bulk water, bulk electrolyte solutions and solutions confined in SBA-15, MCM-41 and grafted MCM-41.

| **bulk water** | | | | | | | | | | | |
|---|---|---|---|---|---|---|---|---|---|---|---|
| $\omega_1$ | $I_1$ | $\Gamma_1$ | $\omega_2$ | $I_2$ | $\Gamma_2$ | $\omega_3$ | $I_3$ | $\Gamma_3$ | $\omega_4$ | $I_4$ | $\Gamma_4$ |
| **3080** | 16.7 | 179.2 | **3248** | 241.2 | 283.2 | **3409** | 64.9 | 167.8 | **3544** | 49.1 | 175.2 |
| **bulk $BaCl_2$ 0.01 M** | | | | | | | | | | | |
| **3080** | 16.7 | 182.3 | **3248** | 241.3 | 283.2 | **3409** | 65.0 | 167.8 | **3544** | 49.1 | 175.2 |
| **bulk $BaCl_2$ 0.2 M** | | | | | | | | | | | |
| **3079** | 23.2 | 225.1 | **3235** | 205.1 | 259.8 | **3405** | 98.6 | 187.1 | **3550** | 44.1 | 170.0 |
| **bulk $BaCl_2$ 1 M** | | | | | | | | | | | |
| **3110** | 99.1 | 273.1 | **3257** | 180.2 | 255.0 | **3403** | 113.8 | 177.6 | **3547** | 49.3 | 164.7 |
| **bulk $CaCl_2$ 0.01 M** | | | | | | | | | | | |
| **3081** | 12.1 | 162.3 | **3247** | 226.8 | 282.1 | **3408** | 58.6 | 167.5 | **3541** | 46.4 | 185.0 |
| **bulk $CaCl_2$ 0.2 M** | | | | | | | | | | | |
| **3083** | 23.1 | 231.2 | **3241** | 215.7 | 272.8 | **3398** | 71.7 | 174.1 | **3538** | 48.8 | 181.5 |
| **bulk $CaCl_2$ 1 M** | | | | | | | | | | | |
| **3110** | 87.9 | 270.9 | **3257** | 171.9 | 251.7 | **3401** | 98.1 | 169.2 | **3541** | 55.9 | 174.9 |
| **bulk $MgCl_2$ 0.01 M** | | | | | | | | | | | |
| **3085** | 5.8 | 160.0 | **3245** | 253.1 | 290.2 | **3409.3** | 63.6 | 171.5 | **3547** | 46.2 | 180.6 |
| **bulk $MgCl_2$ 0.2 M** | | | | | | | | | | | |
| **3082** | 23.0 | 230.2 | **3241** | 215.7 | 273.0 | **3398** | 71.7 | 174.0 | **3538** | 48.8 | 181.5 |
| **bulk $MgCl_2$ 1 M** | | | | | | | | | | | |
| **3110** | 85.0 | 278.0 | **3257** | 173.0 | 229.6 | **3402** | 100.2 | 170.3 | **3541** | 55.1 | 175.1 |

| SBA-15 water | | | | | | | | | | | |
|---|---|---|---|---|---|---|---|---|---|---|---|
| $\omega_1$ | $I_1$ | $\Gamma_1$ | $\omega_2$ | $I_2$ | $\Gamma_2$ | $\omega_3$ | $I_3$ | $\Gamma_3$ | $\omega_4$ | $I_4$ | $\Gamma_4$ |
| **3080** | 2.3 | 94.2 | **3230** | 51.5 | 267.6 | **3405** | 27.1 | 186.1 | **3549** | 18.2 | 194.2 |
| **SBA-15 $BaCl_2$ 0.01 M** | | | | | | | | | | | |
| **3070** | 5.7 | 136.7 | **3230** | 43.6 | 236.4 | **3400** | 27.6 | 182.3 | **3545** | 16.0 | 185.6 |
| **SBA-15 $BaCl_2$ 0.2 M** | | | | | | | | | | | |
| **3110** | 27.1 | 270.4 | **3255** | 35.1 | 205.4 | **3403** | 42.3 | 180.8 | **3549** | 19.1 | 170.2 |
| **SBA-15 $BaCl_2$ 1 M** | | | | | | | | | | | |
| **3110** | 35.6 | 290.1 | **3248** | 29.1 | 202.8 | **3397** | 45.5 | 195.8 | **3545** | 18.6 | 188.3 |
| **SBA-15 $CaCl_2$ 0.01 M** | | | | | | | | | | | |
| **3070** | 4.6 | 205.2 | **3230** | 38.3 | 180.6 | **3400** | 40.2 | 179.2 | **3542** | 15.4 | 170.2 |
| **SBA-15 $CaCl_2$ 0.2 M** | | | | | | | | | | | |
| **3110** | 27.1 | 290.3 | **3255** | 35.1 | 205.6 | **3403** | 42.6 | 180.9 | **3549** | 17.2 | 170.2 |
| **SBA-15 $CaCl_2$ 1 M** | | | | | | | | | | | |
| **3099** | 35.5 | 295.1 | **3251** | 49.5 | 219.6 | **3404** | 43.5 | 184.1 | **3550** | 17.2 | 172.2 |
| **SBA-15 $MgCl_2$ 0.01 M** | | | | | | | | | | | |
| **3070** | 4.6 | 155.2 | **3230** | 38.3 | 219.5 | **3400** | 24.4 | 183.4 | **3544** | 14.0 | 177.0 |
| **SBA-15 $MgCl_2$ 0.2 M** | | | | | | | | | | | |
| **3080** | 5.8 | 180.8 | **3227** | 39.1 | 228.2 | **3399** | 30.2 | 187.9 | **3550** | 13.9 | 174.1 |
| **SBA-15 $MgCl_2$ 1 M** | | | | | | | | | | | |
| **3095** | 30.9 | 245.7 | **3248** | 48.0 | 221.4 | **3398** | 45.2 | 184.2 | **3550** | 18.5 | 176.2 |

| MCM-41 water | | | | | | | | | | | |
|---|---|---|---|---|---|---|---|---|---|---|---|
| $\omega_1$ | $I_1$ | $\Gamma_1$ | $\omega_2$ | $I_2$ | $\Gamma_2$ | $\omega_3$ | $I_3$ | $\Gamma_3$ | $\omega_4$ | $I_4$ | $\Gamma_4$ |
| **3093** | 4.5 | 163.2 | **3235** | 42.7 | 220 | **3396** | 30.4 | 184.3 | **3540** | 19.1 | 196.6 |
| **MCM-41 $BaCl_2$ 0.01 M** | | | | | | | | | | | |
| **3096** | 6.5 | 167.3 | **3238** | 31.1 | 220 | **3398** | 18.6 | 186.6 | **3545** | 11.9 | 195.2 |
| **MCM-41 $BaCl_2$ 0.2 M** | | | | | | | | | | | |
| **3105** | 15 | 176.3 | **3231** | 23.5 | 188.9 | **3383** | 40.2 | 198.8 | **3535** | 20.7 | 205.4 |
| **MCM-41 $BaCl_2$ 1 M** | | | | | | | | | | | |
| **3095** | 25.1 | 290 | **3230** | 18.4 | 189.4 | **3390** | 39.0 | 214 | **3555** | 12.6 | 187.0 |
| **MCM-41 $CaCl_2$ 0.01 M** | | | | | | | | | | | |
| **3093** | 8.3 | 160 | **3240** | 27.2 | 212.6 | **3400** | 20.3 | 181.3 | **3545** | 12.2 | 204.1 |
| **MCM-41 $CaCl_2$ 0.2 M** | | | | | | | | | | | |
| **3098** | 8 | 164.8 | **3235** | 20.3 | 197.1 | **3395** | 20.6 | 189.4 | **3545** | 11.5 | 196.2 |
| **MCM-41 $CaCl_2$ 1 M** | | | | | | | | | | | |
| **3080** | 9.1 | 217.6 | **3225** | 17.7 | 195.5 | **339,** | 27 | 210 | **3500** | 10.9 | 188.9 |
| **MCM-41 $MgCl_2$ 0.01 M** | | | | | | | | | | | |
| **3090** | 9.0 | 155 | **3240** | 26.4 | 205.6 | **3400** | 20.7 | 181.2 | **3545** | 13.9 | 202.4 |
| **MCM-41 $MgCl_2$ 0.2 M** | | | | | | | | | | | |
| **3105** | 10.2 | 154.9 | **3228** | 28.9 | 177.0 | **3385** | 32.2 | 189.0 | **3540** | 21.3 | 184.9 |
| **MCM-41 $MgCl_2$ 1 M** | | | | | | | | | | | |
| **3105** | 23.9 | 258.7 | **3232** | 29 | 193.2 | **3390** | 48.8 | 190.3 | **3545** | 13.9 | 189.4 |

| $\omega_1$ | $I_1$ | $\Gamma_1$ | $\omega_2$ | $I_2$ | $\Gamma_2$ | $\omega_3$ | $I_3$ | $\Gamma_3$ | $\omega_4$ | $I_4$ | $\Gamma_4$ |
|---|---|---|---|---|---|---|---|---|---|---|---|
| **MCM-41-1** | | | | | | | | | | | |
| **3080** | 7.8 | 152.6 | **3225** | 37.9 | 196.9 | **3388** | 28.9 | 191.7 | **3541** | 15.7 | 199.5 |
| **MCM-41-1 $BaCl_2$ 0.01 M** | | | | | | | | | | | |
| **3088** | 11.0 | 174.1 | **3245** | 27.7 | 211.2 | **3400** | 28.8 | 172.9 | **3540** | 18.7 | 220.1 |
| **MCM-41-1 $BaCl_2$ 0.2 M** | | | | | | | | | | | |
| **3098** | 11.5 | 154.4 | **3222** | 19.7 | 168.1 | **3378** | 35.8 | 215.7 | **3550** | 14.1 | 197.1 |
| **MCM-41-1 $BaCl_2$ 1 M** | | | | | | | | | | | |
| **3108** | 31.5 | 301.1 | **3237** | 22 | 199.8 | **3382** | 53.2 | 223 | **3548** | 14.0 | 198.0 |
| **MCM-41-1 $CaCl_2$ 0.01 M** | | | | | | | | | | | |
| **3098** | 8.5 | 182.2 | **3242** | 33.8 | 233.9 | **3407** | 21.7 | 184.1 | **3548** | 14.0 | 194.7 |
| **MCM-41-1 $CaCl_2$ 0.2 M** | | | | | | | | | | | |
| **3105** | 14.2 | 162.6 | **3230** | 27.8 | 175.0 | **3385** | 43.0 | 196.2 | **3545** | 18.2 | 186.4 |
| **MCM-41-1 $CaCl_2$ 1 M** | | | | | | | | | | | |
| **3108** | 30.3 | 241.5 | **3236** | 24.8 | 163.7 | **3380** | 53.1 | 153.8 | **3540** | 22 | 187.5 |
| **MCM-41-1 $MgCl_2$ 0.01 M** | | | | | | | | | | | |
| **3098** | 7.0 | 239.4 | **3397** | 28.1 | 270.5 | **3397** | 18 | 200 | **3545** | 12.3 | 203.4 |
| **MCM-41-1 $MgCl_2$ 0.2 M** | | | | | | | | | | | |
| **3101** | 9.9 | 156.1 | **3230** | 20.1 | 174.7 | **3383** | 28.3 | 195.3 | **3540** | 15.1 | 196.2 |
| **MCM-41-1 $MgCl_2$ 1 M** | | | | | | | | | | | |
| **3105** | 27.1 | 260.7 | **3233** | 32 | 188.4 | **3383** | 49.8 | 197.8 | **3545** | 15 | 173.5 |

## Deviation of the dynamical and structural properties in the interfacial layer

Figure 85 depicts the evolution of the νOH band fraction within the interfacial layer for water and electrolyte solutions confined in SBA-15. The values were calculated using eq. 10.

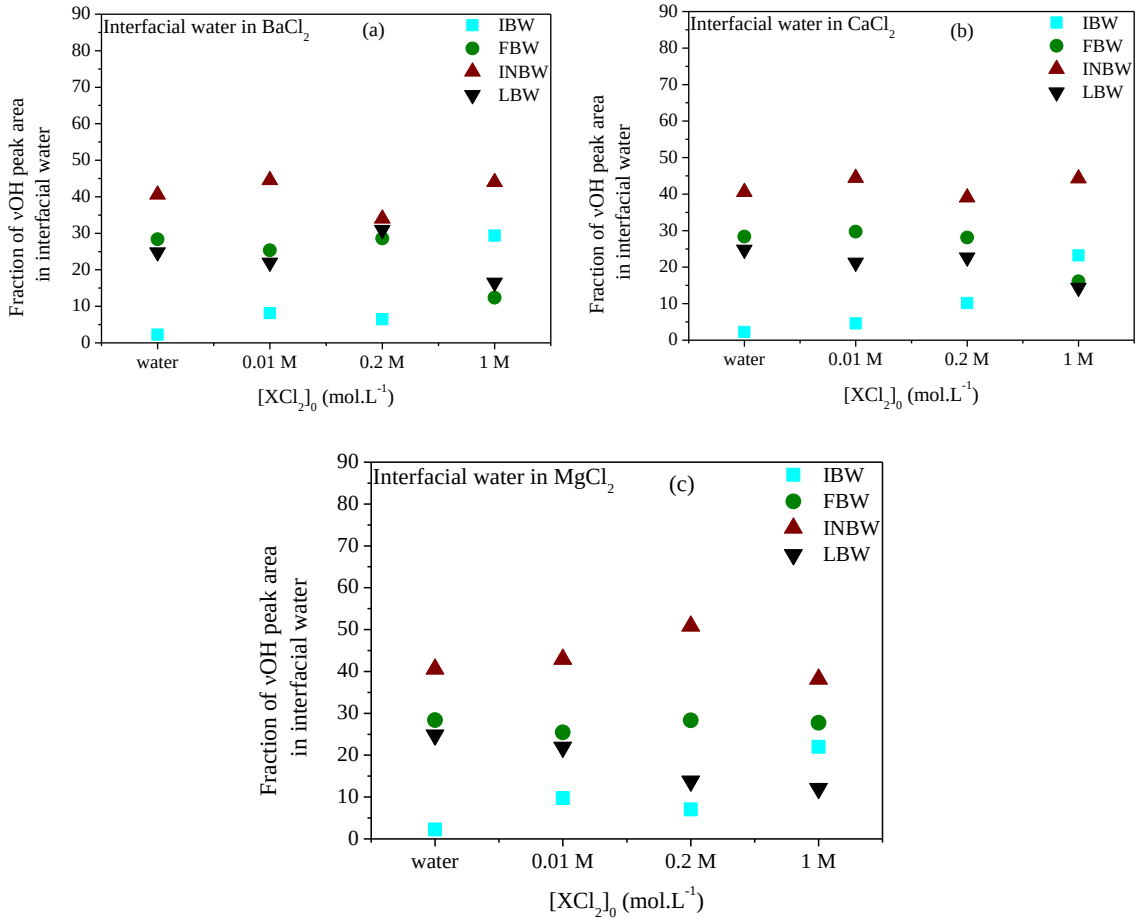


*Figure 85 (a) to (c): Evolutions of the percentages of the various νOH bands within the interfacial layer as a function of electrolyte concentration for water and electrolyte solutions confined in SBA-15.*

## *Small Angle X-Ray Scattering (SAXS)*

SAXS is an accurate, non-destructive and analytical method to obtain information about structure of particle systems, which can be solid, liquid or liquid domains in solids. Normally, the particle or structure size that can be resolved with this technique is in the range from 1 – 100 nm. Due to the fact that the X-Ray beam is sent through the sample, systems consisted of particles made of high atomic numbers show a higher resolution than particles with less atomic numbers.

One can distinguish two different types of interaction of X-Rays with matter. On the one hand X-Rays can be absorbed by matter and be transferred into other types of energy (heat, fluorescence radiation etc.) and on the other hand X-Rays can be scattered into other directions of propagation. Scattering itself can occur with or without the loss of energy (change of wavelength). In terms of SAXS, only the transfer of energy between the X-Rays and the bound electrons in the atom are important, because they contain structural information about the sample.

## General principle

As schematically shown in Figure 86, a X-Ray beam with a defined wavelength $\lambda$ is impinged on a sample. When the incident beam is scattered at atoms, every atoms starts to emit waves. The waves can interact with the incoming waves and produce interference at the detector either in a constructive or in a destructive way. The prinicple is shown in Figure 87. The measured interference pattern is characteristic to the sample structure, for example the interatomic distances and the orientation. Due to the fact that every distance is measured with respect to the incident wavelength $\lambda$, scattering patterns are usually presented as a function of the scattering vector $q$.

$$q = \frac{4\pi}{\lambda} sin(\theta) \qquad (48)$$

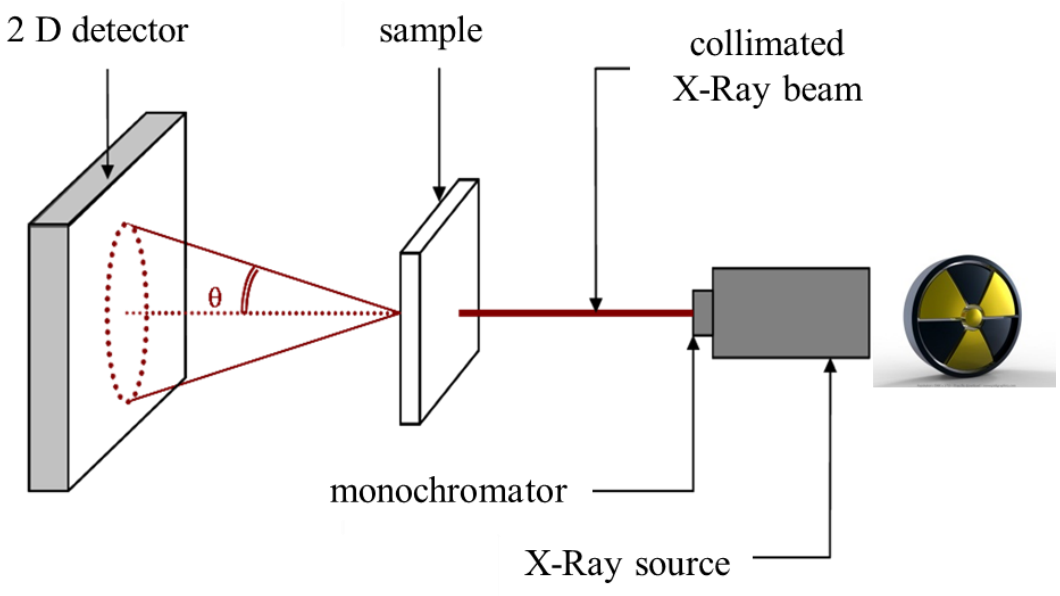


*Figure 86: Schematic representation of a typical SAXS set-up.*

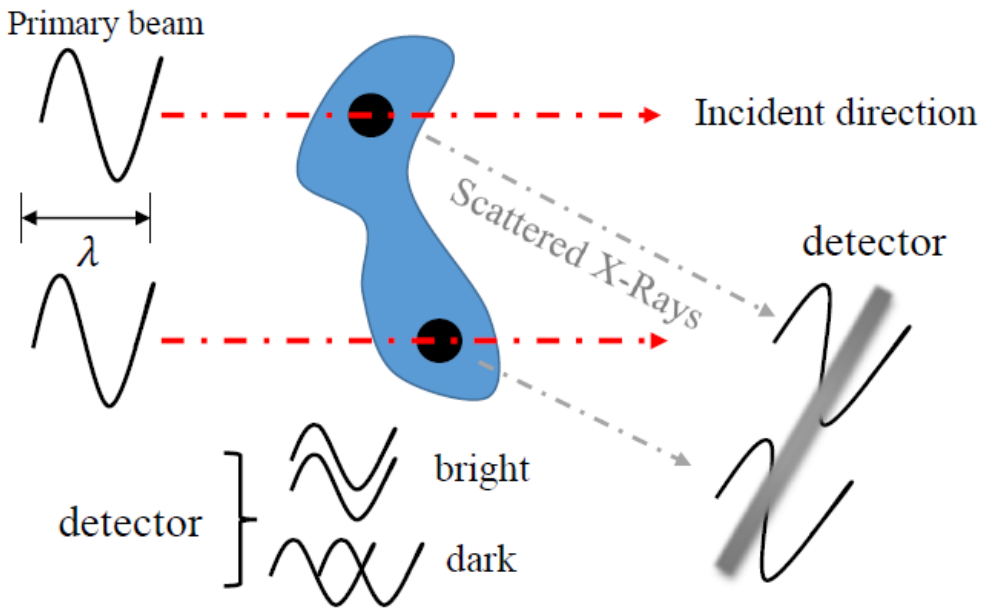


*Figure 87: Depending on constructive or destructive interference the detector receives brightness (in-phase interference) or darkness (out-phase interference)*

Since X-Rays are scattered by electrons, the scattered intensity is increasing with the amounts of electrons placed in the sample volume. The detector read-out (i. e. the intensity) is the square of all waves amplitudes arriving from the sample. The total scattered intensity is proportional to three different factors: the form factor *P(q)*, which is depending on the particle sizes, and the structure factor *S(q)*, which takes the contribution from direct neighbours of the particle into account and the contrast between the scattered electron densities and the environment $\Delta\rho$. Therefore, we can define the intensity:

$$I(q) = NV^2(\Delta\rho)^2F(q)S(q) \tag{49}$$

where *N* and *V* denotes the number and volume of scatterers.

In the case of highly ordered silica materials the particles are densly packed and periodically aligned in a hexagonal lattice, so the interference pattern can develop

pronounced peaks so called “Bragg peaks”. By applying Bragg’s law one can indicate the distance between the particles with the maximum of such Bragg peaks:

$$d_{Bragg} = \frac{2\pi}{q_{Peak}} \qquad (50)$$

## SAXS instrument and measurement

In the framework of this thesis, the SWAXS apparatus at the ICSM was used. The porous structure of SBA-15 and MCM-41 was characterized in the transmission geometry with a molybdenum anode, delivering a wavelength of 0.71 Å. Focusing and wavelength selection are achieved using a Xenocs Fox 2D multilayer mirror. Two sets of scatterless slits allow the beam to be collimated and to have a squared shape of side 0.8 mm. SAXS patterns were recorded on a MAR345 2D image plate (345 mm diameter) which enables the simultaneous detection over scattering vectors q ranging from 0.3 to 20 $nm^{-1}$. Samples were analyzed in glass capillaries of around 2 mm diameter. The capillaries were placed in a sample holder with a sample-detector distance of 0.73 m. For calibration reasons in each measurement, one capillary of silver behenate and polyethylene were analyzed besides an empty one.

## Data treatment

Silver behenate was used as a reference during the SAXS spectra integration. After the sustraction of the empty capillary, the sample intensity $I_{sample}$ has to be normalized with respect to the transmission *T*, to the capillary thickness e, the acquisition time *t* and a instrumental factor *k*. The instrumental factor k can be calculated using a reference with a well-known scattering intensity: polyethylene (at 0.37 $nm^{-1}$ with an absolut intensity of

4.9 $cm^{-1}$. The absolut scattering intensity of the sample can be expressed with the following equation:

$$I_{abs} = \frac{1}{k} \cdot \frac{1}{e}\left[\frac{I_{sample} - 8}{t_{sample}T_{sample}} - \frac{I_{EC} - 8}{t_{EC}T_{EC}}\right] \quad (51)$$

$$\text{and } k = \frac{I_{max,PE}}{T_{PE}t_{PE} \cdot 0.236}$$

where *EC* denote the empty capillary and *PE* polyethylene.

# Quasi-elastic neutron scattering (QENS)

In the following chapter, a brief overview about QENS is given. For a more detailed description we refer the reader to ref 189.

## General principle

Quasi-elastic Neutron Scattering is a spectroscopic method, where the momentum and the corresponding energy transfer of neutrons are measured. This transfer arises when neutrons are impinged ($\lambda_{inc} \approx 1 - 10$ Å normally well adapted to the interatomic distances) onto a sample and interact with the atoms in it. The momentum transfer Q, also called scattering vector depicts the difference before and after penetration the sample and can be used to obtain information about the dynamics in the sample.

## Theoretical background

Neutrons can be generated for example by the fission process of a heavy nucleus and their energy *E* can be expressed using the following equation:

$$\bar{E} = \frac{1}{2} m \bar{v}^2 = \frac{3}{2} k_b T \tag{52}$$

where $k_B$ denotes the Boltzmann constant. The energy can also be written using wavelength $\lambda$ and wave vector *k*:

$$\lambda = \frac{2\pi}{|k|} = \frac{h}{mv} \tag{53}$$

$$E = \frac{\hbar^2 k^2}{2m} = \frac{h^2}{2m\lambda^2} \tag{54}$$

Thermal neutrons with a corresponding temperature $T \approx 300$ K having an energy $E \approx 25$ meV and a wavelength $\lambda \approx 1.8$ Å are perfectly suitable for dynamic investigation because their energy is in the same order of magnitude than the intermolecular energies.

In Quasi-elastic neutron scattering experiments, two different quantities can be measured: i) the energy transfer, $\boldsymbol{\hbar\omega}$, between the initial energy, $E$, and the final energy, $E_0$, of the neutrons

$$\hbar\omega = E - E_0 = \frac{\hbar^2}{2m}(k^2 - k_0^2) \tag{55}$$

and ii) the scattering vector **Q:**

$$Q = k - k_0 \tag{56}$$

Where $k$ and $k_0$ are the corresponding wave vectors. Figure 88 depicts the typical set-up for neutron scattering experiments. The monochromatic beam is sent into a sample whereas scattering processes take place. For a given scattering angle, the scattering vectors change while varying the energy transfer.

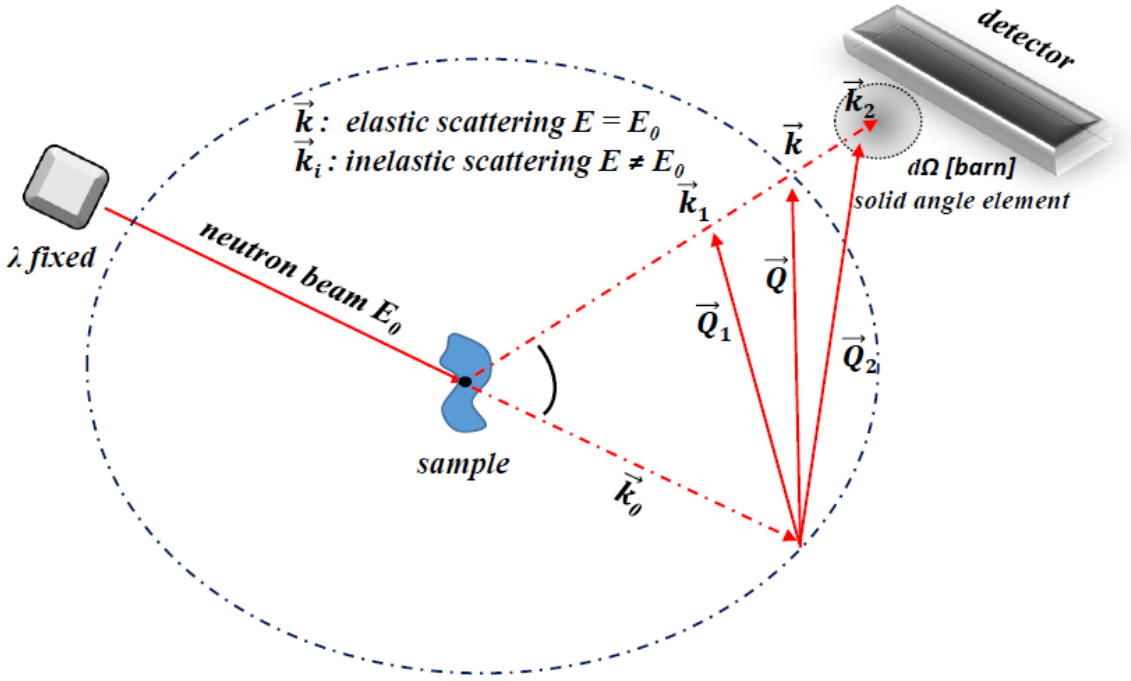


*Figure 88: Schematic overview of QENS experiment showing the variation of wave vectors transfer* $\boldsymbol{Q = k - k_0}$ *as function of energy transfer at constant scattering angle.*

## Basic equations of neutron scattering

There are two possibilities a neutron can interact with the nuclei of sample atoms: i) absorption of neutrons by the nucleus and ii) neutrons are scattered, i.e. direction and energy are changed. Since the first possibility is not of interest here, we only consider the second case. If the energy of incoming neutrons is too small to be absorbed, they can undergo scattering processes. Considering a current $I_0$ of neutrons one can define from the number of scattering events $I_s$ a cross section expressed by the equation:

$$I_s = I_0 \sigma_s \tag{57}$$

In this equation the cross section represents the dimension of a surface (typically indicated by 1 barn = $10^{-24}$ cm²). The probability of a neutron with energy $E_0$, leaving the sample in

the solid angle element $d\Omega$ (see Figure 80) with an energy exchange is given by the double-differential cross section

$$\frac{\partial^2\sigma}{\partial\Omega\partial E} = \frac{1}{\hbar}\frac{\partial^2\sigma}{\partial\Omega\partial\omega} \tag{58}$$

Another important parameter in scattering is the scattering length, $b$. The scattering length depends on the attractive or repulsive interaction of the nucleus with the neutrons and by the presence of different isotopes. The difference between coherent and incoherent scattering is that incoherent scattering contains no information about particle structure in the sample, whereas coherent scattering contains information about the correlation between the particle and collective dynamics. Furthermore, incoherent scattering is related with the dynamics of the individual particles, thus well suitable for investigating water motion. The average value over all isotopes is called *coherent scattering length* $\langle b_i \rangle$. In addition to that, the *incoherent scattering length* $b_i^{inc}$ can be defined as the root mean square deviation of $b_i$ from $\langle b_i \rangle$

$$b_i^{coh} = \langle b_i \rangle \tag{59}$$

$$b_i^{inc} = [\langle b_i^2 \rangle - \langle b_i \rangle^2]^{1/2} \tag{60}$$

Using these for defining the scattering length one can also introduce the so-called total bound scattering cross section, which are expressed in the following equations. Either here there is both a coherent and incoherent contribution

$$\sigma = \sigma_{coh} + \sigma_{inc} \tag{61}$$

$$\sigma_{coh} = 4\pi\langle b \rangle^2 \tag{62}$$

$$\sigma_{inc} = 4\pi\langle(b - \langle b\rangle)^2\rangle \tag{63}$$

Considering the case of hydrogen, where the nucleus is formed of a single proton with spin $\frac{1}{2}$, one can calculate the coherent and incoherent cross sections by using the relevant scattering lengths $b^+ = 1.04 \times 10^{-12} cm$ and $b^- = -4.74 \times 10^{-12} cm$

$$\sigma_{coh}(H) = 1.8\ barns \tag{64}$$

$$\sigma_{inc}(H) = 79.9\ barns \tag{65}$$

The huge difference between the two cross sections of hydrogen makes sure that the QENS spectra of water in confinement contain a contribution of incoherent scattering from hydrogen atoms and thus the incoherent neutron scattering is such a unique tool for the investigation of hydrogenous compounds. Since the values for deuterium $\sigma_{coh}(D) = 5.6\ barns$ and $\sigma_{inc}(D) = 2.0\ barns$ are not as much different as the value for hydrogen, incoherent scattering studies can use the deuteration technique to vary the contributions from different chemical groups and functions to the overall scattering intensity. Regarding the situation for X-Rays instead of neutrons, the situation is the reverse since scattering factors are proportional to the atomic number. In contrast, light elements are nearly invisible in X-Ray investigations. Besides hydrogen there is another element being almost a purely incoherent scatterer, vanadium. For this reason, vanadium is used as standard calibrations for such scattering set-ups.

The basic scattering function gives the probability that a neutron with energy *E* and wave vector $k_0$, impinging onto a sample in a monochromatic beam, is scattered by the number of

scatterers *N* in the sample by a wave vector *k* in a solid angle $d\Omega$ around the direction given by *k*. For a sample, having one type of scatterers the following equation can be used:

$$|k\rangle = \frac{1}{\sqrt{V}} exp(ik * r) \tag{66}$$

$$|k_0\rangle = \frac{1}{\sqrt{V}} exp(ik_0 * r) \tag{67}$$

$$\frac{\partial^2\sigma}{\partial\Omega\partial\omega} = \left(\frac{\partial^2\sigma}{\partial\Omega\partial\omega}\right)^{coh} + \left(\frac{\partial^2\sigma}{\partial\Omega\partial\omega}\right)^{inc} = \frac{|\vec{k}|}{|\vec{k}_0|}\overline{b}^2 \frac{1}{N}\sum_\alpha \sum_\beta \frac{1}{2\pi}\int_{-\infty}^{+\infty} \langle exp\left(-i\vec{Q}\vec{r}_\alpha(0)\right) exp\left(i\vec{Q}\vec{r}_\beta(t)\right)\rangle \, exp(-i\omega t)\, dt$$

+

$$\frac{|\vec{k}|}{|\vec{k}_0|}\overline{b^2} - \overline{b}^2 \frac{1}{N}\sum_\alpha \sum_\beta \frac{1}{2\pi}\int_{-\infty}^{+\infty} \langle \exp\left(-i\vec{Q}\vec{r}_\alpha(0)\right) \exp\left(i\vec{Q}\vec{r}_\beta(t)\right)\rangle \exp(-i\omega t) dt \tag{68}$$

where < > indicating the average temperature regarding the positions $\vec{r}_i(t), i = \alpha, \beta$ of the nuclei in the sample. In this equation, it is obvious that there are two different contributions the coherent and the incoherent cross sections, respectively.

In addition to that, one can define the intermediate scattering functions, since in the experiment each term, coherent and incoherent, is weighted by its respective cross section and can only be measured together:

$$I(\vec{Q}, t) = \frac{1}{N}\frac{1}{N}\sum_\alpha \sum_\beta \langle exp\left(-i\vec{Q}\vec{r}_\alpha(0)\right) exp\left(i\vec{Q}\vec{r}_\beta(t)\right)\rangle \tag{69}$$

and the incoherent form for $I^{inc}(\vec{Q}, t)$:

$$I^{inc}(\vec{Q}, t) = \frac{1}{N}\sum_\alpha \sum_\beta \langle exp\left(-i\vec{Q}\vec{r}_\alpha(0)\right) exp\left(i\vec{Q}\vec{r}_\alpha(t)\right)\rangle \tag{70}$$

These intermediate scattering functions are the time and space Fourier transformed of the self-autocorrelation and pair correlation function, which means they containing information about the particle position in space as a function of time (dynamic properties). Using this function for the intermediate scattering one is able to define the scattering function $S(\vec{Q},\omega)$ and the function for incoherent scattering $S^{inc}(\vec{Q},\omega)$:

$$S(\vec{Q},\omega) = \frac{1}{2\pi}\int_{-\infty}^{+\infty} I(\vec{Q},t)exp(-i\omega t)dt \qquad (71)$$

$$S^{inc}(\vec{Q},\omega) = \frac{1}{2\pi}\int_{-\infty}^{+\infty} I^{inc}(\vec{Q},t)exp(-i\omega t)dt \qquad (72)$$

$S(\vec{Q},\omega)$ contains all the physics of the system (in space and time) and is depending only on the system. So using all the definitions and equations given before, one can finally define an equation having a parameter, which is measurable in the experiment.

$$\frac{\partial\sigma}{\partial\Omega\partial\omega} = \frac{1}{4\pi}\frac{|\vec{k}|}{|\vec{k}_0|}\{\sigma^{coh}S^{coh}(\vec{Q},\omega) + \sigma^{inc}S^{inc}(\vec{Q},\omega)\} \qquad (73)$$

# Annex IV

The model used to perform the calculations of SAXS pattern of MCM-41 and SBA-15 will be briefly presented. Whit this model, it is possible to obtain the theoretical shape of scattering curves at small angles depending on various structural parameters (pore size, distance between pore planes, density of material walls, presence of alteration crown around the pores, etc.). The principle of this model is to calculate numerically the Fourier transform of a material presenting objects within it.

Generally, if we want to describe grains of mesoporous silica, we can distinguish two types of voids: inter-granular voids of macroscopic size and intra-granular voids representing the mesopores of silica. As shown in Figure 59, the silica grain is pierced by arrays of cylindrical pores of infinite length disposed on a hexagonal lattice. By assuming an infinite length of the cylinders, the numerical calculations get less complicated. The hexagonal lattice can be described by three main parameters: the pore size $r_p$, the wall thickness $w$ and the unit cell parameter $a$.

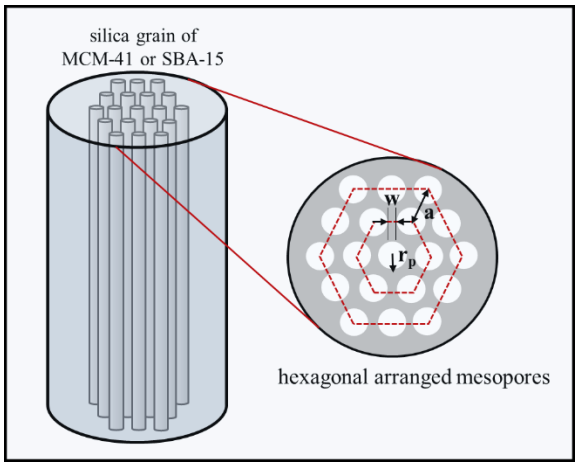


*Figure 89: Schematic representation of the structure used for the model adapted from ref* 205*. The silica grain is perforated with smaller cylinders of mesopores having three characteristic parameters: pore size $r_p$, lattice parameter a and wall width w.*

The mean lattice parameter is given by the distance from one pore center to another and this distance *d* can be calculated using the equation:

$$d = \frac{2\pi}{q} \tag{74}$$

where *d* is the spacing between the {10} planes in the mesoporous lattice; and *q* is the scattering vector. The unit cell parameter *a* was also deduced from eq. 1 and 2:

$$a = \frac{2d_{100}}{\sqrt{3}} \tag{75}$$

The unit cell parameter is accessible from the Bragg peak positions in the experimental data. The next step to compare correctly experimental and calculated SAXS pattern is to estimate the amount of powder in the X-Ray beam and therefore the intensity of the spectra. In the case of liquids, this can be achieved easily by knowing the sample holder geometry, whereas for solids it is less straightforward. In sample holders (glass capillaries with 2 mm diameter), it is complicated to control the density and compactness of the granular materials. In this context, it is more suitable to estimate the powder amount through X-Ray absorption measurements by measuring the intensity of the X-Ray beam with and without sample to determine the sample transmission:

$$T_s = exp(-\mu_b z_b) \tag{76}$$

where $\mu_b$ represents the linear absorption of the bulk (nonporous) material spread on a single layer having the width $z_b$. This width determined by transmission measurements allows us to compare experimental data with the calculated SAXS pattern. Knowing this width and the

thickness of the sample holder *E*, one can easily derive the solid fraction in the X-Ray beam$f_s = z_b/E$.

When water or electrolyte solutions are confined in mesoporous silica, we assume that all voids in the silica are filled with water or electrolyte solutions. This leads to a modified eq. 3:

$$T = exp(-\mu_1 z_1 - \mu_2 z_2) \quad (77)$$

where the first contribution is related to water and the second one to mesoporous silica. The solid fractions are linked with the thickness of the sample holder: $z_1 = E - z_2$.

Taking the two equations together, we obtain the following equation:

$$e_2 = \frac{lnT + \mu_1 E}{\mu_1 \mu_2} \quad (78)$$

This relationship shows that the parameter $f_s$ only causes an absolute decrease or increase of the SAXS spectra intensities. Consequently, one can compare the relative peak intensities of the various Bragg peaks. For a more detailed description of the chosen structural hypothesis and Bessels functions used for the numerical calculation we refer the reader to ref 205.

While the unit cell parameter *a* and the solid fraction $f_s$ are fixed, other parameters are introduced to describe our silica confinement. First, the pore diameter is adjusted in order to optimize the agreement between the experimental and the simulated SAXS pattern. Note that a Gaussian distribution of pore diameters is considered. The full width at half maximum (FWHM) of this distribution (pd) is expressed as a percentage of the lattice parameter. In addition to that, a paracrystalline disorder parameter (pcd) was introduced taking into

account the imperfection of crystals.[138] This parameter considers the progressive loss of correlation between the positions of the pore centers in a hexagonal lattice, as illustrated in Figure 90.[206]

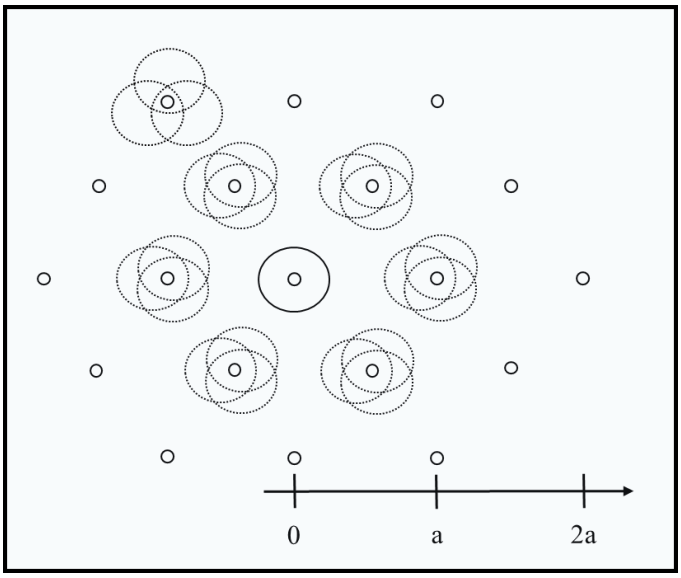


*Figure 90: Schematic representation of the paracrystalline disorder on a 2D hexagonal lattice of mesopores. The dotted circles show the extreme positions of the first neighboring pores and in one case for the second neighboring shell of pores.*

Furthermore, the ratio between the FWHM of the Gaussian distribution describing the dispersion of the position of the first neighbouring pore and the pore lattice parameter is included by defining a paracrystalline degree (pcd).

In the case of SBA-15, the mesoporous silica is represented as silica whose density is equal to that of microporous amorphous silica. The microporosity of the walls is low and it is shown in Figure 91 that the small variations in silica density have no influence on the interpretation of the results.

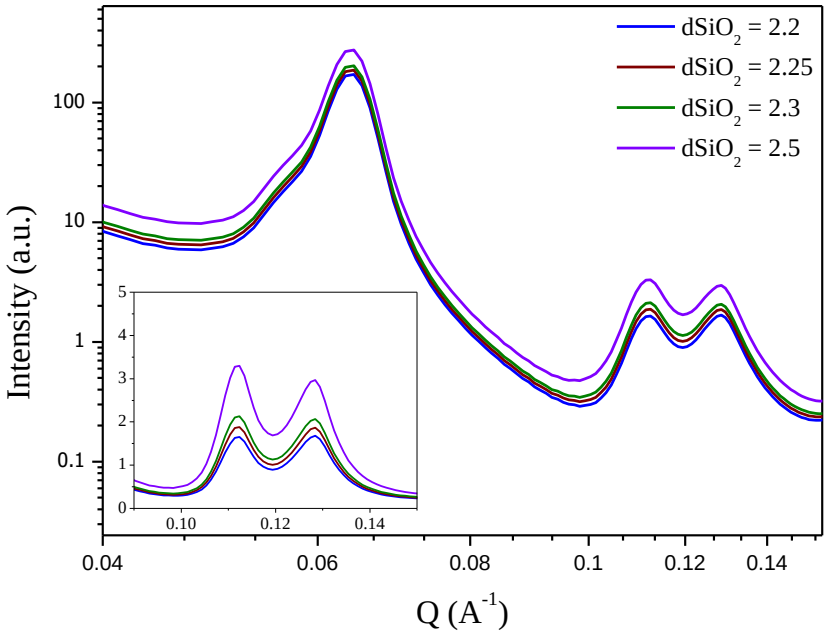


*Figure 91: Calculated SAXS pattern for different silica density values.*

Moreover, it is possible to take into account a layer of different density around the pore having a thickness *hlw*. A descriptive scheme of the structure considered by the model is shown in Figure 92.

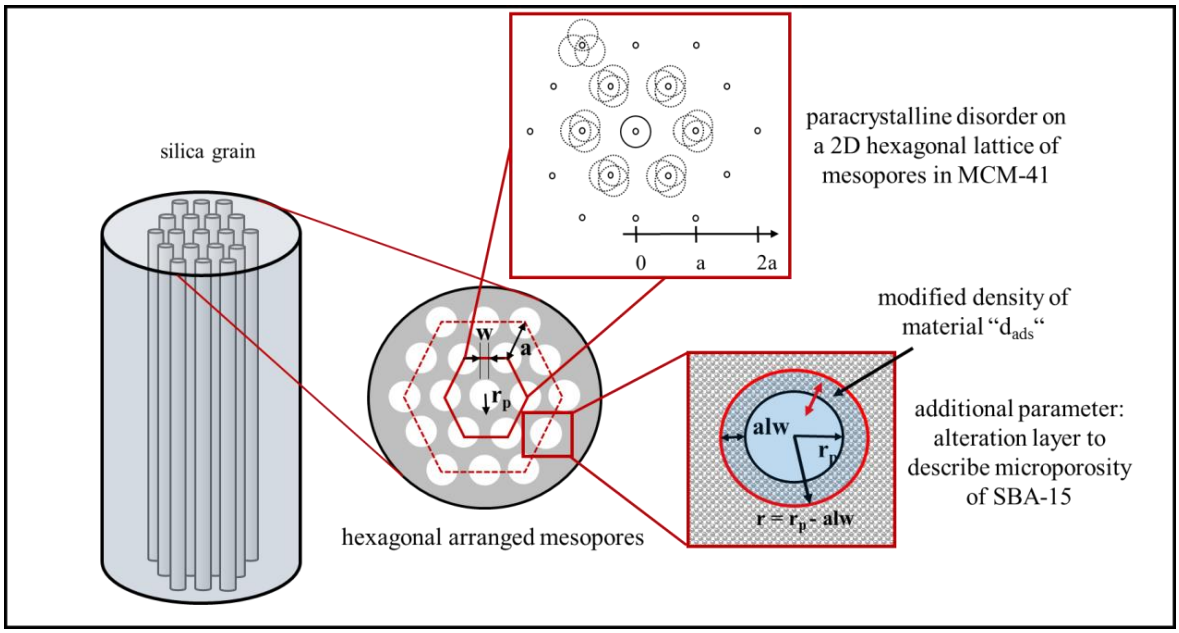


*Figure 92: Schematic representation of the microporosity of SBA-15 filled with water. Water diffusion into the microporosity can cause a alteration layer (alw) in the pore walls that continuously changes the pore size.*

With these basic differences between MCM-41 and SBA-15, we obtained the calculated SAXS spectra presenting the mesoporous silica in contact with water and various electrolyte solutions. The comparison of the theoretical and experimental pattern gives information about the material evolution and the impact of ions on the dissolution mechanisms.

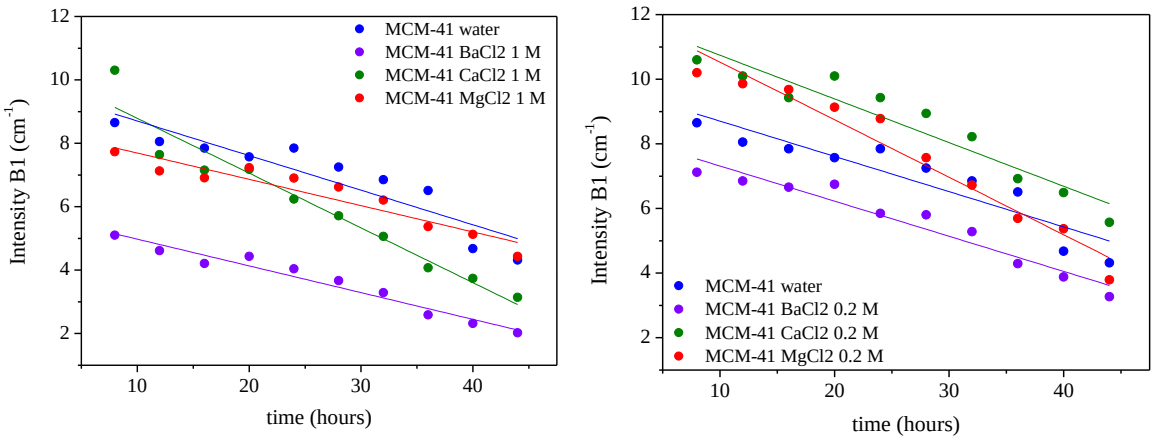


*Figure 93: Evolution of the intensity of the Bragg peak B1 in water and electrolyte solutions at 1 M and 0.2 M as a function of the alteration time.*

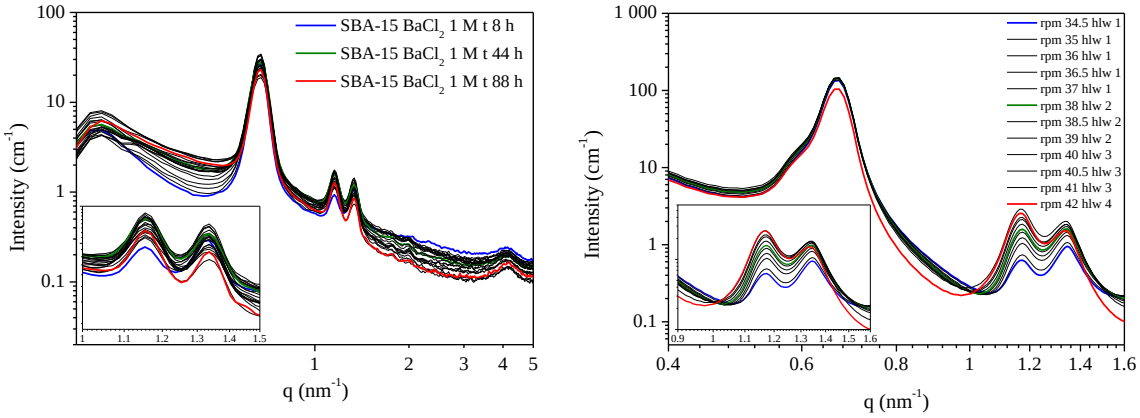


*Figure 94: Experimental SAXS spectra of SBA-15 filled with pure water during 60 h at 50 °C having a pore radius of 2.9 nm (panel a). Calculated SAXS spectra of SBA-15 structures corresponding to a mesoporous lattice with a unit cell parameter of 12.3 nm. The FHWM of the pore diameter distribution (pd) and the parameter of the paracrystalline disorder (pcd) are equal to 20 %. The pore radius and the thickness of the hydration layer were continuously increased (panel b). The insets in both graphs show a detailed evolution of I2 and I3.*

# References

(1) Wang, Y. Nanogeochemistry: Nanostructures, Emergent Properties and Their Control on Geochemical Reactions and Mass Transfers. *Chem. Geol.* **2014**, *378–379*, 1–23.

(2) Mamontov, E.; Cole, D. R.; Dai, S.; Pawel, M. D.; Liang, C. D.; Jenkins, T.; Gasparovic, G.; Kintzel, E. Dynamics of Water in LiCl and CaCl2 Aqueous Solutions Confined in Silica Matrices: A Backscattering Neutron Spectroscopy Study. *Chem. Phys.* **2008**, *352*, 117–124.

(3) Stack, A. G.; Fernandez-Martinez, A.; Allard, L. F.; Bañuelos, J. L.; Rother, G.; Anovitz, L. M.; Cole, D. R.; Waychunas, G. A. Pore-Size-Dependent Calcium Carbonate Precipitation Controlled by Surface Chemistry. *Environ. Sci. Technol.* **2014**, *48*, 6177–6183.

(4) Gouze, B.; Cambedouzou, J.; Parrès-Maynadié, S.; Rébiscoul, D. How Hexagonal Mesoporous Silica Evolves in Water on Short and Long Term: Role of Pore Size and Silica Wall Porosity. *Microporous Mesoporous Mater.* **2014**, *183*, 168–176.

(5) Rébiscoul, D.; Cambedouzou, J.; Brossel, M.; Baum, M.; Szenknect, S. Evolution of Silica Walls of Nanopores Filled with Water and Ions. *Procedia Earth Planet. Sci.* **2017**, *17*, 88–91.

(6) Gupta, P. K.; Meuwly, M. Dynamics and Vibrational Spectroscopy of Water at Hydroxylated Silica Surfaces. *Faraday Discuss.* **2013**, *167*, 329.

(7) Chiavazzo, E.; Fasano, M.; Asinari, P.; Decuzzi, P. Scaling Behaviour for the Water Transport in Nanoconfined Geometries. *Nat. Commun.* **2014**, *5*, 1–11.

(8) Yuan, P.; Annabi-Bergaya, F.; Tao, Q.; Fan, M.; Liu, Z.; Zhu, J.; He, H.; Chen, T. A Combined Study by XRD, FTIR, TG and HRTEM on the Structure of Delaminated Fe-Intercalated/Pillared Clay. *J. Colloid Interface Sci.* **2008**, *324*, 142–149.

(9) Rébiscoul, D.; Cambedouzou, J.; Briman, I.; Cabié, M.; Brau, H.-P.; Diat, O. Water Dynamics in Nanoporous Alteration Layer Coming from Glass Alteration: An Experimental Approach. *J. Phys. Chem. C* **2015**, *119*, 15982–15993.

(10) Dourdain, S.; Gibaud, A.; Delattre, A.; Terech, P. Extended Surfaces Nanopatterned with Functionalized Cavities for Positioning Nanoparticles. *Langmuir* **2010**, *26*, 7565–7568.

(11) Rowles, M. R.; Hanna, J. V; Pike, K. J.; Smith, M. E. Applied Magnetic Resonance Na MAS NMR Study of the Bonding Character in Aluminosilicate Inorganic Polymers. *Appl. Magn. Reson* **2007**, *32*, 663–689.

(12) Kowalczyk, R. M.; Gajewicz, A. M.; McDonald, P. J. The Mechanism of Water–isopropanol Exchange in Cement Pastes Evidenced by NMR Relaxometry. *RSC Adv.* **2014**, *4*, 20709–20715.

(13) Ojovan, M. I.; Lee, W. E. *New Developments in Glassy Nuclear Wasteforms*; Nova Science Publishers, 2007.

(14) Bourg, I. C.; Steefel, C. I. Molecular Dynamics Simulations of Water Structure and Diffusion in Silica Nanopores. *J. Phys. Chem. C* **2012**, *116*, 11556–11564.

(15) Stratmann, M.; Rohwerder, M. Materials Science: A Pore View of Corrosion. *Nature* **2001**, *410*, 420–423.

(16) Weissmüller, J.; Newman, R. C.; Jin, H.-J.; Hodge, A. M.; Kysar, J. W. Nanoporous Metals by Alloy Corrosion: Formation and Mechanical Properties. *MRS Bull.* **2009**, *34*, 577–586.

(17) Erlebacher, J.; Aziz, M. J.; Karma, A.; Dimitrov, N.; Sieradzki, K. Evolution of Nanoporosity in Dealloying. *Nature* **2001**, *410*, 450–453.

(18) Ben-Ishai, P.; Mamontov, E.; Nickels, J. D.; Sokolov, A. P. Influence of Ions on Water Diffusion - a Neutron Scattering Study. *J. Phys. Chem. C* **2013**, *117*, 7724.

(19) Mamontov, E.; Cole, D. R. Quasielastic Neutron Scattering Study of Dynamics of CaCl 2 Aqueous Solution Confined in Vycor Glass. *Phys. Chem. Chem. Phys.* **2006**, *8*, 4908–4914.

(20) Fenter, P.; Kerisit, S.; Raiteri, P.; Gale, J. D. Is the Calcite-Water Interface Understood? Direct Comparisons of Molecular Dynamics Simulations with Specular X-Ray Reflectivity Data. *J. Phys. Chem. C* **2013**, *117*, 5038–5042.

(21) Fenter, P.; Sturchio, N. C. Mineral–water Interfacial Structures Revealed by Synchrotron X-Ray Scattering. *Prog. Surf. Sci.* **2004**, *77*, 171–258.

(22) Skelton, A. A.; Fenter, P.; Kubicki, J. D.; Wesolowski, D. J.; Cummings, P. T. Simulations of the Quartz(1011)/Water Interface: A Comparison of Classical Force Fields, Ab Initio Molecular Dynamics, and X-Ray Reflectivity Experiments. *J. Phys. Chem. C* **2011**, *115*, 2076–2088.

(23) Nibbering, E. T. J.; Elsaesser, T. Ultrafast Vibrational Dynamics of Hydrogen Bonds in the Condensed Phase. *Chem. Rev.* **2004**, *104*, 1887–1914.

(24) Barthel, J.; Krienke, H.; Kunz, W. *Physical Chemistry of Electrolyte Solutions : Modern Aspects*, 5th ed.; Steinkopf: Heidelberg, 1998.

(25) Atkins, P.; De Paula, J. *Physical Chemistry*; 2006.

(26) Marcus, Y. Effect of Ions on the Structure of Water : Structure Making and Breaking Effect of Ions on the Structure of Water : Structure Making and Breaking. *Chem. Rev.* **2009**, *109*, 1346–1370.

(27) Kunz, W.; Henle, J.; Ninham, B. W. 'Zur Lehre von Der Wirkung Der Salze' (about the Science of the Effect of Salts): Franz Hofmeister's Historical Papers. *Curr. Opin. Colloid Interface Sci.* **2004**, *9*, 19–37.

(28) Kunz, W. Specific Ion Effects in Colloidal and Biological Systems. *Curr. Opin. Colloid Interface Sci.* **2010**, *15*, 34–39.

(29) Collins, K. D.; Washabaugh, M. W. The Hofmeister Effect and the Behaviour of Water at Interfaces. *Q. Rev. Biophys.* **1985**, *18*, 323.

(30) Collins, K. D. Charge Density-Dependent Strength of Hydration and Biological Structure. *Biophys. J.* **1997**, *72*, 65–76.

(31) Omta, A. W.; Kropman, M. F.; Woutersen, S.; Bakker, H. J. Negligible Effects o Ions on the Hydrogen-Bond Structure in Liquid Water. *Science (80-. ).* **2003**, *301*, 347.

(32) Walrafen, G. E. Raman Spectral Studies of the Effects of Perchlorate Ion on Water Structure. *J. Chem. Phys.* **1970**, *52*, 4176–4198.

(33) Sun, Q. Vibrational Spectroscopy Raman Spectroscopic Study of the Effects of Dissolved NaCl on Water Structure. *Vib. Spectrosc.* **2012**, *62*, 110–114.

(34) Li, R.; Jiang, Z.; Chen, F.; Yang, H.; Guan, Y. Hydrogen Bonded Structure of Water and Aqueous Solutions of Sodium Halides: A Raman Spectroscopic Study. *J. Mol. Struct.* **2004**, *707*, 83–88.

(35) Mancinelli, R.; Botti, A.; Bruni, F.; Ricci, M. A.; Soper, A. K. Perturbation of Water Structure Due to Monovalent Ions in Solution. *Phys. Chem. Chem. Phys.* **2007**, *9*, 2959.

(36) Bruni, F.; Imberti, S.; Mancinelli, R.; Ricci, M. A. Aqueous Solutions of Divalent Chlorides: Ions Hydration Shell and Water Structure. *J. Chem. Phys.* **2012**, *136*, 064520.

(37) Dagade, D. H.; Barge, S. S. Hydrogen Bonding in Liquid Water and in the Hydration Shell of Salts. *ChemPhysChem* **2016**, *17*, 902–912.

(38) Kropman, M. F.; Bakker, H. J. Effect of Ions on the Vibrational Relaxation of Liquid Water. *J. Am. Chem. Soc.* **2004**, *126*, 9135–9141.

(39) Kropman, M. F.; Nienhuys, H.-K.; Bakker, H. J. Real-Time Measurement of the Orientational Dynamics of Aqueous Solvation Shells in Bulk Liquid Water. *Phys. Rev. Lett.* **2002**, *88*,

077601-4.

(40) Kropman, M. F.; Bakker, H. J. Vibrational Relaxation of Liquid Water in Ionic Solvation Shells. *Chem. Phys. Lett.* **2003**, *370*, 741–746.

(41) Ting, C.; Hefter, G.; Buchner, R. Dielectric Spectroscopy of Aqueous Solutions of KCl and CsCl. *J. Phys. Chem. A* **2003**, *107*, 4025–4031.

(42) Barbara Hribar, †; Noel T. Southall, ‡; Vojko Vlachy, † and; Ken A. Dill*, §. How Ions Affect the Structure of Water. **2002**.

(43) Bakker, H. J. Structural Dynamics of Aqueous Salt Solutions. *Chem. Rev* **2008**, *108*, 1456–1473.

(44) McCall, D. W.; Douglass, D. C. Effect of Ions on the Self-Diffusion of Water. I. Concentration Dependence. *J. Phys. Chem.* **1965**, *69*, 2001–2011.

(45) Endom, L.; Hertz, H. G.; Thül, B.; Zeidler, M. D. A Microdynamic Model of Electrolyte Solutions as Derived from Nuclear Magnetic Relaxation and Self-Diffusion Data. *Berichte der Bunsengesellschaft für Phys. Chemie* **1967**, *71*, 1008–1031.

(46) Harris, K. R.; Mills, R.; Back, P. J.; Webster, D. S. An Improved NMR Spin-Echo Apparatus for the Measurement of Self-Diffusion Coefficients: The Diffusion of Water in Aqueous Electrolyte Solutions. *J. Magn. Reson.* **1978**, *29*, 473–482.

(47) Hewish, N. A.; Enderby, J. E.; Howells, W. S. The Dynamics of Water Molecules in Ionic Solution. *J. Phys. C Solid State Phys.* **1983**, *16*, 1777–1791.

(48) Buchner, R.; Hefter, G. Interactions and Dynamics in Electrolyte Solutions by Dielectric Spectroscopy. *Phys. Chem. Chem. Phys.* **2009**, *11*, 8984.

(49) Post, S. T. van der; Bakker, H. J. The Combined Effect of Cations and Anions on the Dynamics of Water. *Phys. Chem. Chem. Phys.* **2012**, *14*, 6280–6288.

(50) Nightingale, E. R. Phenomenological Theory of Ion Solvation. Effective Radii of Hydrated Ions. *J. Phys. Chem.* **1959**, *63*, 1381–1387.

(51) Jollivet, P.; Gin, S.; Schumacher, S. Forward Dissolution Rate of Silicate Glasses of Nuclear Interest in Clay-Equilibrated Groundwater. *Chem. Geol.* **2012**, *330–331*, 207–217.

(52) Ohtaki, H.; Radnai, T. Structure and Dynamics of Hydrated Ions. *Chem. Rev* **1993**, *93*, 1157–1204.

(53) McCall, D. W.; Douglass, D. C. Effect of Ions on the Self-Diffusion of Water. I.

Concentration Dependence. *J. Phys. Chem.* **1965**.

(54) Harris, K. .; Mills, R.; Back, P. .; Webster, D. . An Improved NMR Spin-Echo Apparatus for the Measurement of Self-Diffusion Coefficients: The Diffusion of Water in Aqueous Electrolyte Solutions. *J. Magn. Reson.* **1978**, *29*, 473–482.

(55) Hewish, N. A.; Enderby, J. E.; Howells, W. S. The Dynamics of Water Molecules in Ionic Solution. *J. Phys. C Solid State Phys.* **1983**, *16*, 1777–1791.

(56) Fenter, P.; Sturchio, N. C. Mineral-Water Interfacial Structures Revealed by Synchrotron X-Ray Scattering. *Prog. Surf. Sci.* **2005**, *77*, 171–258.

(57) Chapman, D. L. LI. A Contribution to the Theory of Electrocapillarity. *London, Edinburgh, Dublin Philos. Mag. J. Sci.* **1913**, *25*, 475–481.

(58) Stern, O. Zur Theorie Der Elektrolytischen Doppelschicht. *Zeitschrift für Elektrochemie und Angew. Phys. Chemie* **1924**, *30*, 508–516.

(59) Evans, D. F.; Wennerström, H. *The Colloidal Domain : Where Physics, Chemistry, Biology, and Technology Meet*, 2nd ed.; Wiley-VCH, 1999.

(60) Du, Q.; Freysz, E.; Shen, Y. R. Surface Vibrational Spectroscopic Studies of Hydrogen Bonding and Hydrophobicity. *Science (80-. ).* **1994**, *264*, 826–828.

(61) Du, Q.; Freysz, E.; Shen, Y. R. Vibrational Spectra of Water Molecules at Quartz/Water Interfaces. *Phys. Rev. Lett.* **1994**, *72*, 238–241.

(62) Ostroverkhov, V.; Waychunas, G. A.; Shen, Y. R. Vibrational Spectra of Water at Water/α-Quartz (0 0 0 1) Interface. *Chem. Phys. Lett.* **2004**, *386*, 144–148.

(63) Ostroverkhov, V.; Waychunas, G. A.; Shen, Y. R. New Information on Water Interfacial Structure Revealed by Phase-Sensitive Surface Spectroscopy. *Phys. Rev. Lett.* **2005**, *94*, 046102-4.

(64) Iler R. K. *The Chemistry of Silica - Solubility, Polymerization, Colloid and Surface Properties, and Biochemisry*; John Wiley & Sons: New York, 1979.

(65) Yang, Z.; Li, Q.; Chou, K. C. Structures of Water Molecules at the Interfaces of Aqueous Salt Solutions and Silica: Cation Effects. *J. Phys. Chem. C* **2009**, *113*, 8201–8205.

(66) Azam, M. S.; Weeraman, C. N.; Gibbs-Davis, J. M. Specific Cation Effects on the Bimodal Acid–Base Behavior of the Silica/Water Interface. *J. Phys. Chem. Lett.* **2012**, *3* (10), 1269–1274.

(67) Azam, M. S.; Darlington, A.; Gibbs-Davis, J. M. The Influence of Concentration on Specific Ion Effects at the Silica/Water Interface. *J. Phys. Condens. Matter* **2014**, *26*, 2441071–10.

(68) Jena, K. C.; Covert, P. A.; Hore, D. K. The Effect of Salt on the Water Structure at a Charged Solid Surface: Differentiating Second- and Third-Order Nonlinear Contributions. *J. Phys. Chem. Lett.* **2011**, *2*, 1056–1061.

(69) Covert, P. A.; Jena, K. C.; Hore, D. K. Throwing Salt into the Mix: Altering Interfacial Water Structure by Electrolyte Addition. *J. Phys. Chem. Lett.* **2014**, *5*, 143–148.

(70) Pezzotti, S.; Galimberti, D. R.; Shen, Y.-R.; Gaigeot, M.-P. Structural Definition of BIL and DL: A New Universal Methodology to Rationalize Non-Linear $\chi^{(2)}(\omega)$ SFG Signals at Charged Interfaces, Including $\chi^{(3)}(\omega)$ Contributions. *Phys. Chem. Chem. Phys.* **2018**, *20*, 5190–5199.

(71) Magda, J. J.; Tirrell, M.; Davis, H. T. Molecular Dynamics of Narrow, Liquid-Filled Pores. *J. Chem. Phys.* **1985**, *83*, 1888–1901.

(72) Aggarwal, N.; Sood, J.; Tankeshwar, K. Related Content Dynamical Model for Restricted Diffusion in Nano-Channels. *Nanotechnology* **2007**, *18*, 3357001–3357007.

(73) Qiao, R.; Aluru, N. R. Multiscale Modeling of Electroosmotic Flow: Effects of Discrete Ion, Enhanced Viscosity, and Surface Friction. *J. Chem. Phys.* **2003**, *118*, 4692–4701.

(74) Jensen, M.; Mouritsen, O. G.; Peters, G. H. The Hydrophobic Effect: Molecular Dynamics Simulations of Water Confined between Extended Hydrophobic and Hydrophilic Surfaces. *J. Chem. Phys.* **2004**, *120*, 9729–9744.

(75) Lee, S. H.; Rossky, P. J. A Comparison of the Structure and Dynamics of Liquid Water at Hydrophobic and Hydrophilic Surfaces-a Molecular Dynamics Simulation Study Comparison of Simple Potential Functions for Simulating Liquid Water A General Purpose Model for the Condensed Phases of Water: TIP4P/ A Comparison of the Structure and Dynamics of Liquid Water at Hydrophobic and Hydrophilic Surfaces-a Molecular Dynamics Simulation Study. *J. Chem. Phys.* **1994**, *100*, 3334–3345.

(76) Freund, J. B. Multiscale Modeling of Electroosmotic Flow: Effects of Discrete Ion, Enhanced Viscosity, and Surface Friction. *J. Chem. Phys.* **2002**, *116*, 2194–2200.

(77) Lyklema, J.; Rovillard, S.; De Coninck, J. Letters Electrokinetics: The Properties of the Stagnant Layer Unraveled. *Langmuir* **1998**, *14*, 5660–5663.

(78) Kim, D.; Darve, E. Molecular Dynamics Simulation of Electro-Osmotic Flows in Rough Wall

Nanochannels. *Phys. Rev. E* **2006**, *73*, 051203.

(79) Allaire, G.; Dufrêche, J.-F.; Mikelić, A.; Piatnitski, A. Asymptotic Analysis of the Poisson–Boltzmann Equation Describing Electrokinetics in Porous Media. *Nonlinearity* **2013**, *26*, 881–910.

(80) Bohinc, K.; Gimsa, J.; Kralj-Iglič, V.; Slivnik, T.; Iglič, A. Excluded Volume Driven Counterion Condensation inside Nanotubes in a Concave Electrical Double Layer Model. *Bioelectrochemistry* **2005**, *67*, 91–99.

(81) Prelot, B.; Lantenois, S.; Chorro, C.; Charbonnel, M.-C.; Zajac, J.; Douillard, J. M. Effect of Nanoscale Pore Space Confinement on Cadmium Adsorption from Aqueous Solution onto Ordered Mesoporous Silica: A Combined Adsorption and Flow Calorimetry Study. *J. Phys. Chem. C* **2011**, *115*, 19686–19695.

(82) Defay, R.; Prigogine, I. Surface Tension of Regular Solutions. *Trans. Faraday Soc.* **1950**, *46*, 199–210.

(83) Findenegg, G. H.; Jähnert, S.; Akcakayiran, D.; Schreiber, A. Freezing and Melting of Water Confined in Silica Nanopores. *ChemPhysChem* **2008**, *9*, 2651–2659.

(84) Alba-Simionesco, C.; Coasne, B.; Dosseh, G.; Dudziak, G.; Gubbins, K. E.; Radhakrishnan, R.; Sliwinska-Bartkowiak, M. Effects of Confinement on Freezing and Melting. *J. Phys. Condens. Matter* **2006**, *18*, R15–R68.

(85) Hansen, E. W.; Schmidt, R.; Stoecker, M.; Akporiaye, D. Water-Saturated Mesoporous MCM-41 Systems Characterized by 1H NMR Spin-Lattice Relaxation Times. *J. Phys. Chem.* **1995**, *99*, 4148–4154.

(86) Akporiaye, D.; Hansen, E. W.; Schmidt, R.; Stocker, M. Water-Saturated Mesoporous MCM-41 Systems Characterized by ’H NMR. *J. Phys. Chem.* **1994**, *98*, 1926–1928.

(87) Overloop, K.; Vangerven, L. Freezing Phenomena in Adsorbed Water as Studied by NMR. *J. Magn. Reson. Ser. A* **1993**, *101*, 179–187.

(88) Korpa, A.; Trettin, R. The Influence of Different Drying Methods on Cement Paste Microstructures as Reflected by Gas Adsorption: Comparison between Freeze-Drying (F-Drying), D-Drying, P-Drying and Oven-Drying Methods. *Cem. Concr. Res. Res.* **2006**, *36*, 634–649.

(89) Pajzderska, A.; Gonzalez, M. A.; Mielcarek, J.; W??sicki, J. Water Behavior in MCM-41 as a Function of Pore Filling and Temperature Studied by NMR and Molecular Dynamics

Simulations. *J. Phys. Chem. C* **2014**, *118*, 23701–23710.

(90) Stapf, S.; Kimmich, R. Molecular Dynamics in Confined Monomolecular Layers. A Field-cycling Nuclear Magnetic Resonance Relaxometry Study of Liquids in Porous Glass. *J. Chem. Phys.* **1995**, *103*, 2247–2250.

(91) Schreiber, A.; Ketelsen, I.; Findenegg, G. H. Melting and Freezing of Water in Ordered Mesoporous Silica Materials. *Phys. Chem. Chem. Phys.* **2001**, *3*, 1185–1195.

(92) Findenegg, G. H.; Jähnert, S.; Akcakayiran, D.; Schreiber, A. Freezing and Melting of Water Confined in Silica Nanopores. *ChemPhysChem* **2008**, *9*, 2651–2659.

(93) Christenson, H. K. Confinement Effects on Freezing and Melting. *J. Phys. Condens. Matter* **2001**, *13*, R95–R133.

(94) Morishige, K.; Nobuoka, K. X-Ray Diffraction Studies of Freezing and Melting of Water Confined in a Mesoporous Adsorbent (MCM-41). *J. Chem. Phys.* **1997**, *107*, 6965–6969.

(95) Morishige, K.; Iwasaki, H. X-Ray Study of Freezing and Melting of Water Confined within SBA-15. *Langmuir* **2003**, *19*, 2808–2811.

(96) Jelassi, J.; Grosz, T.; Bako, I.; Bellissent-Funel, M.-C.; Dore, J. C.; Castricum, H. L.; Sridi-Dorbez, R. Structural Studies of Water in Hydrophilic and Hydrophobic Mesoporous Silicas: An x-Ray and Neutron Diffraction Study at 297 K. *J. Chem. Phys.* **2011**, *134*, 064509.

(97) Gallo, P.; Rapinesi, M.; Rovere, M. Confined Water in the Low Hydration Regime. *J. Chem. Phys.* **2002**, *117*, 369–375.

(98) Smirnov, P.; Yamaguchi, T.; Kittaka, S.; Takahara, S. X-Ray Diffraction Study of Water Confined in Mesoporous MCM-41 Materials over a Temperature Range of 223 - 298 K. *J. Phys. Chem. B* **2000**, *104*, 5498–5504.

(99) Morishige, K.; Kawano, K. Freezing and Melting of Water in a Single Cylindrical Pore: The Pore-Size Dependence of Freezing and Melting Behavior. *J. Chem. Phys.* **1999**, *110*, 4867–4872.

(100) Grünberg, B.; Emmler, T.; Gedat, E.; Shenderovich, I.; Findenegg, G. H.; Limbach, H. H.; Buntkowsky, G. Hydrogen Bonding of Water Confined in Mesoporous Silica MCM-41 and SBA-15 Studied by 1H Solid-State NMR. *Chem. - A Eur. J.* **2004**, *10*, 5689–5696.

(101) Sattig, M.; Reutter, S.; Fujara, F.; Werner, M.; Buntkowsky, G.; Vogel, M.; Rupley, J. A.; Careri, G.; Rasaiah, J.; Garde, S.; et al. NMR Studies on the Temperature-Dependent Dynamics of Confined Water. *Phys. Chem. Chem. Phys.* **2014**, *16*, 19229–19240.

(102) Brubach, J.-B.; Mermet, A.; Filabozzi, A.; Gerschel, A.; Lairez, D.; Krafft, M. P.; Roy, P. Dependence of Water Dynamics upon Confinement Size. *J. Phys. Chem. B* **2001**, *105*, 430–435.

(103) Le Caër, S.; Pin, S.; Esnouf, S.; Raffy, Q.; Renault, J. P.; Brubach, J.-B.; Creff, G.; Roy, P. A Trapped Water Network in Nanoporous Material: The Role of Interfaces. *Phys. Chem. Chem. Phys.* **2011**, *13*, 17658.

(104) Huang, X. F.; Wang, Q.; Liu, X. X.; Yang, S. H.; Li, C. X.; Sun, G.; Pan, L. Q.; Lu, K. Q. Vibrational Dynamics of Water within Mesoporous Materials at Different Hydration Levels during Adsorption and Desorption Processes. *J. Phys. Chem. C* **2009**, *113*, 18768–18771.

(105) Zhang, L.; Singh, S.; Tian, C.; Shen, Y. R.; Wu, Y.; Shannon, M. A.; Brinker, C. J. Nanoporous Silica-Water Interfaces Studied by Sum-Frequency Vibrational Spectroscopy Phase Reference in Phase-Sensitive Sum-Frequency Vibrational Spectroscopy 2D Heterodyne-Detected Sum Frequency Generation Study on the Ultrafast Vibrational Dynamics of H. *J. Chem. Phys.* **2009**, *130*, 1547021–10.

(106) Ostroverkhov, V.; Waychunas, G. A.; Shen, Y. R. New Information on Water Interfacial Structure Revealed by Phase-Sensitive Surface Spectroscopy. *Phys. Rev. Lett.* **2005**, *94*, 2–5.

(107) Banys, J.; Kinka, M.; MacUtkevic, J.; Völkel, G.; Böhlmann, W.; Umamaheswari, V.; Hartmann, M.; Pöppl, A. Broadband Dielectric Spectroscopy of Water Confined in MCM-41 Molecular Sieve Materials - Low-Temperature Freezing Phenomena. *J. Phys. Condens. Matter* **2005**, *17*, 2843–2857.

(108) Martynas, K.; Juras, B.; Jan, M.; Andreas, P.; Winfried, B.; Venkatesan, U.; Martin, H.; Georg, V. Dielectric Response of Water Confined in MCM-41 Molecular Sieve Material. *Phys. Status Solidi* **2005**, *242*, 100–102.

(109) Ryabov, Y.; Gutina, A.; Arkhipov, V.; Feldman, Y. Dielectric Relaxation of Water Absorbed in Porous Glass. *J. Phys. Chem. B* **2001**, *105*, 1845–1850.

(110) Teixeira, J.; Bellissent-Funel, M.-C.; Chen, S. H.; Dianoux, A. J. Experimental Determination of the Nature of Diffusive Motions of Water Molecules at Low Temperatures. *Phys. Rev. A* **1985**, *31*, 1913–1917.

(111) Takahara, S.; Nakano, M.; Kittaka, S.; Kuroda, Y.; Mori, T.; Hamano, H.; Yamaguchi, T. Neutron Scattering Study on Dynamics of Water Molecules in MCM-41. *J. Phys. Chem. B* **1999**, *103*, 5814–5819.

(112) Osti, N. C.; Coté, A.; Mamontov, E.; Ramirez-Cuesta, A.; Wesolowski, D. J.; Diallo, S. O.

Characteristic Features of Water Dynamics in Restricted Geometries Investigated with Quasi-Elastic Neutron Scattering. *Chem. Phys.* **2016**, *465–466*, 1–8.

(113) Bellissent-Funel, M.-C.; Chen, S. H.; Zanotti, J.-M. Single-Particle Dynamics of Water Molecules in Confined Space. *Phys. Rev. E* **1995**, *51*, 4558–4569.

(114) Zanotti, J.-M.; Bellissent-Funel, M.-C.; Chen, S.-H. Relaxational Dynamics of Supercooled Water in Porous Glass. *Phys. Rev. E* **1999**, *59*, 3084–3093.

(115) Bellissent-Funel, M. C.; Chen, S. H.; Zanotti, J. M. Single-Particle Dynamics of Water in Confined Space. *Phys. Rev. E* **1995**, *51*, 4558–4569.

(116) Takahara, S.; Kittaka, S.; Mori, T.; Kuroda, Y.; Yamaguchi, T.; Bellissent-Funel, M. C. Neutron Scattering Study on Dynamics of Water Molecules Confined in MCM-41. *Adsorption* **2005**, *11*, 479–483.

(117) S Mitra, R Mukhopadhyay, I. T. and S. I. Dynamics of Water in Confined Space ( Porous Alumina ): QENS Study. **2001**, *8455*.

(118) Mamontov, E.; Burnham, C. J.; Chen, S. H.; Moravsky, A. P.; Loong, C. K.; De Souza, N. R.; Kolesnikov, A. I. Dynamics of Water Confined in Single- and Double-Wall Carbon Nanotubes. *J. Chem. Phys.* **2006**, *124*.

(119) Briman, I. M.; Rébiscoul, D.; Diat, O.; Zanotti, J.-M.; Jollivet, P.; Barboux, P.; Gin, S. Impact of Pore Size and Pore Surface Composition on the Dynamics of Confined Water in Highly Ordered Porous Silica. *J. Phys. Chem. C* **2012**, *116*, 7021–7028.

(120) Korb, J.-P. Multiscale Nuclear Magnetic Relaxation Dispersion of Complex Liquids in Bulk and Confinement. *Prog. Nucl. Magn. Reson. Spectrosc.* **2018**, *104*, 12–55.

(121) Kimmich, R.; Stapf, S.; Maklakov, A. I.; Skirda, V. D.; Khozina, E. V. Self-Diffusion in Fluids in Porous Glass: Confinement by Pores and Liquid Adsorption Layers. *Magn. Reson. Imaging* **1996**, *14*, 793–797.

(122) Gallo, P.; Rovere, M.; Chen, S.-H. Anomalous Dynamics of Water Confined in MCM- 41 at Different Hydrations Anomalous Dynamics of Water Confined in MCM-41 at Different Hydrations. *J. Phys. Condens. Matter* **2010**, *22*, 284102–284110.

(123) Mamontov, E.; Cole, D. R. Quasielastic Neutron Scattering Study of Dynamics of CaCl2 Aqueous Solution Confined in Vycor Glass. *Phys. Chem. Chem. Phys.* **2006**, *8*, 4908–4914.

(124) Ruiz-Agudo, E.; Urosevic, M.; Putnis, C. V; Rodríguez-Navarro, C.; Cardell, C.; Putnis, A. Ion-Specific Effects on the Kinetics of Mineral Dissolution. *Chem. Geol.* **2011**, *281*, 364–

371.

(125) Ruiz-Agudo, E.; Kowacz, M.; Putnis, C. V.; Putnis, A. The Role of Background Electrolytes on the Kinetics and Mechanism of Calcite Dissolution. *Geochim. Cosmochim. Acta* **2010**, *74*, 1256–1267.

(126) Kowacz, M.; Putnis, A. The Effect of Specific Background Electrolytes on Water Structure and Solute Hydration: Consequences for Crystal Dissolution and Growth. *Geochim. Cosmochim. Acta* **2008**, *72*, 4476–4487.

(127) Dove, P. M.; Crerar, D. A. Kinetics of Quartz Dissolution in Electrolyte Solutions Using a Hydrothermal Mixed Flow Reactor. *Geochim. Cosmochim. Acta* **1990**, *54*, 955–969.

(128) Dove, P. M.; Elston, S. F. Dissolution Kinetics of Quartz in Sodium Chloride Solutions: Analysis of Existing Data and a Rate Model for 25°C. *Geochim. Cosmochim. Acta* **1992**, *56*, 4147–4156.

(129) Dove, P. M.; Nix, C. J. The Influence of the Alkaline Earth Cations, Magnesium, Calcium, and Barium on the Dissolution Kinetics of Quartz. *Geochim. Cosmochim. Acta* **1997**, *61*, 3329–3340.

(130) Jollivet, P.; Gin, S.; Schumacher, S. Forward Dissolution Rate of Silicate Glasses of Nuclear Interest in Clay-Equilibrated Groundwater. *Chem. Geol.* **2012**, *330–331*, 207–217.

(131) Dewan, S.; Yeganeh, M. S.; Borguet, E. Experimental Correlation Between Interfacial Water Structure and Mineral Reactivity. *J. Phys. Chem. Lett.* **2013**, *4*, 1977–1982.

(132) Wallace, A. F.; Gibbs, G. V.; Dove, P. M. Influence of Ion-Associated Water on the Hydrolysis of Si-O Bonded Interactions. *J. Phys. Chem. A* **2010**, *114*, 2534–2542.

(133) El Mourabit, S.; Guillot, M.; Toquer, G.; Cambedouzou, J.; Goettmann, F.; Grandjean, A. Stability of Mesoporous Silica under Acidic Conditions. *RSC Adv.* **2012**, 10916–10924.

(134) Tas, N. R.; Haneveld, J.; Jansen, H. V.; Elwenspoek, M.; Van Den Berg, A. Capillary Filling Speed of Water in Nanochannels. *Appl. Phys. Lett.* **2004**, *85*, 3274–3276.

(135) Hibara, A.; Saito, T.; Kim, H.-B.; Tokeshi, M.; Ooi, T.; Nakao, M.; Kitamori, T. Nanochannels on a Fused-Silica Microchip and Liquid Properties Investigation by Time-Resolved Fluorescence Measurements. *Anal. Chem.* **2002**, *74*, 6170–6176.

(136) Haneveld, J.; Tas, N. R.; Brunets, N.; Jansen, H. V.; Elwenspoek, M. Capillary Filling of Sub-10 Nm Nanochannels. *J. Appl. Phys.* **2008**, *104*.

(137) Bedzyk, M. J.; Bommarito, G. M.; Caffrey, M.; Penner, T. L. Diffuse-Double Layer at a

Membrane-Aqueous Interface Measured with x-Ray Standing Waves. *Science*. 1990, pp 52–56.

(138) Guinier, A.; Lorrain, P.; Lorrain, D. S.; Gillis, J. *X-Ray Diffraction in Crystals, Imperfect Crystals, and Amorphous Bodies*; Dover Publications: New York, 1962.

(139) Hocine, S.; Hartkamp, R.; Siboulet, B.; Duvail, M.; Coasne, B.; Turq, P.; Dufrêche, J.-F. How Ion Condensation Occurs at a Charged Surface: A Molecular Dynamics Investigation of the Stern Layer for Water−Silica Interfaces. *J. Phys. Chem. C* **2016**, *120*, 963–973.

(140) Lorenz, C. D.; Crozier, P. S.; Anderson, J. A.; Travesset, A. Molecular Dynamics of Ionic Transport and Electrokinetic Effects in Realistic Silica Channels. *J. Phys. Chem. C* **2008**, *112*, 10222–10232.

(141) Bogusz, S.; Cheatham, T. E.; Brooks, B. R. Removal of Pressure and Free Energy Artifacts in Charged Periodic Systems via Net Charge Corrections to the Ewald Potential. *J. Chem. Phys.* **1998**, *108*, 7070–7084.

(142) Hub, J. S.; de Groot, B. L.; Grubmüller, H.; Groenhof, G. Quantifying Artifacts in Ewald Simulations of Inhomogeneous Systems with a Net Charge. *J. Chem. Theory Comput.* **2014**, *10*, 381–390.

(143) Berendsen, H. J. C.; Grigera, J. R.; Straatsma, T. P. The Missing Term in Effective Pair Potentials. *J. Phys. Chem.* **1987**, *91* (24), 6269–6271.

(144) Boda*, D.; Henderson, D.; Plaschko‡, P.; Ronald Fawcett¶, W. Monte Carlo and Density Functional Theory Study of the Electrical Double Layer: The Dependence of the Charge/Voltage Relation on the Diameter of the Ions. *Mol. Simul.* **2004**, *30*, 137–141.

(145) Puibasset, J.; Pellenq, R. J.-M. Grand Canonical Monte Carlo Simulation Study of Water Structure on Hydrophilic Mesoporous and Plane Silica Substrates. *J. Chem. Phys.* **2003**, *119* (17), 9226–9232.

(146) Bonnaud, P. A.; Coasne, B.; Pellenq, R. J.-M. Molecular Simulation of Water Confined in Nanoporous Silica. *J. Phys. Condens. Matter* **2010**, *22* (28), 284110.

(147) Dove, P. M. The Dissolution Kinetics of Quartz in Aqueous Mixed Cation Solutions. *Geochim. Cosmochim. Acta* **1999**, *63*, 3715–3727.

(148) IUPAC - NIST Solubility Data Series Database, Version 1.0 https://srdata.nist.gov/solubility/index.aspx (accessed Sep 5, 2018).

(149) Stumm, W. *Chemistry of the Solid-Water Interface: Processes at the Mineral-Water and*

*Particle-Water Interface in Natural Systems.*; John Wiley & Son Inc.: Ney York, 1992.

(150) Putnis, A. Transient Porosity Resulting from Fluid–Mineral Interaction and Its Consequences. *Rev. Mineral. Geochemistry* **2015**, *80*, 1–23.

(151) Nindiyasari, F.; Fernández-Díaz, L.; Griesshaber, E.; Astilleros, J. M.; Sánchez-Pastor, N.; Schmahl, W. W. Influence of Gelatin Hydrogel Porosity on the Crystallization of CaCO3. *Cryst. Growth Des.* **2014**, *14*, 1531–1542.

(152) Putnis, A.; Prieto, M.; Fernandez-Diaz, L. Fluid Supersaturation and Crystallization in Porous Media. *Geol. Mag.* **1995**, *132*, 1–13.

(153) Emmanuel, S.; Ague, J. J.; Walderhaug, O. Interfacial Energy Effects and the Evolution of Pore Size Distributions during Quartz Precipitation in Sandstone. *Geochim. Cosmochim. Acta* **2010**, *74*, 3539–3552.

(154) Emmanuel, S.; Berkowitz, B. Effects of Pore-Size Controlled Solubility on Reactive Transport in Heterogeneous Rock. *Geophys. Res. Lett.* **2007**, *34*, L06404.

(155) Rijniers, L. .; Magusin, P. C. M. .; Huinink, H. .; Pel, L.; Kopinga, K. Sodium NMR Relaxation in Porous Materials. *J. Magn. Reson.* **2004**, *167*, 25–30.

(156) Rijniers, L. A.; Huinink, H. P.; Pel, L.; Kopinga, K. Experimental Evidence of Crystallization Pressure inside Porous Media. *Phys. Rev. Lett.* **2005**, *94*, 075503(4).

(157) Stack, A. G.; Fernandez-Martinez, A.; Allard, L. F.; Bañ, J. J.; Rother, G.; Anovitz, L. M.; Cole, D. R.; Waychunas, G. A. Pore-Size-Dependent Calcium Carbonate Precipitation Controlled by Surface Chemistry. *Enviromental Sci. &Technology* **2014**, *48*, 6177–6183.

(158) Zeng, M.; Kim, Y.-Y.; Anduix-Canto, C.; Frontera, C.; Laundy, D.; Kapur, N.; Christenson, H. K.; Meldrum, F. C. Confinement Generates Single-Crystal Aragonite Rods at Room Temperature. *Proc. Natl. Acad. Sci. U. S. A.* **2018**, *115*, 7670–7675.

(159) Rébiscoul, D.; Tormos, V.; Godon, N.; Mestre, J.-P.; Cabie, M.; Amiard, G.; Foy, E.; Frugier, P.; Gin, S. Reactive Transport Processes Occurring during Nuclear Glass Alteration in Presence of Magnetite. *Appl. Geochemistry* **2015**, *58*, 26–37.

(160) Dillmann, P.; Gin, S.; Neff, D.; Gentaz, L.; Rebiscoul, D. Effect of Natural and Synthetic Iron Corrosion Products on Silicate Glass Alteration Processes. *Geochim. Cosmochim. Acta* **2016**, *172*, 287–305.

(161) Michelin, A.; Burger, E.; Rebiscoul, D.; Neff, D.; Bruguier, F.; Drouet, E.; Dillmann, P.; Gin, S. Silicate Glass Alteration Enhanced by Iron: Origin and Long-Term Implications. *Environ.*

*Sci. Technol.* **2013**, *47* (2), 750–756.

(162) Mansas, C.; Delaye, J.-M.; Charpentier, T.; Bruguier, F.; Bouty, O.; Penelon, B.; Arena, H.; Rébiscoul, D. Drivers of Water Transport in Glass: Chemical or Topological Effect of the Glass Network? *J. Phys. Chem. C* **2017**, *121*, 16201–16215.

(163) Aréna, H.; Godon, N.; Rébiscoul, D.; Podor, R.; Garcès, E.; Cabie, M.; Mestre, J.-P. Impact of Zn, Mg, Ni and Co Elements on Glass Alteration: Additive Effects. *J. Nucl. Mater.* **2016**, *470*, 55–67.

(164) Rouquerol, J.; Avnir, D.; Fairbridge, C. W.; D. H. Everett; Haynes, J. H.; Pernicone, N.; Ramsay, J. D. F.; Unger, K. S. W. S. Recommendations for the Characterization of Porous Solids. *Pure Appl. Chem.* **1994**, *66*, 1739–1758.

(165) Zhao, D.; Huo, Q.; Feng, J.; Chmelka, B. F.; Stucky, G. D. Nonionic Triblock and Star Diblock Copolymer and Oligomeric Surfactant Syntheses of Highly Ordered, Hydrothermally Stable, Mesoporous Silica Structures. *J. Am. Chem. Soc.* **1998**, *120*, 6024–6036.

(166) Chen, H.; Wang, Y. Preparation of MCM-41 with High Thermal Stability and Complementary Textural Porosity. *Ceram. Int.* **2002**, *28*, 541–547.

(167) Ichinose, I.; Senzu, H.; Kunitake, T. Stepwise Adsorption of Metal Alkoxides on Hydrolyzed Surfaces : A Surface Sol-Gel Process. *Chem. Lett.* **1996**, *25*, 831–832.

(168) Gallé, C. Effect of Drying on Cement-Based Materials Pore Structure as Identified by Mercury Intrusion Porosimetry A Comparative Study between Oven-, Vacuum-, and Freeze-Drying. *Cem. Concr. Res. Res.* **2001**, *31*, 1467–1477.

(169) Azuah, R. T.; Kneller, L. R.; Qiu, Y.; Tregenna-Piggott, P. L. W.; Brown, C. M.; Copley, J. R. D.; Dimeo, R. M. DAVE: A Comprehensive Software Suite for the Reduction, Visualization, and Analysis of Low Energy Neutron Spectroscopic Data. *J. Res. Natl. Inst. Stand. Technol.* **2009**, *114*, 341–358.

(170) Rébiscoul, D.; Bruguier, F.; Magnin, V.; Gin, S. Impact of Soda-Lime Borosilicate Glass Composition on Water Penetration and Water Structure at the First Time of Alteration. *J. Non. Cryst. Solids* **2012**, *358*, 2951–2960.

(171) Templin, M.; Franck, A.; Du Chesne A, A. Du; Leist, H.; Zhang, Y.; Ulrich, R.; Schadler, V.; Wiesner, U. Organically Modified Aluminosilicate Mesostructures from Block Copolymer Phases. *Sci.* **1997**, *278*, 1795–1798.

(172) Melosh, N. A.; Lipic, P.; Bates, F. S.; Wudl, F.; Stucky, G. D.; G. H. Fredrickson, A.; Chmelka, B. F. Molecular and Mesoscopic Structures of Transparent Block Copolymer−Silica Monoliths. *Macromolecules* **1999**, *32*, 4332–4342.

(173) Limousin, G.; Gaudet, J.-P.; Charlet, L.; Szenknect, S.; Barthès, V.; Krimissa, M. Sorption Isotherms: A Review on Physical Bases, Modeling and Measurement. *Appl. Geochemistry* **2007**, *22*, 249–275.

(174) Dove, P. M.; Han, N.; Wallace, A. F.; De Yoreo, J. J. Kinetics of Amorphous Silica Dissolution and the Paradox of the Silica Polymorphs. *Proc. Natl. Acad. Sci.* **2008**, *105*, 9903–9908.

(175) C. Brinker; Scherer, G. *Sol-Gel Science: The Physics and Chemistry of Sol-Gel Processing*; Academic Press Co: San Diego, 1990; Vol. 3.

(176) Brubach, J. B.; Mermet, A.; Filabozzi, A.; Gerschel, A.; Roy, P. Signatures of the Hydrogen Bonding in the Infrared Bands of Water. *J. Chem. Phys.* **2005**, *122*, 184509–224511.

(177) Crupi, V.; Longo, F.; Majolino, D.; Venuti, V. T Dependence of Vibrational Dynamics of Water in Ion-Exchanged Zeolites A: A Detailed Fourier Transform Infrared Attenuated Total Reflection Study. *J. Chem. Phys.* **2005**, *123*.

(178) Findenegg, G. H.; Jähnert, S.; Akcakayiran, D.; Schreiber, A. Freezing and Melting of Water Confined in Silica Nanopores. *ChemPhysChem* **2008**, *9*, 2651–2659.

(179) Kittaka, S.; Ishimaru, S.; Kuranishi, M.; Matsuda, T.; Yamaguchi, T. Enthalpy and Interfacial Free Energy Changes of Water Capillary Condensed in Mesoporous Silica, MCM-41 and SBA-15. *Phys. Chem. Chem. Phys.* **2006**, 3223–3231.

(180) Denoyel, R.; Pellenq, R. J. M. Simple Phenomenological Models for Phase Transitions in a Confined Geometry. 1: Melting and Solidification in a Cylindrical Pore. *Langmuir* **2002**, *18*, 2710–2716.

(181) Jähnert, S.; Vaca Chávez, F.; Schaumann, G. E.; Schreiber, A.; Schönhoff, M.; Findenegg, G. H. Melting and Freezing of Water in Cylindrical Silica Nanopores. *Phys. Chem. Chem. Phys.* **2008**, *39*, 6039–6051.

(182) Dagade, D. H.; Barge, S. S. Hydrogen Bonding in Liquid Water and in the Hydration Shell of Salts. *ChemPhysChem* **2016**, *17*, 902–912.

(183) Chen, Y.; Okur, H. I.; Gomopoulos, N.; Macias-Romero, C.; Cremer, P. S.; Petersen, P. B.; Tocci, G.; Wilkins, D. M.; Liang, C.; Ceriotti, M.; et al. Electrolytes Induce Long-Range

Orientational Order and Free Energy Changes in the H-Bond Network of Bulk Water. *Sci. Adv.* **2016**, *2*, 1–8.

(184) Hribar, B.; Southall, N. T.; Vlachy, V.; Dill, K. A. How Ions Affect the Structure of Water. *J. Am. Chem. Soc.* **2002**, *124*, 12302–12311.

(185) Mallamace, F.; Broccio, M.; Corsaro, C.; Faraone, A.; Majolino, D.; Venuti, V.; Liu, L.; Mou, C.-Y.; Chen, S.-H. Evidence of the Existence of the Low-Density Liquid Phase in Supercooled, Confined Water. *Proc. Natl. Acad. Sci. U. S. A.* **2007**, *104*, 424–428.

(186) Crupi, V.; Interdonato, S.; Longo, F.; Majolino, D.; Migliardo, P.; Venuti, V. A New Insight on the Hydrogen Bonding Structures of Nanoconfined Water: A Raman Study. *J. Raman Spectrosc.* **2008**, *39*, 244–249.

(187) Rovere, M.; Gallo, P. Effects of Confinement on Static and Dynamical Properties of Water. *Eur. Phys. J. E* **2003**, *12*, 77–81.

(188) Gallo, P.; Ricci, M. A.; Rovere, M. Layer Analysis of the Structure of Water Confined in Vycor Glass. *J. Chem. Phys.* **2002**, *116*, 342–346.

(189) Marc, B. *Quasielastic Neutron Scatering*; Adam Hilger: Bristol and Philadelphia, 1988.

(190) Teixeira, J.; Bellissent-Funel, M. C.; Chen, S. H.; Dianoux, A. J. Experimental Determination of the Nature of Diffusive Motions of Water Molecules at Low Temperatures. *Phys. Rev. A* **1985**, *31*, 1913–1917.

(191) Sears, V. F. Cold Neutron Scattering by Molecular Liquids: III. Methane. *Can. J. Phys.* **1967**, *45*, 237–254.

(192) Volino, F.; Dianoux, A. J. Neutron Incoherent Scattering Law for Diffusion in a Potential of Spherical Symmetry: General Formalism and Application to Diffusion inside a Sphere. *Mol. Phys.* **1980**, *41*, 271–279.

(193) Singwi, K. S.; Sjölander, A. Diffusive Motions in Water and Cold Neutron Scattering. *Phys. Rev.* **1960**, *119*, 863–871.

(194) Shuichi Takahara; Naoya Sumiyama, A.; Kittaka, S.; Yamaguchi, T.; Bellissent-Funel, M.-C. Neutron Scattering Study on Dynamics of Water Molecules in MCM-41. 2. Determination of Translational Diffusion Coefficient. *J. Phys. Chem. B* **2005**, *109*, 11231–11239.

(195) Qvist, J.; Schober, H.; Halle, B. Structural Dynamics of Supercooled Water from Quasielastic Neutron Scattering and Molecular Simulations. *J. Chem. Phys.* **2011**, *134*, 144508–144520.

(196) Zanotti, J.-M.; Bellissent-Funel, M.-C.; Chen, S.-H. Relaxational Dynamics of Supercooled

Water in Porous Glass. *Phys. Rev.* **1999**, *59*, 3084–3093.

(197) Smirnov, P.; Yamaguchi, T.; Kittaka, S.; Takahara, S.; Kuroda, Y. X-Ray Diffraction Study of Water Confined in Mesoporous MCM-41 Materials over a Temperature Range of 223-298 K. *J. Phys. Chem. B* **2000**, *104*, 5498–5504.

(198) Argyris, D.; Cole, D. R.; Striolo, A. Ion-Specific Effects under Confinement: The Role of Interfacial Water. *Am. Chem. Soc. Nano* **2010**, *4*, 2035–2042.

(199) Grahame, D. C. The Electrical Double Layer and the Theory of Electrocapillarity. *Chem. Rev.* **1947**, *41*, 441–501.

(200) Bockris, J. O.; Devanathan, M. A. V.; Müller, K. On the Structure of Charged Interfaces. *Electrochemistry* **1965**, 832–863.

(201) Darlington, A. M.; Jarisz, T. A.; Dewalt-Kerian, E. L.; Roy, S.; Kim, S.; Azam, M. S.; Hore, D. K.; Gibbs, J. M. Separating the PH-Dependent Behavior of Water in the Stern and Diffuse Layers with Varying Salt Concentration. *J. Phys. Chem. C* **2017**, *121*, 20229–20241.

(202) DeWalt-Kerian, E. L.; Kim, S.; Azam, M. S.; Zeng, H.; Liu, Q.; Gibbs, J. M. PH-Dependent Inversion of Hofmeister Trends in the Water Structure of the Electrical Double Layer. *J. Phys. Chem. Lett.* **2017**, *8*, 2855–2861.

(203) Jena, K. C.; Covert, P. A.; Hore, D. K. The Effect of Salt on the Water Structure at a Charged Solid Surface: Differentiating Second- and Third-Order Nonlinear Contributions. *J. Phys. Chem. Lett.* **2011**, *2*, 1056–1061.

(204) Collins, K. D.; Washabaugh, M. W. The Hofmeister Effect and the Behaviour of Water at Interfaces. *Q. Rev. Biophys.* **1985**, *18*, 323–422.

(205) Cambedouzou, J.; Diat, O. Quantitative Small-Angle Scattering on Mesoporous Silica Powders: From Morphological Features to Specific Surface Estimation. *J. Appl. Crystallogr.* **2012**, *45*, 662–673.

(206) Busson, B.; Doucet, J.; IUCr. Distribution and Interference Functions for Two-Dimensional Hexagonal Paracrystals. *Acta Crystallogr. Sect. A Found. Crystallogr.* **2000**, *56*, 68–72.

(207) Lowell, S. (Seymour). *Characterization of Porous Solids and Powders : Surface Area, Pore Size, and Density*; Kluwer Academic Publishers, 2006.

(208) Guthrie, C. P.; Reardon, E. J. Metastability of MCM-41 and Al-MCM-41. *J. Phys. Chem. A* **2008**, *112*, 3386–3390.

(209) Aréna, H.; Rébiscoul, D.; Podor, R.; Garcès, E.; Cabie, M.; Mestre, J.-P.; Godon, N. Impact

of Fe, Mg and Ca Elements on Glass Alteration: Interconnected Processes. *Geochim. Cosmochim. Acta* **2018**, *239*, 420–445.

(210) Aréna, H.; Godon, N.; Rébiscoul, D.; Frugier, P.; Podor, R.; Garcès, E.; Cabie, M.; Mestre, J.-P. Impact of Iron and Magnesium on Glass Alteration: Characterization of the Secondary Phases and Determination of Their Solubility Constants. *Appl. Geochemistry* **2017**, *82*, 119–133.

# Table of Figures

**Abstract:**

In this study, we investigated the water properties in the presence of ions in silica nanoconfinement. The main objective is to relate these water properties to the evolution of silica mesoporous materials in aqueous solutions. To reach this goal, we used an original approach, consisting in the use of electrolyte solutions having ions with various kosmotropic properties $XCl_2$ (X = Ba, Ca, Mg) confined in model systems such as two parallel and plane silica surfaces spaced of 3 and 5 nm (nanochannels) and highly ordered mesoporous silica materials represented by SBA-15 (6 nm pore size and microporous pore wall) and MCM-41 (3 nm pore size and dense pore wall).

The obtained results indicate that the filling kinetics in nanochannels are driven by the size of the confinement, the nature of ions and the salt solubility of electrolytes. In some cases, the incomplete filling of the nanochannels may be explained by a decrease of water dynamics associated to the saturation of $XCl_2$ salts into the interfacial layer. The possible precipitation of $XCl_2$ phases may explain an incomplete filling by a nanochannels clogging.

Thereafter, the water properties in nanoconfinement made of silica concave surface such as cylinders were studied. The water structure and dynamics at a pico-second time scale in presence of ions were characterized by infrared spectroscopy and quasi-elastic neutron scattering. The results suggest that the structural and dynamical water properties are strongly affected by the size of the confinement, the kosmotropic properties of ions and the surface ion excess in the interfacial layer.

Finally, we characterized the evolution of the two mesoporous silica in electrolyte solutions using in-situ small-angle X-ray scattering. For 3 nm pore size and dense pore wall (MCM-41), the slow dynamics at a pico-second time scale probably lead to a supersaturation of ions in the interfacial layer and thus, to a reprecipitation of $XCl_2$ salts and/or silica phases. In that case, the evolution of the MCM-41 is driven by a dissolution-recondesation/precipitation process. In the bigger mesopores of SBA-15, due to the microporosity in the pore wall, the alteration process is different. During a first stage, an alteration layer is formed and the pore size increases until the silica saturation. Afterwards, a similar recondensation/precipitation process as observed in MCM-41 occurs into the microporosity. These two types silica evolutions could persist until the formation of a thermodynamic stable silica phase.

**Resumé:**

Dans cette thèse, les propriétés de l'eau en présence d'ions dans des nanoconfinement à base de silice ont été étudiées. L'objectif principal est de relier ces propriétés à l'évolution des matériaux mésoporeux de silice dans les solutions aqueuses. Pour atteindre cet objectif, nous avons utilisé une approche originale consistant à remplir avec des solutions électrolytiques comportant des ions ayant des propriétés kosmotropes différentes, $XCl_2$ (X = Ba, Ca, Mg) des systèmes modèles tels que deux surfaces de silice parallèles et planes espacées de 3 et 5 nm (nanocanaux) et des silices à mesoporosité ordonnée comme les silices

SBA-15 (6 nm de taille pores et murs des pores microporeux) et MCM-41 (3 nm de taille de pores et murs des pores denses).

Les résultats obtenus indiquent que la cinétique de remplissage des nanocanaux dépend de la taille du confinement, de la nature des ions et de la solubilité des sels associés aux électrolytes. Dans certains cas, le remplissage incomplet des nanocanaux peut s'expliquer par une diminution de la dynamique de l'eau associée à l'atteinte de la saturation vis-à-vis des sels $XCl_2$ dans la couche interfaciale. La possible précipitation de phases $XCl_2$ pourrait permettre d'expliquer le bouchage de certains nanocanaux. Par la suite, les propriétés de l'eau dans des nanoconfinement concave de silice tels que les cylindres ont également été étudiées. La structure de l'eau en présence d'ions et sa dynamique à l'échelle de la picoseconde caractérisées respectivement par FTIR-ATR et diffusion quasi élastique des neutrons, ont été analysées. Les résultats suggèrent que les propriétés structurales et dynamiques de l'eau sont fortement influencées par la taille du confinement, le caractère kosmotrope des ions et l'excès d'ions dans la couche interfaciale.

Enfin, nous avons déterminé l'évolution des deux silices mésoporeuses dans des solutions électrolytiques par diffusion des rayons X aux petits angles. Pour une taille de pore de 3 nm et des murs de pores denses (MCM-41), une dynamique de l'eau lente à une échelle picoseconde conduit probablement à une sursaturation des ions dans la couche interfaciale et donc à une reprécipitation des sels $XCl_2$ et / ou de la silice plus stable. Dans ce cas, l'évolution du MCM-41 est induite par un processus de dissolution-recondensation / précipitation. Dans les plus grands mésopores du SBA-15, en raison de la microporosité dans la paroi des pores, le processus d'altération est différent. Dès le début, une couche d'altération se forme et la taille des pores augmente jusqu'à saturation de la silice. Par la suite, un processus de recondensation / précipitation similaire à celui observé dans la MCM-41 se produit dans la microporosité. Ces deux types d'évolutions en silice pourraient persister jusqu'à l'obtention d'une phase de silice thermodynamiquement stable.